Technische Universität München

TUM School of Engineering and Design

Integrated Sensor System for Monitoring the Braiding Process as a Use Case for Digitalization in Composite Production Technology

Stephan Johannes Maidl

Vollständiger Abdruck der von der TUM School of Engineering and Design der Technischen Universität München zur Erlangung des akademischen Grades eines

Doktors der Ingenieurwissenschaften (Dr.-Ing.)

genehmigten Dissertation.

Vorsitz:

Prof. Dr.-Ing. Wolfram Volk

Prüfer der Dissertation:

1. Prof. Dr.-Ing. Klaus Drechsler
2. Prof. Paul Robinson, Ph.D.
3. Prof. Dr.-Ing. habil. Yordan Kyosev

Die Dissertation wurde am 23.06.2022 bei der Technischen Universität München eingereicht und durch die TUM School of Engineering and Design am 19.12.2022 angenommen.

Technische Universität München
TUM School of Engineering and Design
Department of Aerospace and Geodesy
Lehrstuhl für Carbon Composites
Boltzmannstraße 15
D-85748 Garching bei München
Tel.: +49 (0) 89 / 289 – 15092
Fax: +49 (0) 89 / 289 – 15097
Email: info.lcc@ed.tum.de
Web: www.asg.ed.tum.de/lcc/de

Technical University of Munich
TUM School of Engineering and Design
Department of Aerospace and Geodesy
Chair of Carbon Composites
Boltzmannstraße 15
D-85748 Garching near Munich
Phone: +49 (0) 89 / 289 – 15092
Fax: +49 (0) 89 / 289 – 15097
Email: info.lcc@ed.tum.de
Web: www.asg.ed.tum.de/lcc/en

ACKNOWLEDGMENT

Firstly, I would like to thank Prof. Dr.-Ing. Klaus Drechsler for giving me the opportunity to conduct my research on braiding technology at his well-established Chair of Carbon Composites at Technical University of Munich. He permitted me ample freedom in my work at the chair while always giving helpful guidance and kind advice in our progress meetings. Many thanks are also due to Prof. Paul Robinson, PhD and Prof. Dr.-Ing. habil. Yordan Kyosev for their valuable advice during the preparation of this dissertation. I have known Prof. Paul Robinson since my master's thesis which I was allowed to conduct under the joint-supervision of him and Prof. Drechsler at the Department of Aeronautics at Imperial College London. His mind full of ideas and his calm way of thoroughly thinking through concepts has been an inspiration for my work at the Chair of Carbon Composites. I also thank him for his time in accompanying the dissertation at hand from the beginning on as a mentor. Prof. Kyosev is the author and editor of the well-known books on braiding technology "Braiding Technology for Textiles" and "Advances in Braiding Technology" (both published by Woodhead Publishing), which I enjoyed consulting as a doctoral candidate. I was delighted to get to know him at the 13th International Conference on Textile Composites in Milan, Italy in 2018. With his enthusiasm for braiding technology, he has given me great confidence that my work is important for the field of braiding and that it is appreciated not only at the Chair of Carbon Composites but also in the scientific community.

Secondly, I would like to thank my colleagues at the Chair of Carbon Composites for their support. I particularly would like to highlight Dr.-Ing. Swen Zaremba for his infinite kindness and understanding also for personal matters, Dr.-Ing. Christoph Ebel and Dr.-Ing. Andreas Mierzwa for helping me define the topic of the dissertation at hand, Dipl.-Ing. Kalle Kind for his guidance as my long-term group leader as well as Mr. Reiner Rauch, Mr. Thomas Witteczek and Daniel Amrein, M.Sc. for their support as technicians in the workshop and laboratory.

Thirdly, I would like to acknowledge the funding for my work, which was provided by the German Federal Ministry of Education and Research (project "InSensoFlecht" under the funding scheme "KMU-innovativ Produktionsforschung", funding code: 02P16K553) and the German Federal Ministry for Economic Affairs and Energy (project: "IMoFlecht" under the funding scheme "Zentrales Innovationsprogramm Mittelstand", funding code: ZF4004324HB9).

Finally, I would like to thank my personal environment, namely my parents Dr. Franz-Xaver Maidl and Dr. Mechthild Bolik-Maidl for their support throughout my entire life, my faithful partner Elisabeth Lorenz for relentlessly pushing me to finish the dissertation at hand and my friend Daniel Riederer for being my best mate. I would also like to thank Dipl.-Ing. Franz Maidl (who just happens to have the same surname as me) for infecting me with the "composites virus" in his role as supervisor during my internship at the department for material development at the Bayerische Motorenwerke AG (BMW AG) in Landshut. Retrospectively, he has helped set the course of my professional life for a significant time.

Oberviehhausen, June 2022 Stephan Maidl

KURZFASSUNG

Das Flechten von Verstärkungsfasern wird in der Luftfahrt, dem Automobilbereich oder der Sport- und Freizeitindustrie angewendet, wenn gekrümmte Hohlbauteile mit variierenden Querschnitten aus faserverstärkten Kunststoffen hergestellt werden sollen. Als direkter Preformingprozess bietet das Flechtverfahren die Möglichkeit – im Vergleich zur Verarbeitung vorgefertigter Textilien oder vorimprägnierten Halbzeugen – kostengünstige Faserstränge zu verarbeiten und dabei hohe Produktionsraten zu realisieren.

Flechtfehler, die während der Verarbeitung des Fasermaterials auftreten, können jedoch nach Harzinjektion und -aushärtung zu einer Beeinträchtigung der mechanischen Festigkeit der fertigen Bauteile führen. Daneben können auf Grund der benötigten Zeit zur Fehlersuche und -behebung erhebliche Maschinenstillstandszeiten hervorgerufen werden. Um Flechtfehler während des Prozesses zu erkennen, existieren bereits verschiedene Ansätze, die in zwei Hauptgruppen eingeteilt werden können. Klöppelunabhängige Sensoren ermöglichen es einerseits bei geringen Investitionskosten, nur größere Flechtfehler zu erkennen. Klöppelabhängige Systeme hingegen erlauben es bei jedoch hohen Installationskosten, Prozessparameter in hoher Genauigkeit zu erheben.

Als Anwendungsbeispiel der Digitalisierung in der Produktion von Faserverbundbauteilen liefert die vorliegende Arbeit neue Ansätze, die eine genaue Überwachung des Flechtprozesses bei zugleich geringem Installationsaufwand und -kosten ermöglichen. Zunächst werden stationäre Hallsensoren vorgestellt, die die Orientierung der Hebel der Fadenspannungseinrichtungen von vorbeifahrenden Klöppeln erfassen können (zeitdiskrete Messung). Im Gegensatz zu kommerziell erhältlichen Systemen ermöglicht es dieser Ansatz, Flechtfehler bereits in frühen Stadien der Entwicklung und deutlich vor einem Fadenriss zu erkennen. Danach werden sensorintegrierte Flechtringe zur Abschätzung von radialen und axialen Reaktionskräften am Flechtring als eine zeitkontinuierliche Messmethode untersucht. Ein trainierbarer Algorithmus wird vorgestellt, der eine Erkennung von Flechtfehlern ohne falsch positive oder falsch negative Detektionen ermöglicht. Weiterhin wird ein Ansatz zur optischen Vermessung der Abstände der Flechtfäden in der Geflechtbildungszone durch eine Kamera entwickelt. Mit diesem Ansatz wird eine Beurteilung der Gleichmäßigkeit des erzeugten Geflechtes ermöglicht. Als letzter Ansatz wird ein sensorintegrierter Flechtmaschinenklöppel vorgestellt, der durch einen eigenen Generator Energie aus der Bewegung des Klöppels erzeugen kann. Dadurch können insbesondere feine, abspulbedingte Anomalien erkannt und auch die verbleibende Menge an Garn auf der Spule abgeschätzt werden.

Wo immer möglich, wurden die neuen Ansätze auf der RF 1/128-100 Radialflechtmaschine des Lehrstuhls für Carbon Composites getestet. Dadurch wird die Nachrüstbarkeit der neu entwickelten Systeme auf Altanlagen nachgewiesen sowie deren Fähigkeit demonstriert, die Maschinenproduktivität in bestehenden Produktionslinien zu steigern und die Qualitätssicherung zu verbessern.

ABSTRACT

Braiding of reinforcement fibers is a process that is often used in the aerospace, automotive or sports and leisure industry when mainly tubular components that may be curved and show varying cross sections need to be manufactured from fiber reinforced composite materials. As a direct preforming process, braiding offers the possibility to use – in comparison to premanufactured textiles or prepreg materials – inexpensive fiber rovings while realizing high production rates.

However, defects that occur during braiding of fibrous material can lead to a deterioration in mechanical strength of the finished parts after resin injection and cure. In addition, significant machine downtime can be induced due to the time it takes to locate and resolve the error cause in the braiding machine. In order to detect braiding defects during the process, two groups of sensor systems can be distinguished. On the one hand, bobbin carrier independent systems generally come with comparatively low investment costs while being only able to detect defects on a coarse level. On the other hand, bobbin carrier dependent sensors usually involve undesirably high installation costs while being able to measure process parameters at a high level of accuracy.

As an application example for digitalization in the sector of composite production technology, the dissertation at hand aims to provide a set of new, additional sensor systems that allow a fine surveillance of the process while maintaining a low degree of installation effort and costs. Firstly, stationary Hall sensors that detect the orientation of the lever of the yarn tensioning unit of the bobbin carriers that pass by the sensors are introduced (discrete-time measurement). In contrast to commercially available systems, the Hall sensors are able to detect even early stages of forming braiding defects well before a yarn breaks. Secondly, sensor integrated braiding rings to estimate the resulting radial and axial reaction forces onto the braiding ring are proposed as a method of time continuous process monitoring. A trainable algorithm is presented that allows a surveillance of the process without any false positive or false negative defect detections. Thirdly, a camera-based system for measuring the distances between braiding yarns in the braid formation zone and thereby the evenness of the formed braid is developed. Fourthly, a sensor integrated bobbin carrier including an energy harvesting module is proposed that generates electric energy from the movement of the carrier itself. By means of this approach, particularly fine unwinding-related process irregularities can be measured and the remaining filling degree of the bobbin can be estimated.

Wherever possible, the new measurement approaches were installed and tested in the RF 1/128-100 radial braiding machine from HERZOG GmbH at the Chair of Carbon Composites. Thus, it is demonstrated that the newly developed sensor systems can be retrofitted to existing braiding machines and thereby enhance machine productivity and improve quality assurance in existing production lines.

Table of Contents

Nomenclature

Formula Symbol	**Unit**	**Description**
a	m	Radial distance between mandrel and braiding ring
acc	$\frac{m}{s^2}$	Acceleration
b	m	Distance between braiding ring and point of deposition of the braid onto the mandrel
d	m	Diameter, e.g. of component to be overbraided
err_{blur}	Pixel	Error due to motion blur in an image
$frame\ rate$	s^{-1}	Frame rate
g	$\frac{m}{s^2} = \frac{N}{kg}$	Gravitational constant
h	m	Height
i	-	Loop variable
l	m	Length
m	kg	Mass
n	-	Count variable, e.g. number of braiding yarns
$offset$	-	Offset value
r	rpm	Speed of horn gear rotation
ra	m	Radius
res	$\frac{Pixel}{m}$	Image resolution per unit length
t	s	Time
v	$\frac{m}{s}$	Speed
w	m	Width of a braiding yarn
CF	-	Cover factor, portion of the surface of a mandrel covered by a single layer of braid
DF	-	Deduction factor
F	N	Force

Formula Symbol	Unit	Description
$Index$	-	Index
J	Nm²	Rotational moment of inertia
M_{fr}	Nm	Frictional moment
MF	-	Momentum factor
P	W	Electrical power
R	Ω	Electrical resistance
U	V	Voltage
α	°	Variable for an angle, e.g. tilt angle of the notched part of a bobbin or deflection angle of a yarn at the braiding ring
β	°	Variable for an angle, e.g. angle under which the braiding yarns are deposited onto a mandrel
γ	°	Variable for an angle, e.g. unwinding angle of the yarn from the bobbin
δ	rad	Variable for an angle, e.g. wrap angle of a yarn around the guiding elements of a carrier
ε	-	Strain rate
θ	rad	Polar angle
μ	-	Coefficient of friction
ρ	$\frac{kg}{m^3}$	Packing density
φ	°	Braiding angle with respect to production direction
ω	rad	Rotational angle, e.g. of a bobbin
$\dot{\omega}$	$\frac{rad}{s}$	Angular velocity, e.g. of a bobbin
$\ddot{\omega}$	$\frac{rad}{s^2}$	Angular acceleration, e.g. of a bobbin

Abbreviations

Abbreviation	Description
2D	Two dimensional
3D	Three dimensional
AD	Anno Domini
BLE	Bluetooth Low Energy
BP	Before Present
DC	Direct current
FSR	Force sensing resistor
IDE	Integrated development environment
IoT	Internet of Things
LiFePo4	Lithium iron phosphate (battery)
Mbit	Megabit
NFC	Near Field Communication
PES	Polyester
PLA	Polylactic acid
PP	Peak prominence
PP/M	Peak prominence per mean
RF	Radial braiding machine (German: Radialflechtmaschine)
RFID	Radio Frequency Identification
RTM	Resin Transfer Molding
Seg. Dev. Comb.	Segment deviation combined
SLR	Single-lens reflex (camera)
UD	Unidirectional

Abbreviation	Description
VAP	Vacuum Assisted Process
WiFi	Wireless Fidelity

List of Figures

List of Tables

1 Introduction

In the second half of the 18th century, a major shift in manufacturing technology from manual labor to mechanized production took place in a wide range of economic sectors [1]. In England, which is seen as the cradle of this development [2–4], particularly the sector of textile production benefited from domestic inventions of groundbreaking machinery (e.g. flying shuttle by John Kay, roller spinning frame by Lewis Paul and John Wyatt, powered loom by Edmund Cartwright; all summarized in [5]). The newly emerging form of production in factories laid the foundation for a profound societal change: Instead of the possession of land in the former agricultural society, labor and capital gradually became the new defining factors of the economic and social fabric. This development is now historically known as the first industrial revolution.

Nowadays, the trend towards digitalization of industrial production processes is anticipated to constitute a similarly substantial change of the economy and is therefore often referred to as “Industry 4.0” or “fourth industrial revolution”. Whereas the origin of the term “Industry 4.0” can be traced back to a report of a working committee to the German government from 2013 (claimed by [6], original source [7]), the first use of the term “fourth industrial revolution” is accredited to Klaus Schwab, former Chairman of the World Economic Forum, in 2015 (claimed by [6], original source [8]). Both terms refer to a progression in industrial production along a succession of four major development steps (cf. Figure 1-1):

- First industrial revolution (1760-1840): Manual labor in manufactures is beginning to be replaced by industrial processing in factories through machines that are driven by water and steam power.
- Second industrial revolution (1871-1914): Industrial machinery is increasingly powered by electricity, logistic infrastructure such as railway enables cost-efficient transport of goods and emerging telecommunication technology allows a transfer of information over large distances. Furthermore, industrial production in factories is rationalized by the introduction of the conveyor belt.
- Third industrial revolution (late 20th century): Productivity is further increased by the introduction of electronic data processing systems such as microcontrollers in machine controls which enable the automatization of production steps.
- Fourth industrial revolution (early 21st century): Improvements in production quality and efficiency are achieved by data driven methods such as an interconnection of people, machines and sensors, transparent and accessible data handling as well as decentralized decision making also by artificially intelligent algorithms. A prerequisite for these methods is a consistent shift from analog to digital data processing (digitalization). [6]

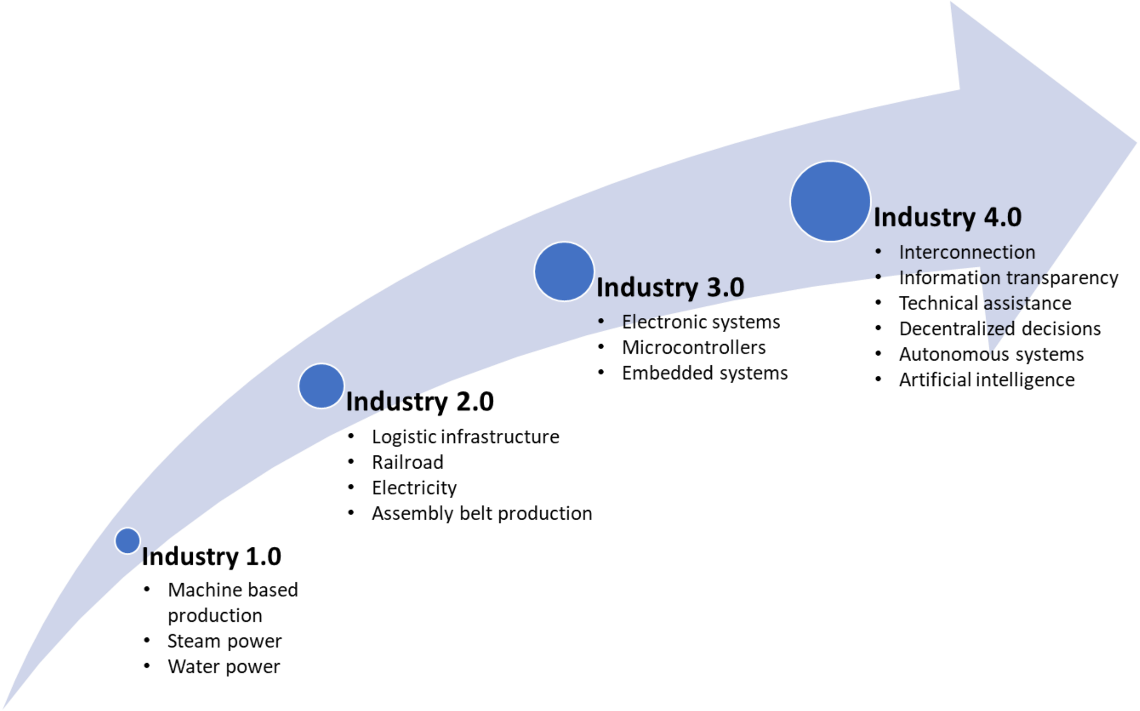

Figure 1-1: Four major development steps of industrial production; redrawn and adapted based on [6]

The terms “digitalization” and “Industry 4.0” reach over an extremely wide field of aspects from data acquisition and process monitoring over cyber physical systems, digital modelling of materials and processes (digital twins), data connectivity, complex customer value chains to digital assistant systems [6]. Thus, it is often unclear, even to technical engineers, what it particularly means for a specific economic sector. In order to establish a broader understanding of the general terms “digitalization” and “Industry 4.0”, the thesis at hand aims to provide an exemplary use case of how a concrete implementation of these two terms can look like for the textile industry of today – the industry sector which has already been at the heart of the first industrial revolution more than two centuries ago. Since a concrete use case shall be provided, the present thesis on the one hand focuses on the braiding process and particularly on the processing of reinforcement fibers as a subfield of the textile sector. On the other hand, the work concentrates on data acquisition and process monitoring as a subarea of “digitalization” and “Industry 4.0”.

With its roots as an ancient social art that can be traced back to 30.000-22.000 BP[1] on the basis of stone figurines [10,11], braiding as a textile production process has gone through all of the three historical industrial development steps. It has transformed from purely manual labor to a mechanized production process with the invention of the braiding machine by the Briton

---

[1] Times of origin of archaeological finds that are dated by means of the radiocarbon method are usually referred to by BP (before present). Since the first radiocarbon dates were published in December 1949, the year 1950 serves as a reference for “present”. To separate the word “present” from the bygone year 1950, BP was recently proposed to be defined as “conventional radiocarbon years before AD 1950” [9].

Thomas Walford in 1748 [12,13], [14] in [15]. These machines have eventually been powered by electricity instead of initially muscle and then steam power [16]. The application of braiding in the production of fiber reinforced composite structures and consequently the shift from mechanical haul-off units to the use of robots that guide overbraidable mandrels have marked the entering of this process into the third industrial development stage ([16], cf. Figure 1-3). The thesis at hand shows how online process monitoring and data analysis, as building blocks of "digitalization" and "Industry 4.0", can help further increase both productivity and product quality in braiding of composites.

1.1 Characterization of the Braiding Process and its Applications

According to the German industrial standard DIN 60000, braids are known as textile products that feature periodic thread density as well as a closed fabric appearance whereby the braiding yarns cross diagonally with respect to the edges of the fabric ([17], original wording see [2]). The simplest braid consists of three threads of which the two outer threads are alternatingly crossed with the middle thread. A mechanical implementation of the braiding principle is depicted in Figure 1-2 on the left. Yarn material is stored on braiding spools, the so-called bobbins. The bobbins are mounted onto bobbin carriers. The bobbin carriers are guided on a flat machine bed by rotating horn gears on a track that resembles an "8". This way, a flat, two-dimensional (2D) braided lace is formed. The finished braid is usually taken-off by slowly rotating disks that are coupled to the gearing mechanism that drives the horn gears [18]. Although there are more elaborate and general classifications of braiding machines and braided products available in the literature from Kyosev [19], Laourine [16] proposes a taxonomy in the context of lightweight design. Due to the focus of this work on braiding of composites, the latter shall be introduced here (cf. Figure 1-2, right). By means of an arrangement of multiple horn gears along a closed circle, a braid with circular cross section such as a rope can be formed. By guiding an overbraidable mandrel n times, usually by means of a robot (cf. Figure 1-3), through a machine with a closed arrangement of horn gears, a three-dimensional (3D) object with n layers can be braided. However, this is still considered a 2D braid since the braided layers do not show any interconnection with each other. A 3D braid is formed when multiple circular sets of horn gears are arranged next to each other in a way that the bobbin carriers engage with more than one set of horn gears. This way, a connection in thickness direction of the braided layers is created by the braiding yarns. By means of a packed, cartesian arrangement of horn gears and bobbin carriers on the flat machine bed, fully 3D interlaced braids such as T-beams or branched profiles can be manufactured [20].

---

[2] „Geflechte: Flächen- oder Körpergebilde mit regelmäßiger Fadendichte und geschlossenem Warenbild, deren Flecht-(Klöppel-)Fäden sich in schräger Richtung zu den Warenkanten verkreuzen." [17]; translated from German into English by the author and therefore marked as indirect citation in the text above.

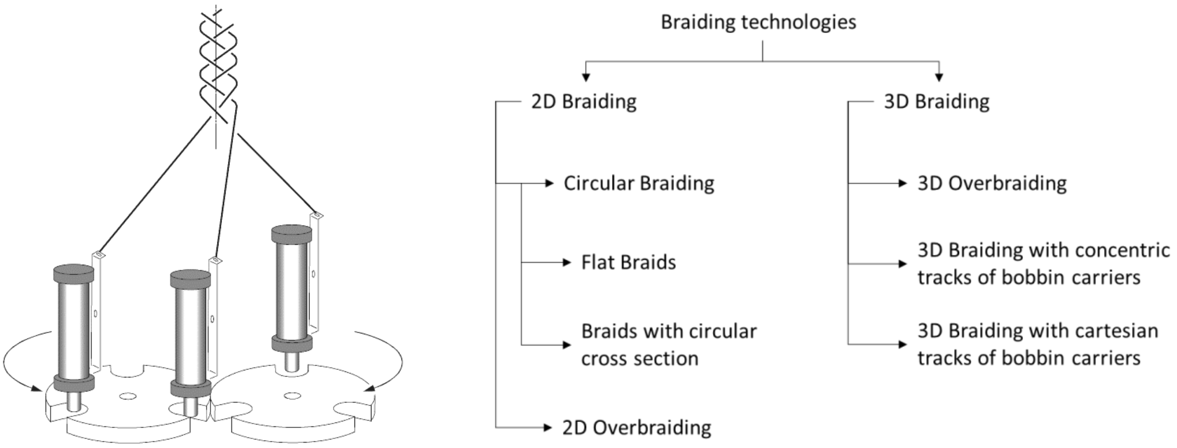

Figure 1-2: Schematic of a basic mechanical implementation of the braiding principle (left; drawing taken from [16]); possible classification of braiding technologies (right; redrawn based on [16] and translated into English)

Thus far, only braiding machines with a flat machine bed have been introduced. Such machines are called *axial* braiding machines because the bobbin carriers point into the direction of the produced braid (cf. Figure 1-2, left). In 1940 however, Muller [21] described that in axial braiding machines, an undesirable eccentric load is exercised onto the bobbin carriers by the tension of the yarns. Moreover, the free yarn length between the carriers and the point where the finished braid forms varies significantly, causing fluctuations in yarn tension and hence yarn damage. Consequently, he invented a type of braiding machine that is now known as *radial* braiding machine. The bobbin carriers are positioned on a cylinder mantle and are oriented towards the center of the cylinder (cf. Figure 1-3, left). Thereby, the bobbin carriers stand perpendicularly to the production direction of the braid. In contrast to axial braiding machines, radial braiding machines offer a gentler handling of the braiding yarns and thus less yarn damage due to smaller amplitudes in yarn length from the bobbin carriers to the braiding point. Due to the often brittle and thus fragile nature of reinforcement fibers in the unimpregnated, dry state, radial braiding machines became particularly useful when braiding of composite preforms gathered pace in the 1980s. In 1989, Culp et al. [22] further developed this principle by grouping multiple sets of circular arrangements of horn gears on a cylinder mantle, thereby creating a possibility to produce 3D braids with the gentler, radial machine principle with concentric tracks of bobbin carriers (cf. taxonomy in Figure 1-2, right). However, due to the fact that the bobbin carriers need to be guided on a curved cylinder mantle rather than on a flat machine bed, radial braiding machines usually achieve lower speeds of horn gear rotation and thus lower material throughput than axial braiding machines. Although there are also other types of braiding machines such as for instance *Wardwellian* or *spiral* braiding machines, the axial and radial types remain the most used when it comes to braiding of composite structures. For an introduction into other types of braiding machines used in the general textile industry, the reader is referred to the book by Kyosev [19] and his work together with Müller [23]. For an even more gentle handling particularly of reinforcement yarns both in axial as well as in radial braiding machines, special carriers with guide plates and bobbins with reduced usable length to avoid acute angles between the unwinding yarn and the material on the bobbin were developed. Figure 1-3 shows the RF 1/128-100 radial braiding machine from HERZOG GmbH at the Chair of Carbon Composites at Technical University of Munich, which was available to the author during preparation of the thesis at hand, and the associated IFDA-100 carriers with guide plates optimized for the processing of carbon fiber.

Figure 1-3: Radial braiding machine RF 1/128-100 with mandrel guidance by robot (left); IFDA-100 carrier with guide plate optimized for low fiber damage during processing of brittle reinforcement fibers as well as modified bobbin with unused bottom in order to avoid acute angles during unwinding of the yarn (right; actual unwinding angle γ drawn-in as white dotted line, acute but avoided unwinding angle drawn-in as red dotted line)

Braids are generally known to the broad population as plaits from human hair, baked plaited loaves, braided plant shoots (e.g. to dry onions or garlic) or braided laces (e.g. shoelaces) [19]. However, there is also a broad range of technical applications for braids: In the marine industry, threads of mooring ropes or fishing nets are usually braided [24,25]. Climbing ropes or parachute cords are exemplary applications from the sports and leisure industry [25,26]. In electrical engineering or oil hydraulics, braids serve as an electric shielding of cables or reinforcement and protection of pipes [23,27]. In medical technology, braids can be used as the underlying structure of stents to support human blood vessels or organs of the gastrointestinal tract [28,29]. In the fiber composites industry, which spans across several industrial fields, the braiding technology is usually used to manufacture hollow components that may be double-curved due to varying cross sections and curved shapes. Well known exemplary parts are for instance pillars of passenger compartments (automotive industry) [30,31], helicopter landing gears (aviation industry) [32,33], rocket nozzles (space industry) [34,35] or lightweight bicycle frames and rims (sports and leisure industry, cf. Figure 1-4) [30,36,37]. In the latter case, special axial braiding machines that can be divided into two halves are used to seamlessly manufacture the closed, tubular profile.

Figure 1-4: Braided bicycle rim developed within a joint research project between the Chair of Carbon Composites at Technical University of Munich and Munich Composites GmbH (overview left, close-up right)

In the field of fiber composites manufacturing, the braiding process can be characterized as a direct preforming process that is generally known for its readiness for a high degree of automation, the possibility to use low-cost reinforcement rovings as raw material (in comparison to prefabricated 2D textiles such as non-crimp fabrics or weaves), low scrap material rates and high material throughput [38–40]. Additionally, braiding supports adjusting the fiber orientation to the desired mechanical load by varying the fiber angle with respect to the longitudinal axis of the braided part (so called braiding angle φ). The achievable braiding angle φ depends on the material that is being processed, the available additional equipment for fiber spreading (e.g. pulsating braiding ring or pneumatic spreading unit [41]) and of course further constraints of the concrete use case such as part geometry. Therefore, the ranges of achievable braiding angles φ stated in the literature vary between smaller windows of $\varphi = 30^\circ - 70^\circ$ [30] and wider windows of $\varphi = 10^\circ - 80^\circ$ [38]. Braiding also offers the possibility to opt for different braid architectures such as *biaxial*, *triaxial*, *0°-braids* and *unidirectional (UD)* braids (cf. Figure 1-5). With the reinforcement yarns being oriented in both braiding yarn directions, the *biaxial braid* is understood as the most conventional form of braids. From a basic mechanical standpoint, a biaxial braid with $\varphi = 45^\circ$ braiding angle (cf. Figure 1-5, left) is well suited for torsional shafts, for instance. The *triaxial braid* can be seen as an extension of the biaxial braid since it comprises additional 0°-reinforcement yarns for enhanced part performance under bending. A drawback of the triaxial braid is however the increased fiber undulation of the braiding yarns. Excessive fiber undulation of the 0°-yarns is usually avoided by selecting a slightly elevated yarn tension for the 0°-yarns compared to the yarn tension of the braiding yarns (as drawn in Figure 1-5, second from left). The *unidirectional (UD) braid* is a derivative of the biaxial braid. The reinforcement yarns of one of the two braiding yarn systems are replaced by thin auxiliary yarns. Due to this, the fiber undulation of the remaining reinforcement yarns is reduced compared to the biaxial braid (cf. Figure 1-5, second from right). Such a type of braid was used for braiding of curved aerospace structures such as airplane frames, for instance

[30,42]. The *0°-braid* can be seen as a derivative of the triaxial braid. Both braiding yarn systems are comprised of thin auxiliary yarns. The 0°-yarn system remains to be comprised of reinforcement fibers (cf. Figure 1-5, right). This braid architecture was used for curved parts that are almost exclusively loaded in bending (e.g. roof frame of a car during a rollover crash [43,44]). Apart from the braid architecture, braiding also allows changing the interlacement structure of the braiding yarns (in composites usually 1x1, 2x2 or 4x4 structures which are comparable to plain, twill and satin weaves in terms of fiber undulation) [30,45]. The 1x1 interlacement structure is schematically drawn in Figure 1-5, left, second from left and right. The rather unusual 3x3 structure is shown in in Figure 1-5, second from right. Whereas in general braiding a broad range of yarn materials from natural fibers [25], plastic fibers [25,29], thin metal wires [23,29] or leather strips [19] is processed, common types of braided fibers in composite material applications are carbon, glass, aramid, basalt and ceramic fibers [30,45,46]. Most often, these reinforcement fibers are braided standalone in their dry state. However, in niche applications, they may also be braided together with thermoplastic components as commingled yarns [47], as thermoplastic tape [48] or as towpreg material [49–51].

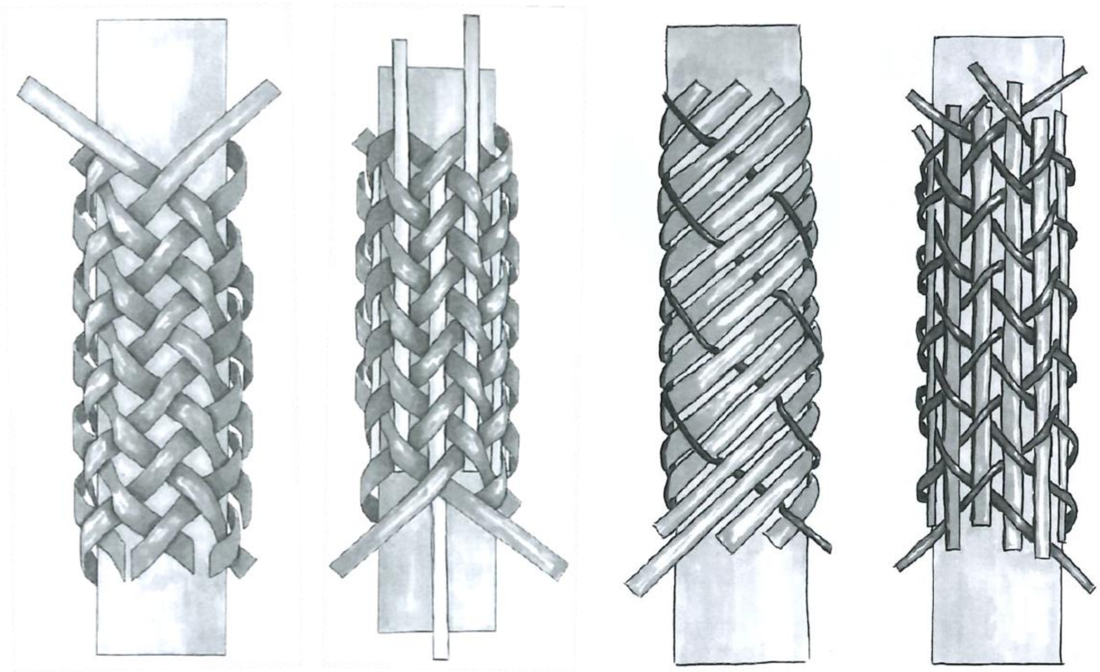

Figure 1-5: Schematic drawings of common braid architectures in composites braiding, from left to right: biaxial braid, triaxial braid, UD braid and 0°-braid; drawings taken from [45]

1.2 Need for Online Process Monitoring in Braiding, Research Questions and Methodical Approach

As stated above, in the field of composites manufacturing, the braiding process is particularly known for its high material throughput and the possibility to use comparatively inexpensive rovings from reinforcement fibers. In combination with the high investment costs of the machine itself and several handling robots in a braiding cell, this makes the braiding process particularly interesting for the production of composite parts of high quantities and production rates [40]. However, due to defects that occur during the process, machine productivity can significantly be reduced. In endurance braiding tests, Ebel et al. [46,52] observed that an important defect during braiding of fibrous reinforcement yarns, namely the fibrous ring on a braiding spool, can lead to a significant portion of machine downtime (in an extreme case up to 26 % of the total testing time). This was due to the fact that a fibrous ring, which is a circular accumulation of broken filaments on a bobbin (cf. Figure 1-6, top left), can lead to an increase in tension of a single braiding yarn, a gap in the braided preform due to the uneven tension of the braiding yarns (cf. Figure 1-6, bottom) and eventually to a breakage of the braiding yarn with increased tension [53]. A breakage of a yarn always required to stop the machine in order to locate the defective bobbin and manually rethread a new braiding yarn through the yarn guiding elements of the bobbin carrier. Other defects in the braided preform that Ebel et al. [46,52] observed, such as yarn loops or gaps in the preform, did not necessarily require a stop of the machine. However, the authors noted that such defects may still hamper the mechanical properties of an infiltrated and cured composite part. In the works from Mierzwa et al. [54] and Mierzwa [55], effects of yarn gaps on the mechanical strength of braided components were investigated. For their experiments, they manually introduced 4 mm wide yarn gaps directly upon each other in each layer of coupons consisting of six braided layers from T700SC50C 24k carbon fibers from Toray Industries, Inc. fabricated at a braiding angle of $\varphi = 45°$ (cf. Figure 2-7). They observed a deterioration in tensile strength of 36 % and a deterioration in compressive strength of 33 % when the specimens were infiltrated through the Vacuum Assisted Process (VAP) and when the yarn gaps were oriented perpendicularly to the loading direction. In specimens that were injected with resin by means of Resin Transfer Molding (RTM) and also when the yarn gap was oriented in parallel to the loading direction, such deteriorating effects were either not observable or considerably smaller. The authors attributed this finding to the fiber undulation that such yarn gaps can create when a flexible upper tooling is used for resin infusion. To put these findings into perspective, it needs to be noted that it is highly unlikely that multiple yarn gaps form at exactly the same position at each layer in a multi-layer braided preform. The findings from above can therefore be regarded as an extreme case scenario. This is why Mierzwa [55] also investigated a more realistic case where only one yarn gap was located in the first layer of his braided coupons consisting of six layers (T700SC50C 24k carbon fibers from Toray Industries, Inc., braiding angle 45°). Under tensile loading, he still observed a reduction by 11% in strength compared to the pristine reference samples. Compression tests were however not conducted with this configuration of yarn gaps. A hint regarding effects of yarn gaps under compressive loading however gives his use case of braided torsional shafts with a 4 mm wide yarn gap in the first of three layers made from T700SC50C 24k carbon fiber yarns from Toray Industries, Inc. As for the testing on coupon level, he used a braiding angle of $\varphi = 45°$. During torsional testing of the shafts, Mierzwa [55] observed that it was always the yarn system that was loaded in compression that failed. He attributed this to the general fact of lower compressive strength of fiber reinforced composites compared to their tensile strength. When the purposefully introduced yarn gap was oriented perpendicularly to the yarn system loaded in compression (thereby inducing pronounced undulation in this yarn system), the bearable torsional moment was reduced by 17 % with respect to defect free reference samples.

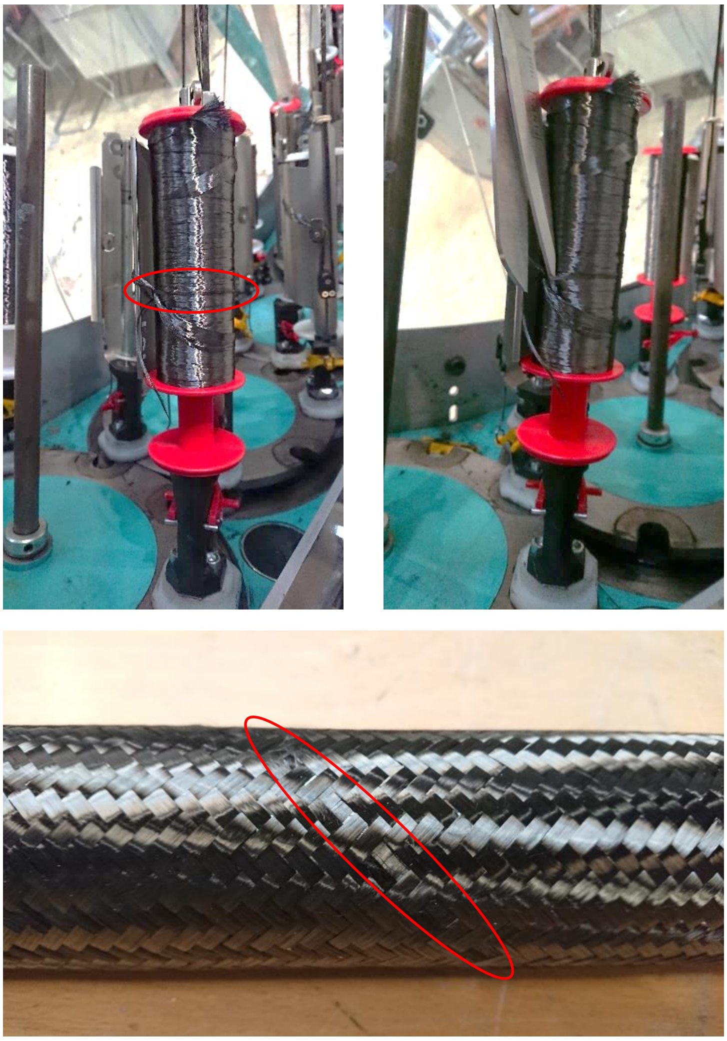

Figure 1-6: Fibrous ring on a braiding spool (top left, marked with red ellipse); removal of a fibrous ring by hand with scissors (top right); resulting yarn gap in a braided, tubular preform if fibrous ring is not removed (bottom, marked with red ellipse)

As shown by the exemplary data above, braiding defects can lead to both excessive loss in machine productivity as well as to a deterioration in mechanical properties of the finished composite parts. Hence, it is desirable to provide the braiding industry with sensor systems that are able to detect the formation of such defects at short response times. The earlier a defect can be detected, the more likely it is that it can easily be resolved and the lower the incurred error costs are ([55], e.g. removing a forming fibrous ring by hand with scissors, thereby avoiding the need to rethread a broken yarn, cf. Figure 1-6, top right). An early defect detection is not only beneficial within the scope of the braiding process chain. In quality management, it is generally agreed that error costs increase exponentially by about a factor of about 10 for every phase the defect is discovered and resolved later along the life cycle of a product ([56], cf. Figure 1-7). Applied to the example of a braided product such as the composite bicycle rim from above (cf. Figure 1-4), this could mean that the choice of a certain fiber type with too high modulus and thus brittleness during the planning and development phase can lead to fibrous rings during braiding (cf. Figure 1-6, top left). In the best case, such fibrous rings lead to clearly visible yarn breakages during production so that the defect attracts the attention of the machine operator. However, it may also be the case that the induced fibrous rings only cause yarn gaps (cf. Figure 1-6, bottom) in the braided preforms and the braiding process is not interrupted. This way, a large number of mechanically defective rim preforms may be produced. In a final leaving inspection of the finished products, the defect may be overlooked due to human error or due to the fact that it may not be visible after resin injection and matt varnishing. Eventually, defective products may be sold to customers in unawareness of the error. Although the waste and financial damage by the unsuitable fiber material could not be avoided by a sensor system for braiding process monitoring in this example, it would at least prevent the production and marketing of the defective products. Thus, a comprehensive sensor system to monitor the braiding process gives the component manufacturer the opportunity to proof part quality also for critical products by documenting the measurement readings. As a side-effect, the possibility of raising design allowables by precisely knowing process deviations is opened.

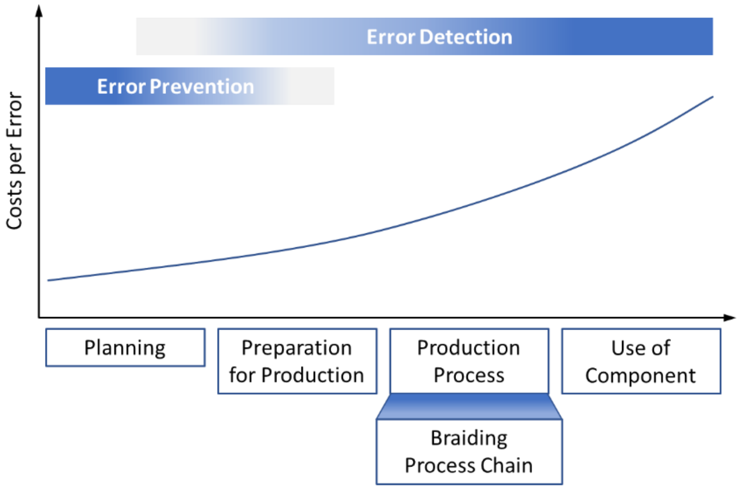

Figure 1-7: Qualitative development of error costs depending on point of prevention or detection along the product life cycle; redrawn based on [55] and translated into English

As will be shown in the subsequent state of the art regarding defects in braiding of composites and already existing sensor systems, there is a research gap in braiding process monitoring. On the one hand, there are commercially available, bobbin carrier independent approaches that are cost-effective due to the low number of sensors it requires to monitor all braiding yarns. However, these approaches tend to detect defects when they have already reached their final stage (e.g. yarn breakage) and caused significant machine downtime (e.g. rethreading of a broken yarn by hand). On the other hand, there are sophisticated, bobbin carrier dependent approaches which feature sensors that are installed directly onto the bobbin carriers themselves. Although these systems allow a detection of defects at short response times, they are comparatively expensive due to the necessity to equip all bobbin carriers of a braiding machine (which may be several hundreds) with sensory devices.

In order to close this research gap, the research goal of the thesis at hand is to provide new types of sensor systems mainly for the composite braiding industry that are, on the one hand, cost-efficient while, on the other hand, able to detect defects early during their formation for both reduced error correction effort and minimized mechanical effects of defects. The developed sensor systems shall be characterized in order to compare them in terms of application range, sensitivity and approximate costs amongst each other and in relation to concepts from the literature.

In order to meet this goal, an invention of Hall sensors that are stationarily attached to the body of the braiding machine is firstly introduced to detect fibrous rings on braiding spools early during their formation. It is shown that this approach only enables a surveillance of the process in a discrete manner while it is able to precisely detect the defective bobbin before a braiding yarn breaks. Secondly, sensor integrated braiding rings that allow an estimation of the resulting radial and axial forces onto the braiding rings are investigated. By means of a trainable, artificially intelligent algorithm, this approach is demonstrated to be able to monitor the process in continuous time while it is only able to distinguish a particular group of bobbins that comprises a yarn tension deviation. Hence, this approach of sensor integrated braiding rings can be regarded as complementary to the first concept of stationary Hall sensors. Thirdly, an optical inspection of the braid formation zone by a light barrier and a camera including an associated algorithm for image analysis is developed. This measurement technique is able to detect yarn gaps that are about to be braided into the preform. Fourthly, a new cost-efficient form of a sensor integrated bobbin carrier is depicted. The defect detection capability as well as the possibility to estimate the remaining amount of yarn on the bobbin is shown with this type of monitoring approach. Furthermore, the sensor integrated bobbin carrier is equipped with an energy harvesting device so to that the battery on the carrier does potentially not need to be changed and recharged while the process is running. Finally, the detection capabilities and fields of application of all of the approaches presented are compared amongst each other and to known detection systems from the literature. Thereby, the reader shall be provided with an in-depth effort-benefit assessment in order to decide which sensor system or which combination of sensor systems best suit a given use case (e.g. type of machine, product to be braided, fibrous raw material).

In order to characterize the behavior of the outlined sensor modules, the author set a standard test scenario for the thesis at hand which includes…

- overbraiding of a cylindrical mandrel with a diameter of $d = 65\ mm$ at a braiding angle of $\varphi = 45°$ with
- Tenax®-E HTS40 F13 12k carbon fibers with a titer of 800 tex from Teijin Carbon Europe GmbH
- on an RF 1/128-100 braiding machine from HERZOG GmbH at a speed of horn gear rotation of $r = 130\ rpm$ and a spring in the carrier with a release force equivalent rating of 350 g.

This means that in every test series presented in this dissertation, the above standard test scenario or reasonable variations thereof can consistently be found. Originating from this standard case, the author introduced either additional materials, mandrel geometries or different machine settings to shed light on the specialties of the respective sensor module (e.g. different types of fibers for characterizing the Hall sensor module to give the reader an impression of its limitations regarding certainty of defect detection in section 3.1, an S-shaped mandrel with similar circumference as the cylindrical reference for characterizing the impact of geometrical variability on the detection capabilities of the sensor integrated braiding rings in section 3.2, different yarn titers for the characterization of frictional interaction in the braid formation zone for an optical inspection thereof in section 3.3). In case a test series does not involve braiding but only unwinding of a single yarn (e.g. the estimation of remaining bobbin weight in section 4.1.2), the unwinding speed is always set closely to the standard braiding scenario for its replication. Wherever possible, the presented sensor systems were implemented into the RF 1/128-100 braiding machine from HERZOG GmbH (cf. Figure 1-3), which was available to the author during the preparation of the thesis at hand at the Chair of Carbon Composites at Technical University of Munich. By testing the approaches in this near-industrial use case, the possibility of retrofitting them to existing braiding machines as well as the potentials of the researched concepts for a digitalization of braiding process monitoring in industrial applications shall be demonstrated.

2 State of the Art

As a background for the present thesis on braiding process monitoring, common defects and their formation mechanisms that can occur particularly during braiding of reinforcement fibers are explained in the following section. Furthermore, currently existing concepts for braiding process monitoring are described. It is distinguished between bobbin carrier independent and bobbin carrier dependent sensor systems. Bobbin carrier independent approaches are understood as systems that make use of sensors that are stationarily attached to the body of the braiding machine. By contrast, bobbin carrier dependent approaches are defined as systems that have their sensors installed directly on the moving bobbin carriers of the braiding machine. As already indicated in the chapter above, bobbin carrier independent approaches generally offer a lower level of detection accuracy while being cost efficient. Bobbin carrier dependent approaches allow a high level of detection accuracy but come with considerable installation effort and costs. The research gap that the thesis at hand addresses is to develop and characterize new sensor systems in this conflict of objectives that offer a beneficial compromise between the best of the two depicted, fundamental approaches.

2.1 Defects during Braiding of Reinforcement Fibers

Frequently occurring braiding defects can be distinguished on the basis of their cause into defects that are due operating errors of the braiding machine and into defects that result from yarn damage. As defects that are due to operating errors of the braiding machine, global yarn gaps and yarn loops in braided preforms are described in the following subsection 2.1.1. As defects that result from yarn damage, a fraying of the braiding yarns in the braid formation zone (so called spider's web) and the resulting hairy braid, fiber fuzz and fuzz balls in the preform as well as fibrous rings at the braiding spools with their resulting effects of local yarn gaps and yarn breakages are explained in the succeeding subsection 2.1.2.

2.1.1 Defects Caused by Operating Errors

As a first defect that is due to an operating error of the machine, so-called global yarn gaps shall be explained. In braiding of composites, it is generally desirable to achieve a full coverage of the mandrel that has to be overbraided (so-called cover factor; $CF = 1$ for full coverage) [57]. According to geometrical considerations made by Rosenbaum in [15], the cover factor CF of a braid can generally be calculated by

$$CF = \frac{w \cdot n_{yarn}}{2 \cdot \pi \cdot d} \cdot \left(\frac{1}{cos\varphi_1} + \frac{1}{cos\varphi_2}\right) - \left(\frac{w \cdot n_{yarn}}{2 \cdot \pi \cdot d}\right)^2 \cdot \frac{1}{cos\varphi_1 \cdot cos\varphi_2} \qquad (2\text{-}1).$$

Whereby w is the width of the braiding yarns, n_{yarn} equals the number of the braiding yarns, d is the diameter of the overbraidable mandrel and φ_1 and φ_2 are the braiding angles of both braiding yarn systems with respect to the production direction.

In the mathematically special case of an undistorted braid (braiding angles $\varphi_1 = \varphi_2 = \varphi$; practically the case when a cylindrical mandrel oriented in production direction is overbraided), equation (2-1) simplifies to

$$CF = \frac{w \cdot n_{yarn}}{\pi \cdot d \cdot cos\varphi} - \left(\frac{w \cdot n_{yarn}}{2 \cdot \pi \cdot d \cdot cos\varphi}\right)^2 \qquad (2\text{-}2).$$

Hence, a full coverage of an overbraidable mandrel is achieved when the condition

$$n_{yarn} = \frac{2 \cdot \pi \cdot d \cdot cos\varphi}{w} \qquad (2\text{-}3)$$

is met. In case of a mandrel with a cross section different from a perfect circle, the term $\pi \cdot d$ in the equations (2-1) to (2-3) needs to be replaced by the real diameter of the mandrel at the braiding point.

The braiding angle φ is in practice set by matching the haul-off speed of the mandrel $v_{mandrel}$ to the speed of horn gear rotation of the braiding machine r in revolutions per time unit following the conditions (2-4) and (2-5).

$$v_{mandrel} = \frac{\pi \cdot d}{t_{360°} \cdot tan\varphi} \qquad (2\text{-}4)$$

$t_{360°}$ is thereby defined as the period of time it takes one bobbin carrier to complete a full 360°-revolution through the braiding machine. This can be calculated from the total number of horn gears $n_{horn\ gear}$ in the braiding machine and their speed of rotation r according to

$$t_{360°} = \frac{n_{horn\ gear}}{2 \cdot r} \qquad (2\text{-}5).$$

However, the width of a particular type of braiding yarn w is not a given parameter. It can vary in a broad range and sets itself according to the geometrical necessities during the deposition of the fibers onto the mandrel specified by equation (2-3). Depending on the means installed in the braiding machine to enhance a spreading of the braiding yarns (e.g. actuated braiding ring, pneumatically supported spreading unit [41]) the smaller the braiding angles φ and the larger the mandrel diameters d may become. If the operator of the braiding machine chooses a parameter set to operate the machine that constitutes a mismatch between…

- speed of horn gear rotation of the machine r,
- haul-off speed of the overbraidable mandrel $v_{mandrel}$,
- diameter of the mandrel d,

- number of braiding yarns n_{yarn} and
- achievable width of the braiding yarns w,

this may result in an incomplete coverage of the mandrel and thus a cover factor $CF < 1$ (cf. Figure 2-1). Mitwalsky [41] investigated the impact of global yarn gaps on the mechanical performance of biaxially braided coupons. At a cover factor of $CF = 0.88$, he observed a deterioration of up to 28 % in tensile strength compared to a closed braid with $CF = 1$. Furthermore, Heieck et al. [57,58] observed a similar knock-down when they tested triaxially braided coupons with a cover factor $CF = 0.94$. Compared to a closed braid, the specimens with global gaps deteriorated by 28 % in tensile strength and by 15 % in tensile modulus. Moreover, Rosenbaum [15] argues that under compressive loading, such global yarn gaps contributed to a premature buckling of the braiding yarns because they were not properly supported by neighboring yarns.

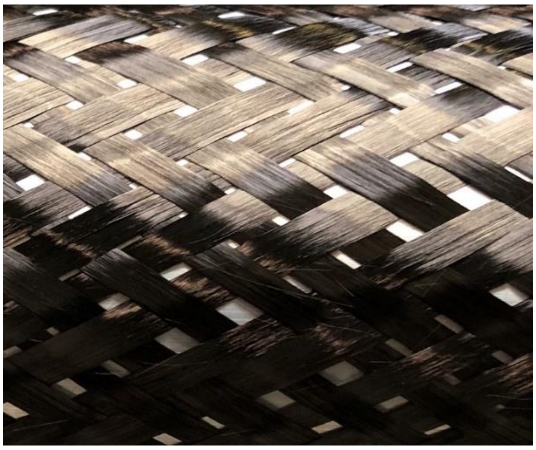

Figure 2-1: Cylindrical mandrel ($d = 65\ mm$) overbraided with $n_{yarn} = 64$ 12k carbon fiber yarns ($w \approx 4\ mm$) at a braiding angle of $\varphi = 30°$; resulting cover factor $CF \approx 0.9$; image taken from supervised student thesis [59]

At this point, it shall be noted that there is not only an upper limit for yarn spreading but also a natural lower limit for yarn compressibility. Particularly when small diameters of mandrels shall be overbraided at large braiding angles φ, this can lead to the problem that the braid cannot be deposited tightly onto the mandrel. Instead, it forms a loose hose around the mandrel (cf. Figure 2-2). It is self-evident that such a loose braid cannot be further processed properly. For instance, in an RTM process, a loose braid would cause fiber clamping and eventually destroy the press tool. In a process for resin infusion under flexible tooling (e.g. VAP), a loose braid would form excessive fiber wrinkles. For detailed considerations on the process window of the braiding process regarding the limits of yarn spreading and compression also under geometrical variability of the mandrel (e.g. curvatures, varying cross sections), the reader is referred to the work by Birkefeld [60].

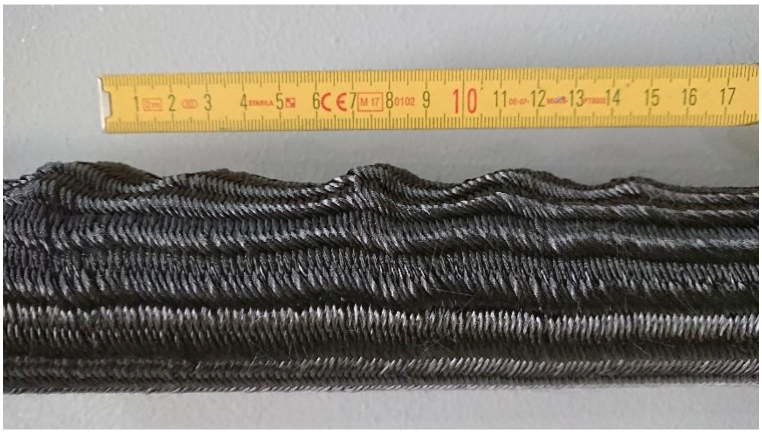

Figure 2-2: Loose braided hose consisting of $n_{yarn} = 128$ 12k carbon fiber yarns at a braiding angle of $\varphi = 60°$ on a cylindrical mandrel with a diameter of $d = 50\ mm$; wrinkles occur because the yarns cannot be compressed to the geometrically necessary width of $w \approx 1.2\ mm$

As another defect that is due to an incorrect setting of the machine, loops in the braided preform shall be mentioned [46,52]. Such loops occur due to an insufficient yarn tension in relation to the frictional forces in the braid formation zone. An insufficient yarn tension can either occur simply due to emptying bobbins or broken yarns (cf. Figure 2-3, top left), due to a too low setting of the yarn brake (e.g. too light springs in bobbin carriers for braiding yarns or insufficient setting of tensioners for 0°-filler yarns, cf. Figure 2-3, bottom) or due to a stuck yarn tensioning mechanism at the bobbin carrier (cf. Figure 2-3, top middle and top right). The latter problem is often caused by poor cleaning and lubrication of the locking pin of the yarn tensioning mechanism. In case of a well-lubricated yarn tensioning mechanism, the locking pin periodically engages and disengages with lateral notches in the bobbin. Thereby, the bobbin is braked and a braiding yarn tension within a constant interval is maintained. However, if the locking pin is stuck in its retracted position, it does not brake the bobbin any more. Hence, a loss in yarn tension occurs. Since such a sticking of the locking pin does not occur suddenly but rather gradually, the resulting loops in braided preforms can often first be observed when the respective bobbin carrier is located at the top position in a radial braiding machine. As will be explained in more detail in section 4.1, this is due to the fact that in a vertically set up radial braiding machine, the bobbin carrier is oriented upside down in the gravitational field when it reaches its uppermost position in the machine. A slight play of the bobbin along the shaft of the carrier causes the locking pin to engage later and disengage earlier with the bobbin. The resulting, slight additional decrease in yarn tension makes effects of insufficient yarn tension such as yarn loops particularly visible when the respective bobbin carrier is oriented upside down at its top position in vertically oriented radial braiding machines. To the knowledge of the author, mechanical effects of yarn loops are at present not characterized in the literature. However, since a yarn loop constitutes a distortion from the regular braid pattern with one yarn not being in its dedicated position and thereby causing additional fiber undulation, the reader is referred to the effects of local yarn gaps in the following subsection for a substantiated estimation of such mechanical effects.

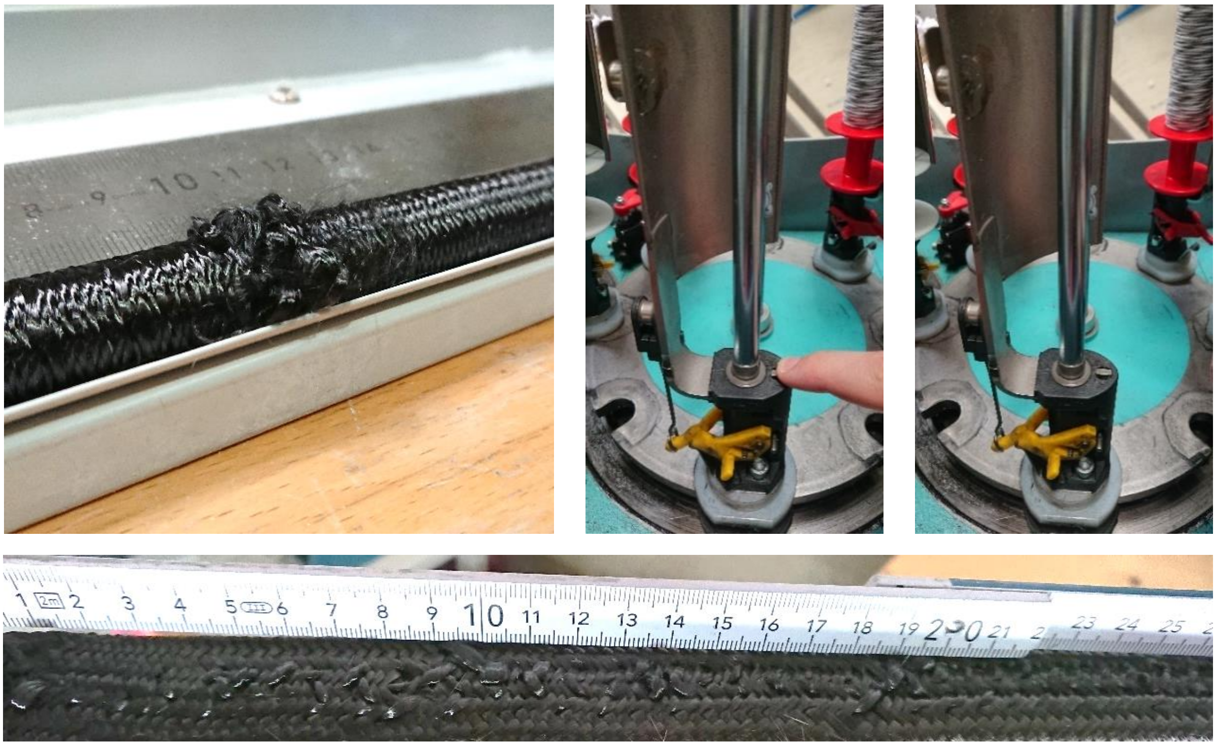

Figure 2-3: Excessive yarn loops following a yarn breakage (top left); stuck locking pin of yarn tensioning mechanism after being pushed down by hand (top middle and top right); yarn loops due to insufficient tensioning of 0°-filler yarns (bottom)

2.1.2 Defects Caused by Yarn Damage

Braiding is a process that involves a considerable extent of frictional interaction between the braiding yarns in the braid formation zone. In the early days of braiding with reinforcement fibers and particularly of carbon fibers from 1980 on, reinforcement yarns were not specifically designed to the requirements of the braiding process. It was normal that the yarns suffered significant damage in the braid formation zone due to frictional interaction among each other [46]. Figure 2-4, left illustrates such fiber damage, which is called spider's web or frayed fibers. Such effects were reduced by the introduction of radial braiding machines, which cause less fiber damage than the standard axial braiding machines, and improved yarn guiding elements at the bobbin carriers. Furthermore, enhanced sizing materials for a better cohesion of the individual filaments in a roving improved the ability of rovings from reinforcement fibers to withstand a higher degree of frictional interaction. However, still today, particularly when the sizing material has been exposed to an ageing process due to long storage or when high yarn tensions for braiding are used, frayed fibers and thus a hairy braid can occur (cf. Figure 2-4, right).

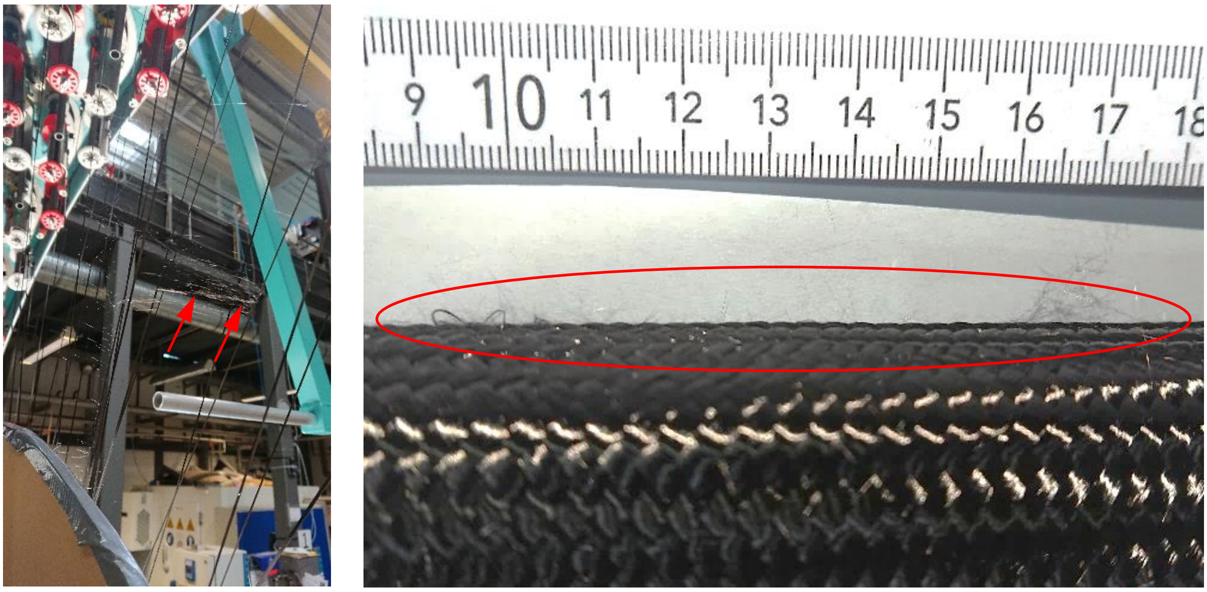

Figure 2-4: Frayed fibers forming a spider's web of thin filaments (left, marked with red arrows); hairy braid due to fiber damage resulting from frictional interaction during the braiding process promoted by aged sizing (right, marked with red ellipse)

Bulat [61] investigated the effects of different levels of yarn damage induced by different yarn tensions during braiding. Whereas no clear effects could be observed for tensile, compressive and intralaminar shear strength, she observed an enhanced interlaminar shear strength by 6.65 % of the samples with most yarn damage compared to the samples with least yarn damage. Due to scattering intervals however, she noted that the latter observation was only a trend and not a significant finding. Still, she attributed a possible effect to a better coherence between braided layers because of single filaments sticking out that could improve delamination resistance. Erber et al. [62] used a specially designed braiding ring with grooves in order to introduce three different levels of yarn damage directly before the formation of the braid on a tubular mandrel. As a characterization of in-plane properties, they conducted tensile tests. The specimens with the most damaged yarns showed a loss of 11 % in strength and of 7 % in Young's Modulus compared to the specimens with least yarn damage. As a characterization of out-of-plane properties, they conducted interlaminar shear tests and compression after impact tests. The specimens with highest yarn damage showed a 7 % higher interlaminar shear strength than the specimens with least yarn damage. The residual compression strength increased by 3.5 % in the variant with medium yarn damage compared to the specimens with least yarn damage. However, the specimens with most yarn damage showed approximately 6 % lower residual compression strength values compared to the least damaged specimens (tipping point).

However, out of personal experience of the author, it is risky in terms of process stability to try to harness such an effect. If the fibers fray in the braid formation zone, it may well be that the frayed fibers do not slip along the intact braiding yarns – as it is required for an even braid formation – but entangle with them. In this case, local holes in the braided preform occur (cf. Figure 2-5). It is self-evident that such holes inevitably require the preform to be scrapped. Furthermore, excessive fiber damage causes fiber dust in the air which can lead to respiratory problems of operating personnel and short circuits in electronic devices (particularly power supply units of machine controls with forced ventilation).

Figure 2-5: Hole in braided preform due to entangling of frayed fibers during formation of a spider's web; spider’s web still visible as thin zigzag thread between the braiding yarns (marked with red circle)

Related to frayed fibers in the braid formation zone are the agglomeration of broken filaments at yarn guiding elements of the bobbin carrier (e.g. yarn deflections at tensioning mechanism, guiding eyelet at yarn outlet). They form due to frictional interaction particularly around small bending radii at the bobbin carrier. Although such agglomerations only rarely cause an interruption of the braiding process, they may come loose and get pulled into the braid where they represent a foreign object.

According to Ebel et al. [46], one of the most frequent braiding defects is the so-called fibrous ring (cf. Figure 1-6, top left). As already introduced in section 1.2, it is described as an accumulation of broken filaments at the bobbin that hampers the unwinding process of yarn from the bobbin during the braiding process. It can always occur with no apparent reason but its likelihood of occurrence is drastically increased by yarn damage. Such yarn damage may be induced by an aged sizing of the reinforcement yarns or by inadequate rewinding parameters. During the rewinding step, yarn material that is delivered on big spools by the manufacturer is rewound onto smaller spools that fit into the braiding machine. During this rewinding step, yarn damage can occur due to…

- too high yarn tension (conflict area for manufacturing engineer since elevated yarn tension is advantageous in terms of setup times because more yarn can be stored on a bobbin with given volume due to increased yarn compression)
- too high rewinding speed (typical recommendation of manufacturers: ~75 % speed reduction for reinforcement yarns compared to thermoplastic yarns (cf. [63] for weaving); also conflict area for manufacturing engineer since higher rewinding speeds enable higher material throughput with a given number of rewinding machines)
- an improper setting of the reversal points of the creel bar causing bulbous or concave cross sections of the wound bobbins as well as
- deflection rollers contaminated with broken fibers. [46]

The major problem of yarn damage induced during the rewinding step is that – except for bulbous or concave cross sections of the wound bobbins – it is not visible to the operator. It may well be that hundreds of bobbins are prepared for the subsequent braiding step and it turns out that all of these bobbins constantly form fibrous rings due to unsuitable rewinding parameters. The mechanism for the formation of fibrous rings of filament-based reinforcement yarns is as follows: During braiding, yarn is unwound from the bobbin. Thereby, the point at which the unwinding yarn loses contact with the yarn material still stored on the bobbin (unwinding point) moves back and forth parallel to the rotational axis of the braiding spool. Since reinforcement yarns consist of several thousands of individual filaments that are grouped together parallelly in a roving, few broken filaments may stick to the remaining material on the bobbin at the unwinding point. The filaments in a roving of reinforcement fibers can be seen as endless. Thus, a helical winding of these few sticking filaments forms on the remaining yarn material as the unwinding point moves forward from one end of the bobbin to the other (cf. Figure 2-6). When the unwinding point has reached its reversal point at the end of the bobbin and starts moving backwards, the helical winding of the sticking filaments impedes a proper unwinding of the yarn. Depending on how tight the sticking filaments lie around the remaining material, they may only get gradually pushed towards the other end of the bobbin and remain there causing no further process impediments until the bobbin is empty. However, if the broken filaments stick tightly to the remaining material, they may impede the unwinding of the braiding yarn to such an extent that the yarn gets severely damaged. Newly created, broken filaments from that additional damage then add to the sticking filaments and form a strong fibrous ring. Such a fibrous ring leads to an increase in yarn tension of a single braiding yarn. This may then disturb the regular deposition process of the braiding yarns on the mandrel which may manifest as a local helical yarn gap in the braided preform (cf. Figure 1-6 bottom). Eventually, the yarn tension may increase to such levels that the yarn breaks.

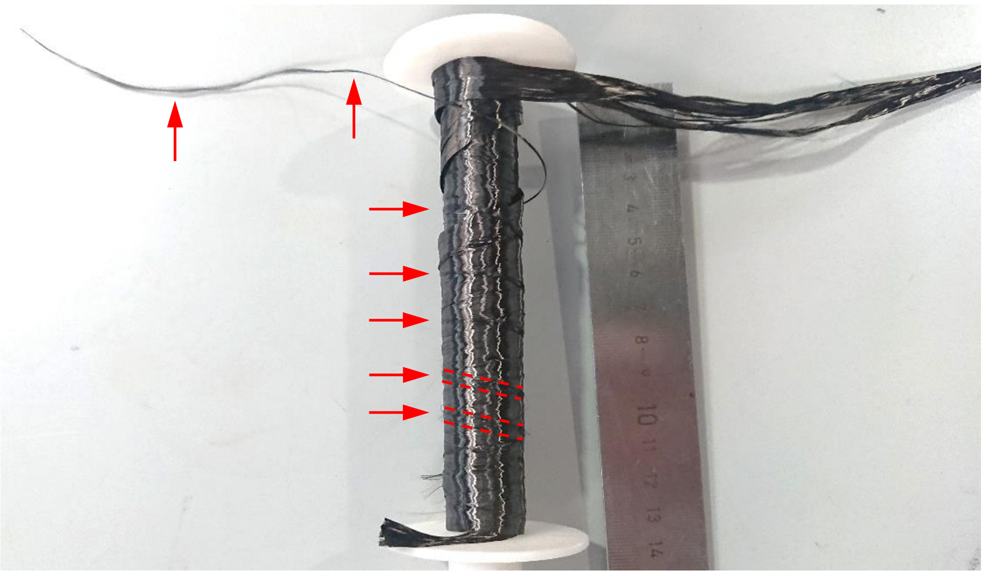

Figure 2-6: Broken filaments sticking to intact yarn material on the bobbin in a helical manner as origin of fibrous rings; thread of broken filaments indicated by red arrows, helical winding of broken filaments around the intact material highlighted by exemplary red-dashed lines

As mentioned as a motivational aspect in the introduction, Mierzwa [55] and Mierzwa et al. [54] found that such yarn gaps, when oriented perpendicularly to the loading direction, led to a deterioration of 36 % in tensile strength and of 33 % in compressive strength of specimens infiltrated by means of the VAP method. Such extreme effects were not observed when the specimens were injected with resin by means of RTM. The authors attributed this knockdown in strength to excessive fiber undulation in the vicinity of the gap created by the flexible VAP membrane as upper tooling. The rigid RTM tooling did not create such fiber undulation even though a yarn gap was present (cf. Figure 2-7). However, it needs to be noted that the authors induced yarn gaps in all layers of their braided preforms consisting of six layers. Additionally, in a cross-sectional view, the yarn gaps were located exactly upon each other. Such a configuration is highly unlikely to occur during braiding of a real component and thus must be regarded as an extreme case scenario. For this reason, Mierzwa [55] also investigated identical specimens except for the fact that only one yarn gap was located in the bottom of the six braided layers. In this more realistic scenario, he then observed a knockdown in tensile strength by 11 %. Compression tests were not conducted. Ebel et al. [46,52] conducted endurance braiding tests to determine to which extent machine productivity is reduced by the occurrence of braiding errors. For these tests, endless triaxial braid hoses with a braiding angle of 45° were produced from 300 m of glass fiber as braiding yarn material and carbon fiber as material for 0°-yarns on a machine with 60 carriers. Whereas they observed a machine downtime of 7 % of the total production time when proper rewinding parameters were used, the machine downtime varied between 23 % and 26 % when improper rewinding parameters led to the formation of fibrous rings and thus to the breakage of braiding and 0°-yarns. The authors concluded that even though other braiding defects (e.g. loops or gaps) may still require preform to be scraped, yarn breakages (that are most often caused by fibrous rings) were the kind of defect that had the most impact on machine productivity due to the necessity to manually rethread broken yarns.

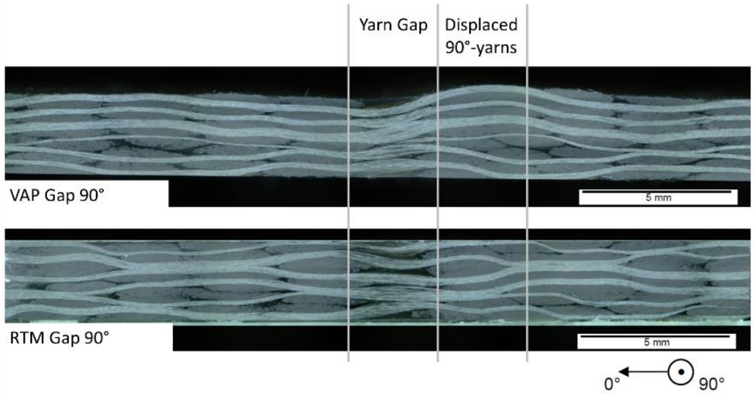

Figure 2-7: Comparison of microsections of a braided specimen infiltrated by means of the VAP method (top) and a specimen injected with resin by means of the RTM process (bottom); note the excessive fiber undulation due to the displaced yarns in the vicinity of the yarn gap in the specimen infiltrated by the VAP method in contrast to the unaffected yarns in the RTM case; image taken from [55], annotations translated into English

2.2 Process Monitoring Systems for Braiding

In order to detect and in the best case even prevent braiding defects as described above, some sensor systems are already obtainable. In the following subsection 2.2.1, sensor systems that are stationarily mounted to the body of the braiding machine are introduced. The systems presented comprise switches that are pushed by the bobbin carrier when a yarn has broken, a tactile system for yarn tension measurement, optical inspection approaches of the braid formation zone as well as sensing braid condensing devices. The succeeding subsection 2.2.2 then focuses on sensor systems that make use of sensors that are directly installed onto the moving bobbin carriers of a braiding machine. The approaches are presented in ascending order of technological complexity and detection capabilities ranging from solely sensing devices that wirelessly transmit their measurement data over sensor integrated bobbin carriers with integrated feedback loops for yarn tension control to concepts that eradicate the need for batteries to power the sensor and transmission devices.

2.2.1 Bobbin Carrier Independent Monitoring Systems

Commercially available and widely used are switches that jut into the tracks of the bobbin carriers. In Figure 2-8, the yarn tensioning mechanism of an IFDA-100 bobbin carrier from the RF 1/128-100 radial braiding machine at the Chair of Carbon Composites and a switch jutting into the track of the bobbin carriers is shown. The braiding yarn is guided through a 180°-deflecting element. By means of a connecting rod, two times the yarn tension plus a frictional component deflects the lever of the yarn tensioning mechanism upwards against the restoring force of the spring inside the shaft of the carrier. At the same time, a locking pin that engages with lateral notches in the bobbin prevents the bobbin from rotating. The lever then pushes the locking pin against the force of a second, smaller spring downwards which causes the pin to retract. Eventually, when the trigger point is reached, the locking pin disengages with the notches in the bobbin and thereby enables the bobbin to rotate. That way, yarn is unwound from the bobbin, the yarn tension decreases and the lever of the yarn tensioning mechanism falls down again. If a braiding yarn breaks, the lever or slider is pushed to its lowest possible position. When a bobbin carrier with its lever or slider in its lowest possible position is moved past the switch by the rotating horn gears, the switch gets pushed by an extension of the lever of the yarn tensioning unit. This in turn causes the machine to stop and operating personnel can resolve the error. Such an approach is cost-efficient because a limited number (at least one for each braiding yarn system) of low-technology switches is required to monitor all bobbin carriers of a machine. However, these switches can only be applied when all the bobbin carriers of the available machine are equipped with yarn material. This is not always the case since the operator may, for instance, only want to use half or a quarter of the available carriers in order to modify the braid pattern. Furthermore, these switches only produce a signal to stop the machine when a braiding yarn has already broken. That way, braiding with a missing yarn can be avoided. The generation of a control signal already during the formation of a yarn gap or when the yarn is about to break is however not possible. Hence, a trigger by such a switch always involves considerable amount of manual labor to replace the bobbin, threading the new yarn through the guiding elements of the bobbin carrier and creating a new settled braid pattern. Moreover 0°-yarns cannot be monitored by this approach.

Figure 2-8: Switch for braiding process interruption and yarn tensioning unit of a bobbin carrier with lever; image taken from own publications [64,65]

The system invented by Lenkeit [66] for Tensometric-Meßtechnik Ströhmann & Co. GmbH, Wuppertal makes use of a force sensor with a skid attached to it. The skid is located in the braid formation zone and deflects the braiding yarns by a defined angle as they slide past the skid (cf. Figure 2-9). By knowing this deflection angle, the tension of each yarn can be calculated. In contrast to the switches from above, yarn entanglements on the bobbins (e.g. fibrous rings) can be detected by this system because they cause an increase in yarn tension before a major failure such as a yarn breakage occurs. Although it is not clearly mentioned in the patent specification [66], it appears likely that the additional yarn contact by the skid in the braid formation zone promotes additional yarn damage. This is of particular interest when reinforcement fibers, which often exhibit brittle behavior, are braided at high production speeds (high impact velocity of the yarn relative to the skid).

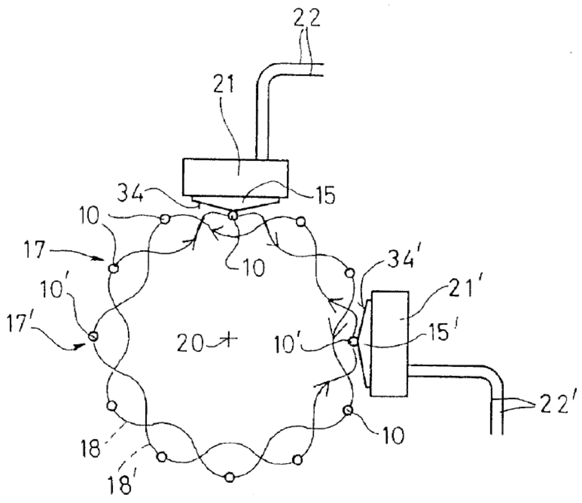

Figure 2-9: Plan view of an axial braiding machine with force sensors (15/15’) and attached skids (34/34’) deflecting braiding yarns for measuring their yarn tension; two sensors are required because each sensor monitors one braiding yarn system; drawing taken from [66]

SGL Kümpers GmbH & Co. KG, Rheine applied for a patent for an invention by Brockmanns et al. [67]. In principle, the application document sets out the same concept of measuring yarn tension in a radial braiding machine by means of a skid and a tactile sensor as the approach by Lenkeit [66] from above. However, Brockmanns et al. [67] added the idea that not only a deviating force signal in absolute value but also differing time intervals between force peaks hint at the presence of an overtightened yarn. This is due to the fact that in a radial braiding machine, the braiding yarns are not straight lines pointing towards the center of the machine. Instead, the yarns resemble an evolvent shape due to frictional yarn-yarn-interaction. Van Ravenhorst [35] and Van Ravenhorst et al. [68] noted this effect and even set up an elaborate yarn interaction model in order to calculate frictional interaction between yarns in radial braiding machines. Brockmanns et al. [67] argue that if all braiding yarns showed the same evolvent shape, then the time intervals between yarns touching the sensor must be identical. If a single yarn with a higher yarn tension is present, then this yarn should show less of an evolvent shape and more of a straight line. Hence, the time interval between touching the sensor of the preceding and the defective yarn should be reduced whereas the time interval between the defective yarn and the succeeding yarn should in turn be increased. Brockmanns et al. [67] mention that the effect of varying time intervals could also be measured by a stationary optical sensor in order not to induce any additional damage of brittle reinforcement fibers. Since [67] is a patent application document, experimental data to verify this claim is however not provided. Furthermore, Brockmanns et al. [67] mention that force sensors may not only be used in the braid formation zone but may also be integrated into the braiding ring (cf. number 2 in Figure 2-10). They mention an array of piezoelectric sensors incorporated into the braiding ring which would also allow a monitoring of, relative to the braiding ring, stationary 0°-filler yarns. Finally, due to the fact that 0°-filler yarns remain stationary, they also describe the monitoring of their tension by means of a stationary deflection roller that is deflected against a spring force by the yarn tension. As soon as the deflection roller leaves a process window between a lower and an upper threshold for its position, the occurrence of a defect is indicated.

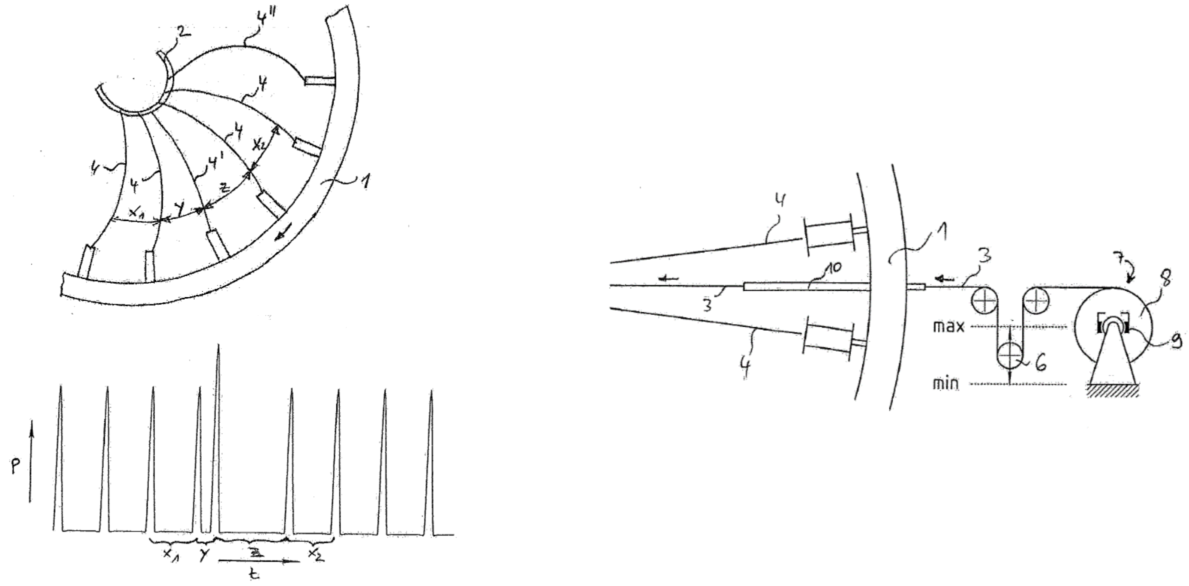

Figure 2-10: Schematic of deviating courses of yarns of different tension and resulting time intervals of the yarns touching a force sensor (x_1, y, z, x_2; left); schematic view of tension monitoring of 0°-filler yarns by means of a stationary deflection roller (6; right); drawings taken from [67]

Branscomb [69] and Branscomb et al. [70] describe an optical monitoring of the braiding point during braiding of endless cords on an axial braiding machine. When setting up a camera viewing in production direction (in Figure 2-11, left the camera would be positioned in the center of the track plate with view towards the braid formation point), they observed that the braid formation point remains in a small defined area in the center of the camera view (cf. Figure 2-11, middle). As soon as an elevated yarn tension was artificially created, the braiding point left this defined area and performed a motion in loops around the center of the camera view (cf. Figure 2-11, right). Additionally, they also investigated how this approach for braiding process monitoring performs when two blocked yarns are located on diametrally opposing bobbin carriers. As can be expected, they observed smaller deviations of the braid formation point than with only one defective yarn because the elevated yarn forces canceled out to a certain extent. However, the defect was still detectable because the detected motion of the braiding point was still significantly outside the small defined area in the center of the camera view during regular braiding. From a composite braiding standpoint, it however needs to be noted that such an approach is unsuitable for monitoring the braiding of composite preforms. This is because usually forming mandrels are used onto which the fibers are deposited. These mandrels are rigidly guided by manufacturing robots. Hence, a variation in the geometrical position of the braid formation point cannot be expected. The approach presented by Branscomb [69] and Branscomb et al. [70] is therefore only vital if the braiding point is free to move (e.g. during braiding of laces, cords or ropes).

Figure 2-11: Schematic of an axial braiding machine including the braid formation point (left); braid formation point in the center of the camera view during regular braiding (middle); braid formation point deviating from the center of the camera view during defective braiding (right); images taken from [70]

Another approach for monitoring the braid formation during manufacturing of laces, cords or ropes on axial braiding machines is provided by an invention from Schneider [71] filed as a patent by AUGUST HERZOG MASCHINENFABRIK GmbH & Co. KG[3], Oldenburg. Whereas in the above Figure 2-11 the braided strand is free to move in radial direction, this is usually not the case when mass products like ropes or laces are braided. Instead, the braid is supported by a braid-condensing device. This is a ring-shaped support that keeps the braided strand radially in place in order to enhance a regular braid formation. The invention by Schneider [71] features a braid-condensing device with a bracket attached to it. The bracket touches the incoming yarns. When the braid formation point gradually moves further down (e.g. due to a slipping haul-off unit which leads to a deviating braiding angle φ), the bracket follows this motion. A sensor that monitors the deflection of the bracket is used to stop the machine in order not to produce huge amounts of braid with the wrong braiding angle. In a further development of this patent, Schneider [73] invented another form of a braid-condensing device for AUGUST HERZOG MASCHINENFABRIK GmbH & Co. KG, Oldenburg which features a sleeve that tightly fits the produced braid diameter instead of a deflectable bracket (cf. Figure 2-12). The sleeve is held in a fixture that is movable around a rotational axis against a spring force. The advantage of this invention [73] compared to [71] is that also knots in a braiding yarn can be detected because a knot would locally thicken the braid. Since the sleeve tightly fits the produced braid diameter, the sleeve and its fixture get pushed upwards by the haul-off mechanism of the braiding machine in case of a knot in a braiding yarn. This deflection is detected by a tactile sensor which in turn generates a signal to stop the machine. Since this invention requires the sleeve to tightly fit the braid diameter, the invention is particularly designed to allow a quick change of the sleeve in order not to create additional machine downtime when a different product needs to be braided on the respective machine.

---

[3] AUGUST HERZOG MASCHINENFABRIK GmbH & Co. KG used to be the name of the renowned braiding machine manufacturer from Oldenburg, Germany. Since 1st January 2017, AUGUST HERZOG MASCHINENFABRIK GmbH & Co. KG acts as the global parent company of the new operational company HERZOG GmbH; sources: BISNODE Firmendatenbank and statement in the Bundesanzeiger [72].

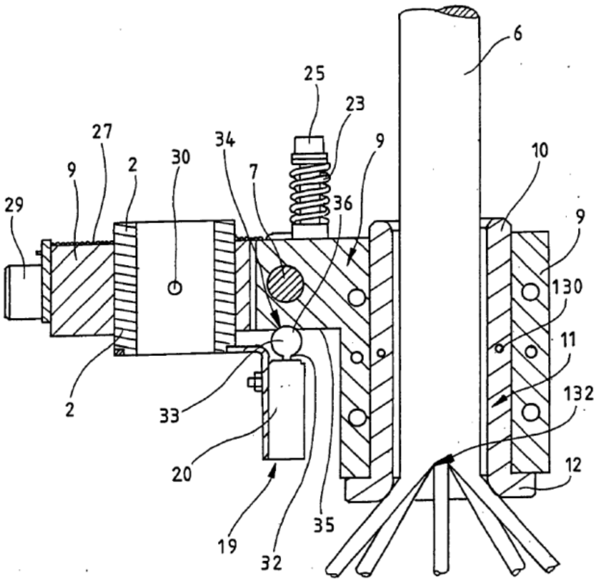

Figure 2-12: Braid-condensing device with sleeve (10) that tightly fits the braided strand (6); the fixture (9) of the sleeve is movable around the rotational axis (7) against the force of a compression spring (23); any deflection is detected by the sensor (20); drawing taken from [73]

2.2.2 Bobbin Carrier Dependent Monitoring Systems

In the final report of the project "AutoBraid" carried out at RWTH Aachen by Reuter et al. [74], a concept of a miniature force sensor installed onto an IFDA-100 bobbin carrier for composites braiding from HERZOG GmbH is described (cf. Figure 2-13). They attached the force sensor as connecting element between the lever of the yarn tensioning unit and the 180°-yarn deflecting element, thereby replacing the connecting rod between these two parts. That way, no additional and potentially damaging yarn contact was necessary. A telemetry unit was able to send the data to an acquisition unit over a distance of 8 m. The electronic device on the bobbin carrier was powered by a rechargeable battery. The authors managed to obtain high accuracy yarn tension measurements during the running process with a standard deviation of 34 cN. However, for a permanent use of the newly developed bobbin carrier, the authors point out that a continuous form of power supply such as induction coils along the tracks of the bobbin carriers would be beneficial. Thereby, the requirement to frequently change and recharge the battery during the process would be eliminated.

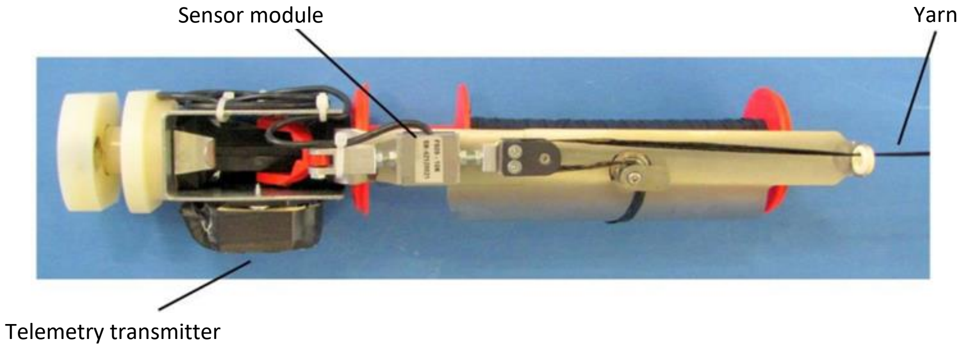

Figure 2-13: Load cell mounted onto modified IFDA-100 bobbin carrier from HERZOG GmbH; image taken from [74], annotations translated into English

Braeuner [75] invented an electronically driven bobbin carrier for Amedes Schuessler GmbH, Pforzheim. Instead of a load cell, he used a position sensor that measures the position of a slider on the bobbin carrier that is deflected against a spring force. Similar to the approach from above, he integrated a telemetry unit on the bobbin carrier for data transfer and also used a rechargeable battery as power supply. But he significantly went beyond the approach by Reuter et al. [74] when he included a motor on the carrier that actively drives the bobbin in order to release or retread yarn. He also proposed the implementation of a feedback loop between motor and sensor in order to allow the operator to set a desired level of yarn tension over a telemetry unit from outside the machine.

Reinisch et al. [76] invented an electronically driven bobbin carrier with sensing elements for measuring yarn tension for Maschinenfabrik Niehoff GmbH & Co. KG, Schwabach. The essence of their invention with sensing element, feedback loop and telemetry unit on the carrier is similar to the idea by Braeuner [75]. A major advancement is however that they elaborately thought about possible ways to eliminate the need for batteries to power the electronic devices on the carrier. For instance, Reinisch et al. [76] proposed using a dynamo that is mechanically driven by a gear or a friction wheel with the stationary bed of the machine as a counterpart. Furthermore, they also thought about stationary magnets attached to the body of the machine and induction coils on the bobbin carrier as means of power transmission. Moreover, the use of an electric motor operated as a generator that brakes the rotating bobbin as well as stationary sliding contacts and energy transmission via inductive coupling were considered. Finally, they also mentioned the possibility of using the braiding yarns as means of energy transfer in case metal wires are braided. However, no concrete design or configuration of any of the thought of concepts is provided.

Unlike the two approaches from Braeuner [75] and Reinisch [76], von Reden [45] and von Reden et al. [77] did not only describe how they intended to design an electronically driven bobbin carrier but also documented how they specifically built it (cf. Figure 2-14). In contrast to Braeuner [75], who used a bobbin carrier with a passive slider, von Reden [45] and von Reden et al. [77] built an entirely new carrier with a yarn eyelet including a yarn tension sensor that was movable on a slider. The bobbin was driven or respectively braked by an electric motor on the basis of the force signal from the yarn tension sensor. In order to achieve an accurate measurement of yarn tension with his design, it was necessary to maintain a constant right angle as unwinding angle from the bobbin. This was realized by the movable eyelet that was driven by a second electric motor. As a telemetry unit, a ZEBRA module from senTec electronic GmbH, which supports ZigBee as broadcasting standard, was used. As a concept for continuous power supply, von Reden [45] and von Reden et al. [77] made use of a significantly different approach than the ones described above. They installed induction coils in the center of the horn gears as transmitters of energy. Another induction coil was incorporated into the foot of the bobbin carrier as a receiver. Due to the fact that the bobbin carrier remains stationary with respect to the horn gear, they derived that the approach is capable of transferring energy to the carrier two thirds of the time the braiding machine was running. Only at the point of transfer of the bobbin carrier from one horn gear to the next (more precisely: in a window of 60° in rotational angle of the horn gears), no energy could be conveyed. This is a significantly longer period that is available for energy transfer compared to the approaches of stationary induction coils or magnets attached to the machine bed from above. The power transferred from the transmitter on the horn gear to the receiver on the carrier during the time period of possible energy transfer was about 1.2 W. However, as elaborate as the concept may be, it needs to be noted that the cost of additional material of more than 1000 € per carrier are a major drawback of this system, especially when it is considered that a braiding machine may comprise several hundreds of bobbin carriers. The approximate costs of the approach are known because Prof. Dr.-Ing. Klaus Drechsler, as head of the Chair of Carbon Composites at Technical University of Munich, acted as an examiner of von Reden's dissertation [45] as he did for the thesis at hand.

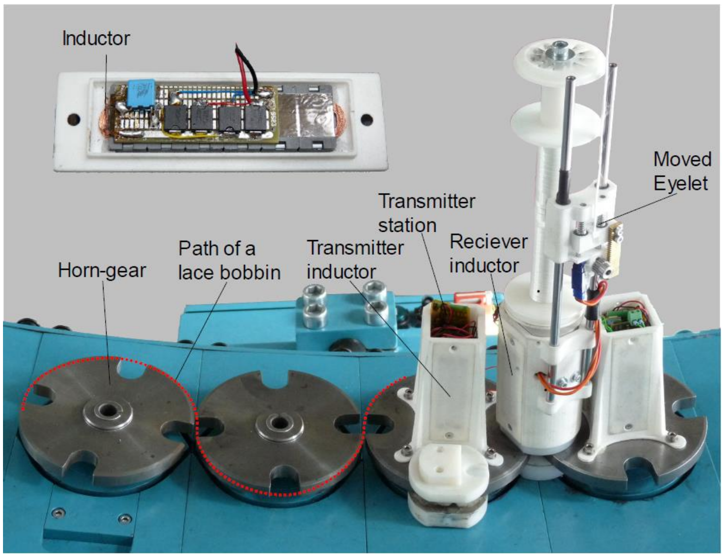

Figure 2-14: Image of the electronic bobbin carrier with transmitter station in the center of the horn gears and receiver unit in the foot of the bobbin carrier (main image); inductor for transmission of energy from horn gear to bobbin carrier (small image, upper left); image taken from [77]

3 Development of Variants of Bobbin Carrier Independent Sensor Modules for Early Defect Detection

As described in the above state of research, the commercially available switches that jut into the tracks of the bobbin carriers only deliver a control signal to stop the braiding machine when a braiding yarn has already broken. The formation of entanglements at the bobbin (e.g. a fibrous ring) and resulting yarn gaps in the preform cannot be detected. The invention by Lenkeit [66] is conceptually able to detect the latter process irregularities but requires additional yarn contact, which is disadvantageous in terms of fiber damage when processing brittle reinforcement yarns. An invention mainly made by the author of the dissertation at hand of stationary Hall effect sensors that detect the position of the lever of the yarn tensioning unit of a bobbin carrier eradicates these shortcomings while still being cost-efficient. This approach is delineated in section 3.1 of this chapter on bobbin carrier independent sensor modules.

The invention by Brockmanns et al. [67] mentions the idea of using piezoelectric sensors incorporated into the braiding ring of a radial braiding machine in order to determine if *stationary* 0°-filler yarns show an anomalously deviating yarn tension. A concrete way of implementing the sensors into the braiding ring is however not provided. Schneider [71,73] uses a mechanically related approach, but his implementation of a braid-condensing device is particularly suitable for axial braiding machines and limited to thin, rope-like braids. In section 3.2 of this chapter, it is shown that force sensors integrated into the braiding ring of a radial braiding machine are also capable of monitoring the tension of *moving* braiding yarns during braiding of preforms from reinforcement yarns even if the overbraidable mandrel shows a complex cross-section and curvature. Two concrete implementations – one for estimating axial and one for estimating radial reaction forces at the braiding ring – are depicted and are compared in terms of sensitivity with regard to natural process fluctuations. Additionally, a self-learning algorithm is developed which is able to distinguish between regular and defective braiding and, if a defect is detected, in which machine segment the defect is located.

Brockmanns et al. [67], Branscomb [69] and Branscomb et al. [70] all pursue the idea of optically inspecting the braid formation zone. Brockmanns et al. [67] propose measuring the distance between the braiding yarns in a radial braiding machine by stationary tactile or optical sensors as an indication of braiding defects. However, they do not provide any details on a technical implementation or data on how sensitive such an approach is. In subsection 3.3.1 of this chapter, this approach is implemented by means of a light barrier in the braid formation zone and tested under different levels of deviating yarn tension. Branscomb [69] and Branscomb et al. [70] use a camera to track the braiding point during manufacturing of rope-like braids. As described in the above state of the art, their approach is not applicable when composite preforms are manufactured by overbraiding rigidly guided mandrels. Therefore, in subsection 3.3.2 of this chapter, a technique for inspecting the braid formation zone during the production of composite preforms by means of a camera is developed. The technique measures the distance of all braiding yarns in the braid formation zone at once and can therefore be seen as an advancement of the stationary light barrier, which can only discretely measure yarn distances as the yarns pass by the stationary light barrier. The detection capabilities of the camera-based method are compared to the approach of measuring yarn distances in the braid formation zone by means of a light barrier.

Optical inspections of the finished braid as carried out by Reuter et al. [74], Hunt [78] or Heß [42] are not further investigated within the scope of this dissertation. The reason for this is that it is takes great effort to conduct image analysis on a low-contrast (black) carbon preform that shows disturbing light reflections due to the sizing of the carbon fibers. Although such approaches enable a quality inspection of braided preforms on a fine level, they can – despite the high effort – conceptually never detect braiding defects before they have manifested in the finished product. It is however particularly the goal of the sensor modules presented in the dissertation at hand to detect defects early during their formation in order to reduce machine downtime and to still be able to resolve the defect by simple means (e.g. removal of a fibrous ring by hand with scissors, cf. Figure 1-6, top right). Moreover, approaches for optical in-plane measurement of fiber orientations in 2D weaves or non-crimp fabrics are already commercially available (e.g. fiber orientation sensor from PROFACTOR GmbH [79]). The use of such a sensor for quality inspection also for 3D preforms from reinforcement yarns is published in recent research from Heieck [80].

3.1 Stationary Hall Sensor Module

The idea of using stationary Hall sensors for the detection of braiding process irregularities was filed as a patent application by Technical University of Munich with the author of the dissertation at hand as the main inventor (share: 65 %) [81]. The patent was granted by the European Patent Office on 16 February 2022. The concept was first presented to the public at the 19th European Conference on Composite Materials (ECCM19) in Athens, Greece [65] and published with additional data as reviewed paper in the proceedings of the 13th International Conference on Textile Composites (TexComp-13) in Milan, Italy [64]. Although the author here gives an independent reproduction of the newly invented concept and achieved results to the best of his ability, occasional similar passages to the patent [81] and papers [64,65] may occur in the description below because they originate from the same person.

In order to understand the measuring principle of the stationary Hall sensor module, the so-called compensation devices of bobbin carriers need to be explained first. During braiding with horn gear-based machines (e.g. with axial and radial braiding machines) the bobbin carriers follow meandering courses, causing the yarns to form the braided interlacement structure. Due to the meandering movement, the yarn length between yarn exit from the bobbin carrier and braiding point varies (cf. Figure 3-1, left). The purpose of the compensation mechanism is to even out this difference in yarn length Δl so that the yarn is kept under a defined tension within a constant range throughout the process.

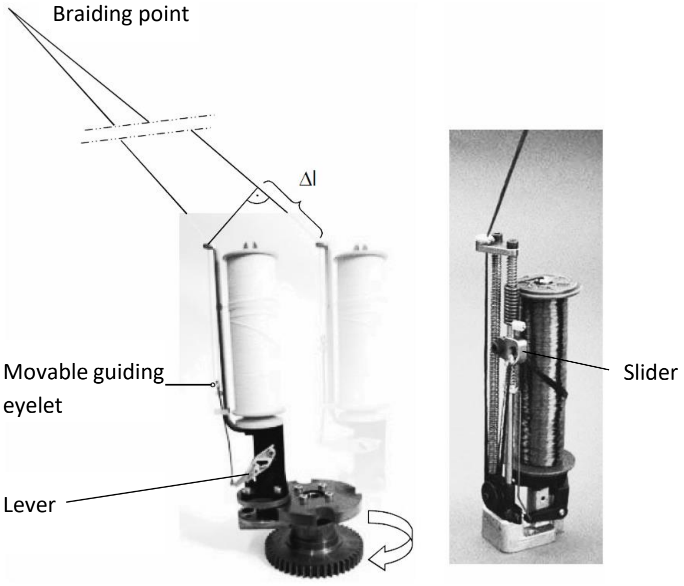

Figure 3-1: Lever-based bobbin carrier with indicated difference in yarn length Δl depending on the position of the carrier with respect to the braiding point (left; image taken from [16], annotations translated into English and complemented); slider-based bobbin carrier (right; image taken from [16], annotation added)

As can be seen in Figure 3-2, there are bobbin independent and bobbin dependent yarn length compensation devices. Bobbin independent compensation devices either use a lever (cf. Figure 3-1, left) or a slider (cf. Figure 3-1, right) as a movable member for yarn length compensation. The bobbin itself does not take part in the compensation action. For the creation of the yarn tension, the lever or slider is impinged with a force either by a weight or a spring. In case of the seldomly used bobbin dependent compensation devices, there is no movable member to create a yarn reserve. The bobbin itself acts as compensation unit because it is unwound against the force of a coiled flat spring or a motor holding it back. According to Kyosev [19], bobbin independent compensation devices that make use of the combinations…

- slider plus weight,
- slider plus spring and
- lever plus spring

are most popular.

Generally speaking, slider-based compensation devices require less space than lever-based devices and offer more space for larger bobbins. Lever-based compensation devices are particularly used when lower levels of yarn tension are required because they involve less friction in contrast to a slider that is guided on a track. The actuation by weight only works with vertically oriented bobbin carriers (axial braiding machines) and when the machine speeds are not too high (moment of inertia of weight). By contrast, springs as actuators of the movable members can be used for all orientations of bobbins (vertical in axial and additionally horizontal or upside down in radial braiding machines). [19]

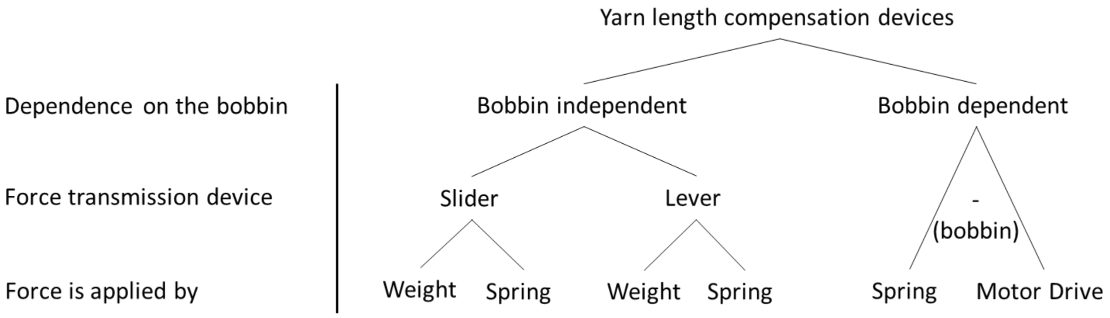

Figure 3-2: Classification of compensation devices; redrawn based on Kyosev [19]

Bobbin independent compensation mechanisms are connected to a brake that prevents the bobbin from rotating freely as long as enough yarn reserve is stored in the compensation device. When the yarn reserve is used up and the yarn tension increases to the trigger point, the brake is released and yarn can be unwound from the bobbin. Such brakes are usually comprised of lateral teeth or notches at the bobbin and a kind of pawl as a part of the carrier (e.g. a locking pin). The movement of the compensation device causes the pawl to engage and disengage with the teeth or notches in the bobbin. The detailed principle of a lever-based bobbin carrier with force application by spring is depicted in Figure 3-3. The lever of the compensation device is pushed downwards by a long spring inside the tube of the bobbin carrier. Consequently, the pawl is pushed upwards by a smaller pawl spring and engages with the lateral notches in the bobbin. The bobbin is now blocked from rotating. As the braiding machine pulls yarn, the yarn tension increases and the lever of the compensation device is pulled upwards against the force of the spring inside the tube. The pawl is in turn pushed downwards by the lever but is still engaged with the notches in the bobbin. Eventually, when the trigger point is reached, the pawl disengages with the notches in the bobbin. The bobbin is now free to rotate and yarn is released. This causes the yarn tension to decrease, the lever gets pushed down again by the spring inside the tube and the pawl engages with the notches in the bobbin again. This cycle of engaging and disengaging the pawl periodically repeats at each carrier during the braiding process.

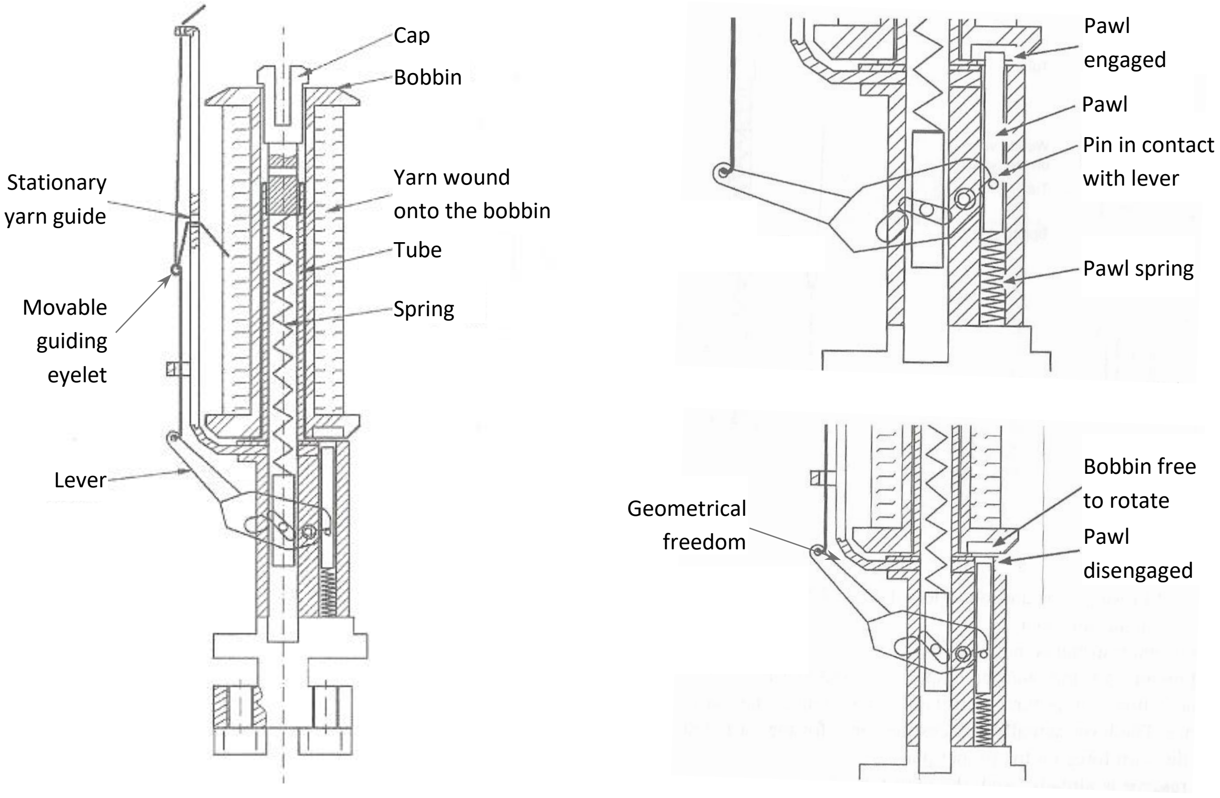

Figure 3-3: Overview of a carrier with a lever as movable member of the compensation device and force application by a spring inside the tube of the carrier (left); detailed view of a pawl engaged (top right) and disengaged with the bobbin (bottom right); drawings taken from Kyosev [19], annotations adapted and complemented

The author of the thesis at hand made the observation that when the trigger point is reached and the pawl is not engaged with the bobbin any more, the lever of the yarn tensioning unit still has some geometrical freedom to be pulled further upwards beyond the trigger point. This geometrical freedom is visible as a gap between the lever and the frame that holds the stationary yarn guiding elements in the drawing in Figure 3-3 at the bottom right. The geometrical freedom beyond the trigger point is in reality even larger than drawn. For instance, for an IFDA-100 carrier from the HERZOG RF 1/128-100 braiding machine at the Chair of Carbon Composites as shown in Figure 1-3, the rotational freedom of movement of the lever beyond the trigger point where the pawl disengages with the bobbin is about 10°. A position of the lever beyond the trigger point is however never reached during regular unwinding of the yarn from the bobbin because when the pawl is disengaged, the decreasing yarn tension in combination with the force applied by the spring inside the tube causes the lever to be pushed down again. Only when there is an unwinding related irregularity such as a fibrous ring, the yarn tension does not decrease when the pawl is disengaged. By contrast, it even increases further since the braiding machine keeps pulling yarn. This causes the lever of the yarn tensioning unit to be lifted upwards beyond the trigger point. Often, the lever is lifted until it comes in contact with the frame that holds the stationary yarn guiding elements. At the lever of the yarn tensioning unit, there are horizontal extensions that push the switches that jut into the tracks of the bobbin carriers upon yarn breakage (cf. Figure 2-8). As introduced in the state of research in section 2.2, such switches are as standard equipment commercially available as defect detection systems in braiding machines.

This is why these horizontal extensions at the levers of the yarn tensioning mechanisms of the bobbin carriers are usually already in place. The author then made the inventive step to clip a magnet in a 3D printed housing onto such an extension. A stationary Hall effect sensor that is placed at the side of the track of the bobbin carrier measures the magnetic flux density which can be translated into the distance between Hall probe and magnet. For calibration purposes, the fixture that holds the Hall sensor in place is height-adjustable. This way, it is made secondary use of the already existing yarn tensioning mechanism at the bobbin carrier as a rudimentary spring balance to indicate the acting yarn tension. Only a limited number of low-cost extra parts is required on each bobbin carrier (3D printed housing and magnet) and, in theory, a single Hall effect sensor per track is sufficient for monitoring the tension of all braiding yarns (cf. subsection 3.1.1 for detailed considerations on required number of sensors). Moreover, the approach is not limited to lever-based carriers with force application by springs. With the necessary adjustments of incorporating a possibility to place the magnet on the movable member of the compensation device and of mounting the Hall effect sensor stationarily to the body of the machine, it has the potential to be used on all bobbin carriers that work with bobbin independent yarn length compensation devices. Figure 3-4 illustrates the setup of the measurement principle implemented into the RF 1/128-100 braiding machine at the Chair of Carbon Composites. In this concrete use case, a neodymium disc magnet with a diameter of 8 mm, a height of 3 mm and quality class N45 as well as an analog IDUINO Hall effect sensor SE022 was used.

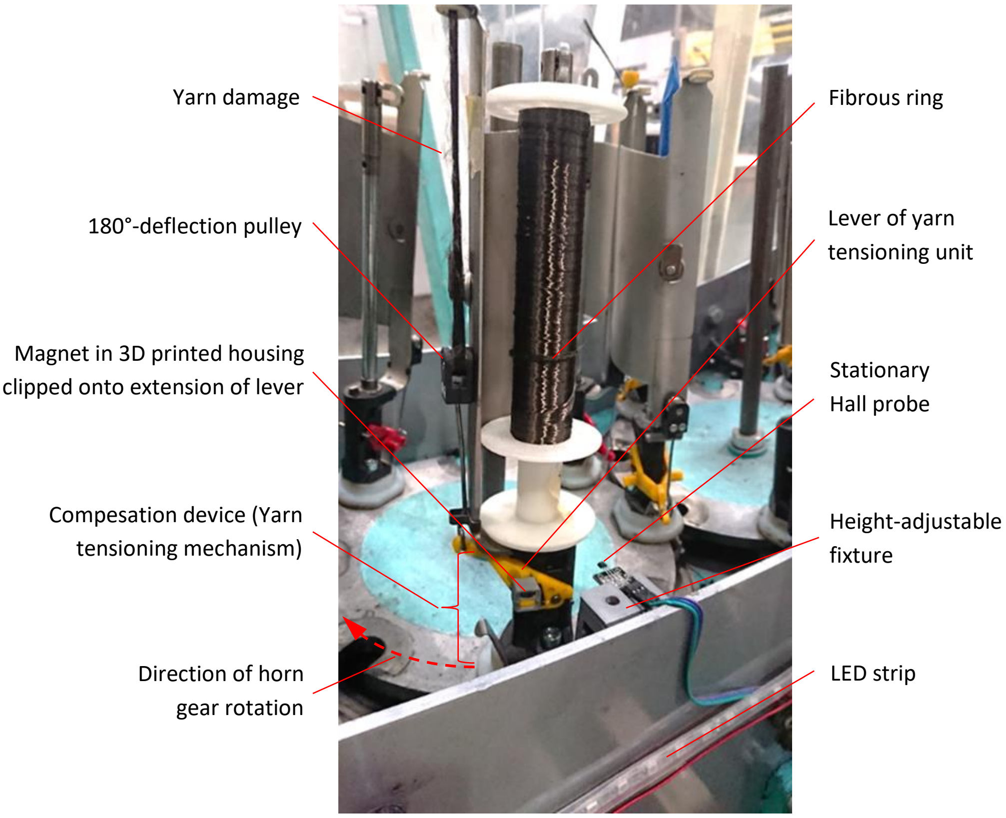

Figure 3-4: Magnet in clippable, 3D printed housing attached to the tension lever of a bobbin carrier as well as a stationary Hall sensor implemented into the radial braiding machine RF 1/128-100 at the Chair of Carbon Composites; note that the tension lever is already in its uppermost position because of the fibrous ring on the bobbin that creates visible yarn damage

In the placement of the sensors, the approach is similar to the switches that jut into the tracks of the bobbin carriers (cf. Figure 2-8). However, the main difference to the existing switches is that the newly proposed approach conceptually has the ability to generate a control signal to stop the machine well before a yarn breaks. Moreover, no additional yarn contact as with the system invented by Lenkeit [66] is required. This makes the approach particularly beneficial for the processing of brittle reinforcement fibers that are susceptible to yarn damage. Detailed tests and results to demonstrate the capabilities of the newly invented approach are given in the following subsections. Subsection 3.1.1 focuses on tests on a stationary unwinding test stand. Measurements from a commercially available deflection roller-based yarn tension measurement device are compared to measurements from the new sensor module. Additionally, a statistical analysis is conducted to determine how many sensors per track of bobbin carriers are required to reliably monitor all yarns of a braiding machine. In subsection 3.1.2, the new sensor module is implemented into the radial braiding machine RF 1/128-100 at the Chair of Carbon Composites. In order to show the universal usability of the approach, the system was also temporarily implemented for research purposes on an axial braiding machine at the production site of the project partner Barthels Feldhoff GmbH & Co. KG in Wuppertal.

3.1.1 Initial Characterization of the Sensor Module on a Stationary Test Stand

The unwinding experiments described in this subsection were mainly conducted within the framework of a bachelor’s thesis by the student Martin Sabieraj [82]. Apart from Prof. Dr.-Ing. Klaus Drechsler, the author of the dissertation at hand acted as a second supervisor for the thesis. The author specified the task of the bachelor’s thesis and the experimental procedure including the test plan. The practical working out of the unwinding experiments was mainly performed by the student with help and under close guidance and supervision from the author. Processing of the raw data (e.g. referring the time-based measurement to the unwound yarn length) was carried out by the student according to detailed instructions from the author. The analysis of the processed measurement data as shown in this dissertation was conducted independently by the author. The test stand itself was available at the Chair of Carbon Composites and originally neither built by the student nor the author. It was originally designed to characterize the extent of yarn damage due to frictional interaction during braiding of brittle reinforcement fibers as described in [46,52,83]. This capability was however not needed for the investigations in this thesis. The student and the author modified the test stand to fulfil specific requirements of the intended experiments (e.g. integration of Hall sensor module, measurement unit for length of unwound yarn) in collaborative work.

Experimental Setup

The setup of the unwinding test stand is illustrated in Figure 3-5. It comprised a stationary IFDA-100 bobbin carrier from HERZOG GmbH on which a bobbin with yarn material was mounted. The yarn was guided over two deflection rollers of which the first one featured an M1391 yarn tension measurement unit from Tensometric Messtechnik GmbH. Right before the reel, on which the yarn was rewound by a NEMA-23 bipolar stepper motor including a 15:1 gearbox from Phidgets Inc., an additional deflection roller was located, which served as a rotary position transducer for the measurement of the length of unwound yarn. According to the setup of the Hall sensor module described above, a neodymium disc magnet of quality class N45, 8 mm in diameter and 3 mm in height was attached to the lever of the compensation device of the bobbin carrier by means of a clippable, 3D printed housing. An Iduino SE022 analog Hall probe in a height-adjustable fixture was placed next to the compensation device of the bobbin carrier in order to measure the magnetic flux density created by the magnet on the lever. The measurement data from the yarn tension measurement device as well as from the Hall effect sensor was acquired by a USB-6009 data acquisition device from National Instruments Corp. and MATLAB R2015b as data acquisition software. Additionally, the unwinding process was recorded by an SLR camera.

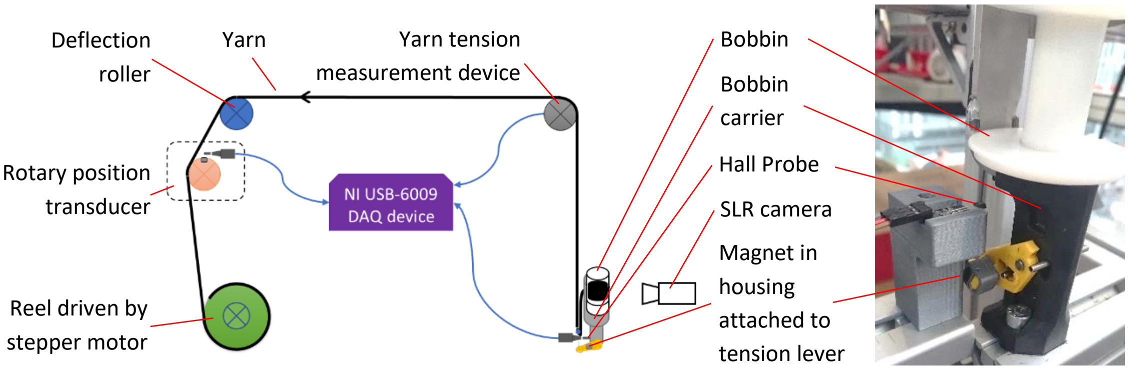

Figure 3-5: Schematic overview of the unwinding test stand (left; image taken from supervised student thesis [82] and adapted); detailed view of the tension lever with attached 3D printed housing containing the magnet as well as the stationary Hall probe (right)

As can be seen from the sample images in Figure 3-6, three different yarn materials were investigated on this test stand with the newly developed sensor module:

- a *carbon fiber yarn* of the type Tenax®-E HTS40 F13 12k with a titer of 800 tex from Teijin Carbon Europe GmbH
- a *double-folded polyester (PES) monofilament yarn* with a diameter of 0.25 mm of the individual threads
- a *double-folded PES multifilament yarn* with a titer of 300 tex of the individual threads

The *carbon yarn* material was chosen in accordance with the standard test scenario as detailed in the introduction (cf. section 1.2) as a representative for reinforcement fibers, which the dissertation at hand focuses on. The latter two *PES yarn materials* were investigated because the invention of using stationary Hall sensors in braiding machines as a defect detection system was made within a project on general (textile) braiding. Although these two material types may appear outside the scope of this thesis, the author deemed it useful to present the findings obtained from these materials anyway. As will be shown below, the modes of entanglement of the PES yarns on the bobbin differ significantly from the characteristic fibrous rings of reinforcement fibers. This has a significant effect on the detection capabilities of the proposed defect detection approach by sensing the position of the movable member of the yarn compensation device of a bobbin carrier. Thus, including the results of the PES yarns in this thesis demonstrates the limits of the newly invented approach and enables the reader to form a more educated opinion on the applicability of the presented approach for a given use case outside the field of braiding of reinforcement fibers.

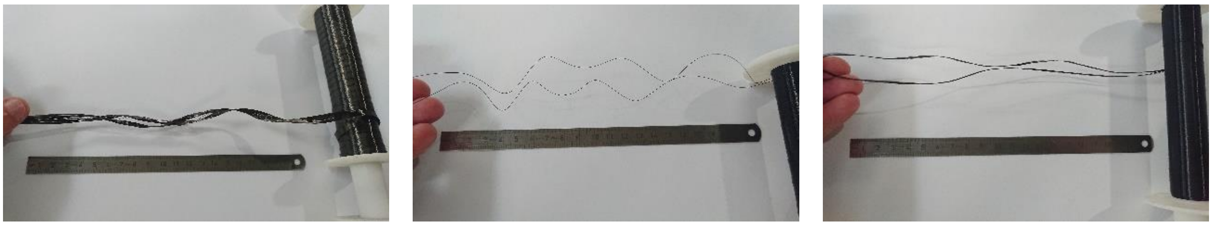

Figure 3-6: Sample images of the three yarn materials investigated on the unwinding test stand: carbon yarn (left), double-folded PES monofilament yarn (middle), double-folded PES multifilament yarn (right)

To generate a broader picture of the unwinding behavior of the three types of yarn material, both the unwinding rate and the level of yarn tension were varied. All of the three materials were tested at unwinding rates of 40 $\frac{mm}{s}$ and 80 $\frac{mm}{s}$, respectively. 40 $\frac{mm}{s}$ was chosen because this is approximately the unwinding rate of the braiding yarn in the standard braiding scenario as specified in the introductory section 1.2. To keep the duration of a single test at about 20 minutes (time limit of the SLR camera for recordings), 50 m of yarn were wound onto the bobbins that were to be unwound at a rate of 40 $\frac{mm}{s}$ and 100 m of yarn were wound onto the bobbins that were to be unwound on the test stand at a rate of 80 $\frac{mm}{s}$. As a yarn tensioning element, a spring in the central tube of the bobbin carrier rated at 350 g (mass equivalent to the applied yarn tension) was used for all of the three materials and unwinding rates according to the standard braiding scenario from section 1.2. As a second level of yarn tension, a spring rated at 130 g was used for the double folded PES monofilament yarn and a spring rated at 700 g was used for both the carbon and the double folded PES multifilament yarn. For each configuration (parameter combination of material, unwinding rate and carrier spring), three reference measurements without any defect were carried out (regular unwinding). In addition to this, five measurements were conducted for each configuration with some kind of provoked irregularity either by yarn damage or by improper parameters during rewinding (provoked entanglement). For reasons of a better overview, the test plan is graphically reproduced in Figure 3-7.

Yarn Material

- **Carbon multifil**
  - Tenax®-E HTS40
  - 800 tex (12k)
  - Single yarn
- **PES monofilament**
  - Ø 0,25 mm
  - Double-folded
- **PES multifilament**
  - 300 tex
  - Double-folded

Unwinding Rate

- **$40\,\frac{mm}{s}$**
  - All materials
- **$80\,\frac{mm}{s}$**
  - All materials

Carrier Spring Rated at

- **350 g**
  - All materials
- **130 g**
  - PES monofilament
- **700 g**
  - PES multifilament
  - Carbon

Provocation of Entanglement

- **Regular unwinding**
  - All Materials
- **Provoked entanglement**
  - Sand paper with 800 Mesh (Carbon)
  - Uneven yarn tension during rewinding (PES monofilament, PES multifilament)
  - Thread with lower tension unwound by one additional revolution (PES multifilament)

Figure 3-7: Test plan for the experiments on the stationary unwinding test stand

The *carbon yarn* was predamaged during the rewinding step by guiding it over a metal rod with a diameter of 30 mm under a wrap angle of approximately 3.2°. To achieve a defined level of yarn damage, 800-grit sand paper was wrapped around the rod. The yarn tension was set to approximately 4 N. The tension was measured by means of a handheld yarn tension measurement device of the type DTMX-500-U from Hans Schmidt & Co. GmbH before the yarn interacted with the sand paper. The roughened yarn was optically not distinguishable from a pristine yarn. However, it reliably led to the formation of fibrous rings during unwinding on the test stand (cf. Figure 3-8, left). To the knowledge of the author, this procedure of predamaging reinforcement yarns for a provocation of fibrous rings was first documented by Mierzwa et al. [53] and Mierzwa [55].

The difficulty of properly rewinding double-folded yarn material in a production environment is to wind exactly the same length of both threads onto one bobbin. What sounds simple is however not an easy task. Due to the fact that several kilometers of yarn material can be wound onto a single bobbin, even slightly different strains between the threads of stretchable yarn material (e.g. the two investigated PES yarns) cause the lengths of the two threads to differ significantly from each other. This way, the thread that has seen the lower level of yarn tension than the other (and whose strain level is therefore lower) forms loops at the bobbin during braiding (cf. Figure 3-8, middle and right). These loops may either entangle with themselves and lead to a yarn breakage or entangle with bobbin carriers going in the opposite direction in the braiding machine.

With this background knowledge on rewinding double-folded yarns, the formation of entanglements of the two PES yarns on the unwinding test stand was actively provoked during the preceding rewinding step by purposefully setting unequal yarn tensions for the two threads. The yarns were braked by means of adjustable plate tensioners (cf. [46,52]). The yarn tension was again determined by means of a portable yarn tension measurement device of the type DTMX-500-U from Hans Schmidt & Co. GmbH. The two threads of the *PES monofilament yarn* material were wound onto the bobbins with a yarn tension of 4.6 N and 12.1 N, respectively. Such a difference in yarn tension represents an extreme maladjustment of the yarn brakes and usually does not occur in industrial production. However, this extreme difference in yarn tension reliably led to the formation of yarn loops at the bobbin carrier even after short unwinding lengths of 50 m or 100 m, respectively. Hence, it was a way to speed up the process of formation of yarn entanglements within the scope of the unwinding tests. Accordingly, the two threads of the *PES multifilament yarn* material were rewound onto the bobbins under a yarn tension of 3.8 N and 8 N, respectively. The different levels of yarn tension of the two types of PES yarn are explained by their different frictional properties against the metal plates of the yarn tensioners. In addition to this, the thread of PES multifilament yarn with the lower tension during rewinding was unwound by one revolution from the bobbin directly before the unwinding test. This is an error that can be introduced in an industrial use case by mistake of operating personnel when it mounts newly wound bobbins onto a braiding machine. Thereby, the tendency of the PES multifilament yarn material to form yarn loops on the unwinding test stand that led to yarn breakages was further increased.

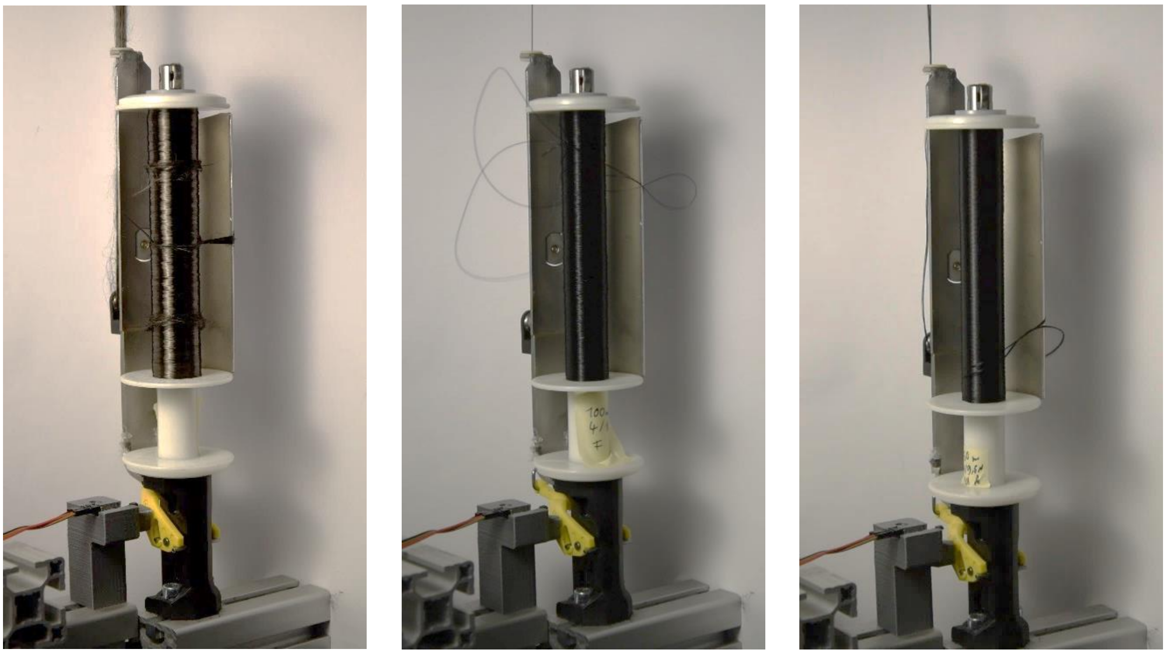

Figure 3-8: Provoked modes of entanglement of the carbon yarn (several fibrous rings at the bobbin and yarn damage in the background; left), the PES monofilament yarn (several yarn loops at the bobbin; middle) and the PES multifilament yarn (single yarn loop at the bobbin; right); images taken from recordings of the SLR camera during the unwinding experiments that were carried out within the framework of supervised student thesis [82]

Results and Discussion of Flawless Reference Measurements as Initial Sensitivity Assessment of the Sensor Module

Firstly, the results from the defect free measurements are presented. They shall serve as a basis to judge the suitability of the presented approach by Hall sensors to measure yarn tension instead of a dedicated yarn tension measurement device. Secondly, results from the manipulated bobbins are presented. This data is intended to evaluate the defect detection capability of the newly invented monitoring approach.

Figure 3-9 shows exemplary data at two different levels of detail gathered by the experiments on the stationary test stand during regular unwinding of the carbon yarn material. The diagrams start at 0.5 m of unwound yarn to exclude settling effects at the beginning of the unwinding experiment. In Figure 3-9 on the left, a comparison between measured yarn tension and measured Hall voltage over 10 cm of unwound yarn is depicted. When comparing the data obtained from the deflection roller-based yarn tension measurement device (blue) to the data from the stationary Hall effect sensor (orange) installed to monitor the position of the tension lever, it is apparent that both ways of measuring reflect the ratcheting mechanism of the yarn tensioning unit of the carrier by their fluctuating measurement values. A time delay between the measurement curves is not observable. In Figure 3-9 on the right, measurement data from a length 50 cm of unwound yarn is illustrated. Apart from the high-frequency fluctuations due to the ratcheting brake mechanism on the carrier, a superimposed fluctuation with a cycle duration of approximately 9 cm in terms of unwound yarn length is observable in the measurement readings from both the yarn tension measurement device and the Hall sensor. However, this superimposed fluctuation is more pronounced in the Hall voltage than in the yarn tension when referred to the amplitude levels of the high-frequency fluctuations. When consulting the recording from the SRL camera on the test stand, this superimposed cycle can timely be matched to the single revolutions of the bobbin on the carrier. Moreover, the bobbin that was used featured 11 lateral notches. Each of the said cycles also exhibits 11 periods of engaging and disengaging the locking pin. Hence, there must be a kind of eccentric frictional or braking moment that causes these fluctuations both in yarn tension and Hall voltage. A contamination of the inner surface of the tube of the bobbin, e.g. by a piece of adhesive tape that is often used to stick one end of a thread to the bobbin at the beginning of the rewinding step, can be ruled out because the fluctuations occurred with most of the tested bobbins. Moreover, a friction-related effect would only affect the values of the local minima of the Hall voltage. The local maxima would remain unaffected because it is a solely geometric dependence when the locking pin (in terms of lever position and therefore Hall voltage) loses contact with the lateral notches of the bobbin. Therefore, it rather appears that the points at which the locking pin engages and disengages with the lateral notches vary geometrically as the bobbin turns. To put it in other words, it seems likely that the superimposed fluctuation in Hall voltage discussed herein origins from a geometric imperfection of the bobbins.

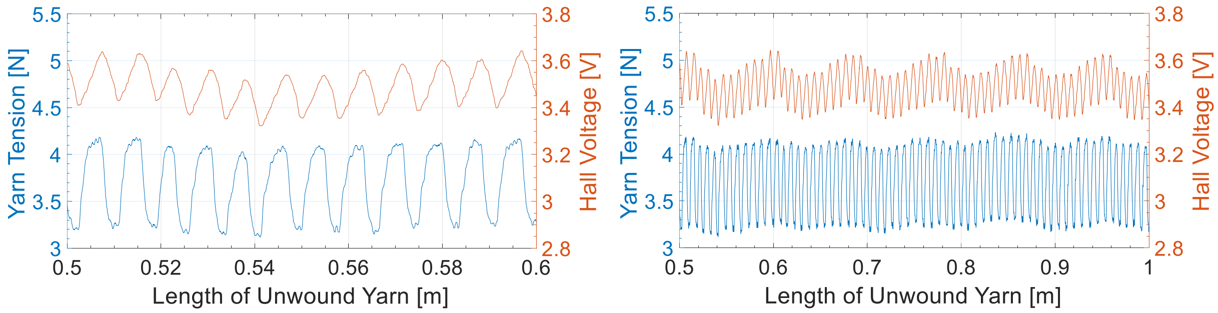

Figure 3-9: Signals of yarn tension (blue) and Hall voltage (orange) obtained from unwinding pristine carbon yarn at 40 $\frac{mm}{s}$ using a spring rated at 350 g; higher level of detail (left); lower level of detail (right); diagrams taken from own publications [64,65], axis labels adapted

For a more detailed consideration, the reader is referred to Figure 3-10, left in which the contact area between carrier and bobbin is depicted both at the carrier and at the bobbin. A metal ring face that is elevated by approximately 0.5 mm with respect to the black plastic surround can be seen on the carrier. During unwinding, the bobbin rests on this ring face with its weight. The ring-shaped area on the bobbin is in contact with the metal ring face of the carrier. Additionally, the lateral notches of the bobbin are visible. As can be seen from the gap in Figure 3-10 on the right, the notched area is not in contact with the plastic surround of the carrier. The locking pin must bridge this gap in order to engage with the notches to brake the bobbin.

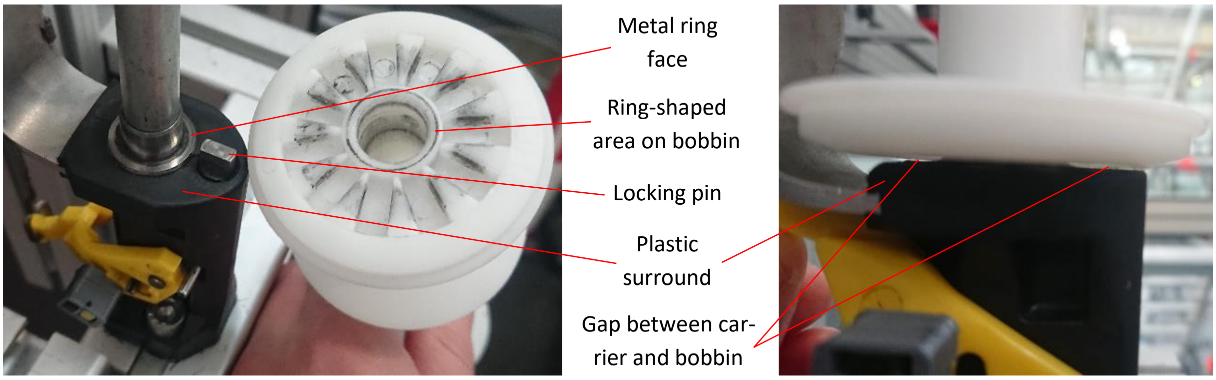

Figure 3-10: Foot of an IFDA-100 bobbin carrier including a metal ring face on which the bobbin rests during unwinding (left); gap between foot of the bobbin carrier and notched area of the bobbin while the locking pin is retracted (right)

The point is now that the gap between the notched area on the bobbin and foot of the carrier appears to vary as the bobbin turns. This would mean that the locking pin had to bridge a varying distance to brake and release the bobbin as the bobbin turns. This would explain the superimposed fluctuation both in yarn tension and Hall voltage in Figure 3-9, right. In order to underpin this presumption, 3D scans of the notched area of ten bobbins were conducted with an ATOS Capsule system from GOM GmbH. To avoid reflecting effects at the surface area to be scanned, it was sprayed with medium number 3 (white matt developer) of the Standard-Chek dye penetrant crack detection system from HELLING GmbH [84]. Of each bobbin, both the notched top and bottom end were scanned. The reason for also scanning the notches at the top, which are usually not in contact with the locking pin of the carrier, was that the manufacturer produces the bobbins with an overlength by an injection molding process. The manufacturer then turns them down at the top side to achieve a precise bobbin length. Hence, the author suspected that any possible geometric imperfection of the notched area could be less pronounced at the turned down area at the top than at the bottom of a bobbin. Moreover, the standard Tenax®-E HTS40 F13 12k carbon yarn material was wound onto all scanned bobbins and their unwinding behavior was monitored on the unwinding test stand (cf. Figure 3-5) by means of the stationary Hall sensor and the deflection roller based yarn tension measurement device. Each bobbin was investigated twice – one time with its bottom in contact with the locking pin (usual arrangement) and one time with its top in contact with the locking pin (unusual arrangement carried out to correlate data to the scanned bobbin tops).

Figure 3-11 illustrates the notched area at the bottom (left) and the notched and turned down area at the top of a bobbin (middle). On the right of Figure 3-11, the 3D scan as calculated by the software GOM ATOS Professional 2020 of the bobbin part visible in the middle is shown. For the sake of a better understanding of the following diagrams on the scanned surface relief, the references for the measurement are drawn-in. A circular cross section over the notched area is drawn-in as a thin, red line. The cross sectional profile was measured with respect to the blue z-axis of the drawn-in coordinate system. The z-axis was aligned with the longitudinal axis of the tube of the bobbin. The origin of the coordinate system was placed at the intersection point between the longitudinal axis of the tube of the bobbin and the drawn-in, green plane. This plane was defined as a Gaussian fitting plane over the ring shaped area at the side of the bobbin. The author puts particular emphasis on the way the cross sectional profile was measured because – as will be seen below – the different parts of the bobbins are both distorted in themselves and against each other. One can already assume this since the green fitting plane does not exactly match the ring-shaped area on the bobbin in Figure 3-11, right but crosses it several times. Hence, defining the reference coordinate system differently, for instance with the x-y-plane of the coordinate system aligned to the green fitting plane, results in different measurement values. However, the main conclusion of the analysis as derived below does not change.

Figure 3-11: Notched area at the bottom of a bobbin (usually in contact with the locking pin; left); notched area at the top of a bobbin (turned down and usually not in contact with the locking pin; middle); 3D scan of the notched area shown in the middle with circular cross section drawn-in as a thin red line (right)

As exemplary data for all the examined bobbins, the surface reliefs of the notched areas of the bobbin displayed in Figure 3-11 are illustrated in Figure 3-12. One can observe that the heights of the triangular tops between the notches both at the bottom and at the top of the bobbin vary along the circular cross sections. In case of the bottom of the bobbin (cf. Figure 3-12, left), the difference in height between the highest and lowest triangular top is about $\Delta h = 0.12\,mm$. Given the fact that the diameter of the central tube of the bobbin is about $d_{Tube} = 13\,mm$ and that the cross section was defined to keep a distance of $d = 10\,mm$ to the tube of the bobbin, the diameter of the cross section is about $d_{cross\,section} = 33\,mm$. This results in an approximate tilt angle α_{bottom} of the notched area with respect to the central axis of the bobbin of

$$\alpha_{bottom} = \tan^{-1}\left(\frac{\frac{\Delta h}{2}}{\frac{d_{cross\,section}}{2}}\right) \approx \tan^{-1}\left(\frac{0.06\,mm}{16.5\,mm}\right) \approx 0.21° \qquad (3\text{-}1).$$

In case of the top of the bobbin (cf. Figure 3-12, right), the tilt angle α_{top} of the notched area with respect to the longitudinal axis of the bobbin calculates to

$$\alpha_{top} \approx \tan^{-1}\left(\frac{0.03\,mm}{16.5\,mm}\right) \approx 0.10° \qquad (3\text{-}2).$$

The unwinding tests of the respective bobbin resulted in regularly fluctuating sensor signals as shown in the diagram in Figure 3-9, right. At first glance, these tilt angles and the thereby resulting variable gap between the foot of the bobbin carrier and the notched area of the bobbin (cf. Figure 3-10, right) explain the regular fluctuations of the sensor signals during the unwinding tests. However, it needs to be noted that the longitudinal axis of the bobbin itself cannot be seen as a well-defined reference. As stated above, one could also measure the surface relief of the notched areas of the bobbin with respect to the green plane over the ring-shaped area at the side of the bobbin (cf. Figure 3-11, right). In fact, such a referencing results in differently tilted notched areas of the bobbin because the plane over the ring-shaped area is itself tilted against the longitudinal axis of the bobbin. Hence, at this point of the analysis, it can only be stated with certainty that the different parts of the plastic bobbins are – on the level of hundredth millimeters – tilted against each other and distorted in themselves. This is even the case for the turned down tops of the bobbins and the initial assumption of the author that the durned down ends of the bobbins are of nearly perfect geometry is therefore incorrect. Regarding the regular fluctuations of the sensor signals during the unwinding tests that are in sync with the rotation of the bobbin (period duration of eleven lever upstrokes, also eleven notches in the bobbin) it can up to now only be said that it is likely that they originate from geometrically imperfect bobbins.

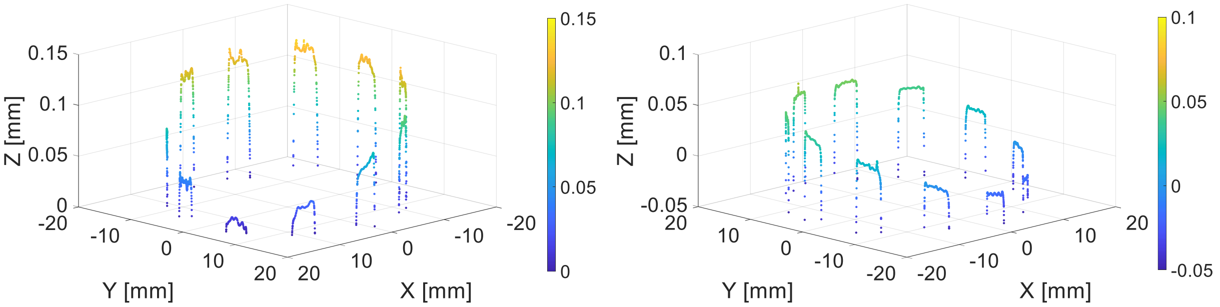

Figure 3-12: Circular cross sectional profile of the notched area at the bottom (left) and at the top (right) of the bobbin displayed in Figure 3-11

Among the closer investigated bobbins were however also bobbins with a different surface relief than shown above. Particularly the tops of some bobbins did not show a tilted but rather a saddle shape of the notched area. An exemplary dataset of the 3D cross section of such a saddle-like distorted notched area is illustrated in Figure 3-13, left. On the right of Figure 3-13, the response of the corresponding bobbin during the unwinding test is shown. Particularly from the envelope of the peaks of the signal from the Hall sensor between 0.6 m and 0.9 m of unwound yarn, it can be observed that this bobbin displays superimposed signal fluctuations with approximately half the period duration of a bobbin with a tilted notched area (period duration of five to six peaks in Figure 3-13, right compared to a period duration of eleven peaks in Figure 3-9, right). However, the signal fluctuations of the saddle-shaped notched area are not as pronounced as those from a tilted notched area. Still, the observation of half the period duration of signal fluctuations both in Hall voltage and yarn tension in combination with a saddle-like distorted notched area of the bobbin makes the explanation of the fluctuations by a varying gap that the locking pin has to bridge as the bobbin turns highly plausible. Note that the higher frequency of strokes of the tension lever in Figure 3-13, right compared to Figure 3-9, right is caused by different bobbin diameters due to different yarn lengths that were initially wound onto the respective bobbins. The different yarn lengths were chosen to keep the duration of the unwinding experiments at 20 min (time limit of the SRL camera for recordings). The reduced unwinding speed of 10 $\frac{mm}{s}$ in Figure 3-13, right was chosen to be able to exclude any secondary effects such as a jumping of the bobbin on the carrier that may disturb the measurement signals.

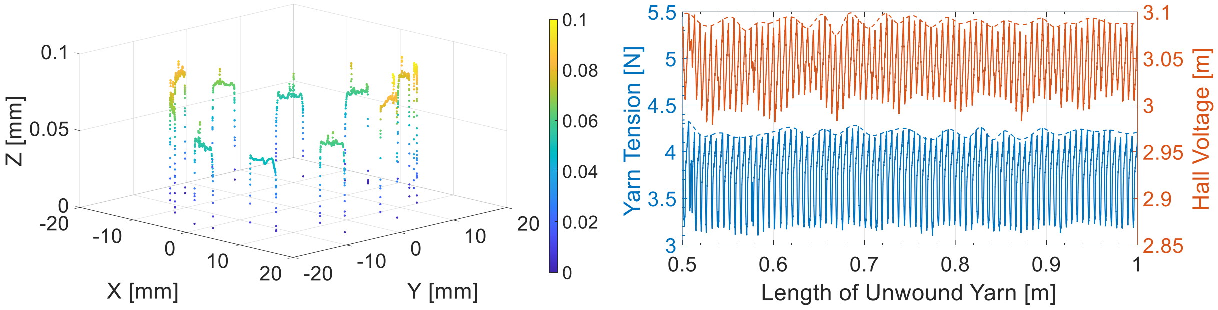

Figure 3-13: Circular cross section of a bobbin top with saddle shape (left); yarn tension and Hall voltage of an unwinding experiment with the corresponding bobbin at 10 $\frac{mm}{s}$ unwinding rate using the 12k carbon yarn (right); upper envelopes of both signals indicated with dashed lines

Although such fine variations in the movement of the tension lever as the superimposed fluctuation shown above can be detected by the proposed measurement approach, an accurate calculation of the acting yarn tension from the Hall voltage is not possible. When regarding the shapes of the fluctuations in yarn tension and Hall voltage in the diagram on the left of Figure 3-9, one may already assume that the relation between yarn tension and measured Hall voltage is not linear. For a detailed explanation on the relation between Hall voltage and yarn tension, the reader is referred to appendix A. For the reasons given there, the measured Hall voltage is not converted into a yarn tension in the following diagrams. The limitation of the proposed approach of not being able to precisely calculate the acting yarn tension is however not obstructive for its usability for the detection of braiding defects. As will be shown in this and also the following subsection, deviations in measurement signals that hint at the presence of unwinding-related braiding defects are much larger than the uncertainty in yarn tension calculation.

During the flawless reference measurements, a further effect manifested in the measurements, especially when unwinding with the stiffer spring in the bobbin carrier rated at 700 g release force mass equivalent. In Figure 3-14, an exemplary comparison between unwinding of the carbon yarn at 40 $\frac{mm}{s}$ with a spring rated at 350 g and a spring rated at 700 g is shown. In case of the 350 g-spring, the readings for yarn tension and Hall voltage remain in a nearly constant corridor. By contrast, the readings in case of the 700 g-spring show distinct fluctuations both in yarn tension as well as in Hall voltage. The cycle duration of these fluctuations is about 4 m in terms of unwound yarn length.

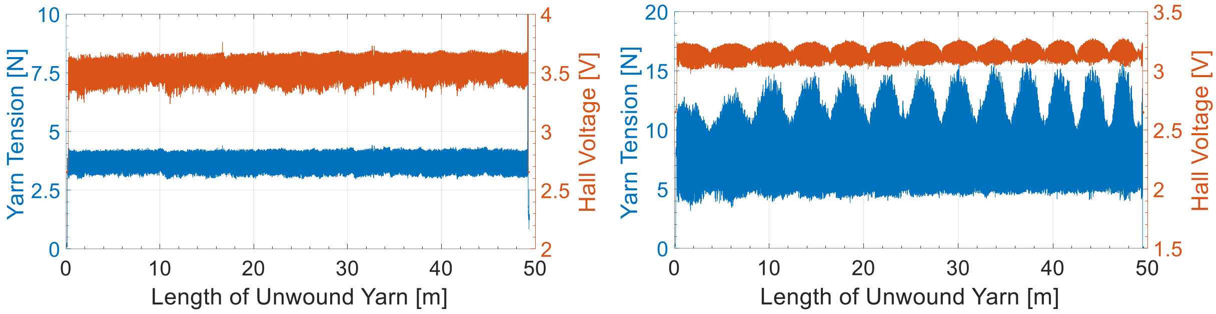

Figure 3-14: Yarn tension and Hall voltage from unwinding the carbon yarn at 40 $\frac{mm}{s}$ with a carrier spring rated at 350 g (left) and 700 g (right); diagrams taken from own publications [64,65]

When consulting the recordings from the SLR camera, it becomes apparent that these fluctuations correlate with the position at which the yarn is unwound from the bobbin. When the yarn is unwound from the top or middle area of the bobbin, both yarn tension and Hall voltage (which indicates the position of the tension lever) are elevated. When the yarn is unwound from the bottom area of the bobbin both yarn tension and Hall voltage drop significantly. This is due to the fact that the bobbin can exhibit a slight vertical play (~0.25 mm) when it is mounted onto the carrier (cf. Figure 3-15). The higher the general level of yarn tension set by the spring is, the easier and earlier (in terms of remaining yarn mass on the bobbin) the bobbin is lifted upwards by the acting yarn tension when the yarn is unwound from the bottom area of the bobbin. When the bobbin is lifted upwards, then the gap between bobbin and quick lock at the top of the carrier disappears. In turn, a gap of the same width between bobbin and foot of the carrier occurs. This new gap causes the locking pin of the yarn tensioning mechanism to engage and disengage with the lateral notches at lower positions of the tension lever compared to a bobbin that is not lifted upwards. Lower positions of the tension lever to evoke an engagement or disengagement of the locking pin correspond to lower levels of yarn tension. Due to the winding pattern of the yarn on the bobbin, the bobbin is periodically lifted upwards against its own weight by the acting yarn tension when yarn is unwound from the bottom area of the bobbin. The bobbin falls back down to its lower position when yarn is unwound from the top or middle area of the bobbin.

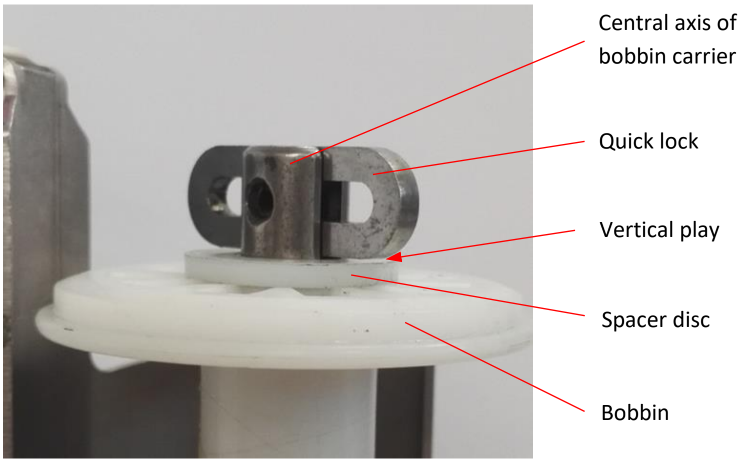

Figure 3-15: Vertical play of the bobbin on the carrier between spacer disc and quick lock; image taken from supervised student thesis [82], annotations adapted

The point at which the acting yarn tension is able to lift the bobbin depends on the remaining weight of the bobbin including the stored yarn material. This dependency can be observed in Figure 3-14 on the left. From the beginning of the experiment to about 25 m of unwound yarn, no fluctuations neither in Hall voltage nor in yarn tension can be observed. This is because the weight of the bobbin including the stored yarn is too high so that the bobbin could be lifted by the yarn tension. From about 25 m of unwound yarn to the end of the test, a slight fluctuation of an imaginary upper envelope of the signal from the Hall sensor is observable. This indicates that when the bobbin is half emptied, even the acting yarn tension of only 3-4 N is able to slightly lift the bobbin against its own weight, which itself decreases as more and more yarn is unwound. However, the effect remains too small that it could also be identified in the readings from the yarn tension sensor.

Further observations from the flawless reference experiments with different unwinding rates or with the PES yarn materials have not been made. This is why data from these other materials is not explicitly presented in this subsection. In summary, the following conclusions can be drawn from the results of the flawless reference measurements on the unwinding test stand:

- The measurement of the position of the tension lever of a bobbin carrier by means of a stationary Hall sensory can serve as an estimation of the acting yarn tension.
- An exact calculation of the acting yarn tension from the measured Hall voltage is not possible because of the nonlinear relation due to frictional forces in the yarn tensioning mechanism (cf. data presented in appendix A) and because of a scatter resulting from geometrical imperfections of the lateral notches in the bobbin. Moreover, the same level of Hall voltage corresponds to a different level of yarn tension when springs with different stiffnesses are used.
- However, fine anomalies during unwinding can still be detected by the proposed approach. These detectable anomalies include…
    - fluctuations in yarn tension and lever position that are in sync with the rotation of the bobbin on the carrier. They are due to geometrical imperfections of the bobbins as delivered the manufacturer.

- fluctuations in yarn tension and lever position that depend on the position from which the yarn is unwound from the bobbin. They are due to a vertical play of the bobbin on the carrier and the fact that the bobbin can be lifted upwards against its own weight by the acting yarn tension.

Since the proposed measuring approach can detect the described fine anomalies during unwinding, it may also be suitable to detect irregularities that hint at the presence of unwinding-related braiding defects. To underpin this presumption, the defect detection capabilities of the presented approach are investigated in the following subsection on results from measurements on the stationary test stand with provoked unwinding irregularities.

Results and Discussion of Measurements with Provoked Irregularities for Derivation of Required Number of Stationary Sensors

In Figure 3-16, an exemplary measurement curve from unwinding the carbon yarn at $40\ \frac{mm}{s}$ with the 350 g-spring is shown. During the first 50 cm of unwinding, the regular pattern from the ratcheting mechanism of the yarn tensioning unit of the bobbin carrier is observable in both the yarn tension and the Hall voltage. From the acquired video it is visible that a fibrous ring starts to form at about 50 cm due the purposefully introduced yarn damage. This is observable in the signal from the Hall sensor between 50 cm and 100 cm. Particularly the envelope of the lower reversal points of the oscillating signal is shifted to higher values due to the additional friction caused by the onset of the fibrous ring. However, this fine variation is not yet visible in the force signal. Only at approximately 1 m a first, clearly distinguishable spike in yarn tension occurs due to an entanglement of the unwinding yarn with the fibrous ring. This spike in yarn tension is accompanied by an equally pronounced spike in Hall voltage which indicates that the tension lever of the carrier is deflected beyond the usual trigger point where the locking pin disengages with the lateral notches in the bobbin. At about 1.5 m, this entanglement has resolved itself and the regular pattern of the ratcheting mechanism is observable again. Over the course of the whole measurement, many events of chaotic yarn entanglement with the fibrous ring and its subsequent resolve take place. Each time, an increase in yarn tension beyond approximately 5 N is mirrored by a saturation in Hall voltage. This saturation is due to the fact that the tension lever eventually touches the frame of the carrier and can geometrically not be pulled further upwards. At about 23 m of unwound yarn, an extreme entanglement between unwinding yarn and fibrous ring starts to form. It even leads to a saturation of the force sensor that measures the yarn tension. At about 24.25 m, the carbon yarn breaks under the excessive frictional yarn damage and high yarn tension. Consequently, the yarn tension drops to zero and the Hall voltage returns to its initial, neutral value as the tension lever falls down to its lowest possible position.

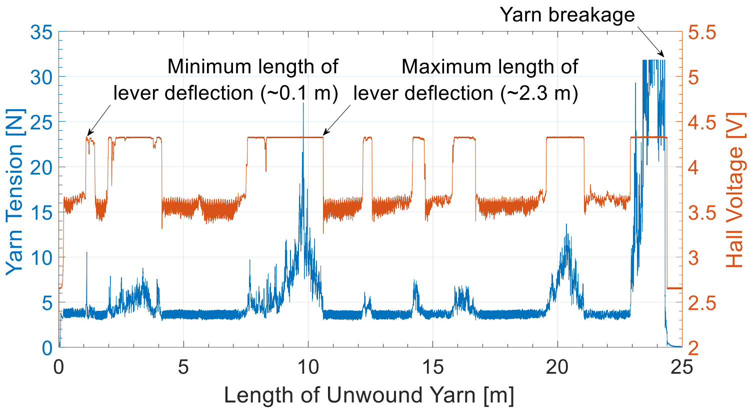

Figure 3-16: Yarn tension and Hall voltage from an unwinding test at 40 $\frac{mm}{s}$ unwinding rate and 350 g-spring with the predamaged carbon yarn leading to fibrous rings and consequently to yarn entanglements on the bobbin; diagram taken from own publications [64,65], annotations complemented

From this exemplary measurement plot, it is imaginable that the definition of a simple threshold in Hall voltage (e.g. 4 V in the case from above) enables the generation of a control signal to stop the braiding and thereby also the unwinding process. In the example from above, the process would have been stopped well before the yarn actually broke by the definition of such a threshold (approximately 23 m or 9.6 min before the actual breakage). Hence, the exemplary data suggests that there is ample lead time to stop the process and remove a fibrous ring by hand before it leads to a yarn breakage and requires a time-consuming replacement of the bobbin and a manual rethreading of the new yarn through the yarn guiding elements of the carrier. Moreover, one can conclude from the data presented that the proposed Hall sensor that detects the position of the tension lever of the carrier is able to indicate even finer increases of yarn tension that do not necessarily lead to a yarn breakage. Such an early indication of a process irregularity is beneficial because also extensive yarn gaps in a braid from reinforcement fibers can be avoided this way. Like a yarn breakage, yarn gaps also occur due to an anomalously increased tension of a braiding yarn. Of course, it requires less tension to induce a yarn gap than a yarn breakage. This is why the occurrence of a yarn gap usually precedes a yarn breakage. In the works by Wolf [85], Rauch [86] and Mierzwa [55], braids from various types of 24k carbon fiber yarns (braiding angle $\varphi = 45°$, effective mandrel circumference: ~200 mm, resulting yarn width: ~4.5 mm) were produced using springs rated at 350 g to tense the braiding yarns (3-4 N standard braiding yarn tension). In this case, relevant yarn gaps with a width of more than 2 mm were created at persistently elevated yarn tensions in the range of 10 N and above. At a tension of a single braiding yarn of about 18 N, their yarn gaps reached widths in the range of 4 mm (similar to yarn width). The exemplary diagram from above was also generated using a spring rated at 350 g. When comparing the data from the force and Hall sensor, it can be concluded that yarn tensions surpassing a value of only 5 N can reliably be detected by the Hall sensor when a 350 g-spring is used. Hence, a yarn tension irregularity that causes yarn gaps would in principle also be detectable by a magnet attached to the tension lever of the carrier and a stationary Hall sensor.

A limitation of the proposed approach of using a Hall sensor to monitor the position of the tension lever of the carrier is however the fact that in an implementation in a braiding machine, the bobbin carriers would be moving and the sensors would remain stationary. This way, only a discrete monitoring of the carriers is possible. The data from above however shows continuously acquired data since both the carrier and the sensor remain stationary on the test stand. Thus, the possibility of comparatively short deflections of the tension lever needs to be considered to assess the defect detection capabilities of the newly invented approach. This is of particular importance in conjunction with the investigated PES yarns. In Figure 3-17, exemplary measurement data from the double-folded PES multifilament yarn and the double-folded PES monofilament yarn at 40 $\frac{mm}{s}$ unwinding rate and the 350 g-spring are shown. Similar to the data from unwinding of the carbon yarn from the above Figure 3-14, superimposed fluctuations due to the lift of the bobbin against its own weight are observable. As a consequence of the different yarn thicknesses and thus different numbers of revolutions during rewinding along the length of the bobbin, the cycle duration of these fluctuations is about 7 m for the PES multifilament yarn and about 32 m for the PES monofilament yarn. A striking difference compared to the carbon yarn is however that the entanglements of the PES yarns cause discrete peaks both in yarn tension and Hall voltage. Pronounced, long-lasting increases in the measurement values as with the carbon yarn are not observable. When regarding the diagram in Figure 3-17, left on the PES multifilament yarn, it is imaginable that a stationary Hall sensor that makes discrete measurements may simply miss the event of an elevated lever position and thus yarn tension on a moving carrier before the yarn breaks. In the diagram in Figure 3-17, right on the PES monofilament yarn, the mode of entanglement is even more difficult to detect for the proposed measurement system. When yarn loops build up during the measurement, there is no sign of the imminent entanglement during the measurement. Only a single spike in yarn tension at the end of the measurement marks the entanglement and the breakage of the yarn. The position of the tension lever delivered a control signal approximately 20 cm before the yarn actually broke.

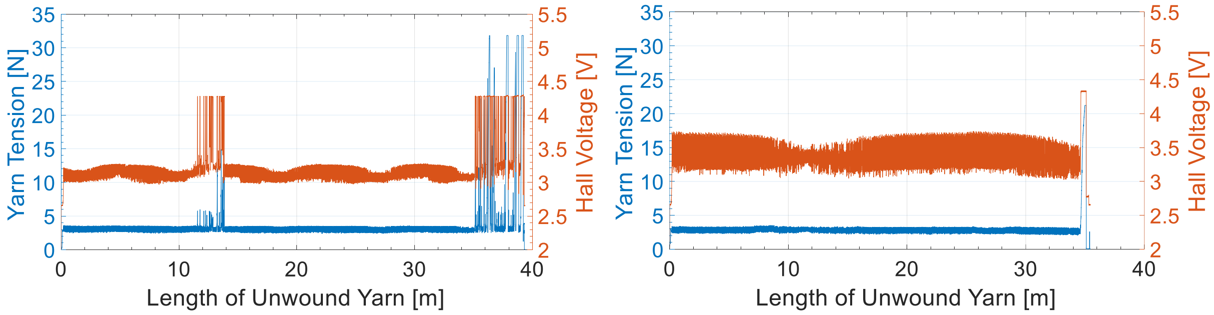

Figure 3-17: Exemplary measurement data from unwinding tests of the PES multifilament (left) and PES monofilament yarn (right) at 40 $\frac{mm}{s}$ unwinding rate and 350 g-spring; diagrams taken from own publications [64,65]

As can be seen from the exemplary measurement data above on the PES yarns, an early indication of a defect by an elevated tension lever of the bobbin carrier is not guaranteed for all types of yarn material. This is because the loops that eventually form around the bobbin do not hamper the unwinding process as it is the case with a fibrous ring. Only when the loops become knotted, they completely impede the unwinding process on the spot and the bobbin cannot turn any more. In many cases the knot unties itself as it is often the case in Figure 3-17, left. However, an application engineer who had to decide if the proposed monitoring approach was suitable for a given use case of braiding stretchable double-folded yarns must take the worst case of the first knot not untying itself and causing the yarn to break (cf. Figure 3-17, right) as the assessment basis. If the yarn fails in this knotting mode and the yarn material does not exhibit a significant amount of strain to failure, the described Hall sensor module is not the right approach for monitoring the braiding process of that kind of yarn. If the yarn shows significant strain to failure, then the following considerations can be made to assess if monitoring the braiding process by the proposed Hall sensors may still be suitable. The usable elongation Δl_{usable} of the yarn can be calculated by

$$\Delta l_{usable} = l \cdot \varepsilon_{failure} \cdot DF - \Delta l \tag{3-3}$$

whereby l is the length of the braiding yarn measured from the exit point from the bobbin carrier to the braiding point, $\varepsilon_{failure}$ is the strain to failure of the yarn material, DF is a deduction factor for reasons of material variability with $DF \in [0; 1]$ and Δl is the difference in yarn length due to the meandering course of the bobbin carriers (cf. Figure 3-1, left). Note that the length l must be measured at the shortest possible distance between carrier and braiding point (in axial braiding machines when the carrier is at its inner reversal point, in radial braiding machines when the carrier is at the transferal point from one horn gear to the next). This way, it is accounted for the case that the knot forms at the point of shortest distance between the carrier and the braiding point. The number of required sensors per track of carriers $n_{Sensors}$ can then be obtained by referring the length of a full 360°-helical winding of a braiding yarn in the braided strand to the usable yarn elongation

$$n_{Sensors} = \frac{\frac{\pi \cdot d}{\cos(90° - \varphi)} \cdot MF}{\Delta l_{usable}} = \frac{\frac{\pi \cdot d}{\sin \varphi} \cdot MF}{\Delta l_{usable}} \tag{3-4}$$

Note that $n_{Sensors}$ needs to be rounded up to the next bigger integer number. In the above equation (3-4), MF is a momentum factor which takes into account that a running braiding machine requires some time to come to a stop after it was powered down due to its moment of inertia. A possibility to define the factor $MF \in]1; \infty[$ can be to count the number of horn gears that a bobbin carrier travels after powering down the running braiding machine and referring this count to the total number of horn gears

$$MF = 1 + \frac{n_{horn\,gear,travel}}{n_{horn\,gear}} \tag{3-5}$$

In case the braided part or strand is not circular, $\pi \cdot d$ needs to be replaced by the true circumference of the braided shape in equation (3-4). If for instance the PES multifilament yarn from above, which features a strain to failure of $\varepsilon_{failure} \approx 0.1$, is used for braiding the standard scenario as described in section 1.2 and we assume a deduction factor of $DF = 0.8$, a small

$\Delta l = 0.005\ m$ because of the favorable geometry of the RF 1/128-100 radial braiding machine as well as a momentum factor of $MF = 1 + \frac{4}{32} = 1.125$, the required number of sensors calculates to

$$\Delta l_{usable} = 1.25\ m \cdot 0.1 \cdot 0.8\ -\ 0.005\ m = 0.095\ m$$

$$n_{Sensors} = \frac{\frac{\pi \cdot 65\ mm}{\sin(45°)} \cdot 1.125}{0.095\ m} \approx 3.4 \approx 4 \qquad (3\text{-}6).$$

Since there are two tracks of horn gears in the braiding machine, a total number of eight sensors would be required for the assumed production scenario.

For the investigated carbon yarn, the above consideration (3-3) is however not applicable. Firstly, dry carbon rovings do not exhibit a significant strain to failure that could compensate any Δl resulting from the movement of the carriers. Secondly, fibrous rings which occur during braiding of fibrous reinforcement material do not impede the unwinding process on the spot but build up over time, eventually hamper the unwinding process until the yarn finally breaks. Hence, a different approach is proposed in this dissertation to estimate the required number of sensors in order not to miss a defect event and to stop the braiding machine before a reinforcement yarn breaks.

To begin with, it needs to be noted that the duration of the individual lever deflections due to entanglement processes in terms of unwound yarn length scatters over several orders of magnitude for the carbon yarn (cf. boxplot in Figure 3-18, left). Furthermore, it can be observed that there is a reduced share of shorter lever deflections for the two test series with the 700 g-spring compared to the two test series with the 350 g-spring. An influence of the different unwinding rates on the lengths of lever deflections cannot be identified. In Figure 3-18 on the right, the number of lever deflections per test series is shown as a boxplot. It is striking that the 700 g-spring results in significantly less lever deflections than the 350 g-spring. Also in Figure 3-18 on the right, the longest lever deflection is drawn-in for each test with the carbon yarn. The reason for assessing this measurement value is that a stationary Hall sensor in a braiding machine may miss shorter lever deflections on a moving bobbin carrier. The highest detection probability of all the lever deflections that occur on a bobbin carrier comes with the longest lever deflection. The reader is referred to Figure 3-16 for an illustration of this issue. The data in this diagram was obtained from a stationary bobbin carrier on the unwinding test stand. Therefore the data is quasi-continuous. When the carrier is moving in the braiding machine but the Hall sensor remains stationary, the sensor can only measure the position of the tension lever on the carrier in a discrete manner. Thus, it is much more likely that the longest lever deflection of, in the example of Figure 3-16, 2.3 m is detected than the other lever deflections of shorter duration. In the diagram in Figure 3-18 on the right, it can be seen from the data points drawn-in as circles that the longest lever deflection per test shows greater values for the 350 g-spring than for the 700 g-spring. Again, a clear influence of the different unwinding rates cannot be identified.

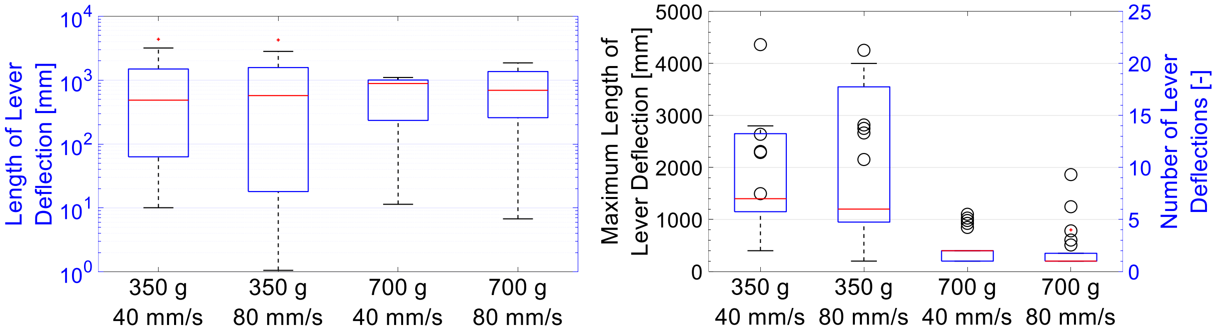

Figure 3-18: Boxplot of the lengths of all lever deflections for the different test variants (spring and unwinding rate) of the carbon yarn (left); maximum lengths of lever deflections of each test as well as boxplot of the number of lever deflections per test series with the carbon yarn (right)

All the three measurement criteria plotted in Figure 3-18 reveal a distinction between the two test series conducted with the different spring ratings. This can be explained by the different levels of yarn tension that the springs create. With a lower yarn tension (350 g-spring) already slight fibrous rings lead to a deflection of the tension lever, which is detected by the stationary Hall sensor. When the yarn tension is higher (700 g-spring), such slight entanglements are not detected because a significantly higher force is required to deflect the tension lever of the bobbin carrier. This explains the lower number of detected lever deflections in Figure 3-18, right in case of the 700 g-spring. Since slight fibrous rings that only cause a moderate increase in yarn tension are expected to resolve themselves quicker than strong fibrous rings, the share of comparatively short lever deflections is increased when a lower yarn tension is used (cf. 350 g-spring in Figure 3-18, left). When a fibrous ring builds up that does not resolve itself quickly, it is detected in early stages when it has only led to a moderate increase in yarn tension in case a lower yarn tension is present. When a higher yarn tension is present, the beginning of the formation even of a later strong fibrous ring is missed by the Hall sensor. This is why the longest lever deflections per test are shorter for the variants with the 700 g-spring than for the 350 g-spring in Figure 3-18, right.

Due to the distinct and well-explainable picture of the measurement data, the author decided to treat the data from the two different carrier springs as separate groups in the subsequent analysis on the statistic distribution of the lengths of lever deflections. This analysis step is intended to derive a statement on how many stationary Hall sensors are required to monitor the braiding process of reinforcement fibers that exhibit fibrous rings in seemingly chaotic entanglement processes. The following statistical models were calculated with the Distribution Fitter App in MATLAB R2021a. The statistical distribution models are necessary because it is not possible to conduct as many experiments as would be necessary to make a statement on how many stationary sensors per machine are needed on the basis of the aimed for false negative detection rates (cf. Table 3-2, e.g. one million experiments for approximately three false negative detections on a six sigma level). Instead, a suitable distribution model needs to be extrapolated from a limited amount of test data to capture such low probability values. In order to find a reasonable distribution model for the longest lever deflections in a test group, several distribution families were tested by means of the Anderson-Darling metric. For this statistic test, the null hypothesis is that a sample data set is part of a larger population with a given type of distribution. The parameters of the given type of distribution do not have to be specified since they are estimated by the test itself. The test rejects the null hypothesis when the calculated p-value is smaller than the specified significance level. A default significance level of 5 % is chosen for the tests herein. If a distribution model does not meet the 5 % significance level, then the data set is stated to not be part of a population that follows the given distribution model. If the significance level is met, this cannot be seen as a proof that the sample data is definitely part of a population that follows the given model. It only means that it cannot be excluded based on the data that was examined. Table 3-1 shows the results of the p-values from the Anderson-Darling test for five different distribution families.

Table 3-1: P-values for different assumed distributions of the longest lever deflections per experiment group according to the Anderson-Darling test

Experiment group	Carbon 350 g-spring	Carbon 700 g-spring
Normal Distribution	0.0532	0.3008
Exponential Distribution	0.0029	0.0060
Extreme Value Distribution	0.0091	0.0239
Lognormal Distribution	0.2289	0.8734
Weibull Distribution	0.0634	0.4198

Based on the 5% significance level, both an exponential as well as an extreme value distribution can be rejected. A normal, lognormal and Weibull distribution can up to this point not be rejected since they all meet the significance criterion of 5 %. However, further plausibility checks can be made. These checks are made by means of the probability plots shown in Figure 3-19. For each query point on the x-axis, the graph illustrates the cumulated probability up to the query point according to the assumed distribution model on the y-axis. Both diagrams in Figure 3-19 show the same data points for the longest lever deflections in the test groups. The groups are defined by the different spring ratings that were used. The diagram on the left contains two normal and two Weibull distributions that were fitted to the data points. The axes are scaled in a way that a Weibull distribution appears as a straight line in the diagram. The diagram on the right contains two lognormal distributions that were fitted to the two data sets. The axes are scaled in a way that a lognormal distribution appears as a straight line. In both diagrams, the y-axis ranges from a cumulative probability of $3.4 \cdot 10^{-6}$ to $1 - 3.4 \cdot 10^{-6} = 0.9999966$. The value $3.4 \cdot 10^{-6}$ was chosen because it corresponds to the six sigma level, a threshold for failure probability that is often striven for in normally distributed technical systems.

To begin with the plausibility checks, it needs to be noted that if the longest lever deflections are assumed to be normally distributed, then negative values would be permitted to occur. This contradicts the real nature of the data points, which are by definition of the experiment exclusively positive survival data. Furthermore, this leads to the problem that the model states that when the 350 g-spring is used, in 1 % of the cases of a yarn breakage the length of the longest lever deflection would be below 1 mm. When the 700 g-spring is used, the model would even state that in 5 % of the cases of a yarn breakage, the length of the longest lever deflection would be below 1 mm (cf. Figure 3-19, left). This is beyond any reality because a 12k carbon yarn can simply not break when it has led to a slight entanglement that has only just caused such an extremely short deflection of the tension lever of the bobbin carrier. For these practical reasons, the normal distribution is also rejected as a statistical model for the distribution of the longest lever deflections. The remaining lognormal and Weibull distribution are both limited to positive values, which reflects the real nature of the data. Also, these distributions are often used to describe times until failure of mechanical systems. However, when regarding the fitted Weibull distributions, especially the model for the 700 g-spring shows an implausibility at its upper end. The summed up probability of x-values from the interval $[2700\ mm; \infty[$ lies beyond the diagram area (> 0.9999966), which means they are, according to this Weibull model, highly unlikely to occur. In Figure 3-18 on the left, it can be seen that the medians of the lengths of lever deflections do not differ significantly for the two different springs. It was explained above, that the 700 g-spring causes an entanglement to be detected with a delay compared to the 350 g-spring (when the entanglement has aggravated). This is why the lever deflections are shorter for the 700 g-spring than for the 350 g-spring. From Figure 3-18 on the right, the minimum of the considered lever deflections for each spring can roughly be estimated for both types of springs. It is $1497\ mm$ for the 350 g-spring and $510\ mm$ for the 700 g-spring. This shows that a delay in detection of an entanglement can be as little as $1497\ mm - 510\ mm = 987\ mm$ between the two types of springs. The longest lever deflection during all the tests with the 350 g-spring was measured to be $4362\ mm$. If we discount a detection delay of $987\ mm$, this would lead to a hypothetical length of lever deflection of $4362\ mm - 987\ mm = 3375\ mm$ if the very same entanglement occurred with the 700 g-spring. As described above, such a value would be highly unlikely for the 700 g-spring if a Weibull distribution was assumed ($3375\ mm > 2700\ mm$). For this reason of too little overlap between actually measured values with the 350 g-spring and the extrapolation of the Weibull distribution for the 700 g-spring towards the upper end of the diagram, the author also deems this distribution not to be a plausible model for the distribution of the lever longest deflections in the experiment groups.

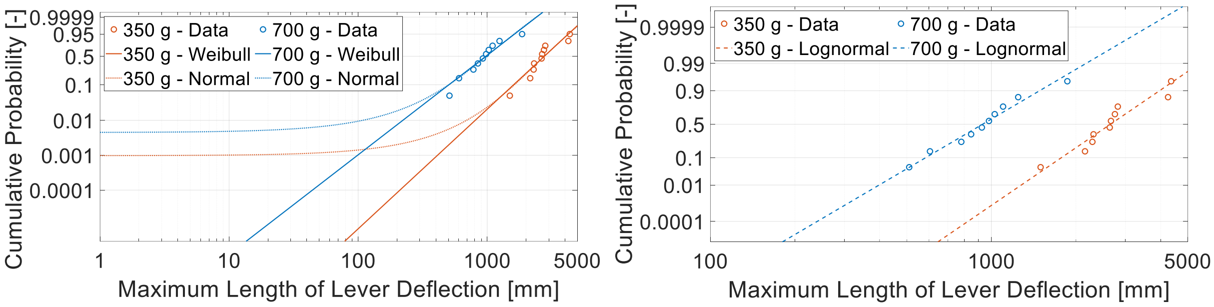

Figure 3-19: Cumulative probability of the longest lever deflections per test considering the different spring ratings of 350 g and 700 g as separating variation parameter; normal and Weibull distribution (left), lognormal distribution (right)

Thus, the lognormal distribution is used for the following calculations on how many stationary sensors are required to monitor the moving carriers of a braiding machine when fibrous reinforcement material is processed. This distribution already showed the highest p-values in Table 3-1. However, this finding alone does not mean that the data most likely follows a lognormal distribution. It means that the given distribution result is least extreme for the lognormal distribution compared to the other distribution models investigated. The fits of the lognormal distribution to the data for the two different springs is shown in Figure 3-19, right. As for the diagram on the left, the y-axis shows the probability interval $[3.4 \cdot 10^{-6}; 0.9999966]$. From this diagram, it can now be derived how much yarn a braiding machine may use before an entanglement needs to be detected by a stationary sensor based on an allowed probability of missing a lever deflection (false negative rate). In the upper half of Table 3-2, exemplary false negative rates based on multiples of the standard deviation of a normal distribution are listed. Although the lever deflections do not follow a normal distribution, these values were chosen as examples because they are often used in production engineering to characterize the stability of a process. The derivation of the values in Table 3-2 shall be explained at the example of the six sigma level. According to the fitted models shown in Figure 3-19, right, the probability of occurrence of a lever deflection with a length of 646 mm is $3.4 \cdot 10^{-6}$ for the 350 g-spring. For the 700 g-spring, the respective length is 181 mm. These values can roughly be estimated from the probability plot in Figure 3-19, right because the x-axis was set for the reader to intersect with the y-axis at exactly $3.4 \cdot 10^{-6}$. This lengths can now be used as minuend in formula (3-3) to derive a new Δl_{usable}. The calculations are shown at the example of the 700 g-spring. The same braiding scenario as discussed above with the PES yarns is assumed (cf. explanations introducing relation (3-6)).

$$\Delta l_{usable} = 0.181\,m - 0.005\,m = 0.176\,m \tag{3-7}$$

This is the length of yarn that the braiding machine may use as a bobbin carrier travels from one stationary sensor to the next assuming a probability of $3.4 \cdot 10^{-6}$ of the sensors missing a deflected lever. Based on the geometry of the braided component, the braiding angle φ and the moment of inertia of the machine MF, the necessary number of sensors per track of bobbin carriers can be calculated to

$$n_{Sensors} = \frac{\frac{\pi \cdot 65\,mm}{\sin(45°)} \cdot 1.125}{0.176\,m} \approx 1.8 \approx 2 \qquad (3\text{-}8).$$

This calculation result is then entered into the lower half of Table 3-2 in the line of 65 mm part diameter and the column of the 700 g-spring. It can be observed that for part diameters of up to 100 mm, one sensor per track of carriers (a total of two because there are two tracks for the carriers) is required to monitor the braiding process when the 350 g-spring and the 12k carbon fiber yarn is used. For the 700 g-spring, which creates the higher yarn tension, an increasing number of sensors is required as the part diameters increase and an acceptable false negative detection rate of $3.4 \cdot 10^{-6}$ shall be maintained. This variation in the calculation results shows that the table can only serve as an estimation for different production scenarios. For exact considerations, the distribution of the lever deflections needs to be determined for each specific type of yarn material and also for the desired braiding yarn tension. However, the low count of required sensors still reveals that limited installation effort and thus limited investment costs are incurred in order to detect a fibrous ring before a yarn breaks even at high degrees of certainty with the proposed sensor arrangement. Moreover, this calculation result can still be seen as a conservative assumption because shorter lever deflections are not taken into account in the considerations. The models are set up as if only the longest lever deflection per test had foreshadowed a yarn breakage and as if any shorter lever deflections did not exist. In reality, the numerous shorter lever deflections give the sensor module an even higher chance to detect an entanglement such as a fibrous ring before it has led to a yarn breakage. As a final remark on this statistical analysis, the author would like to note that a gamma distribution was not explicitly considered in the analysis within this written document. The reason for this is that the cumulative probability function of the gamma distribution is of close similarity to a lognormal distribution. The results in the lower half of Table 3-2 were also calculated for an assumed gamma distribution of the test data. This however did not result in significant changes to the calculation outcomes. Hence, a judgement on the practical usability of the stationary Hall sensors for defect detection during braiding of reinforcement fibers is not affected by assuming a gamma instead of a lognormal distribution of the longest lever deflections during the unwinding experiments.

Table 3-2: Required lengths of lever deflections per confidence level and recommended number of stationary Hall sensors per track of bobbin carriers depending on part size

Experiment variant	Carbon 350 g-spring	Carbon 700 g-spring
Necessary detectable length of lever deflection for different acceptable false negative rates [mm]		
6.7 % false negatives (3 sigma level)	1657	539
0.62 % false negatives (4 sigma level)	1210	374
0.023 % false negatives (5 sigma level)	883	260
0.00034 % false negatives (6 sigma level)	**646**	**181**
0.0000019 % false negatives (7 sigma level)	472	126
Recommended number of stationary Hall sensors per track for a cylindrical component with 45° braiding angle and different part diameters on ***6 sigma level*** *[-]*		
130 mm part diameter	2	4
100 mm part diameter	1	3
65 mm part diameter	1	2
10 mm part diameter	1	1

As a summary of the measurements with provoked irregularities on the unwinding test stand, the following statements can be made:

- As presumed from the detection of fine anomalies during the tests with regular unwinding, the proposed way of using a Hall sensor to monitor the position of the tension lever of a bobbin carrier can serve as a defect detection system on a stationary test stand.
- The carbon reinforcement yarn produced long-lasting elevations both in yarn tension and Hall voltage before the yarn broke.
- By contrast, the mode of entanglement the double-folded PES yarns differs in the way that these yarns become knotted suddenly. With yarns of this mode of entanglement,

only their elastic deformation can provide enough lead time for the stationary sensors to detect an entanglement before a yarn breaks.

- A statistical analysis of the measured lever deflections with the carbon yarn revealed that an early defect detection before a yarn breakage by stationary Hall sensors in an operating braiding machine…
  - depends on the braiding yarn tension because the deflection of the lever of the carrier is delayed at higher yarn tensions.
  - is in general possible because the number of required low-cost sensors is low even if high levels of certainty of defect detection are demanded.
- The behavior from the 12k carbon yarn is expected to be transferrable to other reinforcement yarns that form fibrous rings during braiding. However, the respective material properties (distribution of longest lever deflections) need to be determined for an exact and guaranteed compliance with allowed false negative detection rates.

Up to this point, it was only theoretically shown by statistical analysis from data on a stationary test stand that the proposed approach is suitable for detecting defects in a braiding machine. In order to demonstrate the industrial applicability of the approach, the system is implemented both in a radial as well as in an axial braiding machine in the following subsection.

3.1.2 Integration of the Sensor Module in Operating Braiding Machines

For a verification in a near-industrial use case, the sensor system was first installed in the RF 1/128-100 radial braiding machine at the Chair of Carbon Composites. Since this machine features rather large horn gears with eight grooves per horn gear, the system was also temporarily tested for scientific purposes on an axial braiding machine with smaller horn gears with only four grooves at the production site of Barthels-Feldhoff GmbH & Co. KG in Wuppertal. This way, possible problems regarding a lack of space to install magnets and sensors could be ruled out. Furthermore, in axial braiding machines, there is a larger difference in yarn length Δl that the yarn tensioning mechanism has to compensate when a carrier travels from its inner to its outer reversal point compared to radial braiding machines (cf. explanation in section 1.1 and Figure 3-1). Thus, any disturbances of the movement of the tension lever would have occurred with this different test setup.

Experimental Setup

Concerning the test on the RF 1/128-100 braiding machine at the Chair of Carbon Composites, a total of eight bobbin carriers (four going in clockwise and four going in counterclockwise direction) were equipped with magnets to their tension levers by means of clippable, 3D printed housings. Additionally, eight Hall sensors (four per track of carriers) were attached to 3D printed, height-adjustable fixtures and installed into the machine in a way that the sensors could measure the magnetic field of the magnets but did not collide with the moving bobbin carriers (cf. Figure 3-4). Furthermore, the heights of the sensor holders were adjusted so that all of the sensors delivered similar readings (± 1 ‰) close to but not beyond the saturation point of the sensor when the tension lever of a carrier equipped with a magnet was moved to its uppermost position. Note that this saturation is different from the saturation that is observable in Figure 3-16. The saturation in Figure 3-16 is due to the fact that the tension lever cannot be pulled further upwards by the acting yarn tension because it touches the frame of the carrier. The saturation discussed in this paragraph is however due to the sensor itself. By adjusting the height of the sensor holder in a way that the saturation point of the Hall sensor is almost reached when the tension lever is deflected to its maximum, it is made sure that the magnet attached to the tension lever is still within the measurement range of the sensor when the tension lever is in its lowest position (e.g. due to a yarn breakage). For the test of the system, a cylindrical mandrel with a length of $l = 1.5\,m$ and a diameter of $d = 65\,mm$ was overbraided with Tenax®-E HTS40 12k carbon yarns at a speed of horn gear rotation of $r = 60\,rpm$ and a haul-off speed of the mandrel of $v = 12\,\frac{mm}{s}$, thereby creating a braiding angle of approximately $\varphi = 47°$. 64 of the available 128 carriers were equipped with yarn material. For the first test on regular braiding, the yarn was unwound defect-free from all 64 bobbins. For the second test on defective braiding, one bobbin was replaced by a prepared bobbin that showed a fibrous ring that was at the onset of formation. Note that the comparatively low speed of horn gear rotation (maximum speed of the machine: 139 rpm) was only chosen out of precaution to avoid collisions between the sensors and the carriers. At the time of the experiment, it was not yet certain if the provisional fastening of the sensor holders to the machine bed by a magnet and hot glue could reliably withstand the vibrations from the machine. At the time of authoring the dissertation at hand, the fastening has since withstood years of operation also at full machine speed. The author chose to show the test run with the low speed of horn gear rotation because the stationary Hall sensor had coincidentally captured the moment when a braiding yarn was about to break (cf. signal peak at 65s in Figure 3-20, right). Moreover, the author would like to make clear that the operating speed of the machine has no negative effect on the detection capabilities of the sensors themselves. The rate of data acquisition was set to 1000 scans/s for the experiment and the resulting peaks in Hall voltage were clearly resolved (see following results section). Since Hall sensors react extremely fast, the rate of data acquisition can easily be set to 10000 scans/s or more if deemed necessary for a good resolution of the passing by of carriers also at higher machine speeds.

The test of the sensor module on an axial braiding machine was carried out as a final assessment within the research project “InSensoFlecht” at the production site of the project partner Barthels-Feldhoff GmbH & Co. KG. The task of the author of the dissertation at hand was to prepare one bobbin carrier of the axial machine so that it could be monitored by the Hall sensors that the author also had to install. The sensors were connected to a real-time data analysis unit that had been built by another project partner, namely Gemini Business Solutions GmbH. The test was carried out on this different machine because it featured horn gears that were approximately half the diameter of the horn gears on the RF 1/128-100 braiding machine at the Chair of Carbon Composites (four grooves vs. eight grooves per horn gear). This posed the additional difficulty of geometrical integration of the sensors without colliding with the carriers. This is significantly more challenging with smaller horn gears because the carriers do not only perform a translational but also a significant rotational movement (compared to larger horn gears) when they pass by the stationary Hall sensor. Due to components pointing away from the foot of the carrier (especially the tension lever), the possibility of collisions between the carrier and the stationary sensor is increased. Thus, the sensors had to be moved further away from the tracks of the horn gears which could have caused the magnets on the tension lever of the carriers to be outside the measurement range of the sensors.

Results and Discussion

At first, the results from the test of the stationary Hall sensors implemented into the RF 1/128-100 braiding machine at the Chair of Carbon Composites are discussed. The readings from a single Hall sensor obtained during regular braiding and braiding with a fibrous ring as an irregularity are illustrated in Figure 3-20. In both diagrams, peaks in the Hall voltage are observable when a carrier that was equipped with a magnet on its tension lever passes by the sensor. The peaks are 4 s apart. This corresponds to the speed of horn gear rotation of 60 rpm. Since there are 32 horn gears in the machine, it takes a bobbin carrier 16 s to complete a full 360°-revolution through the machine. Since four carriers per track were equipped with magnets, there is a peak every 4 s in the reading from the stationary Hall sensor. The first peak in both diagrams on the left and right of Figure 3-20 is considerably smaller in amplitude compared to the succeeding ones. The author attributes this to the fact that the braiding yarn of the respective carrier was not fully tensed and the ratcheting mechanism had not started operating when the respective carrier first passed by the Hall sensor. In case of regular braiding (cf. Figure 3-20, left), all the following peak values lie around 3 V, depending to which height the tension lever is deflected according to the acting yarn tension. By contrast, in case of braiding with a bobbin that showed a fibrous ring that created an unusually high yarn tension (cf. Figure 3-20, right), the reading from the Hall sensor shows dominant peaks with values of 4.15 V. These peaks reveal that the tension lever of the respective carrier is elevated to its uppermost position (until it touches the frame of the carrier) due to the high yarn tension created by the fibrous ring on the bobbin. The fact that these dominant peaks are four peaks apart is again explained by the fact that four carriers per track were equipped with magnets. The overshoot of the sensor signal below the neutral value of about 2.4 V can be explained by the reversal of the magnetic field that the sensor measures when it enters and leaves the field of the magnet. When following the succeeding peaks that originate from the same carrier, it is observable that their amplitudes decrease until they are only just distinguishable from the neutral reading of the sensor. This indicates that the carbon yarn is about to break at around 65 s experiment time and that it has broken and the lever has fallen to its lowest position at about 80 s experiment time. This experiment in a near-industrial use case thereby provides a confirmatory example of the statistical analysis of the lead time before a yarn breaks given in the previous subsection 3.1.1. In the experiment, the implementation of a simple threshold of 4 V would have led to a detection of the yarn tension anomaly caused by the fibrous ring approximately 30 s or 36 cm in terms of unwound yarn length before the yarn actually broke.

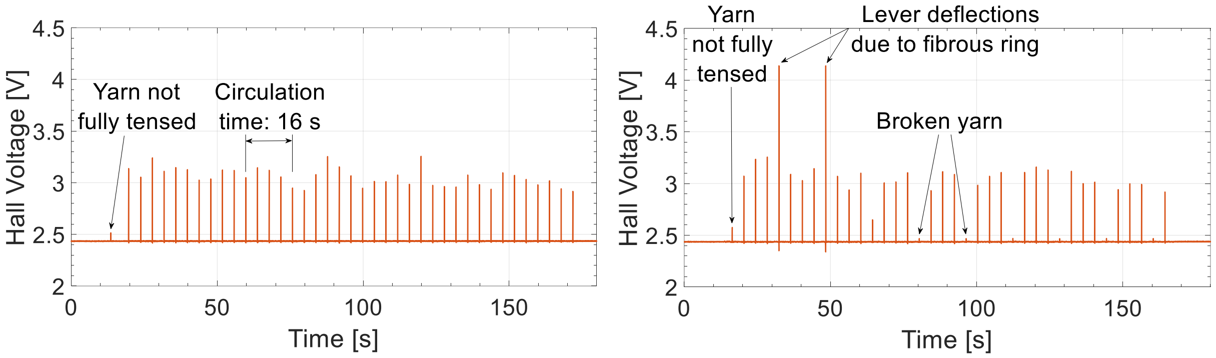

Figure 3-20: Measurement readings obtained from an individual Hall sensor installed into the RF 1/128-100 braiding machine at the Chair of Carbon Composites during regular (left) and defective braiding (right); diagrams taken from own publication [64], annotations complemented

The above described implementation of the Hall sensor module into the RF 1/128-100 braiding machine at the Chair of Carbon Composites was subsequently extended by an LED strip that displays the position of the defective carrier and on which track the defect is located (yellow or red light signal corresponding to color of tension levers) to the operating personnel (cf. Figure 3-21, left). Since this particular braiding machine is for reasons of safety only allowed to be operated as long as a dead man's switch is pressed (no automatic mode), the machine is stopped by the operating personnel as soon as it notices the light signal. When the braiding machine is stopped, the power supply to the driving motors is simply interrupted by the machine control unit. The machine is not actively braked. This means that the machine runs a bit further after the power supply is interrupted due to the moment of inertia of the machine itself (cf. momentum factor MF in relations (3-4) and (3-5). A correction of the display of the error position by this effect was not implemented. However, such a feature can easily be amended in case of an industrial application – either by adding a fixed distance that the defective carrier must have travelled after interruption of the power supply or by sensing the actual machine motion, e.g. by means of the stationary Hall sensors themselves or by a rotary position transducer to a horn gear. In the vast majority of braiding machines in industrial production, there already exists an electric circuit from the switches that jut into the tracks of the bobbin carriers (cf. Figure 2-8) to stop a braiding machine in case a yarn has broken. It is imaginable that a relay could be integrated into that circuit. The relay could be opened as soon as a microcontroller detects a defect in the signals from the Hall sensors. Regarding the data in Figure 3-20, such a defect event could be defined as the exceedance of a threshold of 4 V in Hall voltage, for instance.

During the test of the sensor module on an axial braiding machine, the stationary Hall sensors were connected to an analysis unit that had been built by the project partner Gemini Business Solutions GmbH. This analysis unit was not able to store the acquired process data. Only a light signal was displayed and the braiding machine was stopped upon occurrence of an irregularity during braiding. As with the radial braiding machine from above, an irregularity was defined as exceedance of a predefined threshold in Hall voltage. This is why no concrete data can be shown at this point. The image in Figure 3-21, right can however serve as an affirmation that the system was also practically proven to work in conjunction with an axial braiding machine at full machine speed. The sensors in deed did have to be placed farther away from the moving carriers to avoid collisions due to the smaller horn gears. The cylindrical neodymium magnets with a diameter of 8 mm and a thickness of 3 mm were however not out of reach of the chosen Iduino SE022 analog Hall sensors. Moreover, problems related to sudden tension increases at the outer reversal points of the bobbins due to inertia effects of the bobbins could not be observed.

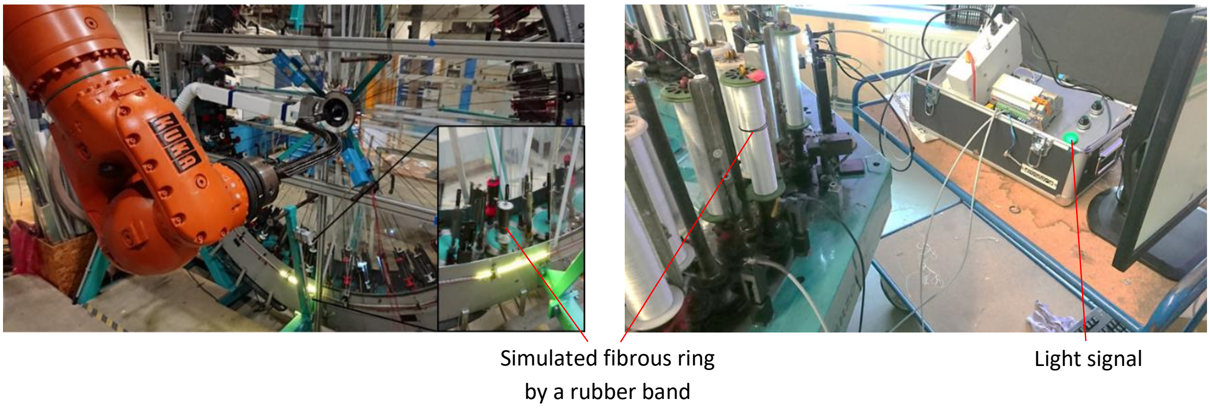

Figure 3-21: Stationary Hall sensors implemented into the RF 1/128-100 braiding machine at the Chair of Carbon Composites giving a light signal via an LED strip to the operator upon occurrence of a fibrous ring (left); test of the stationary Hall sensors on an axial braiding machine at the production site of Barthels-Feldhoff GmbH & Co. KG together with a data analysis unit from Gemini Business Solutions GmbH giving a light signal (right)

In conclusion of the test of the stationary Hall sensors implemented into two different types of braiding machines, the following statements can be made:

- During regular braiding, the peaks in Hall voltage created by the carriers that pass by the stationary sensors and which have been equipped with magnets lie in a similar range. This indicates that the positions of the tension levers and thus the tensions of the braiding yarns are of similar values.
- When the tension of a single braiding yarn is elevated (e.g. by a simulated entanglement by means of a rubber band or by a real fibrous ring), distinct peaks in Hall voltage are observable. The definition of a threshold in Hall voltage can serve as a criterion for defect detection.
- The approach of detecting yarn entanglements as the root cause of braiding defects such as yarn gaps or yarn breakages by means of stationary Hall sensors was proven to work in near-industrial use cases both on a radial as well as on an axial braiding machine.

3.2 Sensor Integrated Braiding Rings

The sensor system from above uses stationary sensors to detect the position of levers or slivers of bobbin carriers that pass by the sensors. This approach is advantageous because it is cost-efficient, simple to implement and it precisely identifies the defective bobbin carrier. As discussed in detail in subsection 3.1.1, the concept however only allows a discrete monitoring of the bobbin carriers with a dead time when a carrier travels from one sensor to the next. Depending on the material to be braided and on the requirements regarding confidence of defect detection, the approach from above may not always be suitable for a given use case. Moreover, other constraints stemming from the machine setup (e.g. carriers without lever or slider, cf. Figure 3-2) may limit the applicability of stationary Hall sensors as defect detection devices. Therefore, another concept, namely sensor integrated braiding rings, was developed. The sensor concept including algorithmic defect detection was initially conceived by the author of the dissertation at hand. First experiments were carried out within the framework of a master's thesis by the student Álvaro Fernández Villalba [87], which was conducted under the guidance and supervision of the author along with Prof. Dr.-Ing. Klaus Drechsler. The setup was then further refined, tested and a working defect detection by neural networks was developed by the author of this dissertation. The data presented herein solely originates from experiments that were conducted by the author in the said refinement stage. The concept was first presented to the scientific community at the 12th International Conference on Composite Science and Technology (ICCST12) in Milan, Italy and published together with data on a use case of overbraiding a cylindrical mandrel in the reviewed proceedings book [88]. As with the stationary Hall sensors in the section above, the author here gives an independent reproduction of the concept and the findings. Similar passages particularly to the publication [88] may occur because of identical authorship.

The braiding ring is that part of the machine which is used to deflect the yarns before they are deposited onto the mandrel under the braiding angle φ (cf. Figure 3-22). A braiding ring is always present in radial braiding machines but does not necessarily have to be used in axial machines because the braid is in many applications properly deposited by its closing motion. This is why the concept of sensor integrated braiding rings is again investigated on the radial braiding machine RF 1/128-100 of the Chair of Carbon Composites at Technical University of Munich. The idea behind the concept is that the braiding ring is the only part of the machine that is stationary but at the same time in contact with all of the braiding yarns at any time during the process. This enables the use of a limited number of force sensors (thereby being cost-efficient) to be incorporated into the braiding ring for a comprehensive tension monitoring of all braiding yarns. Moreover, all yarns can not only discretely (as with the stationary Hall sensors) but also continuously be monitored, thereby eliminating any uncertainty in defect detection due to dead times of the sensor setup. Furthermore, additional components that touch the yarns (e.g. tactile force sensors such as in the approach by Lenkeit [66]), which may cause additional yarn damage in case of brittle reinforcement fibers, are not required with this approach. However, as will be shown in this chapter and as a trade-off, the sensor integrated braiding rings only allow the identification of a certain group of carriers of which the defective carrier is part of. Thus, the concept presented in this chapter can be seen as complementary to the above-discussed stationary Hall sensors, which allowed a precise identification of a defective carrier but worked on a discrete monitoring basis.

During braiding, each yarn exercises a certain force onto the braiding ring. Figure 3-22 depicts the relevant parameters for a theoretical derivation of these reaction forces in case of a radial braiding machine. After the braiding yarns have exited the bobbin carriers, they are deflected at the braiding ring by the angle α and are deposited onto the mandrel under the angle β. The deflection angle α can approximately be calculated by a trigonometric relation using the, in

Figure 3-22, vertical distance a between braiding ring and mandrel and the, in Figure 3-22, horizontal distance b between front of the braiding ring and point of yarn deposition on the mandrel.

$$\alpha = \frac{\pi}{2} + \beta \approx \frac{\pi}{2} + tan^{-1}\left(\frac{a}{b}\right) \tag{3-9}$$

Note that it is considered that, when viewing from the side of the braiding machine, the middle between bobbin carrier reversal point 1 and reversal point 2 lies in the plane of the front edge of the braiding ring. The slight deviations in deflection angle α originating from the meandering course of the carriers around the horn gears (cf. reversal points 1 and 2 in Figure 3-22) are not further accounted for. The reason for this is that the detection concept relies on forces cancelling out or being evenly distributed around the circumference of the braiding ring. The consideration of time-dependent deflection angles α would therefore add unnecessary complexity only for them to be canceled out in the calculation of the overall reaction forces.

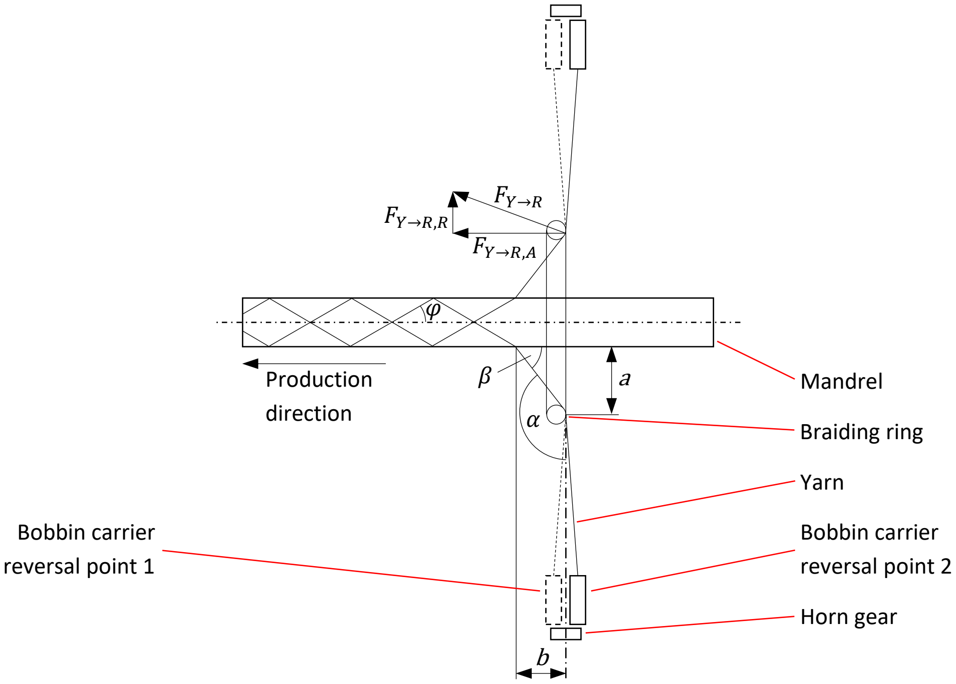

Figure 3-22: Illustration of the deflection of the braiding yarns at the braiding ring including relevant deflection angles and occurring interaction forces in a radial braiding machine; drawing taken from own publication [88]

Each yarn exits the bobbin carrier with a yarn tension F_Y. Due to frictional interaction at the braiding ring, the yarn tension is considered to increase to $F_{Y,Fr}$ after having been deflected at the braiding ring. Thereby, the yarn exercises a force $F_{Y\to R}$ onto the braiding ring. This force can be decomposed into a component pointing in radial $F_{Y\to R,R}$ and into another component pointing in axial (production) direction $F_{Y\to R,A}$. The equilibrium of forces in axial direction of a single yarn that is deflected at the braiding ring then writes as:

$$\sum F_A = 0 = F_{Y,Fr} \cdot \cos\beta - F_{Y\rightarrow R,A} \tag{3-10}$$

Accounting for frictional interaction with a coefficient of friction μ according to the Euler-Eytelwein relation at the braiding ring gives the term for the axial reaction force $F_{Y\rightarrow R,A}$ that a single yarn induces:

$$F_{Y\rightarrow R,A} = F_{Y,Fr} \cdot \cos\beta = F_Y \cdot e^{\mu\left(\frac{\pi}{2}-\beta\right)} \cdot cos\beta \tag{3-11}$$

Likewise, the equilibrium of forces of a single yarn in radial direction can be expressed as:

$$\sum F_R = 0 = F_Y - F_{Y\rightarrow R,R} - F_{Y,Fr} \cdot \sin\beta \tag{3-12}$$

Note that in the above Figure 3-22, $F_{Y\rightarrow R}$, $F_{Y\rightarrow R,A}$ and $F_{Y\rightarrow R,R}$ are drawn-in as forces acting onto the braiding ring because this is the more intuitive illustration when interpreting the diagrams in the following subsections 3.2.1 and 3.2.2. For the equilibrium of forces at the yarn however, the respective reaction forces that act onto the yarn need to be considered. With the imaginary A-axis being directed to the left (production direction) and the imaginary R-axis being directed upwards in Figure 3-22, this is why both $F_{Y\rightarrow R,A}$ and $F_{Y\rightarrow R,R}$ have a negative algebraic sign in (3-10) and (3-12), respectively. Resolving (3-12) for the radial force component that a single yarn induces at the braiding ring yields

$$\begin{aligned} F_{Y\rightarrow R,R} &= F_Y - F_{Y,FR} \cdot \sin\beta = F_Y - F_Y \cdot e^{\mu\left(\frac{\pi}{2}-\beta\right)} \cdot \sin\beta = \\ &= F_Y \cdot \left(1 - e^{\mu\left(\frac{\pi}{2}-\beta\right)} \cdot sin\beta\right) \end{aligned} \tag{3-13}.$$

Note that the relations (3-10) to (3-13) represent a simplification in the sense that the yarns are considered to run perfectly radially aligned towards the center of the braiding machine. When viewing from the front (cf. Figure 3-42), the yarns actually touch the braiding ring under an angle different from a right angle due to the geometric dimensions of the overbraided mandrel and the evolvent course of the yarns, which is caused by frictional yarn-yarn interaction (cf. section 3.3). However, a further consideration of this condition would not add explanatory value to the relations from above but further complexity. As will be shown in the following subsection on the conducted experiments, the stated degree of abstraction of the analytical considerations is well-suited to explain the observed dependencies between reaction forces and process parameters.

The hypothesis for a defect detection by reaction forces at the braiding ring is as follows. During regular braiding without any defect, the radial forces of all yarns that act onto the braiding ring $F_{Y\rightarrow R,R}$ are expected to cancel out. When an irregularity that creates a yarn tension increase is present (e.g. a fibrous ring), there should be a resulting radial force pointing into the direction of the defect. Likewise, the axial forces $F_{Y\rightarrow R,A}$ are anticipated to be evenly distributed around the circumference of the braiding ring. Upon occurrence of a defect, a deviation in the force distribution along the circumference of the braiding ring should be measurable.

In order to verify the hypotheses from the above paragraph and to investigate the suitability of this approach for braiding process monitoring, two different designs of sensor integrated braiding rings were developed and manufactured. The first type of braiding ring was intended to provide an estimation of the distribution of axial forces onto the braiding ring (cf. Figure 3-23). For reasons of simplicity in expression, this ring is referred to as *axial ring* in the following sections. The ring consists of an outer part, a middle part (both 3D printed from polylactic acid (PLA) by Fused Deposition Modeling), an inner deflecting ring from stainless steel and four compression sensors. As standard equipment, the RF 1/128-100 braiding machine at the Chair of Carbon Composites comes with several plastic inserts of varying inner diameter for the braiding ring. These inserts are meant to adjust the diameter of the braiding ring to the component that needs to be overbraided. The 3D printed outer part of the sensor integrated ring was designed to fit tightly into the plastic insert with a diameter of $d = 190\ mm$. The 3D printed middle part was radially constrained by means of a cylindrical fit to the outer part. The rotational degree of freedom of the middle part was constrained by an alignment pin that fitted into a recess in the outer part. Between the outer and middle part, four compression sensors were evenly distributed and oriented so that they can measure axial compression forces. The reader may wonder why four and not three sensing elements, which would have been sufficient for the middle part to be statically determinante under axial compression loading, were used in this setup. The reason for this is that the author wanted to keep the number of sensors consistent to the ring measuring the radial reaction forces. The considerations for using four sensors in the ring measuring the radial reaction forces are described in the next paragraph. The inner deflecting ring with an inner diameter of $d = 100\ mm$ was successively treated with sand paper of grit sizes of 80, 120 and 240. It was then attached to the middle part of the assembly. The inner ring was introduced because stainless steel that is sanded down results in less yarn damage when the braiding threads are deflected than the rough, layered surface from the 3D printed middle part.

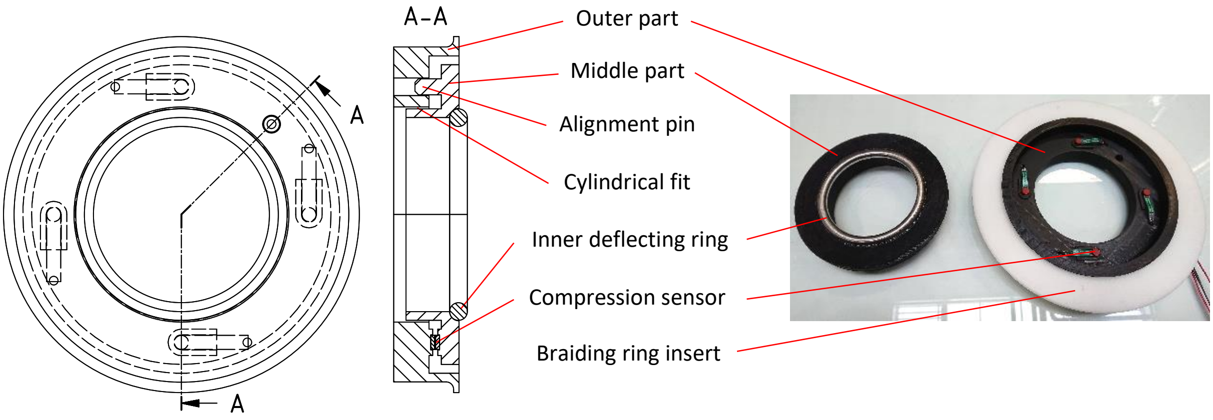

Figure 3-23: Drawings of the sensor integrated braiding ring for the estimation of axial forces (left) and photography in partly assembled state (right); illustration taken from own publication [88], annotations adapted

The ring for estimating the radial reaction forces comprises a one piece outer part, which was 3D printed from PLA, and an inner deflecting ring from stainless steel. For reasons of simplicity in expression, this ring is referred to as *radial ring* in the following sections. As with the axial ring, the outer part fitted tightly into the standard plastic braiding ring insert with a diameter of $d = 190\ mm$. The outer part featured four spring elements. In the center of each spring element, a bolt with a self-securing nut was located. The bolts directly pressed on the compression sensors. The self-securing nuts were used to avoid a loosening of the nuts when the setup was tested under the application of shaker motors that actuate the braiding ring for an enhanced yarn spreading (cf. subsection 3.2.2). The use of shaker motors was also one of the reasons for arranging four and not three spring elements (and consequently also four compression sensors) along the circumference of this type of braiding ring. In the design phase of the ring, an initial assessment of the required material thicknesses and dimensions of the spring elements was conducted by means of a finite element analysis in Autodesk Inventor Professional 2017. As forces acting onto the braiding ring, results from previously conducted student thesis by Rauch [86] and Wolf [85] were used as estimates. These works both investigated the interdependency between yarn tension increase as consequence of a fibrous ring and resulting widths of yarn gaps in a braided preform. For their measurements of reaction forces, they used a six axis force-torque sensor of the type 160M50A3 from JR3, Inc. The sensor was mounted between the flange of the braiding robot and the three-jaw chuck, which held their overbraidable mandrel. From their measurements with $n_{yarn} = 64$ braiding yarns and 350 g-springs in the carriers, it became clear that the spring elements of the radial ring needed to withstand force levels of up to 200 N in axial force without significant deformation but allow a deformation in radial direction to measure radial forces in the single digit order. The initial assessment showed that the load could be carried by three spring elements. However, the force measurements in the works [85,86] are smoothed, therefore not showing the force peaks that the shaker motors create. Furthermore, only properties of bulk PLA were available for the finite element analysis. Considering the facts that the properties of printed PLA by Fused Deposition Modeling are worse than the properties of the bulk material plus the unknown force peaks of the shaker motors, a fourth spring element was added in the design phase of the radial ring as a matter of precaution to bear the occurring loads. To allow sufficient bending of the spring elements in radial direction but secure enough stiffness in axial direction so that the bolts do not slip off the sensors, the spring elements were designed to be only 2 mm thick but 50 mm high. The large height only goes in to the power of one into the calculation of the bending stiffness in radial direction but to the power of three into the bending stiffness in axial direction.

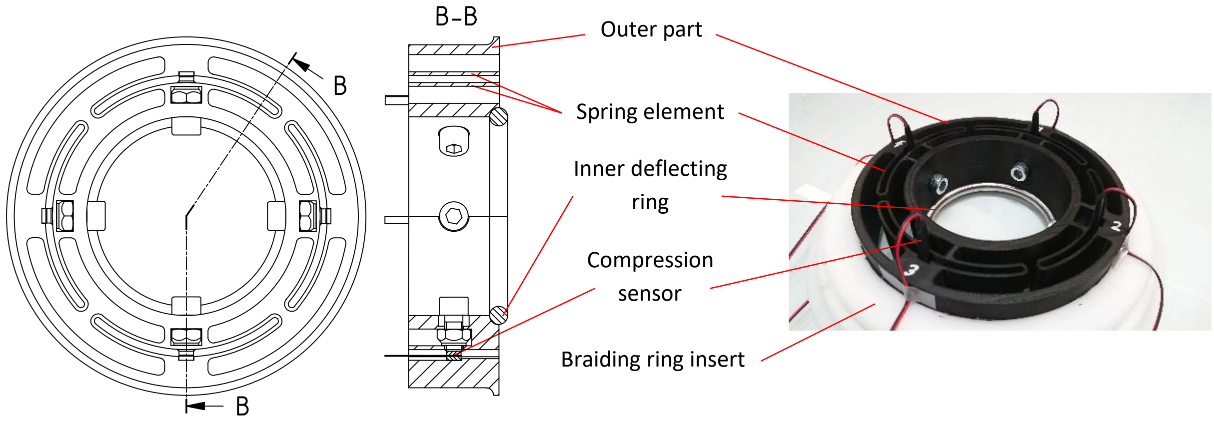

Figure 3-24: Drawings of the sensor integrated braiding ring for the estimation of resulting radial forces (left) and photography in assembled state (right); illustration taken from own publication [88], annotations adapted

As sensing elements, force sensing resistors (FSR) of the type CP 149 from International Electronics & Engineering S.A. were used. These are film resistors whose resistance is inversely proportional to the applied force. Due to the fact that the resistance of the sensors decreases so quickly that a maximum signal is obtained when they are only lightly touched (quasi-digital behavior), the sensors were integrated into a voltage divider circuit. This way, more gradually increasing characteristic curves were obtained (cf. Figure 3-25). The voltage divider circuit was not only used in the sensor integrated braiding rings but also in prior compression tests for determining the characteristic curves for each individual sensor. The compression tests were carried out at a rate of $1\ \frac{mm}{s}$. In order to achieve a uniform stress distribution over the sensor area, rubber pads with a thickness of 2 mm were attached to both sides of the flat sensors. The supply voltage of $U = 5\ V$ for the circuit was supplied by a USB-6210 data acquisition device from National Instruments Corp., which was at the same time used for reading the voltage U_R. Three different resistors of values $R = \{200\ \Omega;\ 2000\ \Omega;\ 20000\ \Omega\}$ and a deviation of ±1 % were tested to determine which resistor suits the FSRs best in the voltage divider circuit. The raw test data was used to derive smoothing splines as mapping functions between measured voltage and applied force. The smoothing splines were calculated in MATLAB R2017b and reached coefficients of determination >0.99. The splines for the three different resistors of values R and an individual FSR are shown in Figure 3-25, right. It can be observed that the resistor with $R = 200\ \Omega$ results in an extremely flat force-voltage relation, which is likely to cause large deviations in converted force upon noise in the voltage signal during braiding. The resistor with $R = 20000\ \Omega$ creates a response that is close to the quasi-digital behavior of the sensor without voltage divider circuit. Hence, resistors with $R = 2000\ \Omega$ were chosen for the voltage divider circuits in the sensor integrated braiding rings.

As a general remark, the author would like to point out that the chosen FSR are not as accurate as laboratory equipment like strain gauges and measurement amplifiers, for instance. The approach presented herein was developed within a research project on general textile braiding, which also includes braiding of mass goods such as shoelaces or ropes. Against this economic background, the use of expensive laboratory equipment could not be justified. Furthermore, laboratory equipment like amplifiers is prone to failure in a rough production environment, particularly when it is contaminated with electrically conductive fiber dust, which it is created when dry carbon fiber is braided. By contrast, the simple voltage divider as a replacement for measurement amplifiers is insensitive to such environmental influences. Due to the reduced accuracy of the FSR compared to dedicated laboratory equipment, the author purposefully speaks of “estimating” instead of “measuring” the relevant reaction forces at the braiding ring. Particularly in subsection 3.2.2 in algorithmic defect detection, the author shows that low-cost sensors with reduced accuracy can still be used for defect detection provided that the measurement results are repeatable. This condition is met by the chosen FSR.

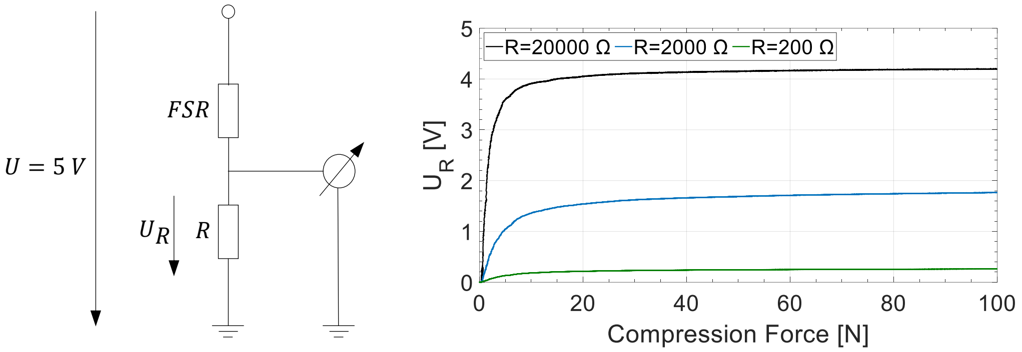

Figure 3-25: Voltage divider circuit for calibration and use of the FSR in the sensor integrated braiding rings (left); calibration curves for different values of the resistor R (right); illustrations taken from own publication [88]

3.2.1 Overbraiding of a Cylindrical Mandrel as Initial Sensitivity Analysis of the Sensor Module

In the following subsection, the two types of sensor integrated braiding rings are compared in terms of defect detection capabilities during braiding with a simulated defect. For this initial assessment, a cylindrical mandrel is overbraided. Shaker motors to actuate the braiding ring for a better yarn spreading are not yet used. This is an important difference to subsection 3.2.2. In this advanced assessment, braiding of an S-shaped mandrel with trapezoidal cross section including the use of shaker motors that actuate the sensor integrated braiding rings is investigated.

Experimental Setup

For this initial assessment of the detection concept, a cylindrical mandrel with a diameter of $d = 65\ mm$ was overbraided with carbon fiber yarns of the type Tenax®-E HTS40 F13 12k on the RF 1/128-100 braiding machine at the Chair of Carbon Composites. 64 of the available 128 bobbin carriers were equipped with yarn material. Springs with a rating of 350 g were used in the central tubes of the bobbin carriers to create a tension of the braiding yarns in a range of 3-4.5 N (cf. Figure 3-9). Both the axial as well as the radial sensor integrated ring were successively fitted into the machine (cf. Figure 3-26, left). The same four force sensing resistors were used in the two different types of braiding rings. Corresponding to the enumeration in the diagrams below, FSR 1 was always located at the top position, FSR 2 on the left, FSR 3 at the bottom and FSR 4 on the right of the modified braiding rings when looking in production direction. The data from the voltage divider circuits of the FSR was gathered at a rate of 100 scans/s by a USB-6210 data acquisition device from National Instruments Corp. Due to the fact that the sensors can only measure compression but no tension forces, the bolts in the radial ring were slightly tightened before the braiding tests so that the sensors still produced a proper reading even if there was a defect present that caused a resulting force pointing away from a specific sensor. At first, flawless reference measurements were conducted during regular operation of the braiding machine. After that, measurements with a controlled simulation of a defect were carried out. For these experiments, a screw-on barrel tensioner, which was previously developed at the institute [86], was added to one of the 64 bobbin carriers that were equipped with yarn material (cf. Figure 3-26, right).

Figure 3-26: Sensor integrated braiding ring for measuring resulting radial forces fitted into the RF 1/128-100 braiding machine at the Chair of Carbon Composites (left, image taken from own publication [88]); screw-on barrel tensioner added to a bobbin carrier for replication of a yarn tension anomaly (right, image from own publication [89])

Winding the yarn 1.5 times around the barrel increased the yarn tension of this individual yarn by approximately 25 N [59]. Thereby, the occurrence of a fibrous ring was simulated but with the advantage that the elevated yarn tension created by the brake was rather constant compared to the chaotic entanglement processes during formation of a fibrous ring. The speed of horn gear rotation of the machine was changed between $r = \{65\ rpm; 130\ rpm\}$. The braiding angle was varied between $\varphi = \{30°;\ 45°;\ 60°\}$. As already indicated above, a shaker motor to actuate the braiding ring was not used. For the sake of a better overview, the full factorial test plan is graphically reproduced in Figure 3-27.

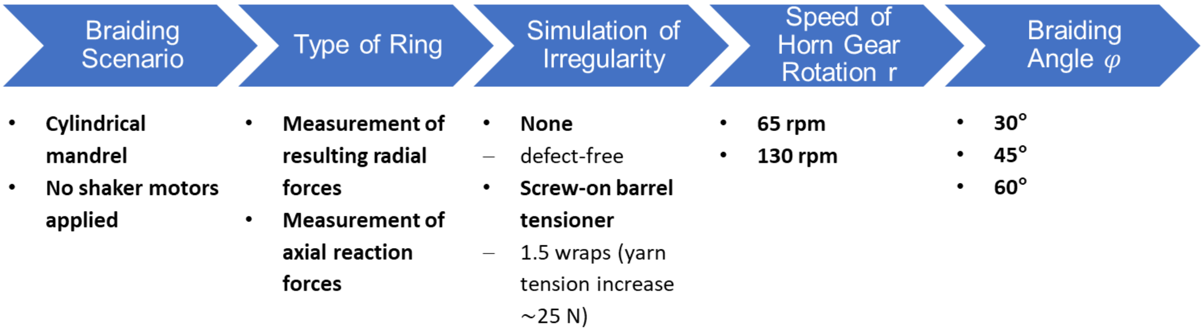

Braiding Scenario	Type of Ring	Simulation of Irregularity	Speed of Horn Gear Rotation r	Braiding Angle φ
• **Cylindrical mandrel** • **No shaker motors applied**	• **Measurement of resulting radial forces** • **Measurement of axial reaction forces**	• **None** – defect-free • **Screw-on barrel tensioner** – 1.5 wraps (yarn tension increase ~25 N)	• **65 rpm** • **130 rpm**	• **30°** • **45°** • **60°**

Figure 3-27: Test plan for the initial characterization of the sensor integrated braiding rings by overbraiding a cylindrical mandrel

The deflection of the yarns at the braiding ring is a dynamic process that creates considerable noise in the signals from the voltage dividers of the FSR. This noise mainly results from two sources. Firstly, the braiding yarns do not only move in circumferential direction but also back and forth in axial direction since the carriers travel between the reversal points as illustrated in Figure 3-22. Secondly, the ratcheting mechanism of the carriers do not create a uniform but an oscillating yarn tension within a corridor of 3-4.5 N. Due to the fact that each tensioning mechanism works independently, noise in the measured reaction forces at the braiding ring is generated. To cope with this noise, a second order butterworth low-pass filter with a cut-off frequency of 0.5 Hz was used to process the raw data from the experiments with a speed of horn gear rotation of $r = 65\ rpm$. For the tests with $r = 130\ rpm$, the cut-off frequency of the low-pass filter was set to 1 Hz. For a conversion of the measured voltages to force, the mapping functions obtained from the prior compression tests were applied to each sensor signal. Due to the different braiding speeds, the timely measurement data was referred to the braided distance on the mandrel. For reasons of settling effects at the beginning of each braiding test run, the first 25 cm are not shown in the diagrams in the following results section.

Results and Discussion

Figure 3-28 shows exemplary data from braiding tests at a speed of horn gear rotation of $r = 130\ rpm$ and a braiding angle of $\varphi = 45°$. The dashed lines correspond to defect-free braiding tests. The solid lines correspond to test runs with the barrel-tensioner in place. On the left of the figure, data acquired by the four sensors of the braiding ring for estimating the axial reaction forces is shown. Firstly, from the dashed curve in light blue, it can be noticed that the raw data as obtained from the sensor setup comes with a significant amount of noise. Only when the butterworth low-pass filter is applied, the data is interpretable (dashed line in dark blue). Moreover, it can be observed that during defect-free braiding, the readings from each sensor remain in a constant range over the course of the measurement. By contrast, during braiding with the barrel-tensioner in place, there are distinct fluctuations in the measured reaction forces observable, which are phase shifted by 90°. On the right of Figure 3-28, data acquired by the sensor integrated braiding ring for estimating the resulting radial forces is illustrated. Additionally, the prominences of the peaks in reaction force are drawn-in at the example of FSR 1. The parameter of peak prominence is used in the diagrams further down and is introduced here for a better understanding of the subsequent analysis. It can be observed that the values of the measured radial forces are generally on a lower level than the axial forces. Similar to the measurements of the axial forces, the individual sensor signals remain in a narrow range over the course of the braiding experiment in the case of defect-free braiding. Also, the radial forces measured by the four sensors of the braiding ring fluctuate and are phase shifted when the tension of a single yarn is elevated by the barrel-tensioner. However, the peak prominences of this fluctuation in radial forces are in the range of 1-2 N, compared to 5-10 N for the axial forces. Both for the axial and radial forces, the individual sensors do not measure in the same range. The relative spread between the sensor readings is however larger in case of the radial forces.

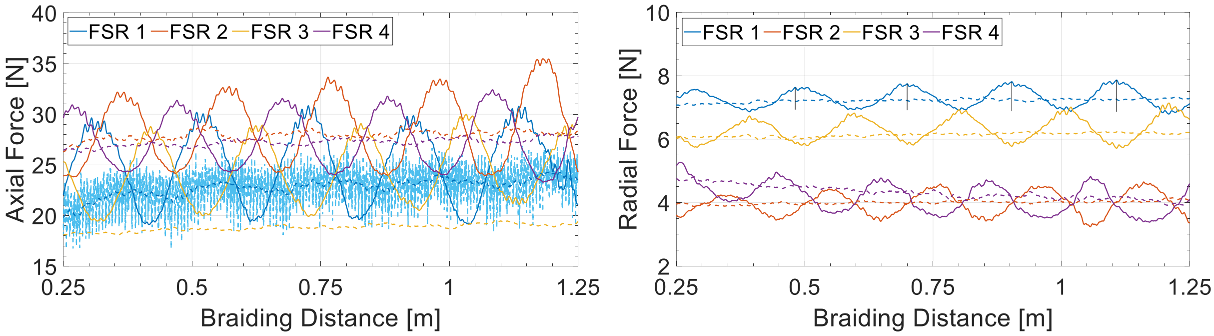

Figure 3-28: Measurement curves obtained from the axial braiding ring (left) and from the radial braiding ring (right) during braiding at an angle of $\varphi = 45°$ and a speed of horn gear rotation of $r = 130\ rpm$; dashed lines represent defect-free braiding tests, solid lines represent braiding tests with the screw-on barrel tensioner in place; different colors correspond to the different FSRs; the dashed line in light blue shows unfiltered raw data from FSR 1; diagrams taken from own publication [88]

The distinct fluctuations both in axial as well as in radial reaction forces during defective braiding compared to the rather constant reaction forces during defect-free braiding suggest that both measurement approaches may in principle be suitable for defect detection. The fact that the same level of increased yarn tension causes fluctuations of a higher prominence in axial forces than in radial forces can be explained by the analytic relations (3-11) and (3-13). Calculating the difference between axial and radial reaction force that a single yarn creates when it is deflected at the braiding ring results in

$$\begin{aligned} F_{Y\to R,A} - F_{Y\to R,R} &= F_Y \cdot e^{\mu\left(\frac{\pi}{2}-\beta\right)} \cdot cos\beta - F_Y \cdot \left(1 - e^{\mu\left(\frac{\pi}{2}-\beta\right)} \cdot sin\beta\right) = \\ &= F_Y \cdot \left(e^{\mu\left(\frac{\pi}{2}-\beta\right)} \cdot cos\beta - 1 + e^{\mu\left(\frac{\pi}{2}-\beta\right)} \cdot sin\beta\right) = \\ &= F_Y \cdot \left(e^{\mu\left(\frac{\pi}{2}-\beta\right)} \cdot (cos\beta + sin\beta) - 1\right) \end{aligned} \quad (3\text{-}14).$$

Considering that $\mu > 0$ and $0 < \beta < \frac{\pi}{2}$, both of the terms $e^{\mu\left(\frac{\pi}{2}-\beta\right)}$ and $cos\beta + sin\beta$ are greater than 1. This leads to the fact that $F_{Y\to R,A}$ must always be greater than $F_{Y\to R,R}$. This is in line with the higher prominence of the force peaks in axial than in radial direction. The generally higher level of axial forces can only partly be explained by this relation. This is due to the fact that the level of measured radial forces merely depends on the preload applied by tightening the bolts.

An uneven tightening of the bolts is also one of the reasons for the different range of measurement readings from the individual sensors. An explanation for the different force ranges of the individual sensors in the axial case can be that the sensors, unlike dedicated laboratory equipment, behave differently under persistent loads during braiding than under a force ramp during a compression test. It can however be said that the behavior of each individual sensor was observed to be repeatable between the different test runs.

In Figure 3-29, the mean and standard deviation for the axial (left) and resulting radial forces (right) are shown for the different test variants. For interpretation of the standard deviations, note that these also include the deviations among the four individual sensors themselves as described above. It can be observed that the overall level of axial reaction forces decreases with increasing braiding angle. Moreover, the axial forces appear slightly higher when a defect was simulated by the barrel-tensioner compared to defect-free braiding. However, due to the drawn-in deviations, this effect can only be regarded as a trend and not as a significant finding. A clear influence of the different braiding speeds cannot be recognized. Furthermore, the author would like to draw the reader's attention to the bar corresponding to the experiment on defective braiding at $\varphi = 60°$ and $r = 130\ rpm$ at the very right of the diagram on the axial forces. This data is marked with an asterisk in order to indicate that, in addition to the increased yarn tension of a single yarn due to the barrel tensioner, a real fibrous ring coincidentally occurred during this experiment. This will be referred to in Figure 3-31 further down. In contrast to the axial reaction forces, the measured radial forces remain in a constant range for all of the tested variants.

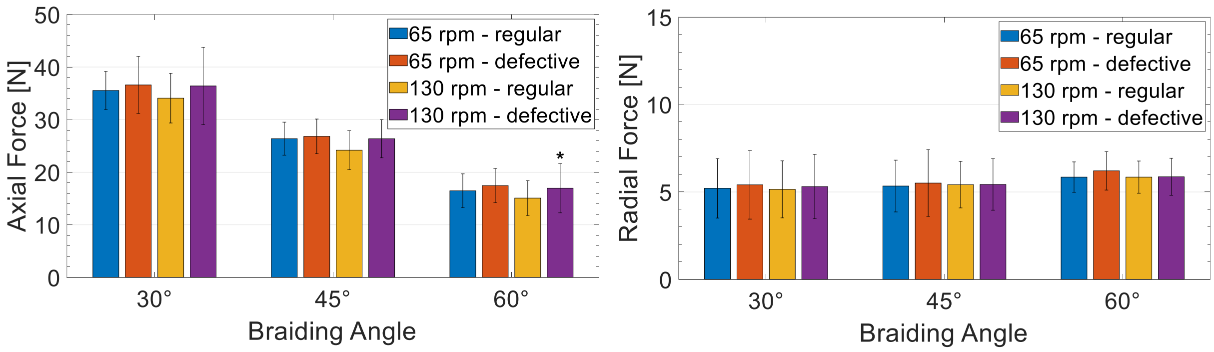

Figure 3-29: Mean values of axial (left) and resulting radial forces (right) including their standard deviations depending on braiding angle, speed of horn gear rotation and error status; the asterisk * marks data where a real fibrous ring spontaneously occurred; diagrams taken from own publication [88]

The reduction in axial reaction force can be explained by the analytic relation (3-13). With increasing braiding angle φ, the cone angle β under which the braid is deposited onto the mandrel increases (cf. Table 3-3). The measurements from Table 3-3 were calculated by the trigonometric relation (3-9). Given the basic considerations that $\mu > 0$ and $0 < \beta < \frac{\pi}{2}$, it can be said that both terms $e^{\mu\left(\frac{\pi}{2}-\beta\right)}$ and $\cos\beta$ in formula (3-13) decrease with increasing cone angle β. Thus, the axial force $F_{Y\rightarrow R,A}$ must decrease with increasing braiding angle φ. The fact that the measurements of the radial forces remain unaffected by a change in braiding angle φ proves that the design of the radial ring from Figure 3-24 is well capable of decoupling axial from radial reaction forces. On the basis of mean reaction forces, the radial forces must remain unaffected even when a defect is present. This is because a higher reading of a specific sensor is canceled out in the calculation of the mean by an equally reduced measurement value of the opposite sensor.

Table 3-3: Mean cone angles β and their standard deviations depending on braiding angle φ; table taken from own publication [88]

Braiding angle φ	Mean cone angle β	Standard deviation
30°	26.8°	3.7°
45°	40.4°	4.2°
60°	51.9°	3.2°

In order to form an educated judgement on which sensor configuration (axial or radial sensor integrated braiding ring) is better-suited for braiding process monitoring also under varying production parameters, the prominences of the fluctuations in reaction forces need to be analyzed in detail (cf. vertical black lines in Figure 3-28, right for definition of peak prominences). Figure 3-30, left illustrates the peak prominences (PP in the legend of the figure) for the axial reaction forces against the varied test parameters. As with the overall level of reaction forces from Figure 3-29, the peak prominences decrease with increasing braiding angle φ. Moreover, the axial peak prominences of the braiding tests at a speed of $r = 130\ rpm$ appear to show higher values than the axial peak prominences of the tests that were carried out at a reduced speed of $r = 65\ rpm$. The peak prominences are also referred to the mean reaction forces of each variant (PP/M in the legend of the figure). Unlike the absolute values of the peak prominences, these relative values remain in a constant range of approximately 0.4 for the experiments with reduced speed and approximately 0.5 for the experiments with the higher braiding speed. Figure 3-30, right shows the peak prominences obtained from the braiding ring intended for measuring resulting radial forces. Similar to the case of the axial forces, the radial peak prominences decrease as the braiding angle φ increases. Beyond that, there is a trend towards higher peak prominences for the higher braiding speed. When the peak prominences are referred to the mean level of the measured radial forces, they decrease with increasing braiding angle φ. This is in contrast to the findings for the axial forces.

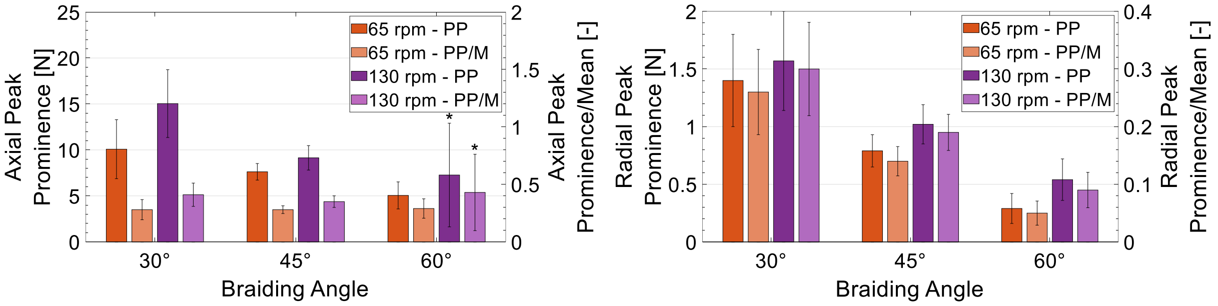

Figure 3-30: Peak prominences of the axial reaction forces (left) and resulting radial forces (right); mean values of the peak prominences including their standard deviations are plotted against the left y-axis; the values of the peak prominences are related to the mean reaction forces as displayed in Figure 3-29 and drawn-in with respect to the right y-axis; the asterisk * marks data where a real fibrous ring spontaneously occurred; diagrams taken from own publication [88]

As with the mean values of the axial reaction forces, the trend towards lower axial peak prominences at higher braiding angles can again be explained by the analytic relation (3-13) and the respective angles of yarn deflection. Unlike the mean radial reaction forces, which remain constant under varying braiding angles φ, the radial peak prominences decrease with increasing braiding angle. This is because in the calculation of the mean radial peak prominence, a higher force on one sensor does not cancel out with a lower force on the opposite sensor. Important to note is that the axial peak prominences are reduced by the same fraction as the mean axial reaction forces. This results in a constant quotient of these two parameters over the different braiding angles. Hence, the fluctuations in axial forces that distinguish defect-free from defective braiding always remain clearly distinguishable from the natural process-induced fluctuations of the axial forces. By contrast, decreasing radial peak prominences in combination with constant mean radial forces result in a decrease of the quotient of the two parameters. This means that at higher braiding angles, it becomes difficult to distinguish naturally occurring deviations from fluctuations that result from a defect. With the relative measure of peak prominence against mean radial force being in the range of only 0.05 in the case of $\varphi = 65°$ and $r = 65\ rpm$, an automatic defect detection by monitoring software is hardly conceivable.

As indicated by the asterisk * in Figure 3-29 and Figure 3-30, there was a fibrous ring that spontaneously occurred during one of the braiding experiments. The data on defective braiding from above is created by a screw-on barrel tensioner for a controlled and therefore repeatable *simulation* of a defect during the process. Since the sensor integrated braiding rings are proposed as an industry-near method for defect detection during braiding, the data from the spontaneous, *real* fibrous ring shall also be discussed at this point. In Figure 3-31 on the left, the measurement curves from the braiding test under simulation of a defect, a braiding angle of $\varphi = 60°$ and a speed of horn gear rotation of $r = 130\ rpm$ are shown. From the beginning of the measurement, the distinct phase-shifted fluctuations in axial reaction force originating from the screw-on barrel tensioner can be observed. Starting at about 0.8 m of braided distance on the mandrel, anomalous courses of the measured axial forces are noticeable. At approximately 1.05-1.1 m, it is recognizable that the fibrous ring causes fluctuations in reaction forces that are about two to three times as extreme as those from the barrel tensioner. After these extreme fluctuations, the yarn broke and the regular fluctuations from the barrel tensioner dominate the readings again. Due to the fact that the yarn tension increase induced by the barrel tensioner is significantly smaller than the real tension increase when a fibrous ring forms and the respective yarn breaks, the sensor integrated braiding rings, and especially the ring measuring the axial forces, have demonstrated their potential to detect real defects that occur during braiding of reinforcement fibers.

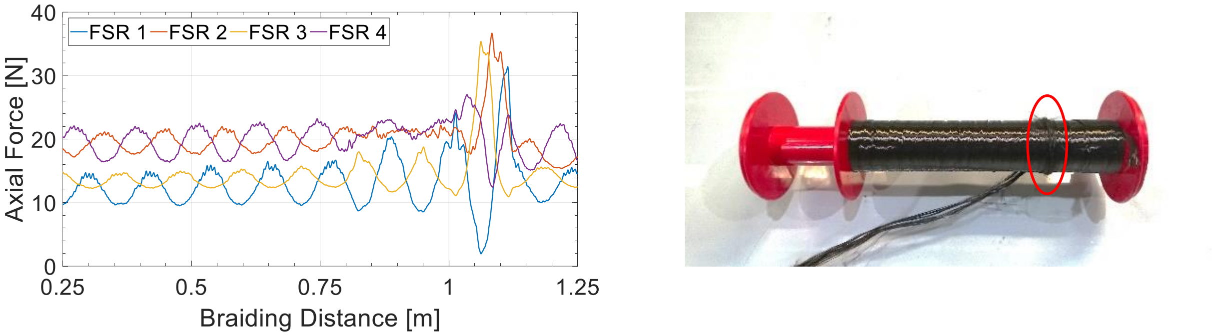

Figure 3-31: Measurement curves obtained from the ring measuring axial reaction forces during braiding with the screw-on barrel tensioner in place under a braiding angle of $\varphi = 60°$ and a speed of horn gear rotation of $r = 130\ rpm$ (left); at ~1.1 m of braided distance on the mandrel, a single yarn broke due to the illustrated fibrous ring (right); illustrations taken from own publication [88]

As a conclusion of the initial tests on the two types of sensor integrated braiding rings, the following points can be made:

- Force sensing resistors in conjunction with voltage dividers as robust measurement circuit can serve as a low-cost approach for a monitoring of reaction forces at the braiding ring.
- On an absolute basis, the calculated force readings can only be seen as a rough estimation. Due to the good repeatability of the measurement results, the sensors are however still capable of detecting changes in reaction forces at the braiding ring, which is crucial for detecting braiding defects.
- A tension increase of a single braiding yarn by means of a screw-on barrel tensioner can be detected both in the distribution of axial reaction forces as well as in the resulting radial forces at the braiding ring.
- The induced fluctuations in reaction forces are more prominent in the axial than in the radial forces. This makes the axial sensor integrated braiding ring more favorable than the radial ring. This is of particular importance at higher braiding angles where the overall level of reaction forces is reduced.
- The controlled simulation of a braiding defect by a screw-on barrel tensioner constitutes a moderate increase in tension of a single braiding yarn compared to the excessive forces during formation of a fibrous ring that lead to a yarn breakage. Hence, the proposed approach of sensor integrated braiding rings is expected to be a suitable method for defect detection when reinforcement yarns of comparable strength or above are processed.

In Figure 3-31, it was demonstrated that the sensor setup is capable of detecting a fibrous ring as a braiding defect along the length of a mandrel. A prior warning of in this case ~0.3 m in terms of braiding distance before the yarn breaks results in a lead time of approximately

$$t_{lead} \approx \frac{0.3\,m}{\dfrac{\pi \cdot d}{t_{360^\circ} \cdot \tan\varphi}} = \frac{0.3\,m}{\dfrac{\pi \cdot d}{\dfrac{n_{horn\,gear}}{2 \cdot r} \cdot \tan\varphi}} = \frac{0.3\,m}{\dfrac{\pi \cdot 65\,mm}{\dfrac{32}{2 \cdot \dfrac{130\,rpm}{60\,\dfrac{s}{min}}} \cdot \tan(60^\circ)}} \approx 18.8\,s \qquad (3\text{-}15).$$

The reader is referred to relations (2-4) and (2-5) for the derivation of the above calculation. During the time period t_{lead}, a control signal can be generated by a data analysis algorithm in order to stop the braiding machine before the breakage of the yarn, thereby offering the opportunity to remove a fibrous ring and avoiding a manual rethreading of a new, intact braiding yarn. In order to further reduce the error correction time, it is desirable to also provide the operating personnel with information on which carrier or at least in which group of carriers the defect is located. This way, the search time for a localization of the defect can be minimized, especially in case of a number of braiding yarns in the hundreds. An algorithm both for defect detection and localization of the defect in the machine on the basis of signals from the sensor integrated braiding rings is derived in the next subsection.

3.2.2 Algorithm Development for Defect Detection and Localization during Overbraiding of a Complexly Shaped Mandrel

For the investigations described in this subsection, the same sensor integrated braiding rings as presented in the above subsection are applied. Since braiding is particularly used in the fiber composite industry for the production of tubular and complexly shaped preforms, the defect detection capabilities of the two types of rings are assessed during overbraiding of a generic demonstrator mandrel that shows an S-shape and a trapezoidal cross section. Moreover, shaker motors, which are commonly used for braiding of composite parts to achieve a better spreading of the yarns, are applied to actuate the sensor integrated rings during braiding. A self-learning algorithm is proposed that can be trained by means of data acquired by the sensor integrated rings during braiding with a simulated defect. The capabilities of the trained detection algorithm regarding distinction between regular and defective braiding as well as localization of a defect in the braiding machine are examined on independent test data sets that were gathered during braiding with a simulated defect as well as with a real fibrous ring. The application of the shaker motors in combination with the complex geometry of the mandrel shall thereby serve as a replication of a near-industrial use case of the detection algorithm under deliberately adverse circumstances.

Experimental Setup

In accordance with the standard braiding scenario as defined in section 1.2, the S-shaped mandrel with trapezoidal cross-section (cf. Figure 3-32) was overbraided with dry carbon fiber yarns of the type Tenax®-E HTS40 F13 12k. To achieve a full coverage of the surface of the mandrel, the RF 1/128-100 braiding machine from HERZOG GmbH was equipped with 64 bobbins of the said material. By using springs with a release force equivalent to a mass of 350 g in the bobbin carriers, the tension of the individual braiding yarns was kept within an interval of 3-4.5 N. The robot, which guided the mandrel through the center of the braiding machine, was set to operate with the center of the braiding machine as an external tool center point. The curved path of the robot was programmed in a way that any perpendicular cross section of the mandrel, as shown on the right hand side of Figure 3-32, was kept parallel to the machine at the moment it was overbraided. This way, a theoretically constant haul-off speed of the mandrel with respect to its central axis was aimed for in order that a constant braiding angle of $\varphi = 45^\circ$ could be achieved. At the same time, the braiding machine was set to operate at a constant speed of horn gear rotation of $r = 130\ rpm$. Two shaker motors of the type HV1/4-3 from Würges Vibrationsmotoren GmbH were used to actuate the sensor integrated braiding rings (cf. Figure 3-34). These shaker motors caused the braiding rings to visibly vibrate at an amplitude of about 1 cm at a frequency of approximately 13 Hz. As with the setup in the above subsection 3.2.1, four force sensing resistors (FSR) of the type CP 149 from International Electronics & Engineering S.A. were integrated into the braiding rings. Viewing in production direction, FSR 1 was placed at the top, FSR 2 on the left, FSR 3 at the bottom and FSR 4 on the right.

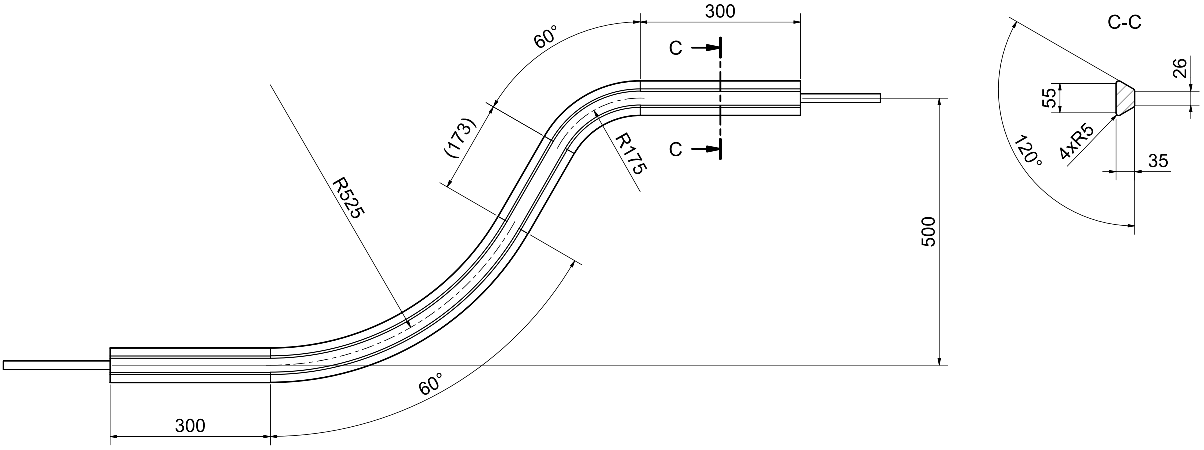

Figure 3-32: Drawings of the S-shaped mandrel with trapezoidal cross-section as generic representative of complexly shaped braided components; view from above (left); cross sectional view (right); dimensions in millimeters

Five reference measurements were conducted for each type of sensor integrated braiding ring during regular, defect-free overbraiding of the S-shaped mandrel. Additionally, five measurements were carried out for each type of ring under controlled *simulation* of a braiding irregularity at a single braiding spool. As in the subsection above, the defect was simulated by adding a screw-on barrel tensioner to a single bobbin carrier and by winding the respective braiding yarn 1.5 times around the barrel (cf. Figure 3-26, right). The modified bobbin carrier was marked by attaching a magnet to the lever of its yarn tensioning unit. Four stationary Hall sensors, which jutted into the tracks of the bobbin carriers and which were spaced evenly around the circumference of the braiding machine, enabled a precise tracking of the position of the modified bobbin carrier in the machine during braiding. Finally, a manipulated braiding spool on which a *real* fibrous ring was at the onset of formation was mounted onto a single bobbin carrier instead of the barrel tensioner for one braiding test with each type of sensor integrated ring. For reasons of a better overview and in consistency with the presentation of other test series, the test plan is illustrated in Figure 3-33.

Braiding Scenario	Type of Ring	Introduction of Irregularity	Speed of Horn Gear Rotation r	Braiding Angle φ
• **S-shaped mandrel** • **Shaker motors applied**	• **Measurement of resulting radial forces** • **Measurement of axial reaction forces**	• **None** – defect-free • **Screw-on barrel tensioner** – 1.5 wraps (yarn tension increase ~25 N) • **Bobbin with real fibrous ring**	• **130 rpm**	• **45°**

Figure 3-33: Test plan for the derivation of a defect detection algorithm operating on data from the sensor integrated braiding rings

The sensor data was gathered by a USB-6210 data acquisition device from National Instruments Corp., which was set to operate at a rate of 100 scans/s. As described in the subsection above, the measurements obtained from the force sensing resistors in the braiding rings naturally fluctuated due to the ratcheting mechanism of the yarn tensioning units of the bobbin carriers and the back and forth movement of the yarns in the braid formation zone. The vibrations induced by the two shaker motors (cf. Figure 3-34) led to further noise in the sensor signals. This noise in the signals was eliminated by a second order butterworth low-pass filter with a cut-off frequency of 1 Hz. The individual mapping functions for each sensor obtained from compression tests as described in the above subsection were applied to the filtered sensor signals to convert the voltage readings into estimated compression forces.

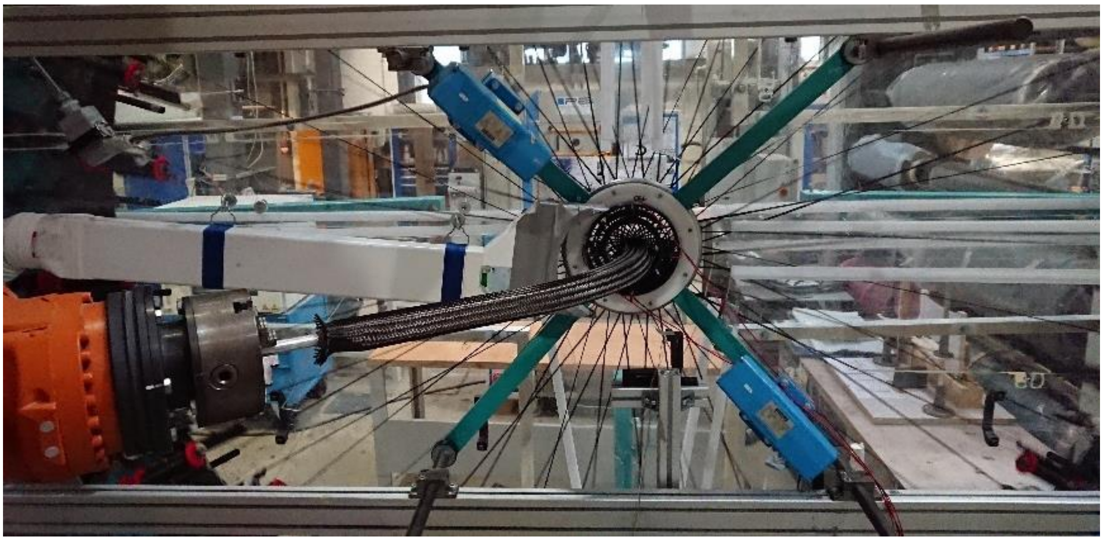

Figure 3-34: Sensor integrated ring for estimating resulting radial forces during overbraiding of the S-shaped mandrel as well as two blue shaker motors mounted to the fixture of the braiding ring

Derivation of the Defect Detection Algorithms

For the detection and localization of yarn tension anomalies in a braiding machine, a separate algorithm was developed for each type of sensor integrated ring. For the derivation of each algorithm, the data obtained from the experimental setup as described above was subdivided into *three* different data sets. Of the five reference braiding tests, the first four tests (80 % of reference data) were used for generating the algorithm. Of these first four tests, another 80 % of the data tuples were declared as reference *training data*. A data tuple is herein understood as an array of readings from FSR 1, FSR 2, FSR 3 and FSR 4 at a given position on the mandrel that was processed by the low-pass filter. Following the method of supervised learning, training data is that kind of data from which an algorithm iteratively learns to make the correct prediction. After each learning iteration (so-called epoch), the prediction performance of the trained algorithm was examined on a dedicated reference *validation data* set. As validation data, the remaining 20 % of the data tuples of the first four tests were used. The reason for distinguishing between training and validation data is to stop the iterative learning process when the algorithm begins to adopt itself too closely to the training data and loses its ability to generalize on unknown data. This point is indicated by a worsening validation performance. As method to divide the data into training and validation data, the interleaved method was applied in MATLAB R2021a. The reason for not using a random subdivision of the data was that the data tuples of training and validation would otherwise be acquired at too similar positions along the length of the mandrel. The validation data would consequently be expected to be similar to the training data. By choosing the interleaved data division method, data corresponding to longer distances on the mandrel is assigned to the different data sets. This way, natural fluctuations that occur during braiding are better accounted for during training and validation of the neural networks and higher generalization capabilities of the trained algorithms were maintained. For a comparison of the prediction results to a random subdivision of data, the reader is referred to appendix A. The fifth test (20 % of reference data) was treated as an independent data set that was strictly reserved for testing the trained algorithm (test data set 1). In principle, the treatment of this reference *test data* is similar to the validation data. Both groups of data are used to measure the performance of a trained algorithm on data that was not included in the training process itself (generalization performance). However, a data scientist may still optimize the hyperparameters of a self-learning algorithm in a way that the algorithm ends up being tailored too closely to the validation data (thereby producing good validation performances) but has lost its ability to work properly on unknown data (poor prediction performance in real application). In order to avoid such a manmade distortion, the algorithm was tested on an independent test data set once the validation performance was deemed satisfactory after optimization of the hyperparameters of the algorithm. The subdivision of the experimental data into three data sets was explained at the example of the five reference measurements. An analogous subdivision was carried out for the data from the five measurements with a simulated defect. The union of a given data set from the reference measurements (e.g. reference training data) with the respective data set from the measurements with a simulated defect (e.g. defect training data) constituted the respective full data set for the derivation of the defect detection algorithm. The data from the measurement with a real fibrous ring was used as a second independent test data set (test data set 2). It was applied to examine how well an algorithm trained on data with a *simulated* defect can generalize on data with a *real* defect that occurs in a near-industrial use case. For reasons of a better overview, the generation of the different data sets is illustrated in Figure 3-35. The subdivision of data into the different data sets was handled exactly identically for both the axial as well as the radial sensor integrated braiding ring.

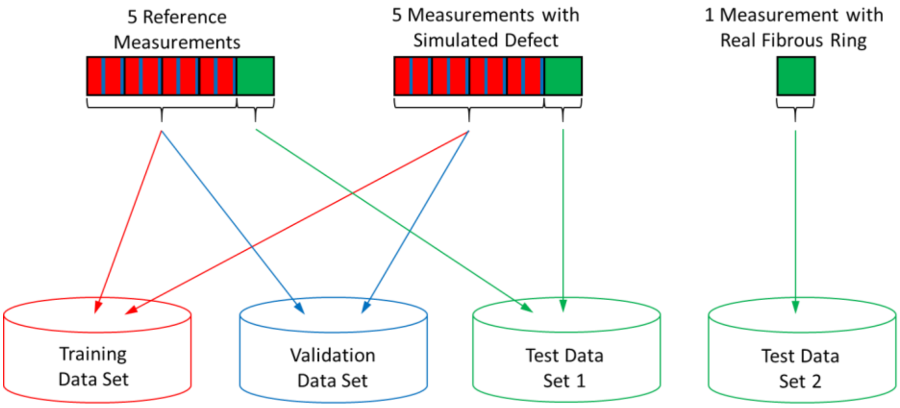

Figure 3-35: Generation of training data set, validation data set and test data set 1 from reference measurements and measurements with a simulated defect as well as test data set 2 being entirely comprised of measurement data from the experiment with a real fibrous ring; the first four reference measurements and the first four measurements with a simulated defect are colored in an interleaved manner to indicate the interleaved method of data subdivision into training and validation data

For the derivation of the defect detection algorithms, the following standardized procedure was developed. The full procedure was carried out with the data from the axial as well as with the data from the radial ring independently from each other. As a first step, the mean reading per sensor at each position during braiding along the central axis of the S-shaped mandrel was calculated from the first four of the five reference measurements. Secondly, the sensor readings obtained from all tests conducted with a given type of braiding ring were referenced by subtracting the mean readings per sensor and position as calculated in the first step. This correction was necessary in order to prevent any confusion of the self-learning algorithm by signal fluctuations that are caused by the S-shape of the mandrel and not by yarn tension anomalies. Thirdly, the referenced data was labeled. For this, the braiding machine was subdivided into 16 overlapping segments as depicted in Figure 3-36, left. These segments were used as classes during training of the defect detection algorithm. Since the corrected data from the five reference measurements contained no braiding irregularities, all tuples of corrected data from these test runs received the label “0”. The four-tuples of corrected data from the measurements with a defect received two separate labels. The first set of labels ranged from “1” to “8”, thereby corresponding to the segments 1-8 of the braiding machine in which the defect was located at the moment of acquisition of the data tuple. The second set of labels ranged from “9” to “16”, corresponding to the segments 9-16 of the braiding machine in which the defect was also located at the moment of acquisition of the data tuple. Due to the fact that the segments overlapped with each other, a defect was always located in two segments at the same time. As a fourth step, a first shallow feed-forward neural network consisting of four input neurons, four neurons in the hidden layer and nine neurons in the output layer (cf. Figure 3-36, right) was created by means of the “patternnet”-function in MATLAB R2021a. Such a minimal network architecture was chosen in order to keep training effort low and to enable a process monitoring in real-time even on microcontrollers with limited computing power. As will be shown in the results section, the performance of this minimal network architecture is already satisfactory. For considerations on more elaborate network architectures, the reader is referred to appendix A. According to the “patternnet”-function, the hyperbolic tangent sigmoid function was applied as transfer function for the neurons in the hidden layer. The softmax transfer function was used for the neurons in the output layer. The weight and bias parameters of the network were initialized by the Nguyen-Widrow function. The training step itself involved both the referenced and labeled training data set (first set of labels “0” and “1” to “8”) as well as the referenced and labeled validation data set (first set of labels “0” and “1” to “8”). The adjustment of the parameters of the network was performed iteratively by minimizing the difference in prediction of the network based on a given data tuple and its label from the training data set (so-called loss). As a measure for the difference between prediction and label, the cross-entropy loss function was applied. This loss function was minimized by adjusting the network parameters according to the scaled conjugate gradient method. After each step of the iterative parameter adjustment, the loss of the network on the validation data was evaluated. As soon as the validation loss of the network continuously increased over six successive iteration steps, the training process was stopped. This measure was implemented in order to avoid that the network adjusts too closely to the given set of training data (so-called overfitting) and in order to maintain the network’s ability to make correct predictions on unknown data. In parallel, a second feed-forward neural network of identical architecture was trained and validated with the same methods and datasets but with the second set of labels (“0” and “9” to “16”).

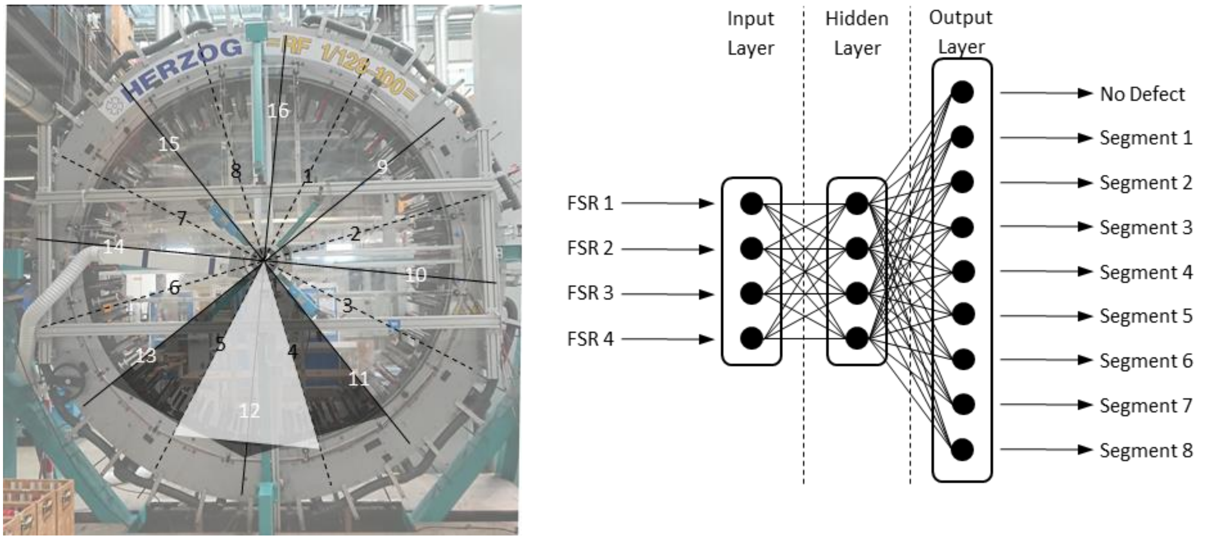

Figure 3-36: Overlapping segmentation of the radial braiding machine RF 1/128-100 for defect localization (left) as well as graphical reproduction of the architecture of the shallow neural network used for defect detection (right)

The prediction function was obtained in the fifth step by coupling both network results. The predicted class (segment of the braiding machine in which the defect was predicted to be located) of an unknown data tuple was defined as the output class with the highest probability (output of the softmax neurons) of both networks combined. Implementing the approach of overlapping segments was meant to avoid that data tuples that were acquired near the edge of a segment were designated as falsely predicted when they were assigned to the directly adjacent segment by the network. Instead, the combined prediction function offered the algorithm the possibility to choose that segment which covers the edge regions of the two neighboring segments in question. Figure 3-37 illustrates the concept of the combined prediction function. If, for instance, in Figure 3-36, left a defect was located in the transition zone between segments 4 and 5 but its exact true location was segment 4, then the outputs of both neural networks could be as exemplarily shown in Figure 3-37 on the left. Network 1 would make a false prediction because it is hard for this network to distinguish between classes “4” and “5” when the defective carrier is just about to transfer from one segment to the next. By contrast, the localization task is significantly easier for network 2 because the defect is located right in the middle of segment 12. Such a case can be seen from the output values of the different neurons. The occurrence of two outputs of similar absolute values (0.41 and 0.46 in this exemplary case) suggests that there is significant level of uncertainty in the network prediction. The occurrence of only one output value that is much greater than the other values (0.86 in this case) suggests that there is less uncertainty in this prediction. When that network prediction with the highest maximum output value is chosen as output of a combined prediction, then segment 12 is correctly assigned as location of the defective bobbin carrier (cf. Figure 3-37, right).

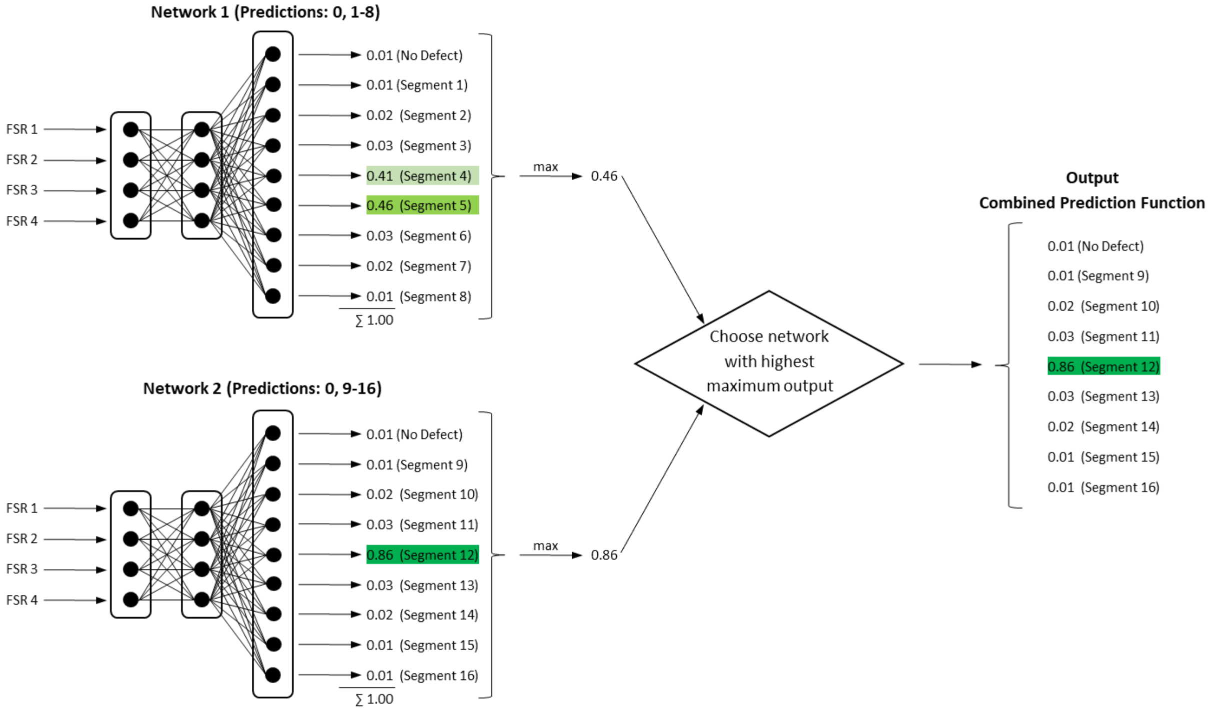

Figure 3-37: Exemplary prediction results of networks 1 and 2 trained on labeled data with classes “0”, ”1” to “8” and “0”, “9” to “16”, respectively; the combined prediction function for each input data tuple is defined as the output from the network with the highest maximum output value for any class

In the concluding sixth step of the derivation and test of the algorithms for defect detection, the combined prediction function was tested and evaluated on independent test data sets of corrected data from the fifth reference measurement, the fifth measurement with a simulated defect as well as with data from braiding with a manipulated bobbin that showed a real fibrous ring. All of the three tests were conducted both with data from the axial and with data from the radial ring.

Results and Discussion

In the first part of this subsection, the characteristics of the measurement results obtained from the axial as well as from the radial braiding ring are described and explained. For reasons of a better reference to the geometry of the overbraided mandrel, the time-related measurement data is referred to the position along the central axis of the mandrel. Data from the first 10 cm of braiding on the mandrel is excluded from the analysis in order to cut-off visible settling effects at the beginning of the process and to reduce a potentially negative impact on the training of the defect detection and localization algorithms. In the second part of this section, the performance of the separate algorithms for the two types of sensor integrated rings, which were derived according to the standardized procedure described above, is determined by testing them on independent data sets with *simulated* (test data set 1) as well as with *real* defects (test data set 2).

Exemplary measurement curves obtained from overbraiding the S-shaped mandrel under regular (dashed lines) as well as defective braiding with the screw-on barrel tensioner in place (solid lines) are shown in the figure below. In Figure 3-38, left, the reaction forces measured by the axial braiding ring are depicted. The dashed line in light blue represents unfiltered data from FSR 1. A considerable amount of noise, which is even more pronounced than during overbraiding of the cylindrical mandrel (cf. Figure 3-28), is observable in this sensor signal. Only when the butterworth low-pass filter with a cut-off frequency of 1 Hz is applied, an interpretable sensor reading is generated. Although there are no defects present during regular braiding, it can be observed from the dashed lines that the measurement curves of the four sensors still show significant fluctuations over the braiding distance. Moreover, it can be seen that the sensors do not measure in the same range of axial forces. Especially the curve of FSR 1 is generally at a lower level than the curves of the other sensors. When regarding the solid measurement curves from defective braiding, it stands out that there are sinusoidal fluctuations which appear to be superimposed on the curves from regular braiding. The amplitudes of the sinusoidal fluctuations are similar in the same area on the mandrel but increase with larger braiding distance. In Figure 3-38, right, exemplary reaction forces measured by the radial braiding ring are illustrated. The radial forces are only at approximately a third of the absolute level of the axial reaction forces. There are still fluctuations in the signals during regular braiding over the braiding distance. However, in comparison to the axial forces, these fluctuations are on an absolute as well as on a relative basis less pronounced. Similar to the axial forces, the sensors do not measure in the same range when installed into the radial braiding ring. Also similar are the sinusoidal courses of the measurement curves acquired during defective braiding, which are smaller at the beginning than during the rest of braiding.

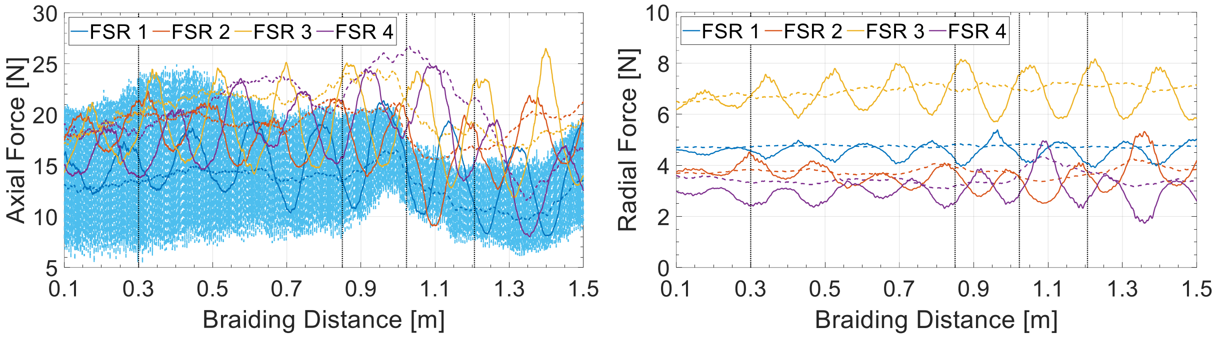

Figure 3-38: Measurement curves obtained from the axial (left) as well as from the radial braiding ring (right) during regular (dashed lines) and defective braiding (solid lines); different colors correspond to individual sensors; the dashed line in light blue shows unfiltered raw data from FSR 1; vertical dotted lines mark the transition between differently curved areas of the mandrel

The considerable amount of noise in the sensor signal, which is more pronounced than in the case of overbraiding the cylindrical mandrel, can be attributed to the additional use of shaker motors to actuate the braiding ring. The fact that the low-pass filter is capable of eliminating this noise shows that the approach of measuring reaction forces at the braiding ring is still viable in a near-industrial use case when shaker motors are used to achieve a better spreading of the braiding yarns. When a cylindrical mandrel was overbraided in subsection 3.2.1, rather constant signals from the sensor integrated braiding rings were observable during regular braiding. Hence, the fluctuations in sensor signals during regular braiding in this subsection can be attributed to the S-shape of the mandrel. As can be seen in Figure 3-34, the mandrel is not always exactly guided through the center of the braiding ring. This is due to the fact that the S-shaped mandrel, which is made from ureol, significantly bends during braiding. This bending is caused by the resulting reaction force that the yarns exercise onto the mandrel. Especially at the curvature of the mandrel with a radius of 175 mm, this bending also led to a temporarily reduced haul-off speed of the mandrel with respect to the braiding ring. Besides this, the lower reading of FSR 1, which is located at the top of the braiding ring, is explainable by a reduced axial pressure that is exercised onto this sensor. The stainless steel rim, which is used for smoothly deflecting the carbon yarns, is of considerable weight. This weight leads to a moment which tilts the inner part of the axial braiding ring and slightly reliefs the pressure on FSR 1. The reason for the different levels of force readings is however different for the radial braiding ring. They are attributable to an uneven tightening of the bolts which transmit a portion of the radial forces to the sensors. Nevertheless, the factors causing fluctuations in and different levels of measured forces are either constant throughout the whole braiding process (weight of stainless steel rim, uneven tightening of the bolts) or at least of the same extent at the same position along the mandrel when the process is repeated (bending of the mandrel). This means that by referencing the force readings at each position along the mandrel to the mean value of each sensor from the first four defect-free reference measurements has the potential to cancel out these factors. However, such a referencing also implies that any defect detection algorithm is only suitable for the shape of the mandrel it was trained for.

During overbraiding of the cylindrical mandrel in subsection 3.2.1, distinct sinusoidal fluctuations both in the axial as well as in the resulting radial reaction forces were already distinguishable when a single yarn with an irregular tension was present. The fact that these fluctuations are similarly observable during overbraiding of a mandrel with trapezoidal cross section as used in this subsection shows that a defect detection by means of these fluctuations is per se not impeded by a complex cross section of the overbraided mandrel. Moreover, the observation of larger sinusoidal fluctuations in reaction forces towards the end of the braiding experiments can again be explained by a bending of the ureol mandrel. If a yarn with an unusually high tension is present in the braiding machine, it pulls the mandrel into the direction of the yarn with increased tension. The longer the mandrel, the higher is the respective bending moment. The lower the bending stiffness of the mandrel, the higher the impact on the amplitude of the sinusoidal fluctuations in reaction forces.

As explained in detail in the above subsection on the derivation of the defect detection algorithms, two shallow neural networks were trained independently with referenced data from the first four reference measurements and the first four measurements with a simulated defect for each type of sensor integrated braiding ring. The first neural network was intended to distinguish between defect-free braiding (class “0”) and the segments 1-8 of the machine (classes “1” to “8”) in which a defect – if detected – is located. Analogously, the second neural network was created to distinguish between defect-free braiding (class “0”) and the segments 9-16 of the machine (classes “9” to “16”) in which a defect – if detected – is located.

When the first network for the axial braiding ring was tested on the independent test data set 1 consisting of the fifth braiding test with a simulated defect (cf. Figure 3-35), it achieved a test accuracy of 85.8 %. The detailed results from the test of the first network can be seen from the test confusion matrix in Figure 3-39, left. This matrix shows the true location of the simulated defect, which is known because of the tracking of the defective bobbin carrier by the magnet and the stationary Hall sensors, in the vertical columns (target class). The horizontal lines of the matrix correspond to the prediction made by the neural network (output class). In each cell, the absolute number of data tuples from the respective target and output class as well as their proportion in relation to all the data tuples (total of 5906) gathered during the fifth measurement with simulated defect are indicated. In the bottom line, the probability of detection (green color) and the miss rate (red color) for each target class are given. In the column on the right, the positive predictive value (green color) and the false discovery rate (red color) are listed for each predicted class. The cell on the bottom right shows the overall probability of a correct detection (test accuracy, green color) and the overall probability of a false detection (red color). It can be observed that the large majority of data tuples (85,8 %) lies on the diagonal of the matrix, which means that they were correctly predicted. Moreover, it can be said that if a false prediction is made by the network, it exclusively predicts incorrectly by one segment of the braiding machine. This can be seen from the confusion matrix because the falsely predicted data points lie on the two secondary diagonals of the matrix. Note that the incorrectly predicted data points with target class “1” and output class “8” as well as with target class “8” and output class “1” do not contradict this finding. In fact, they verify it because the classes “1” and “8” are directly adjacent in the segmentation of the braiding machine in Figure 3-36. Hence, the fact that these data points are not part of the secondary diagonal is only a result of displaying a circular arrangement of segments in a diagram with linear axes. The test was conducted with a simulated defect. Hence, no classification of “no defect” (class “0”) was made. The second network for the axial braiding ring achieved a test accuracy of 83.0 % when tested on the fifth measurement with a simulated defect. When looking at the corresponding test confusion matrix in Figure 3-39, right, a similar picture as for the first network can be observed. The only difference to the confusion matrix from the first network is that there is a small number of 24 data points that was predicted incorrectly by two segments (segment 11 instead of segment 9). For reasons of space and due to the fact that there is a similar situation for the networks trained on data from the radial sensor integrated braiding ring, their confusion matrices are not explicitly shown here. The confusion matrices for the tests of the networks on the fifth reference measurement (defect-free) are also waived at this point. The reason for this is that all data tuples of the defect-free measurements were correctly categorized into output class “0” by all networks. This results in confusion matrices being almost exclusively comprised of zero entries. The overall results on test accuracy of all networks applied to defective and defect-free test data can be read from Table 3-4. For the detailed test confusion matrices omitted here, the reader is referred to appendix A.

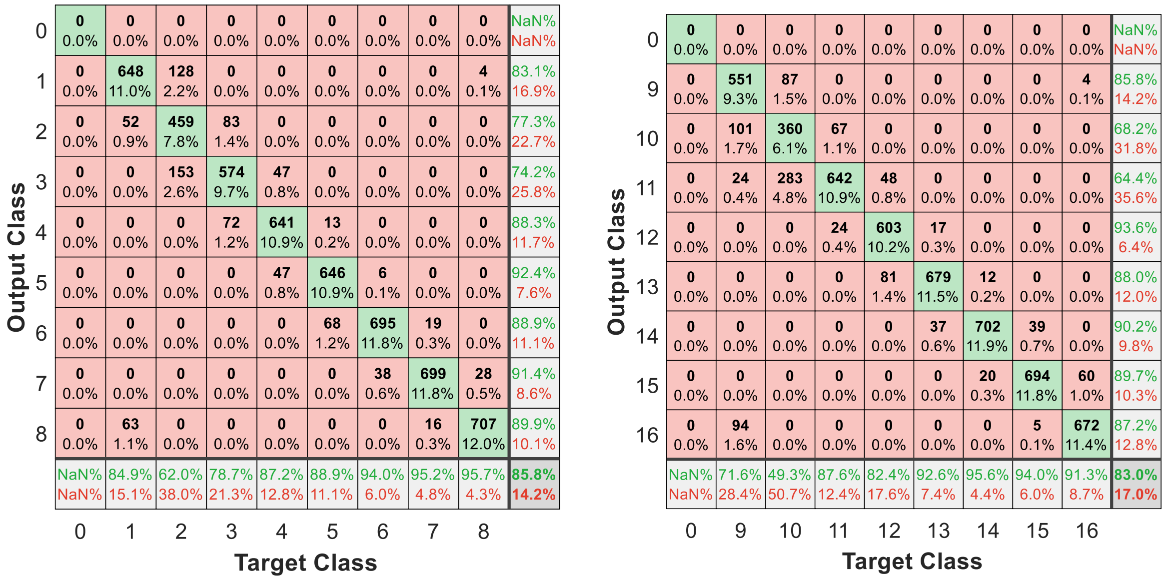

	0	1	2	3	4	5	6	7	8	
0	0 0.0%	0 0.0%	0 0.0%	0 0.0%	0 0.0%	0 0.0%	0 0.0%	0 0.0%	0 0.0%	NaN% NaN%
1	0 0.0%	648 11.0%	128 2.2%	0 0.0%	0 0.0%	0 0.0%	0 0.0%	0 0.0%	4 0.1%	83.1% 16.9%
2	0 0.0%	52 0.9%	459 7.8%	83 1.4%	0 0.0%	0 0.0%	0 0.0%	0 0.0%	0 0.0%	77.3% 22.7%
3	0 0.0%	0 0.0%	153 2.6%	574 9.7%	47 0.8%	0 0.0%	0 0.0%	0 0.0%	0 0.0%	74.2% 25.8%
4	0 0.0%	0 0.0%	0 0.0%	72 1.2%	641 10.9%	13 0.2%	0 0.0%	0 0.0%	0 0.0%	88.3% 11.7%
5	0 0.0%	0 0.0%	0 0.0%	0 0.0%	47 0.8%	646 10.9%	6 0.1%	0 0.0%	0 0.0%	92.4% 7.6%
6	0 0.0%	0 0.0%	0 0.0%	0 0.0%	0 0.0%	68 1.2%	695 11.8%	19 0.3%	0 0.0%	88.9% 11.1%
7	0 0.0%	0 0.0%	0 0.0%	0 0.0%	0 0.0%	0 0.0%	38 0.6%	699 11.8%	28 0.5%	91.4% 8.6%
8	0 0.0%	63 1.1%	0 0.0%	0 0.0%	0 0.0%	0 0.0%	0 0.0%	16 0.3%	707 12.0%	89.9% 10.1%
	NaN% NaN%	84.9% 15.1%	62.0% 38.0%	78.7% 21.3%	87.2% 12.8%	88.9% 11.1%	94.0% 6.0%	95.2% 4.8%	95.7% 4.3%	**85.8%** **14.2%**

	0	9	10	11	12	13	14	15	16	
0	0 0.0%	0 0.0%	0 0.0%	0 0.0%	0 0.0%	0 0.0%	0 0.0%	0 0.0%	0 0.0%	NaN% NaN%
9	0 0.0%	551 9.3%	87 1.5%	0 0.0%	0 0.0%	0 0.0%	0 0.0%	0 0.0%	4 0.1%	85.8% 14.2%
10	0 0.0%	101 1.7%	360 6.1%	67 1.1%	0 0.0%	0 0.0%	0 0.0%	0 0.0%	0 0.0%	68.2% 31.8%
11	0 0.0%	24 0.4%	283 4.8%	642 10.9%	48 0.8%	0 0.0%	0 0.0%	0 0.0%	0 0.0%	64.4% 35.6%
12	0 0.0%	0 0.0%	0 0.0%	24 0.4%	603 10.2%	17 0.3%	0 0.0%	0 0.0%	0 0.0%	93.6% 6.4%
13	0 0.0%	0 0.0%	0 0.0%	0 0.0%	81 1.4%	679 11.5%	12 0.2%	0 0.0%	0 0.0%	88.0% 12.0%
14	0 0.0%	0 0.0%	0 0.0%	0 0.0%	0 0.0%	37 0.6%	702 11.9%	39 0.7%	0 0.0%	90.2% 9.8%
15	0 0.0%	0 0.0%	0 0.0%	0 0.0%	0 0.0%	0 0.0%	20 0.3%	694 11.8%	60 1.0%	89.7% 10.3%
16	0 0.0%	94 1.6%	0 0.0%	0 0.0%	0 0.0%	0 0.0%	0 0.0%	5 0.1%	672 11.4%	87.2% 12.8%
	NaN% NaN%	71.6% 28.4%	49.3% 50.7%	87.6% 12.4%	82.4% 17.6%	92.6% 7.4%	95.6% 4.4%	94.0% 6.0%	91.3% 8.7%	**83.0%** **17.0%**

Figure 3-39: Test confusion matrices of the neural network trained to distinguish between “no defect” (class “0”) and a defect location in the segments 1-8 (left) as well as confusion matrix of the network trained to distinguish between “no defect” and a defect location in the segments 9-16 (right) by means of sensor data obtained from the axial braiding ring during braiding with a simulated defect

Since the test accuracy is a measure of the ability of the network to generalize on unknown data, it can be seen as an indication of how the network will perform on data from a real production scenario. Against this background, it can be regarded as an affirmatory finding that neither of the independently trained networks for the axial braiding ring (cf. Figure 3-39) nor the networks for the radial braiding ring (not explicitly shown for reasons of similarity) assign any data tuples to output class “0”. This means that if a defect is present, it is never overlooked by the detection algorithms. In conjunction with a test accuracy in the range of 80-90 %, as the two separate networks achieve it, this can be seen as satisfactory for the task of detecting and localizing a defect in a segment of a braiding machine. However, it is striking that if the networks make a false prediction it is in the large majority of cases only one segment off the ground truth. This is an indication that the false predictions occur in the transition zones between the segments of the braiding machine. At this point, the combination of the two networks (one network predicting segments “1”-“8” and the other predicting segments “9”-“16”) comes into play.

The assumption that false assignments occur at the edges of the segments is underpinned when regarding the deviation of the prediction made by a single neural network on the independent data set from the fifth measurement with a simulated defect (cf. red line in the diagrams in Figure 3-40). In the diagrams, a segment deviation of 0 corresponds to a correct prediction, a segment deviation of +1 or -1 corresponds to a deviation of the prediction of one segment in clockwise or counter clockwise direction, respectively (direction of sight as in Figure 3-34). Since the vertical dotted lines correspond to transitions of the true defect location between two adjacent segments, it can be observed that the majority of false predictions of a single network predicting classes “1”-“8” occurs at the edges of the segments. This problem can be relieved by the combined prediction function and the overlapping segments of the braiding machine, which were already mentioned in the explanations corresponding to Figure 3-36 and Figure 3-37. If the class prediction of a data tuple is defined as the output of the two neural networks with the highest probability measure (output of the softmax neurons) the number of false predictions is further reduced (green line compared to red line in the diagrams in Figure 3-40). It can be observed that areas of false predictions along the mandrel either disappear completely or are reduced in length with the combined approach. Only in some isolated cases, the combined approach leads to a deviation by two segments or to false predictions by one segment where there would be none if only a single network was used. The remaining segment deviations of the combined approach lie in the large majority of cases still either directly adjacent to one of the drawn-in transition lines between the segments 1-8 or exactly in the middle between two of these transition lines. Due to the fact that the two sets of segments overlap with each other, the latter case means that these false predictions of the combined approach occur at the transition between segments of the second set 9-16.

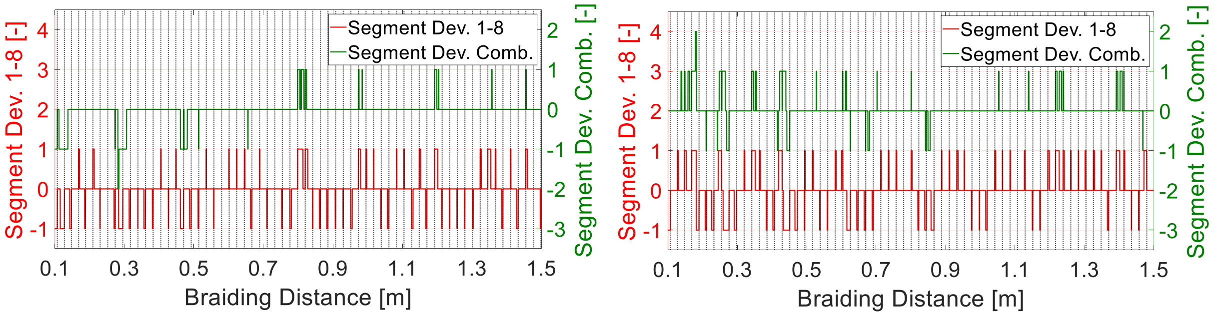

Figure 3-40: Segment deviation of a single network that predicts classes “1”-“8” (red) and of the combined prediction function (green) on independent test data acquired by the axial braiding ring (left) and the radial braiding ring (right) during braiding with a simulated defect; vertical dotted lines represent boundaries between the segments “1”-“8” of the braiding machine

The accuracies regarding segment prediction of the different approaches can only be estimated from Figure 3-40. The detailed accuracy figures of the two individual networks and the combined approach for both the axial and radial braiding ring are given in Table 3-4. It can be observed that the portion of incorrectly classified segments by the individual networks can roughly be halved when the combined approach is applied. Processing data from the axial braiding ring consistently results in a slightly higher accuracy of segment prediction than processing data from the radial braiding ring. As already mentioned above when the confusion matrices were explained, there are no false negative detections of any of the proposed algorithms. This means that when a simulated defect was present in the test data set, the networks reliably detected this. There was no occasion when a present defect was overlooked by the networks. At the same time, no false positive detections were observable for any of the algorithms. This means that data from the independent braiding experiments without a simulated defect was unexceptionally classified as defect-free. This is of vital importance because the data was gathered during the braiding experiments at a rate of 100 scans/s. Even a comparatively low false positive detection rate of only 0.1 % would cause a defect to be detected where there is none every 10 s during the braiding process. Hence, a regular braiding process would constantly be interrupted by the detection algorithm. From the data presented in Table 3-4, such a behavior cannot be expected. On the contrary, it can be expected that a defect alarm is only raised when there really is a defect present. If a defect is present, it can be expected that it is never overlooked. If a defect alarm is raised, then the segment prediction of the combined approach can be expected to be correct in about 90 % of the cases. After all, the low degree of complexity of the prediction function needs to be noted. The combined prediction function is only comprised of two shallow neural networks consisting of few neurons and is therefore expected to be executable in real-time on a microcontroller which could be retrofitted to any braiding machine.

Table 3-4: Accuracies of segment prediction, false negative and false positive rates for the networks processing data from the axial as well as from the radial braiding ring; data obtained by applying the networks to independent test data sets that were not used for training (defect-free and simulated defect, test data set 1)

	Axial Braiding Ring			**Radial Braiding Ring**		
	Accuracy Segment Prediction	False Negative Rate	False Positive Rate	Accuracy Segment Prediction	False Negative Rate	False Positive Rate
Network 1 Seg. 1-8	85.8 %	0 %	0 %	80.2 %	0 %	0 %
Network 2 Seg. 9-16	83.0 %	0 %	0 %	81.7 %	0 %	0 %
Combined Approach	92.2 %	0 %	0 %	90.7 %	0 %	0 %

Up to this point, the combined prediction function was tested on an independent data set obtained from braiding with a *simulated* defect. In the final step of the analysis of the proposed approach, the combined detection algorithms for both types of braiding rings shall be tested on data obtained from braiding experiments with a *real* fibrous ring (cf. test data set 2 in Figure 3-35).

The axial reaction forces as well as the behavior of the combined prediction function during braiding with a bobbin that showed a real fibrous ring are plotted in Figure 3-41, left. From the beginning up to approximately 0.25 m braiding distance, prominent fluctuations in reaction forces are observable. From 0.25 m on, the curves of the force sensing resistors qualitatively follow courses similar to those from the reference measurement as displayed in Figure 3-38, left. However, slight superimposed sinusoidal fluctuations can still be observed. The prediction function detects the real defect from the beginning of the test on and shows absolute deviations in segment prediction of no more than one segment. The segment prediction accuracy is 77.3 %. The prediction function is not plotted beyond approximately 0.25 m because this is the point at which the yarn that corresponds to the manipulated bobbin breaks. A similar picture of pronounced fluctuations in reaction forces in the beginning followed by more regular measurement curves is observable for the resulting radial reaction forces (cf. Figure 3-41, right). As with the axial forces, the combined prediction function reliably detects the real defect from the beginning on. The predicted segment of defect location is only one segment off the true segment. However, the portion of misclassified segments appears higher than in the axial case. The segment prediction accuracy from the data acquired by the radial ring until the yarn breaks is only 53.7 %.

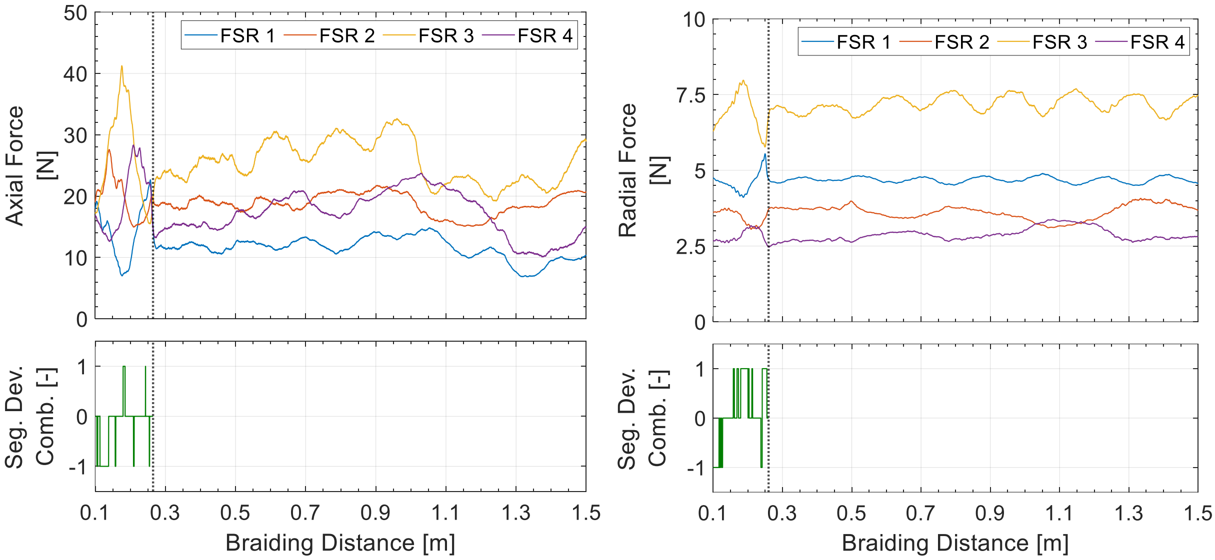

Figure 3-41: Measurement curves (top) and the behavior of the combined prediction functions (bottom) obtained from the axial (left) as well as from the radial braiding ring (right) during braiding with a bobbin that showed a real fibrous ring (test data set 2); different colors correspond to individual sensors; the vertical dotted lines mark the point at which the defective yarn breaks due to the fibrous ring

The fibrous ring, which was purposefully created at one braiding spool, hampered the unwinding process of the respective braiding yarn. The yarn tension increase of this single yarn caused the prominent fluctuations in reaction forces that are observable at the beginning of both braiding experiments. The algorithms detect the yarn tension increase without any false negative prediction. A prediction accuracy of 77.3 % in case of the axial braiding ring can still be regarded as satisfactory given the fact that any false segment prediction is only one segment off the true segment. The prediction accuracy of 53.7 % for the radial ring is considerably lower than for the axial ring. However, the false predictions are only one segment off the true location of the defect. Depending on the given use case (e.g. a braiding machine with ≤64 bobbins for a quick manual defect detection) this may still be an acceptable result. However, taking into account that the radial braiding ring also shows less sensitivity than the axial braiding ring especially at higher braiding angles φ (cf. Figure 3-30), the measurement of axial reaction forces appears more favorable over a measurement of radial reaction forces for the purpose of algorithmic defect detection. At approximately 0.25 m, the yarn with increased tension breaks. From then on, the curves of the reaction forces show slight periodic fluctuations because the broken yarn does not exercise any force on the braiding ring any more. Due to the lack of reaction force of the broken yarn on the braiding ring, the prediction function does not provide a meaningful result after the yarn breakage. This is because it was not trained for the case of a missing yarn. For this reason, the arbitrary behavior of the prediction function is not plotted beyond the point of yarn breakage in the above diagrams.

In the derivation and characterization of trainable defect detection functions above, the case of a balanced 2x2 braid was investigated because this braid interlacement structure is commonly used in braided composite parts. During braiding of such an interlacement structure on a radial braiding machine that features the widely spread type of horn gears with four grooves, one half of the braiding yarns always moves forwards and the other half backwards with respect to the production direction when the carriers travel between their reversal points (cf. Figure 3-22). As shown by the unfiltered measurement data in Figure 3-28, the back and forth movement of the yarns and the ratcheting mechanism in the carriers cause significant noise in the sensor signals. However, due to the opposite movement of the yarns with respect to the production direction, the effects on the reaction forces at the braiding ring still cancel out to a certain extent. In the introductory section 1.1, other interlacement structures such as a 3x3 interlacement as well as different braid architectures such as the UD-braid are mentioned. In such configurations and depending on the type of horn gears used, strongly fluctuating reaction forces that act onto the braiding rings are conceivable due to an uneven movement of the reinforcement yarns with respect to the production direction. Such cases and their effects on defect detection were not investigated in detail within the framework of this dissertation. From a theoretical standpoint, it can however be said that such fluctuations in reaction forces are not expected to prevent a defect detection by force sensors integrated into the braiding rings. The reason for this is that butterworth low-pass filters with a cut-off frequency of up to 1 Hz had to be used for removing noise from the sensor data within the scope of the above investigations anyway (cf. massive noise induced by shaker motors in Figure 3-38). Given typical speeds of horn gear rotation (under which it takes a carrier much less than 1s to travel between its reversal points), it appears plausible that such signal filters, possibly with adjusted cut-off frequencies, can also smooth out signal fluctuations due to an uneven movement of the braiding yarns. Moreover, when braiding rings are used in axial braiding machines, strong fluctuations in reaction forces can also be expected because of a deflection angle α of the yarns at the braiding ring that oscillates in a wider window than in radial braiding machines. Similarly, the deployment of sensor integrated braiding rings in axial machines for defect detection and localization is per se not precluded by the expectable strong fluctuations in reaction forces since real-time capable smoothing filters can be applied to the sensor signals.

As a summary of the investigations on the defect detection algorithms in the use case of overbraiding an S-shaped mandrel with trapezoidal cross-section, the following conclusions can be drawn:

- In contrast to overbraiding of a cylindrical mandrel, the response of the low-cost compression sensors varies along the braiding distance also in the case of the defect-free reference measurements. This is due to the fact that the S-shaped mandrel bends during braiding. Therefore, the mandrel is not always centrally guided through the braiding ring and the true haul-off speed of the mandrel with respect to the braiding ring cannot be kept constant.
- The axial braiding ring resolves these geometry-induced fluctuations in reaction forces better than the radial braiding ring. This is in line with the finding of a reduced sensitivity of the radial braiding ring – especially at higher braiding angles – from subsection 3.2.1.
- An effect of the trapezoidal cross section of the mandrel on the reaction forces could not be observed.
- The application of shaker motors to actuate the braiding ring caused significant noise in the sensor signals. However, this noise can reliably be eliminated by a butterworth low-pass filter and thus does not hamper an automatic defect detection by a trainable algorithm.
- For training a defect detection algorithm, the geometry-related fluctuations in reaction forces can be eliminated by referencing any measurement data at a given position on the overbraidable mandrel with the mean reaction forces during defect-free braiding at that particular position on the mandrel.
- Two shallow neural networks were trained for the two types of braiding rings (total of four networks) with sets of defect-free data and data recorded during braiding with a simulated defect:
    - When the networks were tested on independent data that was not used for training, no false positive or false negative detections were observable.
    - Particularly the fact of no false positive detections is an important finding because this suggests an interruption-free braiding when the process does not show a defect and the detection system is applied.
    - The accuracy in segment prediction of the neural networks can be improved by applying an approach of two combined networks that are trained independently on overlapping sets of segments of the braiding machine. This is due to the fact that false segment predictions mainly occur at the edges of the predefined machine segments.
    - When the combined prediction functions were tested on data from braiding tests with a real fibrous ring, they reliably detected that a defect was present. The algorithm processing the axial reaction forces however led to a higher accuracy in segment prediction.

- The satisfactory results regarding defect detection and localization demonstrate that even low-cost sensors of low accuracy can be used for process monitoring when a self-learning approach is applied. An important prerequisite is however that the measurements of the sensors are repeatable.
- Taking into account that the radial ring provides less sensitivity, particularly at larger braiding angles, and that the axial ring achieves higher values in prediction accuracy on both test data sets, the axial ring can be regarded as the more favorable solution for acquiring process data for the task of defect detection and localization (process monitoring).

3.3 Optical Inspection of the Braid Formation Zone

The newly invented concept of stationary Hall sensors that measure the position of the tension levers of the carriers as described in section 3.1 was shown to be able to precisely detect a defective bobbin before a reinforcement yarn breaks. However, the concept involves a dead time when a defective carrier is about to move from one sensor to the next. Depending on the number of stationary sensors used, a yarn gap may form in the preform before the process irregularity is detected. In order to eliminate the dead time, the approach of sensor integrated bobbin carriers was proposed in section 3.2. This complementary concept with its self-learning algorithm is however only able to identify a group of carriers which the defective carrier is part of. In this section 3.3, the idea of optically inspecting the braid formation zone is investigated. The idea conceptually opens the possibility to continuously monitor all braiding yarns (thereby eliminating any dead time) and at the same time to precisely spot a defective yarn.

The detection principle is described by Brockmanns et al. in their patent application [67]. When the braiding yarns exit the bobbins, they do not follow a straight line on their path to the braid formation point. Instead, the courses of the yarns are bent to a shape similar to an evolvent (cf. yarn marked with white-dotted line in Figure 3-42). This is due to the frictional interaction between the yarns of different directions of circulation through the braiding machine. Van Ravenhorst [35] and van Ravenhorst et al. [68] already developed a yarn interaction model for a detailed consideration of this effect within the framework of an overbraiding simulation of components with varying cross section. Besides the frictional interaction between the yarns themselves, friction between the yarns and the braiding ring is a further reason for the yarns not following a straight path towards the braid formation point. The detection concept relies on the fact that, during regular braiding, all braiding yarns are similarly tensed. The frictional forces in the braid formation zone result in similar curvatures of the yarns. This causes the yarns to be evenly spaced in the braid formation zone. As soon as a single yarn shows a higher tension, for instance due to a fibrous ring on its bobbin, its curvature is reduced due to the essentially unchanged frictional forces. Hence, the distance of the defective yarn to its preceding yarn in the same direction of rotation is reduced (cf. orange-marked area in Figure 3-42). In turn, the distance to its succeeding yarn is increased (cf. blue-marked area in Figure 3-42). This deviating distance between the yarns can be measured as a sign of a process irregularity.

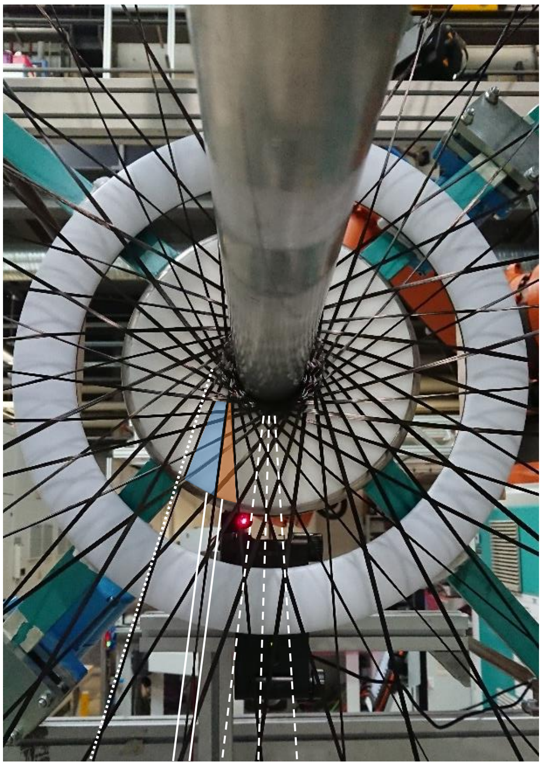

Figure 3-42: Braid formation zone of $n_{yarn} = 64$ carbon yarns of the type Tenax®-E HTS40 F13 24k in the RF 1/128-100 braiding machine; curvature of an exemplary yarn indicated by a tangential white-dotted line; yarn with elevated tension indicated by two solid white lines; reduced distance to the preceding yarn highlighted with orange color; increased distance to the succeeding yarn highlighted with blue color; exemplary centric white-dashed lines indicate possible positions of yarn intersection during regular braiding; image taken from own publication [90] and adapted from own publication [89]

Among other ideas in their patent application [67], Brockmanns et al. propose the use of an optical or a tactile sensor with an attached skid to measure the effect explained above at one discrete location in the braid formation zone. Since no experimental data or recommendations on the application of the measurement principle are given, its characteristics shall at first be investigated by means of a light barrier in subsection 3.3.1. In order to exploit the full potential of the detection concept without conceptual dead times, the approach of locally measuring yarn distances is subsequently extended a full coverage of the whole braid formation zone by a monitoring by camera in section 3.3.2. The measurement of yarn distances by light barrier was initially explored within a bachelor's thesis by the student Leoni Putze [59]. The acquired measurement data was presented to the public within the scope of the 20th European Conference on Composite Materials in Lausanne, Switzerland. Since the author of the dissertation at hand was the lead author of the corresponding conference paper [90], similar passages to the paper may occur in this section 3.3. The concept was further refined and extended to a full coverage of the whole braid formation zone within a term project by the student Maximilian Hilbck [91]. The full coverage of the braid formation zone was published in the paper [89] with the author of the dissertation at hand as lead author, which again may explain similar passages herein. Both student theses were conducted under the guidance and supervision from the author of the dissertation at hand. The author specified the tasks for both theses including the experimental test plan and conducted the braiding experiments together with the students. The MATLAB code for processing the raw data from the light barrier was initially written by Leoni Putze based on detailed instructions from the author of the dissertation at hand and modified by the author for the analysis purposes herein. The MATLAB code for an image analysis of the full braid formation zone was written by the author of the thesis at hand. The analysis of the processed measurement data presented herein was conducted independently by the author.

3.3.1 Discrete Monitoring by Light Barrier as Initial Investigation on the Detection Principle

The study presented in this subsection was intended to verify if the above-described detection principle by varying yarn curvatures is suitable for braiding process monitoring. It is demonstrated that an implementation of the detection principle by Brockmanns et al. [67] by means of a discrete light barrier is in principle capable of detecting anomalously tensed yarns. However, it is shown that, due to natural process fluctuations, the approach does not always guarantee a reliable defect detection. This is why the study within this subsection was conducted with limited scope. A more elaborate experimental analysis was carried out in subsection 3.3.2 on the continuous camera-based monitoring of the braid formation zone, since this allowed a more robust and reliable defect detection. Nevertheless, the author deemed it useful to elaborate on the limitations of the discrete monitoring approach in order to justify the need for a camera-based method.

Experimental Setup

In accordance with the standard braiding scenario specified for this thesis (cf. section 1.2), a cylindrical mandrel with a diameter of $d = 65\ mm$ and a length of $l = 1.5\ m$ was overbraided under braiding angles of $\varphi = \{30°, 45°, 60°\}$. For the experiments, the RF 1/128-100 braiding machine at the Chair of Carbon Composites was equipped with 64 yarns of the type Tenax®-E HTS40 F13 12k from Teijin Carbon Europe GmbH. Due to the preliminary character of this initial investigation, the speed of horn gear rotation was set to a reduced speed of $r = 65\ rpm$. The shaker motors for an actuation of the braiding ring were applied. For testing a flawless reference, all yarns were tensed evenly by applying springs inside the tubes of the carriers with a rating of 350 g. Additional braiding tests with a simulated defect were conducted with three different levels of elevated yarn tension of a single braiding yarn. The elevated yarn tension was created by adding the screw-on barrel tensioner from section 3.2 (cf. Figure 3-26, right) to a single bobbin carrier that circulated in counterclockwise direction through the machine. The yarn from the respective carrier was wrapped 1.5 times around the barrel tensioner. The different levels of elevated yarn tension were created by changing the spring inside the tube of the carrier between ratings of 350 g, 600 g and 900 g. According to measurements conducted by Putze [59] with 12k carbon yarns on the unwinding test stand from subsection 3.1.1, the resulting yarn tensions listed in Table 3-5 were achieved with the different setups of the yarn brake.

Table 3-5: Resulting levels of yarn tension for the 12k carbon yarns depending on the application of barrel tensioner and different ratings of the carrier springs; values taken from supervised student thesis [59]

Number of wraps around barrel tensioner	Rating of carrier spring	Resulting yarn tension
0	350 g	~4 N
1.5	350 g	~20 N
1.5	600 g	~35 N
1.5	950 g	>45 N

Given the preliminary character of the experiments, each configuration was tested once. Due to the length of the mandrel, it however needs to be noted that several data points on the defective yarn passing through the light barrier could be generated from a single braiding test (three yarn transits for $\varphi = 30°$, five yarn transits for $\varphi = 45°$, nine yarn transits for $\varphi = 60°$). This way, a certain statistical basis could still be maintained. For reasons of a better overview, the test plan is given in Figure 3-43.

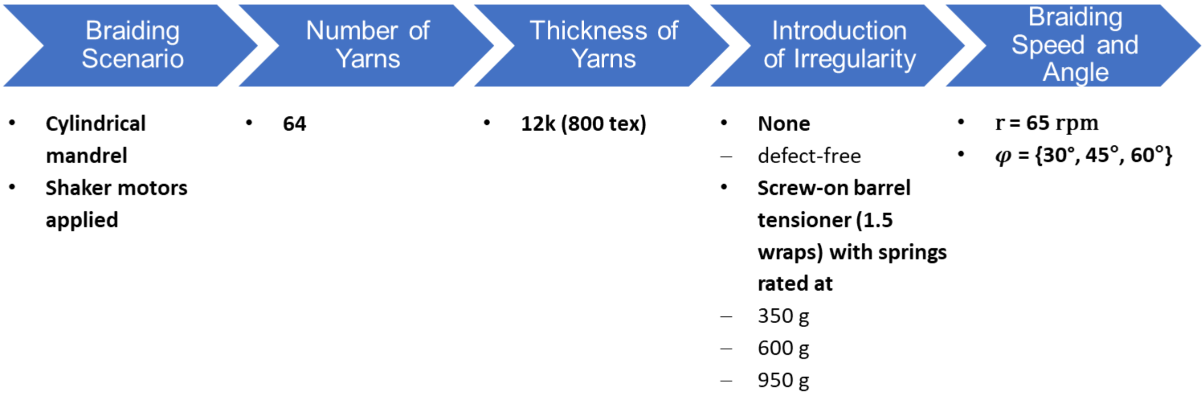

Braiding Scenario	Number of Yarns	Thickness of Yarns	Introduction of Irregularity	Braiding Speed and Angle
• **Cylindrical mandrel** • **Shaker motors applied**	• **64**	• **12k (800 tex)**	• **None** – defect-free • **Screw-on barrel tensioner (1.5 wraps) with springs rated at** – 350 g – 600 g – 950 g	• **r = 65 rpm** • **φ = {30°, 45°, 60°}**

Figure 3-43: Test plan for the characterization of the light barrier as means for optically inspecting the braid formation zone

The light barrier was made up of a DG650-1-5(12x34) laser from Picotronic GmbH as light source and a BPW46 photodiode from Vishay Intertechnology, Inc. as detector. The photodiode was operated in the mode of a photovoltaic cell. Its output voltage was measured by a USB-6910 data acquisition device from National Instruments Corporation at a rate of 1000 scans/s. In order to allow an automated peak detection by the "findpeaks"-function in MATLAB R2021a, the acquired data was smoothed by a moving average filter over ten data points. The light barrier was placed in a way that the laser beam intersected the plane of braiding yarns between the centric lines of yarn intersection (cf. dashed lines in Figure 3-50). Such a positioning of the light barrier is required in order to be able to resolve each individual braiding yarn when it shades the laser light. The data shown in the subsequent results section was acquired with the photodiode being placed directly behind the plane of braiding yarns at a distance of approximately 15 cm to the center of the machine. The laser was placed at the opposite side of the plane of braiding yarns at a distance of about 1.5 m. Thereby, the laser could be focused to a diameter of approximately 0.5 mm by means of its internal focusing lens. This enabled a precise detection of the braiding yarns, which move in circumferential direction through the light barrier during the braiding process. Note that the opposite arrangement in Figure 3-50 with the laser being placed directly behind the plane of braiding yarns is for illustration purposes and a proper visibility of the laser light in the image only. In order to be able to explain anomalous measurement signals, the braid formation zone was additionally recorded by a Nikon D3300 SLR camera.

Results and Discussion

Figure 3-44, left shows exemplary data acquired by the photodiode during flawless braiding at an angle of $\varphi = 45^\circ$. It is observable that the photovoltage saturates at approximately 0.48 V upon full exposure to the laser light. Each time a yarn passes through the laser and thereby shades it, a drop in the photovoltage occurs (cf. automatically generated marks by red circles). As explained above, the laser beam is positioned between the imaginary lines of yarn intersection. This is why every second drop in photovoltage corresponds to a yarn of the same direction of circulation through the machine. Exemplary time intervals between successive transits of two yarns of the clockwise (C) and counterclockwise (CC) direction are indicated in Figure 3-44, left with I_C and I_{CC}, respectively. In Figure 3-44, right, the interval duration per direction of yarn circulation is plotted against the braiding distance on the cylindrical mandrel. The diagram area shows five 360°-revolutions of the braiding yarns through the braiding machine, which corresponds to a braiding distance of approximately 1 m. For reasons of settling effects at the beginning of braiding, the first 30 cm of braiding are excluded from the diagram and also from any further evaluation. It is noticeable that even though the process was running regularly, there are considerable naturally occurring deviations from the mean in the yarn transit intervals in both directions of yarn circulation.

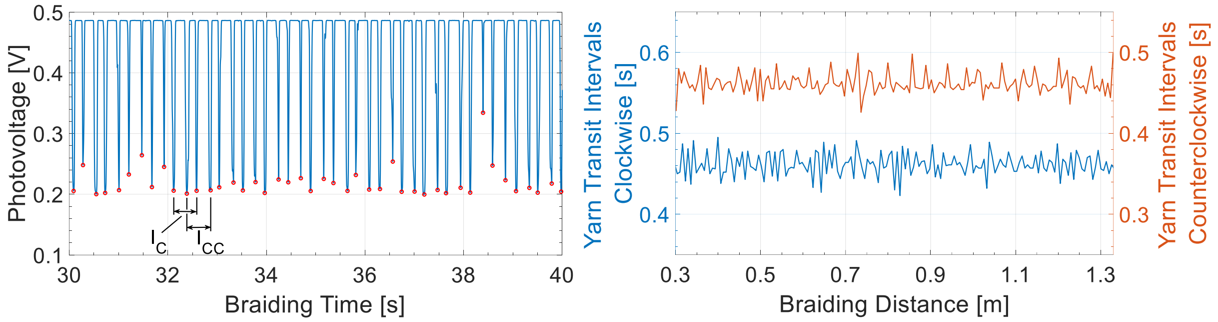

Figure 3-44: Measurement data from the photodiode during flawless braiding at an angle of $\varphi = 45^\circ$ (left) and calculated yarn transit intervals per direction of circulation (right); diagrams taken from own publication [90]

Results from braiding at an angle of $\varphi = 45^\circ$ and with elevated tension of a single yarn in counterclockwise direction are illustrated in Figure 3-45. The diagram on the left shows the case of an elevated tension of ~20 N. The transit intervals that correspond to the defective yarn are marked with red circles in the data for the counterclockwise direction. From these marks, it can be seen that a comparatively short interval that precedes the transit of the defective yarn is directly followed by a longer interval that succeeds the defective yarn. However, given the natural fluctuations of the intervals, this defect-related pattern cannot clearly be identified from the scattered data. In the case of the elevated tension of a single yarn being set at ~35 N (cf. Figure 3-45, right), this pattern is much more accentuated. Additionally, also the measurement data from the opposite (clockwise) direction shows an anomaly. Approximately 2 cm in braiding distance after each defect-related pattern in counterclockwise direction, a particularly long yarn transit interval is directly followed by a short interval in clockwise direction. Moreover, at a braiding distance of approximately 1.25 m, an isolated strong disruption in the measurement results to extremely high measurement values is observable both in clockwise and counterclockwise direction.

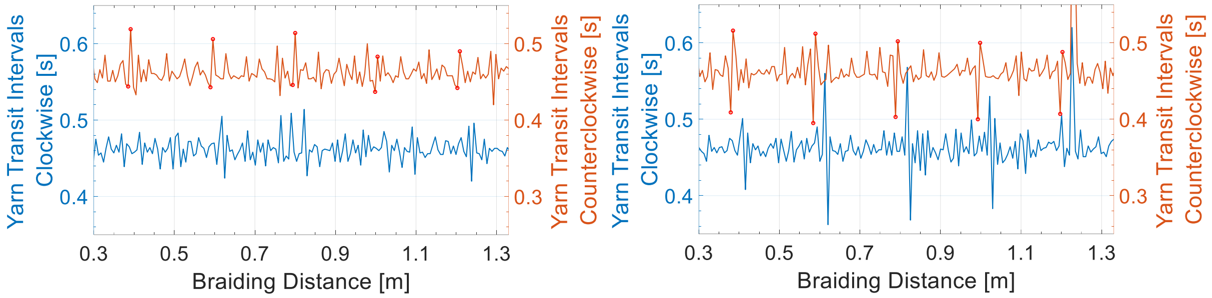

Figure 3-45: Yarn transit intervals per direction of circulation under a braiding angle of $\varphi = 45°$ and an elevated yarn tension of a single yarn of ~20 N (left) and ~35 N (right); diagrams taken from own publication [90]

The fluctuations in the measurements of the yarn transit intervals during regular braiding can be explained by naturally occurring process fluctuations in combination with the discrete detection method. Firstly, due to the ratcheting mechanism on the carriers that maintains the yarn tension in a predefined window, the tension of each yarn is technically not constant but fluctuates during the process. This may cause varying yarn curvatures during braiding. Secondly, due to the comparatively large free length of approximately 1 m between the bobbin carriers and the braiding ring of the RF 1/128-100 braiding machine, the frictional interaction between the yarns is to some degree an undefined process. It may always be the case that a specific yarn sticks to a yarn going the opposite direction, e.g. due to early stages of a spider's web (cf. Figure 2-4, left). The characteristic pattern of a yarn with elevated tension provoking a short transit interval that is directly followed by a long transit interval is well explained by the description to Figure 3-42. The defective yarn shows less curvature and the distance to its preceding yarn is therefore reduced (short transit interval). In turn, its distance to the succeeding yarn is increased (long transit interval). This shows that the detection method by light barrier is in principle capable of detecting anomalously tensed yarns. The anomaly of a long transit interval being directly followed by a short transit interval in the opposite direction of yarn circulation can be explained by analyzing the video recording from the braid formation zone during the experiments. At the point where the defective yarn is deflected at the braiding ring, it interacts with a yarn from the opposite direction and holds it back (cf. Figure 3-46, left). This is why the distance of the influenced yarn to its preceding yarn is increased and its distance to the succeeding yarn is reduced. This is reflected by the succession of a long transit interval by a short transit interval in the measurement data (opposite as with a yarn of too high tension). This effect of holding back a yarn of the opposite direction can be so extreme that two yarns of opposite directions intersect exactly on the laser beam, even though the laser was placed between the lines of yarn intersection during regular braiding (cf. dashed lines in Figure 3-42). Such a situation is shown in Figure 3-46, left. The intersection point between the held-back yarn (marked by two white-dotted lines) and a yarn from the opposite direction happens to coincide with the point where the laser beam intersects with the braid formation plane. In such a case, there is only one drop in photovoltage that can be detected. This however severely disrupts the calculation of the transit intervals per direction of circulation because an automated detection algorithm has no possibility of knowing that one drop in photovoltage actually corresponds to the transit of two yarns at once. This causes the disruption in the measurement data that is visible in Figure 3-45, right at 1.25 m braiding distance. In the said diagram, this confusion of the detection algorithm even causes the assignment of clockwise and counterclockwise transit intervals to be swapped and therefore being wrong from 1.25 m braiding distance onwards. Such a behavior questions the suitability of the presented discrete monitoring of yarn transit intervals for a reliable defect detection during braiding.

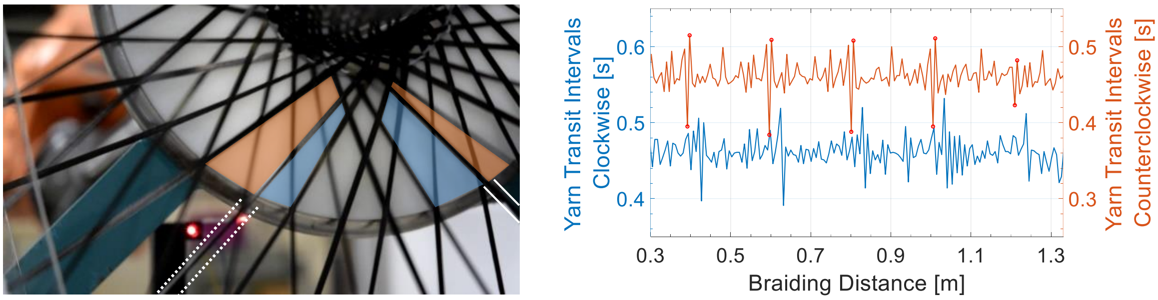

Figure 3-46: Still image of the braid formation zone during the experiment at $\varphi = 45°$ and an elevated tension of a single yarn of ~35 N (left); yarn with elevated tension marked with two solid white lines; influenced yarn of opposite direction indicated by two white-dotted lines; intersection point of the said yarns happens to coincide with laser beam; yarn transit intervals per direction of circulation during braiding at $\varphi = 45°$ and an elevated tension of a single yarn of >45 N (right); diagram on the right taken from own publication [90]

For a completion of the diagrams on the test series on a braiding angle of $\varphi = 45°$, Figure 3-46, right shows the measurement data from the braiding experiment with the highest level of induced tension of a single yarn (>45 N). In principle, the same periodically occurring pattern of a short transit interval being directly followed by a long transit interval indicating the presence of a yarn with too high tension in counterclockwise direction can be observed (cf. red circles in Figure 3-46, right). At a braiding distance of approximately 1.2 m however, this defect-characteristic pattern can hardly be distinguished from naturally occurring fluctuations. As in Figure 3-45, right, an interference of the yarn with elevated tension with yarns of the opposite (clockwise) direction is observable by the direct succession of a particularly long by a short transit interval in the blue measurement curve.

The fact that the defect-characteristic pattern is hardly distinguishable from natural fluctuations at a braiding distance of approximately 1.2 m shows that even under the highest level (>45 N) of the predefined levels of elevated yarn tension, naturally occurring process fluctuations may even out a defect-characteristic change in yarn curvature. This effect is best visible in a recording from the braiding experiment at $\varphi = 60°$ and an elevated yarn tension of ~35 N (cf. Figure 3-47). In the image on the left, it is observable that the yarn with the elevated tension causes the characteristic small (orange) and larger (blue) yarn distances. In the image in the middle however, right when the defective yarn passes through the light barrier, this characteristic distribution of yarn distances disappears due to natural fluctuations and therefore cannot be detected as anomalous. After the defective yarn has passed through the light barrier in the right image, the expected yarn distances are restored again. From these images, it becomes apparent that a discrete monitoring of the yarn distances is strongly influenced by naturally occurring process fluctuations and therefore constitutes another point that questions the suitability of the presented method for braiding process monitoring.

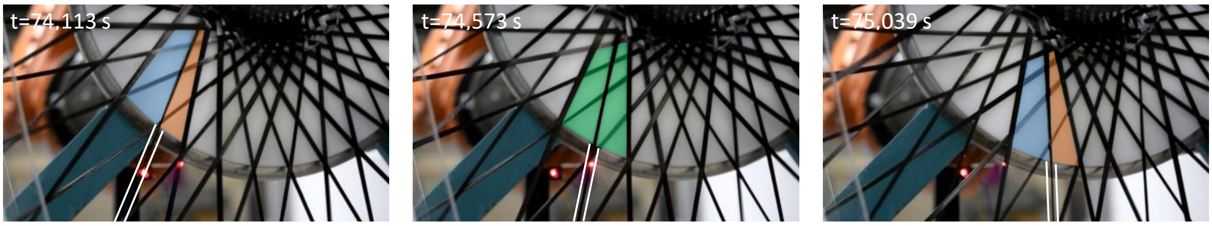

Figure 3-47: Succession of still images during braiding at $\varphi = 60°$ with an elevated tension of a single yarn of ~35 N; yarn with elevated tension marked by two solid white lines; time specification t from the corresponding video file; sequence of images found by Putze in her student thesis [59] supervised by the author

A third and final point that negatively affects a correct defect detection by a stationary optical sensor can also be observed when analyzing the braiding experiment at $\varphi = 60°$ and an elevated yarn tension of ~35 N. As illustrated in Figure 3-48, a clockwise yarn (C-Yarn) is detected first (left image, drop in photovoltage at 165.9 s in the diagram), then the defective yarn passes through the light barrier (drop in photovoltage at 166.0 s in the diagram) and eventually the clockwise yarn that had already been detected is pulled backwards by the defective yarn and shades the laser again (image in the middle, drop in photovoltage at 166.1 s). This affects the calculation of the yarn transit intervals and also the assignment of the drops in photovoltage to clockwise and counterclockwise yarns. One could argue to introduce a threshold criterion below which a drop in photovoltage is regarded to indicate a yarn transit. Such a criterion would however not completely solve the described detection problem because it is simply a coincidence that the pulled-back yarn only partly shades the laser in the shown case.

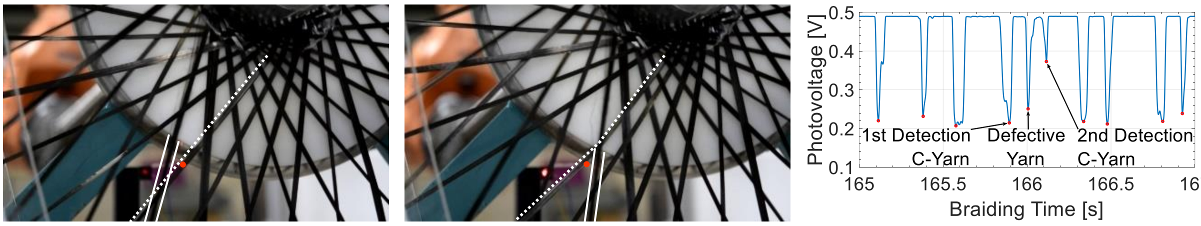

Figure 3-48: Still images during braiding at $\varphi = 60°$ and an elevated yarn tension of ~35 N of a single yarn (left and middle); yarn with elevated tension marked by two solid white lines; clockwise yarn that is detected twice marked by a white-dotted line; note the kink of the yarn/the white-dotted line in the image in the middle; for reasons of a better visibility of the laser light on the carbon yarns, it is drawn-in manually by a red dot; corresponding measurement reading from the photodiode (right)

Further data on the other braiding experiments from this preliminary test series is not presented in the main part of this dissertation. The reason for this is that the other tests did not show any new effects than the ones already described above. Nevertheless, a short analysis on the yarn transit intervals per braiding angle and level of elevated yarn tension is included in appendix A. It shall reassure the reader that the detection method by yarn curvatures is not negatively affected by a change in braiding angle φ.

As conclusions from the preliminary test series on the defect detection principle by yarn curvatures, the following statements can be made:

- Due to frictional interaction between the braiding yarns themselves and the braiding ring, the braiding yarns do not show a straight but a curved, evolvent shape between their exit points at the carriers and the braid formation point.
- Anomalously tensed yarns show different yarn curvatures than the other regularly tensed braiding yarns. This results in different distances of the braiding yarns in the braid formation zone.
- In principle, the resulting deviations in yarn distances have shown to be detectable by a discrete light barrier in the braid formation zone and therefore can be used as an indication of braiding defects.
- Due to the discrete nature of the applied monitoring approach however, natural process fluctuations may impede the detection of anomalies in the braid formation zone. This is particularly the case when smaller anomalies (low levels of yarn tension increase) are present. However, in isolated cases, natural process fluctuations may even out defect-characteristic patterns right at the moment when the measurement of the defective yarn takes place even at high levels of yarn tension increases.
- The yarn detection by a discrete sensor and a corresponding algorithm may further be confused by interactions between the defective yarn and yarns of the opposite direction of circulation (held or pulled-back yarns). This results in strong disruptions of the measurement data and falsifies the assignment of the direction of circulation of the yarns.

3.3.2 Continuous Monitoring by Camera as Verified Configuration of the Detection Principle in a Near-Production Environment

From the data on possible disruptions shown above, a discrete inspection of the braid formation zone by a single sensor such as a light barrier does not appear to be a reliable method for detecting anomalous yarn tensions during braiding. Nevertheless, since the detection principle has shown to be in principle functional, the author further advanced the optical inspection of the braid formation zone to a monitoring by camera because this opens the possibility to keep all braiding yarns under surveillance of a single sensor at any time during the process (no significant conceptual dead time as with stationary Hall sensors from section 3.1) while still being able to precisely indicate which yarn is the defective one to operating personnel that quickly has to resolve the error cause (not only indication of a group of possible carriers as with sensor integrated braiding rings from section 3.2). The main difference of the camera-based approach to the discrete monitoring by light barrier is that the video camera is able to gather up to 25 data points on each braiding yarn per second. This way, natural process fluctuations can be evened out by taking a short period (and therefore a statistically relevant basis of data points) of yarn distance measurements into account. Also, the described confusion of direction of circulation of the yarns cannot occur with the camera-based approach because this information can clearly be extracted from each video frame for each individual braiding yarn. The following subsection therefore describes the development of such a camera-based monitoring algorithm and gives a deepened experimental analysis on its capabilities.

Experimental Setup

For the development and characterization of the camera-based monitoring of the braid formation zone, a cylindrical mandrel with an increased length of $l = 2.5\ m$ was overbraided with carbon fiber yarns of the type Tenax®-E HTS40 from Teijin Carbon Europe GmbH under a braiding angle of $\varphi = 45°$ on the RF 1/128-100 braiding machine from HERZOG GmbH. The speed of horn gear rotation was set to $r = 130\ rpm$ and the shaker motors to actuate the braiding ring were used in order to reproduce and test the camera-based monitoring approach in a near-industrial use case. The increased length of the mandrel compared to the initial experiments on the light barrier from the subsection above was chosen in order to obtain a broader statistical basis of the measurement values. The braiding angle φ was not further varied because the initial experiments on the light barrier had shown that there was no negative influence of the braiding angle φ on the detection principle (cf. additional data in appendix A). Instead, the yarn thickness of the Tenax®-E HTS40 material was varied between filament counts of 6k (400 tex), 12k (800 tex), and 24k (1600 tex). The sizing of the 12k- and 24k-yarns was the same as specified in the standard braiding scenario for this thesis (F13 polyurethane sizing). The sizing of the 6k-yarns had to be changed to the E13 epoxy sizing because this yarn thickness is not produced with the F13 sizing by the manufacturer. The variation in yarn thickness was introduced because the author suspected different levels of frictional interaction between yarns of different titers, which may influence the detection principle by yarn curvatures. Additionally, the number of braiding yarns n_{yarn} was varied between $n_{yarn} = 32$ and $n_{yarn} = 64$. This variation was also introduced because of a suspected influence on yarn curvature and therefore on the capabilities of a possible camera-based inspection of the braid formation zone. A yarn number of $n_{yarns} = 128$ was also tested but had shown to not be evaluable by an algorithm because the yarns were located so closely together in the monitoring area that they could not reliably be distinguished from each other. A ring light as backlight illumination (cf. Figure 3-50) with a larger diameter in the order of 500 mm would have been required to be able to monitor an outer region of the braid formation zone where the yarns are spaced further apart from each other. Such a light source was however not available during preparation of the thesis at hand. This is why this maximum yarn number is left aside from the analysis herein. Finally, as with the initial experiments on the light barrier, four different levels of process impairments were investigated. These included no process impairment (regular braiding under a braiding yarn tension of approximately 4 N) as well as increased tensions of a single yarn of ~20 N, ~35 N and >45 N created by the screw-on barrel tensioner (cf. Figure 3-26, right and Table 3-5). The set out variations were carried out full factorially except for the fact that the 6k yarn could not be tested at elevated yarn tensions of ~35 N and >45 N because it repeatedly broke at these levels of yarn tension. Each configuration was tested once. Given the increased length of the mandrel of $l = 2.5\ m$ and accounting for a cut-off length of 30 cm to exclude settling effects at the beginning of braiding, a total of ten 360°-revolutions of the carriers through the machine could be taken into account for the analysis of measurement data from each configuration. According to formula (2-5), a full 360°-revolution of a carrier takes 7.38 s at a speed of horn gear rotation of $r = 130\ rpm$. Given the fact that the camera was set to record at 25 frames/s, this resulted in more than 1800 frames per experiment configuration that could be analyzed. For reasons of a better overview, the test plan is graphically reproduced in Figure 3-49.

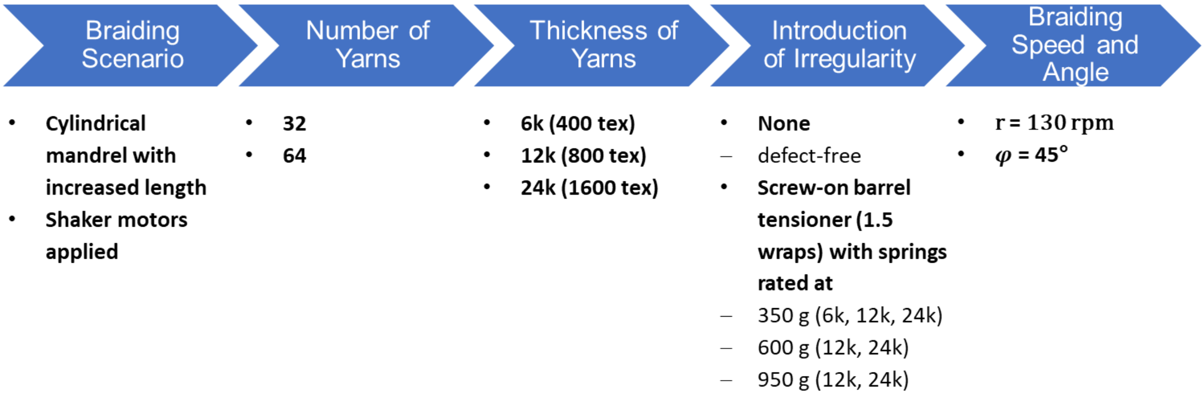

Figure 3-49: Test plan for the characterization of the camera-based monitoring of the braid formation zone

The overall setup of SLR camera, backlight illumination and braiding machine is depicted in Figure 3-50. The camera was placed at the side of the unbraided mandrel at a distance of approximately 3.3 m from the braid formation plane. As camera, a Nikon D3300 was used. It was set to record at 25 frames/s and at a resolution of 1920x1080 pixels. Given the chosen setting of the zoom, a resolution of the braid formation zone of $res_{bfz} = 1.62\ \frac{Pixel}{mm}$ was achieved. A backlight illumination by a ring light (also visible in Figure 3-42) in combination with camera settings of an ISO value of 400 and an aperture value of $\frac{1}{8}$ eliminated disturbing reflections from the shimmering sizing of the carbon yarns due to ambient light. The exposure time was set to 0.002 s for a clear, blur-free capture of the moving braiding yarns. This value was calculated under the premise that a braiding yarn must not move by more than one pixel during the exposure time. With view from the camera, the maximum speed of a braiding yarn $v_{yarn,max}$ occurs when its carrier is at its reversal point (cf. Figure 3-22 for definition of carrier reversal point). The maximum speed can be calculated by multiplying the circumference of the horn gear by the number of revolutions of the horn gear per time unit.

$$v_{yarn,max} = \pi \cdot d_{horn\ gear} \cdot r = \pi \cdot 225\ mm \cdot \frac{130\ \frac{1}{min}}{60\ \frac{s}{min}} \approx 1531.5\ \frac{mm}{s} \tag{3-16}$$

This maximum speed of a braiding yarn can, according to intercept theorems, be scaled down to the speed of the yarn at the outside edge of the ring light

$$v_{yarn,ring\ light} = v_{yarn,max} \cdot \frac{\frac{d_{ring\ light,outside}}{2}}{d_{horn\ gear-machine\ center}} \approx \approx 1531.5\ \frac{mm}{s} \cdot \frac{252.5\ mm}{1325\ mm} \approx 291.9\ \frac{mm}{s} \quad (3\text{-}17),$$

whereby $d_{ring\ light,outside}$ equals the outside diameter of the ring light and $d_{horn\ gear-machine\ center}$ the radial distance between horn gears and center of the braiding machine. The maximum allowed exposure time $t_{exposure,max}$ can be determined by referring the image resolution times the accepted error due to motion blur err_{blur} to the speed of the yarn at the outside edge of the ring light.

$$t_{exposure,max} = \frac{\frac{1}{res_{bfz}} \cdot err_{blur}}{v_{yarn,ring\ light}} \approx \frac{\frac{1}{1.62} \cdot \frac{mm}{Pixel} \cdot 1\ Pixel}{291.9\ \frac{mm}{s}} \approx 0.0021\ s \quad (3\text{-}18)$$

This can be rounded down to the next possible exposure time setting of 0.002 s. Possible vibrations of the braiding yarns are not considered in the derivation of the exposure time from above. However, in preliminarily acquired videos of the braiding process, no blur due to yarn vibrations was observable under an exposure time of 0.002 s.

Figure 3-50: Arrangement of the camera at the side of the unbraided mandrel and of the ring light as backlight illumination behind the braid formation plane of the RF 1/128-100 braiding machine; illustration adapted from own publication [89]

Derivation of the Image Analysis Algorithm

Figure 3-51, left shows an exemplary video frame acquired by the SLR camera during the braiding experiments according to the setup shown in Figure 3-50. Due to the comparatively short exposure time of the camera of 0.002 s, the image is dark expect for the regions illuminated by the ring light. This way, disturbing light reflections from the fiber sizing are eliminated. The video frames were processed using a Script written in MATLAB R2021a. Its image analysis operations can be subdivided into the three steps pre-processing, main processing and post-processing (visualization). In the pre-processing step, a video frame is first complemented by the “imcomplement”-function and then binarized by the “imbinarize”-function. Thereupon, the image is cropped by circular masks so that only the illuminated part of the original video frame remains. The result of the pre-processing is illustrated in Figure 3-51, right. Additionally, the method for the main processing is drawn-in. In this second step, the algorithm draws a pair of imaginary circles into the pre-processed image that are concentric to the ring light. The outer circle (cf. solid blue circle in Figure 3-51, right) is programmed to be 10 pixels larger in radius than the inner circle (cf. solid red circle in Figure 3-51, right). It is then checked how often both circles intersect with a white object (a braiding yarn). Three cases may occur from this plausibility check. The first case is when the number of intersections equals the number of braiding yarns for both circles. In this case, the main processing can continue. The second case is when the number of yarn intersections only equals the number of braiding yarns for the outer circle. In this case the previously outer circle is taken as the new inner circle and a new outer, concentric circle is drawn that is again 10 pixels larger in radius than the new inner circle. The check for the number of yarn intersections is then carried out again with this new pair of circles. The third case is when the number of yarn intersections does not equal the number of braiding yarns for the outer circle. This is the case in Figure 3-51, right. Two orange ellipses mark the area where the outer (solid blue) circle coincides with points of intersection of a clockwise and counterclockwise yarn. The number of intersections of this outer circle is therefore only 62 and does not match the number of braiding yarns $n_{yarn} = 64$. In this case, a whole new pair of inner and outer circle is drawn-in by the algorithm (cf. dashed circles in Figure 3-51, right). The radius of the new inner circle is 10 pixels larger than the previous outer circle. Again, it is checked if both circles intersect with as many white objects as there are yarns in the machine. Due to the width of the ring light, up to eight circles can be drawn-in and tested for yarn intersections.

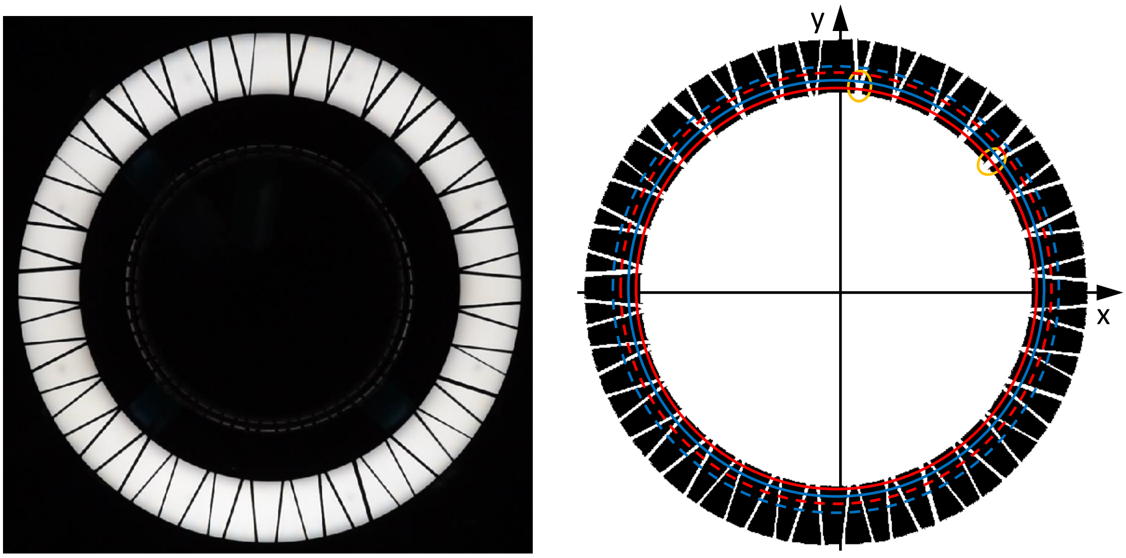

Figure 3-51: First video frame of the braid formation zone acquired during overbraiding of the cylindrical mandrel with $n_{yarn} = 64$ 12k carbon yarns and an increased tension of a single yarn of ~35 N (left); corresponding black-white image after pre-processing with exemplary circles drawn-in (not to scale) that intersect with the braiding yarns (right); outer circle of the first pair of circles (solid lines) coinciding with two points of yarn intersection marked by orange ellipses; illustrations from own publication [89]

If no pair of circles of which both circles intersect with as many white objects as there are braiding yarns in the machine can be found, the video frame is dropped and the next frame is pre-processed and enters the main processing. If such a pair of circles can be found, the main processing of the corresponding video frame continues. For each intersection object between yarn and imaginary circle, the center point is calculated by means of the "regionprops"-function in MATLAB R2021a. Exemplary intersection objects that originate from four clockwise and four counterclockwise yarns are shown in Figure 3-52, left. The corresponding center points are indicated by semi-transparent red (inner circle) and blue (outer circle) dots. For each center point on the inner circle, the corresponding center point on the outer circle is calculated by means of a nearest neighbor search ("knnsearch"-function in MATLAB R2021a). This step is intended to match pairs of center points that originate from the same braiding yarn in order to determine if a particular braiding yarn circulates in clockwise or in counterclockwise direction through the braiding machine. Plausibility checks in the form that the distance between assigned nearest neighbors must not fall below nine pixels or exceed 11 pixels are implemented. Such plausibility checks are of particular importance when intersection objects are close to a point of yarn intersection. If the plausibility check fails for a single pair of center points, the corresponding video frame is dropped and the next frame is processed. The determination of the direction of circulation of the braiding yarns is carried out by comparing the polar angles $\theta \in]-\pi; +\pi]$ of the matched center points on the inner and outer circle. In Figure 3-52, the polar angle θ of the center points on the inner and outer circle are indicated by one exemplary pair of center points. The polar angle of the center point on the inner circle (red dot) is slightly smaller than the polar angle of the center point on the outer circle (blue dot). This means that the yarn must circulate in counterclockwise direction through the braiding machine. If the polar angle of the point on the inner circle was larger than the polar angle of the point on the outer circle, this would mean that the corresponding yarn must circulate in clockwise direction through the braiding machine. Exceptions due to the two center points being located at opposite sides of the negative x-axis (transition $-\pi \rightarrow +\pi$) are implemented in the MATLAB Script. If there are not $\frac{n_{yarn}}{2}$ assignments for both directions of circulation, the corresponding video frame is dropped and the next frame is processed. If there are $\frac{n_{yarn}}{2}$ assignments for both directions of circulation, the main processing continues by sorting the inner center points of each direction of circulation in ascending order of their polar angle. The angular distance of two neighboring yarns of the same direction of rotation is then calculated by the difference between two polar angles that are adjacent to each other in the array of the sorted angles. The angular distance of two counterclockwise (CC) yarns is indicated as $\Delta\theta_{1,CC}$ in Figure 3-52. This calculation is repeated for each pair of yarns and concludes the main processing of a video frame.

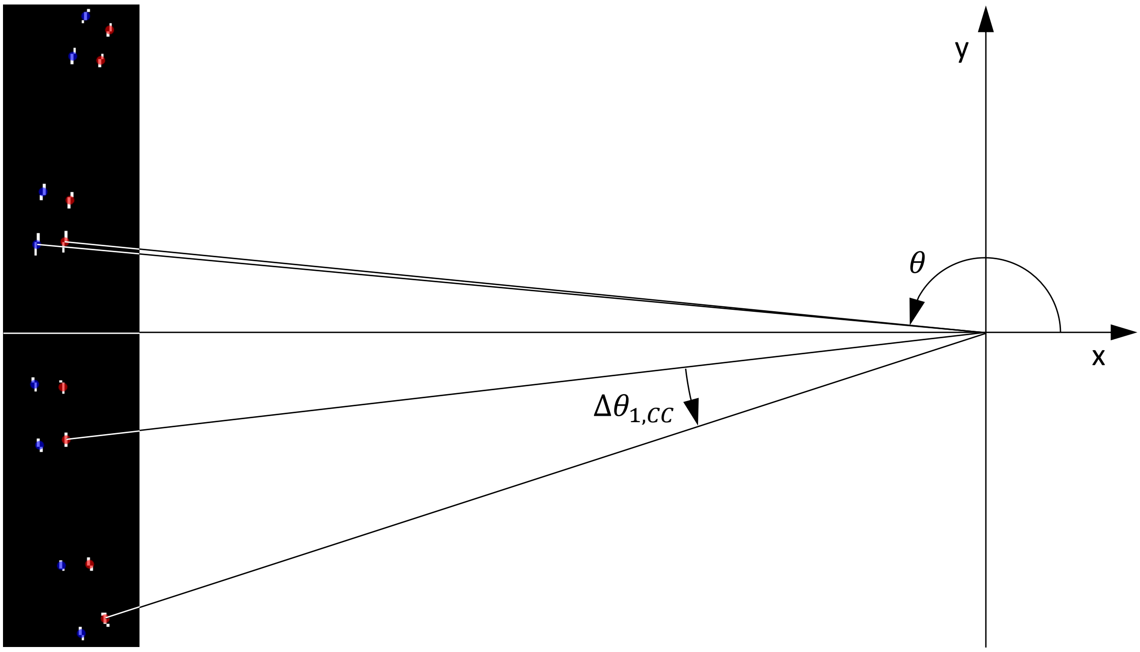

Figure 3-52: Determination of clockwise and counterclockwise yarns by polar angle θ as well as angular distance $\Delta\theta_{1,CC}$ between two yarns of the same direction of circulation; illustration from own publication [89]

The post-processing step involves the final averaging of the acquired data over several video frames, a visualization and the data storage. In order to exemplify the importance of the averaging step, the angular yarn distances $\Delta\theta_{i,CC}$ with $i = \left\{1; 2; \dots; \frac{n_{yarn}}{2}\right\}$ of the counterclockwise yarns from the first frames of the experiment with the 12k yarns and an increased tension of a single yarn of ~35 N are illustrated in Figure 3-53. On the x-axis, the numbers i of the yarn distances are plotted in ascending order (mathematically positive sense of rotation). The starting point ($i = 1$) is thereby defined as the $\Delta\theta_{i,CC}$ which completely lies in the third quadrant and is closest to the x-axis ($\theta = -\pi$). On the y-axis, the measurement value for each $\Delta\theta_{i,CC}$ is given in radians. In the data on the first frame at the top left, a distinct anomaly that stands out from the scattered measurement data is observable between the 24th and 25th yarn distance measurement. This hints at the presence of a yarn with elevated yarn tension due to a reduced distance to its preceding and an increased distance to its succeeding yarn. Note that the direct succession of a large yarn distance by a particularly short yarn distance does in this case not mean that a yarn with too low yarn tension is present (as it would have meant if this was data from the light barrier). The reason for this is that the angular yarn distances are ordered on the x-axis as they appear in the video frame from polar angles of $-\pi$ to $+\pi$ (mathematically positive sense of rotation). This in combination with the fact that the diagrams in Figure 3-53 show angular yarn distances of counterclockwise yarns explains that a yarn with elevated tension manifests by a direct succession of a long and short yarn distance. In the data on the second, fourth and fifth frame, the same anomaly as in frame one is present but it is more difficult to distinguish it from the scattered data. In frame 7 and 10, the defect-characteristic anomaly is not observable any more. In frames 11, 13 and 15, it becomes noticeable again, but remains difficult to distinguish from the scattered data. Apart from the unsteadiness in observability of the defect-characteristic data pattern, it can be observed that the defect-characteristic pattern travels from left to right (yarn distance numbers 24/25 in frame 1 to 27/28 in frame 15) through the diagrams of the presented sequence of video frames.

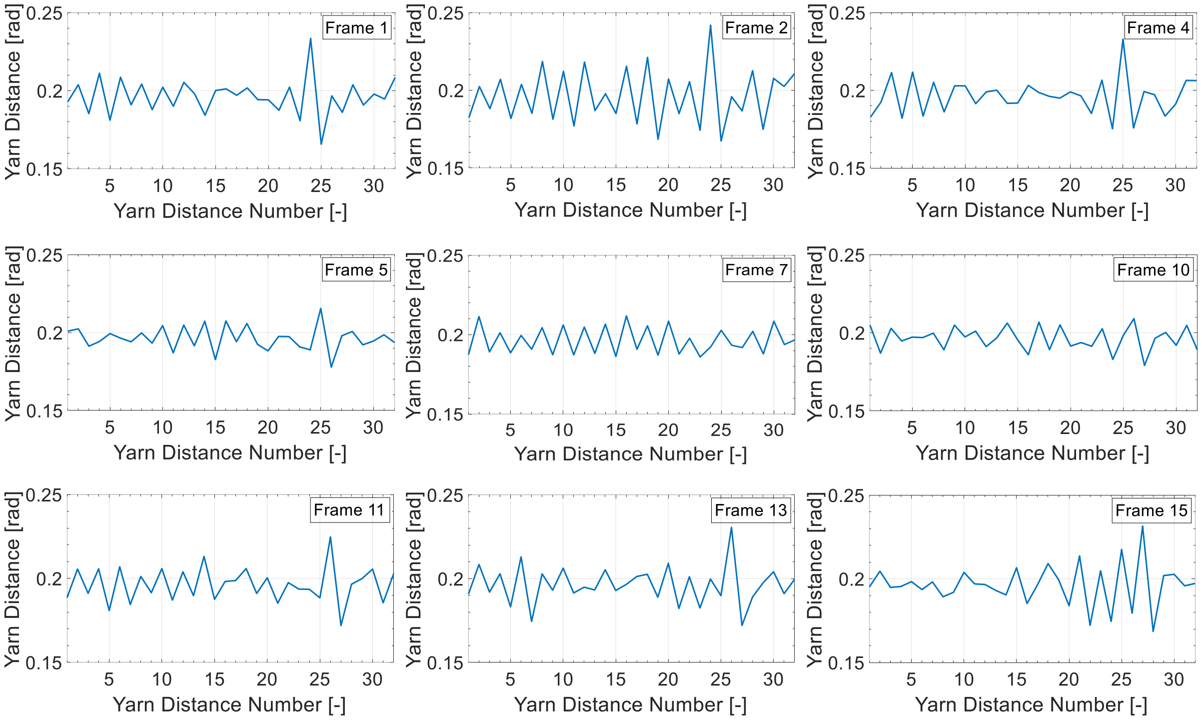

Figure 3-53: Angular yarn distances of the counterclockwise yarns for the first 15 video frames from the experiment with the 12k yarns and an increased tension of a single yarn of ~35 N; diagrams from own publication [89]

The fact that the frame numbers 3, 6, 8, 9, 12 and 14 are missing in the figure above is due to the fact that the analysis of these frames failed to pass one of the several plausibility checks explained above. These frames are therefore not taken into account for the post-processing step of the yarn detection algorithm. The defect-characteristic pattern propagating from left to right through the sequence of diagrams is explained by the ordering of the yarn distances along the x-axis in the mathematically positive sense of rotation in combination with the fact that the yarn with the elevated tension is part of the group of counterclockwise yarns. The unsteadiness in observability of the defect-characteristic data pattern reflects the influence that natural process fluctuations have on the yarn distances. This is why a monitoring of the yarn transit intervals by a stationary light barrier or an isolated analysis of a single video frame is not expedient. As a reassurance that this is not due to shortcomings of the measurement algorithm, the reader may consult Figure 3-55. This figure shows the graphical output of the measurement algorithm for the same video frames as discussed in Figure 3-53. On close inspection by eye, it can be observed that the defective yarn (marked with a yellow dot) shows a reduced distance to its preceding and an increased distance to its succeeding yarn in the frames 1, 2, 4, 5, 11, 13 and 15. In frames 7 and 10, a comparatively even distance of the defective yarn to its neighboring yarns can be observed. This in in line with the observability of the defect-characteristic pattern in the measurement data from the algorithm plotted in the diagrams in Figure 3-53.

In order to overcome the problem of observability and distinguishability of a defect-characteristic pattern from the scattered data, the yarn distance measurements for each yarn need to be averaged over several video frames. The idea behind this approach is that naturally occurring fluctuations in yarn distances should be normally distributed and should therefore even out when averaged over a longer period of braiding time. At the same time, systematic deviations from normally distributed fluctuations, such as due to a yarn with anomalous yarn tension, should remain observable and become more clearly detectable in an automated data evaluation step.

For an averaging over several video frames, it needs to be made sure that any measured yarn distance from different video frames is always assigned to the correct two braiding yarns. Mathematically, this problem translates into shifting the x-axis of the diagrams in Figure 3-53 in sync with the rotation of the braiding yarns through the machine. This way, a defect-characteristic pattern is always located at the same x-value in the yarn distance diagrams. Such a shift or offset of the x-axis could be calculated by

$$offset = round\left(\frac{\frac{n_{frame}}{frame\ rate}}{t_{360°}} \cdot \frac{n_{yarn}}{2}\right) \qquad (3\text{-}19),$$

whereby n_{frame} is the number of video frames since the beginning of the measurement and $frame\ rate$ is the number of frames the camera records per time unit. Such a simplified approach is however prone to assignments of yarn distance measurements that are one yarn off the true pair of yarns that the measurement value should be assigned to. This is due to the fact that the yarns vibrate and therefore their distances naturally fluctuate. Particularly when the offset value is about to change its value, such wrong assignments occur. This leads to the result of the averaging step to be inaccurate. In the graphical output of the measurement algorithm as shown in Figure 3-55, such a problem would express itself in a yellow dot, which marks the defective yarn in a video frame, toggling between two neighboring yarns in a sequence of video frames.

As solution to this problem, the offset value $offset_{n_{frame}}$ for the n-th frame since the beginning of the measurement is calculated by the following set of formulas in the video processing script in MATLAB R2021a.

$$\theta_{i=1,CC,n_{frame}=1,mean} = mean\left(\theta_{i,CC,n_{frame}=1} - \frac{2\pi}{\frac{n_{yarn}}{2}} \cdot (i-1)\right), \quad whereby\ i = \left\{1; 2; \dots; \frac{n_{yarn}}{2}\right\} \tag{3-20}$$

$$\theta_{i=1,CC,n_{frame},expected} = = wrapToPi\left(\theta_{i=1,CC,n_{frame}=1,mean} + \frac{\frac{n_{frame}}{frame\ rate}}{t_{360°}} \cdot 2\pi\right) \tag{3-21}$$

$$Index_{n_{frame}} = knnsearch\left(\theta_{i,CC,n_{frame}}, \theta_{i=1,CC,n_{frame},expected}\right), \quad whereby\ i = \left\{1; 2; \dots; \frac{n_{yarn}}{2}\right\} \tag{3-22}$$

$$offset_{n_{frame}} = Index_{n_{frame}}(1) - 1 \tag{3-23}$$

Firstly, the polar angle of the yarn in the third quadrant closest to the x-axis (“first yarn”, $i = 1$) is determined for the first frame ($n_{frame} = 1$, beginning of the measurement). Since a simple measurement of this angle $\theta_{i=1,CC,n_{frame}=1}$ may be influenced by a vibration of this particular yarn, the angle $\theta_{i=1,CC,n_{frame}=1,mean}$ is calculated as a mean of the polar angles of all braiding yarns corrected by the theoretical yarn spacing. Thereby formula (3-20) eliminates any arbitrary displacement of the first yarn due to its manufacturing process inherent vibration. Secondly, in formula (3-21), the expected polar angle $\theta_{i=1,CC,n_{frame},expected}$ of this first yarn (which has now moved to a different position) at frame number n_{frame} is calculated. The obtained value is projected to the interval $]-\pi; +\pi]$ by the MATLAB function “wrapToPi”. Thirdly, among the measured polar angles in the n-th frame $\theta_{i,CC,n_{frame}}$, the closest match to the expected position of the first yarn ($i = 1$) from the first frame is determined by the “knnsearch”-function. Since the polar angles $\theta_{i,CC,n_{frame}}$ are also sorted in ascending order from $-\pi$ to $+\pi$, the index of the found closest point minus 1 gives the value for $offset_{n_{frame}}$. The negative of this offset value is used in the “circshift”-function in MATLAB to keep a propagating defect-related anomaly stationary with respect to the x-axis in the diagram of angular yarn distances. Note that the above formulae (3-20)-(3-23) are written for the case of inspecting counterclockwise yarns (subscript CC). In case the offset value for clockwise yarns shall be determined, the polar angles θ_C need to be used accordingly and the “+”-sign in formula (3-21) needs to be replaced by a “–“-sign due to the different direction of yarn circulation. Moreover, not the negative but the positive offset value $offset_{n_{frame}}$ needs to be inserted into the “circshift”-function in case of monitoring clockwise yarns.

For an illustration of the approach of averaging the distance measurements for each yarn over several video frames, the said average is calculated for the nine frames shown in Figure 3-53 and depicted in the diagram in Figure 3-54. The x-values and therefore the position of the defect-characteristic pattern is corrected according to the above formulae (3-20)-(3-23). In the figure, it is observable that the scatter that is present in numerous of the diagrams in Figure 3-53 has already significantly evened out over the sequence of nine video frames. Additionally, the defect-characteristic pattern of a large yarn distance being directly followed by a small yarn distance can clearly be distinguished from the other averaged distance measurements. In the following results section, the prominence of this pattern (distance between defective and succeeding yarn minus distance between defective and preceding yarn, drawn-in with a double arrow in Figure 3-54) is used as a comparable measurement output of the different experiment variants.

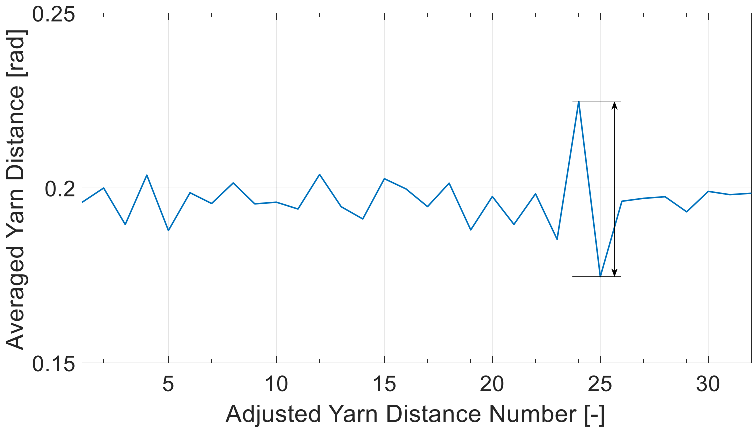

Figure 3-54: Averaged yarn distances calculated over the nine diagrams shown in Figure 3-53; yarn distance numbers referenced to frame number 1 in Figure 3-53; prominence of defect-characteristic pattern marked by a double arrow; diagram from own publication [89]

The defective yarn can be marked in the original video frames according to the x-values of this characteristic pattern in the averaged data. This was carried out in Figure 3-55 for the nine frames that were processed for Figure 3-53 and Figure 3-54, respectively. Based on the comparison of polar angles between center points on the inner and outer circle, clockwise yarns are marked by red and counterclockwise yarns are marked by blue dots. The defective yarn is indicated by a yellow dot. It can be observed that over the sequence of the frames, the radii of the circles of the colored markings change. Whereas for frames 2, 4, 5, 10, 11 and 13, the markings are close to the inner diameter of the ring light, the markings for frames one, seven and 15 are located further outwards. This is due to the search for a pair of circles from which each circle intersects with the braiding yarns n_{yarn} times as illustrated in Figure 3-51, right. In the latter three frames, the yarns of opposite directions happen to intersect close to the inner diameter of the ring light, thereby causing less intersections with each circle of the innermost pair of circles than n_{yarn}. This forces the pairs of circles further outwards until they both intersect with the braiding yarns n_{yarn} times. With the complete background on the developed measurement algorithm, the reader can now understand that it is crucial to assign each yarn its correct direction of rotation. In the way this was implemented, this can only be achieved if for each center point of an intersection object on the inner circle there is a one-to-one match on the outer circle. It can further be observed in Figure 3-55 that the yellow-marked defective yarn moves in counterclockwise direction over the course of the sequence of frames. As already mentioned in the explanation to Figure 3-53, the defect-characteristic distances to the neighboring yarns can particularly be observed in frames of the first and third row.

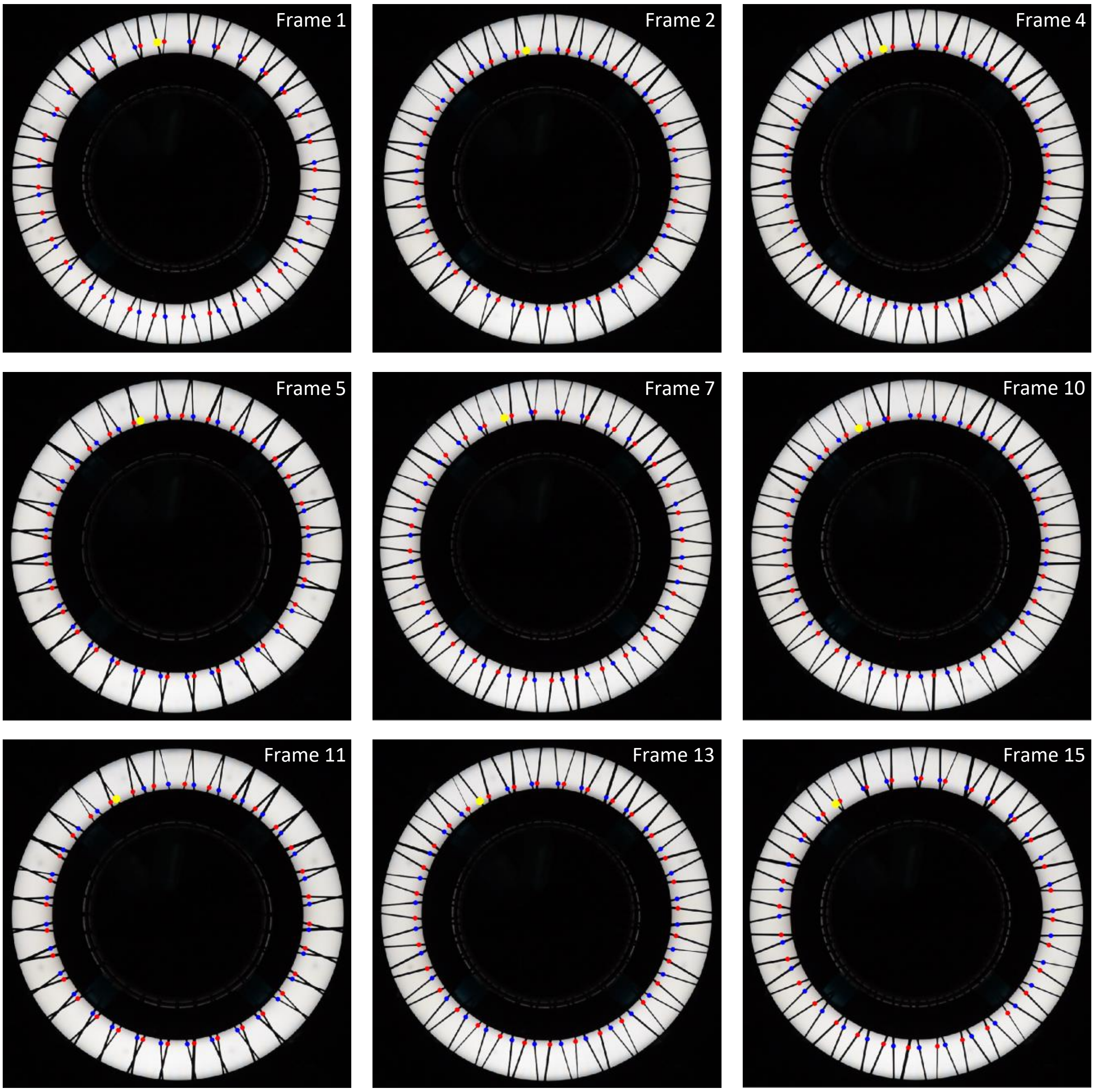

Figure 3-55: Graphical output of the yarn distance measurement algorithm for the first 15 video frames from the experiment with the 12k yarns and an increased tension of a single yarn of ~35 N; clockwise yarns marked by red dots; counterclockwise yarns marked by blue dots; yarn with increased tension marked by a yellow dot; images from own publication [89]

The reader may argue that the described detection algorithm only works when cylindrical mandrels are overbraided because only in these cases, the whole braid formation zone is visible. This is however not the case. The algorithm can be modified in a way that it separately measures the yarn distances in three quarters of the braid formation zone. If the view from the camera to one, two or even three quarters of the braid formation zone is obstructed, the modified algorithm can still measure the yarn distances in the remaining quarter(s). Also, the automatic assignment of measurement values to the correct moving yarn is guaranteed because the offset calculation as shown in formulas (3-20) to (3-23) remains essentially unchanged. For additional data on this modified version of the algorithm, the reader is referred to appendix A.

Results and Discussion

Parts of the results on braiding with the 12k yarns under an elevated tension of a single yarn of ~35 N have already been exemplarily shown in the above section on the explanation of the image analysis algorithm. Figure 3-54 illustrates the result of averaging the optical measurement data from the first 15 frames. The prominence of the defect-characteristic pattern is drawn-in with a double arrow. In Figure 3-56, the averaged prominences of this pattern over the whole experiment are shown for the different test variants (braiding distance of 2.05 m, mandrel length of 2.5 m minus an unusable length of approximately 15 cm minus 30 cm for cutting off settling effects at the beginning of braiding). Standard deviations are not drawn-in on purpose because in this particular case of scattered data, they do not provide any meaningful information. As can be seen from the diagrams in the second row of Figure 3-53, the defect-characteristic pattern of a large yarn distance followed by a short one is not present in all video frames. In some cases, the pattern is even reversed due to natural process fluctuations. Due to the definition of the value for the prominence of the (distance between defective and succeeding yarn minus distance between defective and preceding yarn), this value may in these cases even become negative. This results in enormous standard deviations which only reflect the extent of natural process fluctuations. Despite enormous standard deviations, the mean values for the prominence of the defect-characteristic patterns can still be used to at least derive trends in the measurement data because each mean value is calculated from data acquired over 1853 video frames. Some video frames fail to pass the plausibility checks implemented in the developed measurement algorithm but it can still be said that each mean value plotted in Figure 3-56 is calculated from more than 1000 acquired data points. Note that in case of the 6k yarns and increased yarn tensions of ~35 N as well as >45 N the bars are not actually missing but reflect the fact that this thin yarn could not withstand the higher levels of tension in the braiding experiments.

From the diagram in Figure 3-56, it can be observed that the mean values of the prominence of the defect-characteristic pattern are consistently smaller for the cases of $n_{yarn} = 32$ (light colors) than for the cases of $n_{yarn} = 64$ (intense colors). With increasing tension of the defective yarn, the prominence of the defect-characteristic pattern tends to increase, although the values for an increased tension of ~35 N do not consistently follow this trend. Comparing the prominence values of the same yarn number and yarn tension but for the different yarn thicknesses reveals an increase of the prominence of the defect-characteristic pattern with increasing yarn thickness in almost all cases. Only the data point on the 6k yarn and $n_{yarn} = 64$ does not fit into this trend.

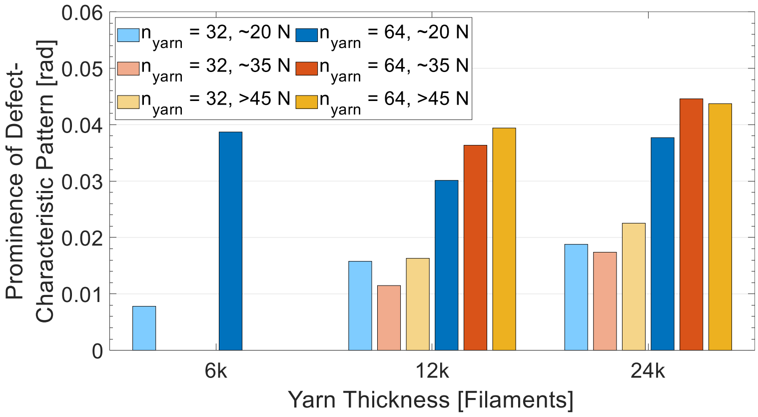

Figure 3-56: Prominence of defect-characteristic pattern averaged over a braiding distance of 2.05 m (1853 video frames) depending on yarn thickness, yarn number and tension of the defective yarn; diagram from own publication [89]

The observation of less prominent defect-characteristic patterns for the cases of $n_{yarn} = 32$ can be explained by the reduced number of frictional yarn-yarn interactions in the braid formation zone. Therefore, the yarns show less curvature. If a yarn is straightened by an elevated tension, the difference to its initial curvature is less for $n_{yarn} = 32$ than for $n_{yarn} = 64$. This results in a reduced prominence of the defect-characteristic pattern. The trend of increased defect-characteristic patterns with increased tension of the defective yarn can be explained by a more pronounced straightening of the defective yarn the higher its tension is. Similar to an increase in yarn number, an increase in yarn thickness appears to increase the curvature of normally tensed yarns. This can plausibly be explained by stronger frictional interactions between thicker braiding yarns. Firstly, the stronger frictional interaction may result from a more pronounced undulation (deflection at each yarn intersection point) of the thicker yarns in the braid formation zone. Secondly, also the contact area between thicker yarns is expected to be larger than between thinner braiding yarns, thereby also leading to increased frictional interaction. However, it cannot be ruled out that the barrel tensioner may brake thicker yarns more than thinner yarns due to a larger frictional contact area. The fact that the latter two trends are not exclusively followed by all data points hints at the influence of imperfect testing conditions. As will be shown in subsection 4.1.2, there is a slight dependency between the tension of a braiding yarn and the filling degree of its bobbin. A difference in yarn tension due to an uneven filling of the bobbins is even multiplied when the screw-on barrel tensioner is added to a carrier. Yarn tensions deviating from the expected level of tension could explain individual data points that do not follow the derived trends. Moreover, moisture is generally known to play an important role in frictional yarn-yarn interaction during braiding. The degree of moisture could however not be controlled in the environment of the production laboratory.

The results presented so far show that there are differences in yarn curvature that are created by anomalous tensions of individual yarns. The resulting deviation in yarn distances can well be detected by a camera-based monitoring in combination with the developed measurement algorithm. For the discrete measurement by light barrier, a reliable defect detection criterion could not be found due to natural process fluctuations such as vibrating yarns. In this paragraph, it is investigated if a yarn with anomalously high tension can automatically be detected in the acquired experimental data. For this, data from the defective measurements for each combination of yarn thickness and yarn number is compared to data from the defect-free measurement. From the defective measurements, the minimum of the prominence of the defect-characteristic pattern is calculated over moving average windows of different sizes. From the defect-free reference measurements, the maximum of the difference in yarn distance of any two neighboring yarns is also determined over moving average windows of different sizes. The purpose of the moving average windows is to eliminate or at least reduce natural process fluctuations (cf. data in Figure 3-54, which was averaged for each yarn over 15 frames). By calculating the minimum of the prominence of the defect-characteristic pattern over sliding windows of a certain size, an upper boundary for a defect detection threshold can be defined. By calculating the maximum of the difference in yarn distance of any two neighboring yarns from the flawless reference measurements, a lower boundary for a defect detection threshold can be defined. These boundaries shall be explained by means of the data shown on the braiding experiments with the $n_{yarn} = 64$ 12k yarns in the middle of Figure 3-57. If the moving average windows is chosen to be 500 frames long, the upper boundary (minimum of the prominence of the defect-characteristic pattern) would be approximately 0.026 radians (cf. solid line in dark blue). If the threshold for the distinction between defect-characteristic pattern or natural process fluctuation was set to 0.026 radians or smaller, no defect-characteristic pattern would have been missed in the corresponding experiment with the simulated defect (no false negative detection). This is because the smallest defect-characteristic pattern (minimum) that was observed during the experiment was of a size of 0.0266 radians. If we stick to the example of a moving average window of a length of 500 frames, the lower boundary (maximum of the difference in yarn distances of any two neighboring yarns from a defect-free reference measurement) would be approximately 0.017 radians (cf. solid line in black). If the threshold for the distinction between defect-characteristic pattern or process fluctuation was set to 0.017 radians or greater, no natural process fluctuation would have been declared as a defect-characteristic pattern in the corresponding reference experiment (no false positive detection). This is because the largest natural process fluctuation (maximum) that was observed during the reference measurement was of a size of 0.0166 radians. If the length of the sliding window is varied, an area between upper and lower boundary for the distinction threshold is opened (cf. transparent blue area). If any combination of length of averaging window and detection threshold is selected from that area, at least in the conducted experiments, no false positive or false negative detections would have occurred. When taking the data from the 6k (top diagram) and 24k yarns (bottom diagram) into account, it becomes apparent that the area between the minimum and maximum curves opens at significantly larger window lengths for the cases of $n_{yarn} = 32$ than for the cases of $n_{yarn} = 64$ (6k: ~600 frames compared to ~50 frames, 12k: ~1200 frames compared to ~200 frames, 24k: ~500 frames compared to ~200 frames). Also, the difference between upper and lower threshold boundary is considerably smaller for $n_{yarn} = 32$ than for $n_{yarn} = 64$ over all three tested yarn thicknesses.

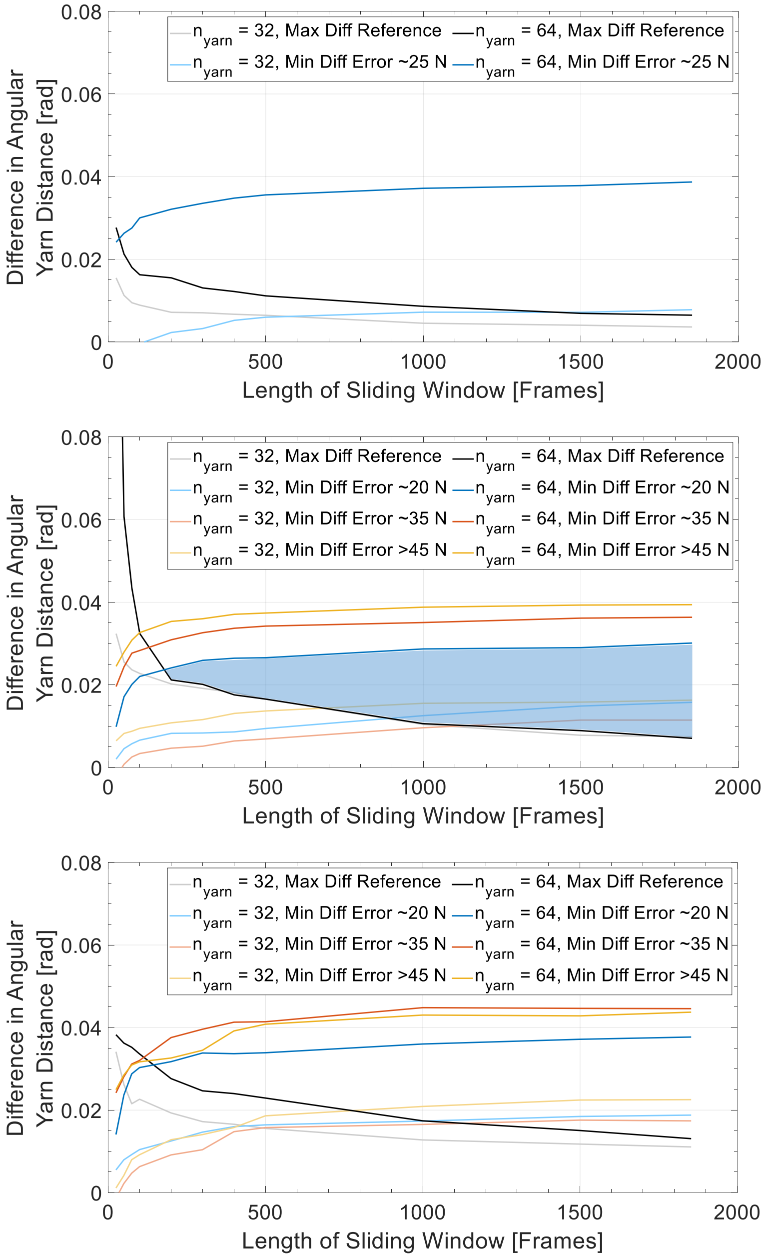

Figure 3-57: Comparison of maximum difference in yarn distances from flawless reference measurements to minimum of defect-characteristic pattern calculated over sliding windows of different lengths for 6k yarns (top), 12k yarns (middle, from own paper [89]) and 24k yarns (bottom); area of a possible threshold for defect detection without any false positive or false negative detections for the given experimental data exemplarily drawn-in in light blue for the case of $n_{yarn} = 64$ 12k yarns and an elevated tension of the defective yarn of ~20 N

The fact that the minima and maxima curves intersect at higher values for the window length in case of the lower yarn number means that if no false positive or false negative detections are accepted at all, it takes significantly more time (more measured video frames) to reach a definite statement on the presence of a yarn tension anomaly for the cases of $n_{yarn} = 32$ than for the cases of $n_{yarn} = 64$. The smaller difference between upper and lower boundary for $n_{yarn} = 32$ than for $n_{yarn} = 64$ points into the same direction. Taking into account that the above-explained threshold boundaries originate from a limited number of braiding experiments and that the tests on the different levels of elevated yarn tension for the 12k and 24k yarns show that there is significant scatter among the curves, one may doubt that there is actually a combination of window length and threshold value for the case of $n_{yarn} = 32$ that guarantees no false positive or false negative detection. As could be expected, this indicates that the method of scanning the braid formation zone for differently curved yarns works better if the yarns show more curvature in the first place. This is the case for higher yarn numbers because of the increased number of frictional yarn intersections between yarns of opposite directions of circulation.

However, it needs to be weighed up if really no false negative detections can be accepted at all in a production scenario. Given the fact that up to 25 measurement values are acquired per second, even a limited percentage of false positive detections would massively reduce machine productivity. In the view of the author, this cannot be accepted because a high productivity is a defining process characteristic of composites braiding. A false negative defect detection does however not mean that an anomalous yarn tension is not detected at all. This is due to the fact that the data in Figure 3-57 was calculated from moving or sliding averaging windows. An anomalously tensed yarn may not be detected when the averaging window spans over frames 1 to 500, leading to one false negative detection. It may however well be detected when the averaging window spans over frames 2 to 501. Such a constellation would only result in a small duration of an undetected defect and not in a complete failure of its detection. Hence, the author recommends to define a detection threshold that is further away from the lower boundary and closer to or even beyond the upper boundary. This way, the likelihood of a false positive detection can be reduced at the expense of a possibly acceptable increasing likelihood of a false negative detection. For reasons of space, this dependency cannot be detailed for all experiment configurations. Nevertheless, the author would like to give the reader an impression of the effect of the duration of undetected defects. This shall be shown at the example of the configuration of $n_{yarn} = 64$ 12k yarns. The area between the maximum (black line in the middle of Figure 3-57) and the lowest minimum curve (dark blue line in the middle of Figure 3-57) opens at a window length of about 200 frames. At this averaging window length, the lower boundary for a threshold without any false positive detections in the conducted experiments is approximately 0.021 radians and the upper boundary for a threshold without any false negative detection is approximately 0.024 radians. In Figure 3-58, the maximum duration of a defect not being detected is plotted over a varying detection threshold for the three levels of elevated yarn tension. The lower boundary for the detection threshold is drawn-in as a vertical dashed line. Any detection threshold below or equal to this value would have led to false positive defect detections in the conducted reference measurement. This is to be avoided. A detection threshold of up to 0.024 radians would have caused the anomalously tensed yarn to be detected in all video frames. At a threshold of 0.026 radians, an anomalous yarn tension of ~20 N would only have been missed 10 frames in a row. The higher elevated tensions would still have been detected in any video frame. If only an elevated tension of ~35 N or even >45 N is required to be detected without any false negative result, then the threshold could even be set to 0.03 radians or 0.035 radians, respectively. If the detection threshold was set to 0.044 radians and beyond, all defective yarns would have been missed in the experiments with elevated tension of a single yarn, which is expressed in the saturation of all three data curves in Figure 3-58.

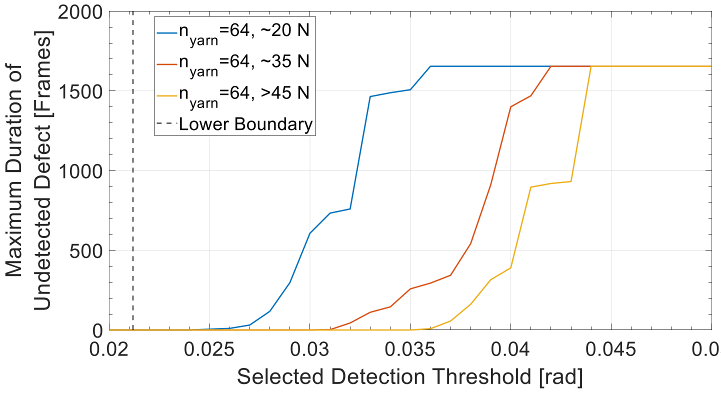

Figure 3-58: Duration of undetected defect for an averaging window length of 200 frames depending on the selected detection threshold and the severity of the anomalous yarn tension for $n_{yarn} = 64$ 12k yarns; diagram from own publication [89]

The above figure shows the situation for an averaging window of 200 frames. Given the frame rate of the camera of 25 frames/s, this implies a theoretical maximum delay between occurrence and detection of a defect of 8 s. Under the given machine speed, this corresponds to approximately 1.08 full 360°-revolutions of a carrier through the braiding machine. Setting a detection threshold beyond the upper boundary, e.g. 0.026 radians, would only have caused a slight increase in detection delay of 10 video frames, which corresponds to a total detection delay of approximately 1.14 full 360°-revolutions of the braiding machine. This is only marginally more than the delay that is in a worst case incurred by the selected length of the averaging window and shows that the upper boundary can be regarded as a “soft” boundary when setting an appropriate detection threshold. It also becomes apparent that an automated defect detection is more robust when only the higher levels of yarn tension increases shall be detected. This can be read from the greater distance of the orange and yellow curves to the lower “strict” boundary in Figure 3-58. A threshold of for instance 0.025 radians would on the one hand maintain a significant distance to the lower boundary, thereby minimizing the possibility of a false positive detection. On the other hand, such a threshold value would also keep a certain distance to the curves that correspond to the higher elevated tensions, thereby allowing their detection at a high level of certainty.

In general, it becomes apparent that the approach of optically inspecting the braid formation zone by a camera only theoretically eliminates detection dead times. Although a defect can often be distinguished from only a limited number of video frames (cf. Figure 3-54), the presented data shows that for a stable detection without false positives and false negatives a length of an averaging window in the order of 200 frames is required in a near-production scenario. Given the chosen frame rate, this may lead to a dead time of up to 8 s. If an anomalous yarn tension is particularly pronounced, this dead time may be reduced since it does not require the defect to be reflected in all data points of the averaging window. An instantaneous defect detection as with the sensor integrated braiding rings is however not possible. Moreover, when judging the applicability of the presented approach of monitoring the braid formation zone by camera, it needs to be taken into account that it requires powerful computer hardware in order to carry out the image analysis in real time.

As an intermediary summary, the following conclusions can be drawn from the algorithm development and the experiments on an optical inspection of the braid formation zone:

- The defect-characteristic pattern of a reduced distance between a yarn with elevated tension and its preceding yarn as well as an increased distance to its succeeding yarn can well be observed by a camera-based monitoring setup. The monitoring setup uses a standard SLR camera at a frame rate of 25 frames/s and a shutter speed of 0.002 s as well as a ring light as backlight illumination in order to eliminate any shimmering of the sizing of the carbon yarns that could negatively influence the pre-processing step of the image analysis.
- Unlike the discrete monitoring by light barrier, the newly-developed optical detection algorithm cannot be confused by vibrating yarns or other anomalies in the braid formation zone. Each yarn is assigned to its correct direction of circulation by means of its orientation with respect to the center of the braiding machine. Furthermore, isolatedly occurring process fluctuations are evened out by means of averaging windows over several video frames. The yarns are automatically tracked along the length of the averaging window so that each measurement value is assigned to the correct yarn even though the yarns move through the braiding machine during the averaging period.
- The developed algorithm does not necessarily have to scan the whole braid formation zone. It can also be modified so that it operates on the four quarters of the braid formation zone independently (cf. appendix A). This way, a monitoring of the braiding process by camera is enabled even if curved mandrels, which obstruct the view to parts of the braid formation zone, need to be overbraided.
- The defect-characteristic pattern of anomalously tensed yarns in a yarn distance diagram tends to be more pronounced the more braiding yarns are used, the thicker the yarns are and the more extreme the anomalous yarn tension is.
- In many cases, a defective yarn can already be spotted from a low two digit number of video frames. However, for the case of $n_{yarn} = 64$ and the given diameter of the ring light of approximately 250 mm, a length of an averaging window of 200 frames can be recommended for a stable defect detection. For the case of $n_{yarn} = 32$, the defect detection appears difficult because large window lengths of 1000 frames and more are required to detect small changes in yarn curvature of the already less curves yarns.
- The stability of the defect detection by optical inspection of the braid formation zone can be increased if the detection threshold can be set in a way that only the higher elevated yarn tensions are definitively detected.
- A complete elimination of dead times is in practice not possible by a continuous monitoring of the braid formation zone by camera. Additionally, the high computational power to process the acquired video frames in real time needs to be taken into account when weighing the presented approach against other options for braiding process monitoring.

4 Development of a Retrofittable and Cost-Efficient Sensor Integrated Bobbin Carrier

The above chapter 3 solely focused on the development of bobbin carrier independent sensor modules. The reason for the emphasis of this work on carrier independent sensor modules is that a limited number of stationary sensors requires less installation effort and incurs less costs than carrier dependent approaches with sensors on each carrier. Although the advancement of the state of the art regarding defect detection capabilities of stationary sensor modules for braiding process monitoring was demonstrated by the approaches from above, there may still be high-quality applications that require an even finer and more direct surveillance of the process. Such applications may, for instance, include braiding of critical aerospace structures (e.g. fuselage stiffeners), processing of cost-intensive silicon carbide fibers for ceramic composites (e.g. braided rocket motors and nozzles) or the production of safety ropes or medical products where a full documentation of a defect-free manufacturing process is required.

As detailed in the state of the art in subsection 2.2.2, there are several concepts of sensor integrated bobbin carriers. Reuter et al. [74] built a carrier including a laboratory load cell and a battery-powered telemetry unit. The invention by Braeuner [75] also uses a battery as energy supply but relies on an indirect yarn tension monitoring via sensing the position of a movable slider that is deflected against a spring force. Additionally, an electric motor to brake the bobbin and to tense the yarn is applied. In the invention by Reinisch et al. [76], the bobbin is also braked by a motor, but the motor is integrated into a closed-loop control with a yarn tension sensor. Means for energy harvesting in order to avoid the need for replacing batteries as energy supply units via a frictional wheel or by stationary magnets attached to the body of the machine and induction coils on the carrier are proposed. Von Reden [45] built a carrier that is conceptually comparable to the invention by Reinisch et al. [76]. The main difference is however his realization of inductive transmitter stations in the center of the horn gears (cf. Figure 2-14).

To the knowledge of the author, such sensor integrated carriers are not currently in operation in braiding of composites. One of the reasons is that all of the systems from above require either significant modifications to the standard carriers with guide plate that are optimized for composites braiding or even completely new carriers. This incurs high initial installation effort and costs. Another reason is the need for changing empty batteries after a certain production time. Since composite braiding machines are often comprised of 64 or more carriers for a producibility of large structures, this creates significant additional make-ready times. The approach of battery-less inductive power supply as implemented by von Reden [45] is known to be extremely cost-intensive (about four times the usual costs of a carrier with guide plate optimized for composites braiding; costs are approximately known because Prof. Dr.-Ing. Klaus Drechsler acted as a supervisor of von Reden's dissertation [45] as he did for the thesis at hand). The approaches for battery-less energy supply by Reinisch et al. [76] (e.g. braking of the bobbin by an electric generator, dynamo with friction wheel, energy transfer via conductive braiding yarns) are only mentioned as ideas in the patent application without any technical details or drawings. Therefore, it remains unclear how much energy these approaches create and how cost-intensive they are. Within this chapter, the author aims to provide a possible solution for sensor integration on a bobbin carrier that is on the one hand retrofittable to an existing IFDA-100 carrier with guide plate that is often used for braiding of composites. On the other hand, the proposed method of energy harvesting shall eradicate the need for changing batteries while allowing about 10-15 % of the costs of a standard IFDA-100 carrier for additional material expenses per carrier ($\approx 250\ € \cdot 0.1 \approx 25\ €$, $\approx 250\ € \cdot 0.15 \approx 37.5\ €$).

The concept of the sensor integrated bobbin carrier presented herein was initially conceived by the author. An early version of the carrier with limited measurement capabilities was realized within the framework of a TUMKolleg project by the student Benedikt Eckardt [92]. This is a type of project in which a student in his or her final year at high school can work on a small research task at Technical University of Munich in order to get to know an academic environment. The author of the dissertation at hand acted as a co-supervisor of the project. The practical working out of the project regarding braiding process monitoring was jointly conducted by the student and the author. The author thereby detailed and showed each step to the student as a kind of teacher, which made the project similar to an internship. An improved version of the sensor integrated carrier was developed within the framework of a bachelor's thesis by the student Francesco Mondelli [93], which the author of the dissertation at hand guided and supervised together with Prof. Dr.-Ing. Klaus Drechsler. The author specified the task of the thesis and the measurement principle, proposed the sensor chip to be used, conducted the experiments on the braiding machine together with the student and suggested the the type of eddy current generator for energy harvesting detailed in subsection 4.2.2. The student carried out the initial programming of the chip, designed a fixture for the electronic parts in order to attach them to the foot of the carrier and assembled a first version of the new sensor integrated carrier as well as a first version of the eddy current generator.

4.1 Concept Derivation and Sensitivity Assessment of the Sensor Integrated Carrier

As first development step, the measurement principle of the sensor integrated carrier needed to be specified. For this, the author partly reused the detection concept from subsection 3.1 since the Hall sensor arrangement had shown good sensitivity on a stationary test stand. As already visible in Figure 3-4, a magnet was added to the extension of the lever of the compensation mechanism of an IFDA-100 carrier from HERZOG GmbH so that the compensation device could again be used as a spring balance. Differing from Figure 3-4, the Hall sensor was not mounted stationarily to the body of the braiding machine but directly to the foot of the carrier. In a second step, the specific types of sensor, programmable processing unit as well as the radio transmission device needed to be specified. In order to keep the retrofitting effort to an existing carrier as low as possible, commercially available devices that united the required capabilities in a single chip were researched. As additional qualitative requirements, a small form factor to avoid collisions with carriers going the opposite direction as well as a low energy consumption for powering the device by self-sufficient energy harvesting were defined. An ESP32-SOLO-1 from Espressif Systems Co., Ltd. was found to be a freely programmable controller of small form factor (26 mm x 18 mm x 3 mm) that featured an onboard Hall sensor plus an interface for Bluetooth Low Energy (BLE) for data transfer. According to Gessler and Krause [94], BLE is a radio standard for close range that requires less energy than other well-known standards such as Wireless Fidelity (WiFi), Bluetooth or ZigBee. Only Near Field Communication (NFC) and Radio Frequency Identification (RFID) require even less energy. The reasons for not choosing the latter two standards were their low data transferal rates (<0.1 Megabits per second (Mbit/s) [94]), the low range of only a few centimeters (particularly NFC) and the lack of available freely programmable controllers with integrated sensors. As a third step, the ESP32 was programmed to read the measurement values of the internal Hall sensor and send it to an external computing device via BLE. As programming environment, the Arduino Integrated Development Environment (IDE) of version 1.8.15 was used. Additionally, a script in MATLAB R2021a was written to receive the measurement data via BLE on an office laptop. In the final step, a fixture for the chip so that it could be attached to the foot of the IFDA-100 carrier was designed and 3D printed. For the scope of the initial sensitivity assessment in this section 4.1, the chip was powered by a rechargeable IFR14500 lithium iron phosphate (LiFePo4) battery with a capacity of 600 mAh. Due to the fact that the battery delivers a nominal voltage of 3.2 V but the chip requires a voltage of 3.3 V, a step-up converter of the type U1V11F3 from Pololu Corporation was included in the electric circuit between the battery and the chip. The described steps three and four were conducted within the framework of the bachelor’s thesis [93] that was supervised by the author. The assembly of the sensor integrated carrier used in this section 4.1 is depicted in Figure 4-1.

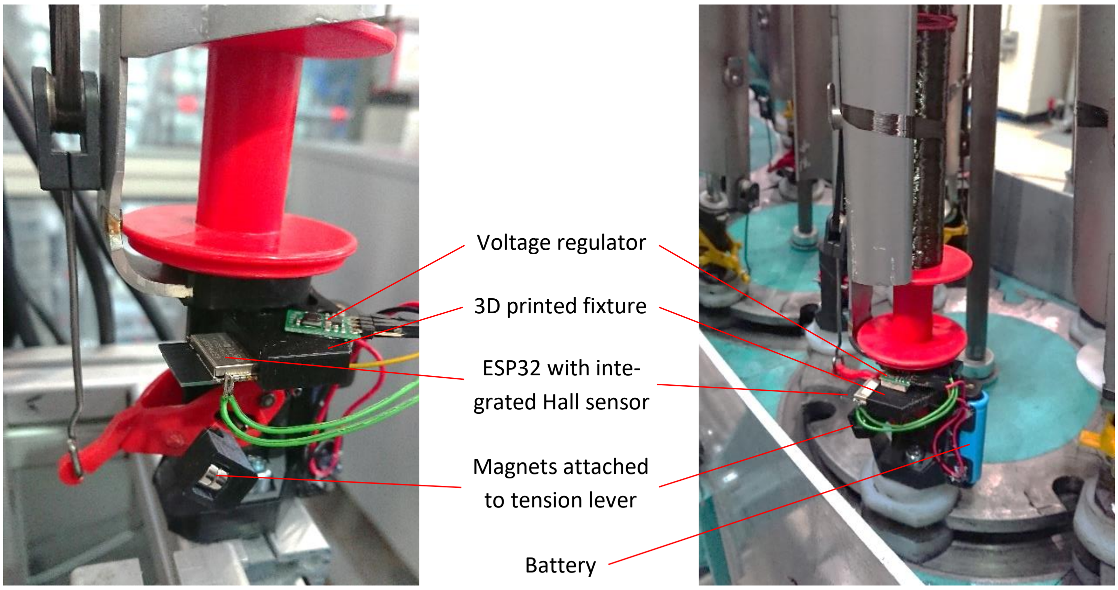

Figure 4-1: IFDA-100 carrier from HERZOG GmbH retrofitted with sensor circuit on a stationary test stand (left) and integrated into the RF 1/128-100 braiding machine (right); displayed assembly conducted within the framework of supervised student thesis [93]

The net material costs of this initial setup can, according to Table 4-1, roughly be summed up to 13 € (years of bid solicitation for taking inflation into account: 2020-2022). Note that the given approximate prices are for single pieces and do not include any discount for a commercial customer such as a braiding machine manufacturer that may want to equip all carriers of a braiding machine with the sensor setup.

Table 4-1: List of main components for an initial setup of the sensor integrated carrier and approximate net prices from the years 2020-2022

Component	Approximate net price
ESP32-SOLO-1	~3 €
Voltage regulator U1V11F3	~4 €
Battery IFR14500 600 mAh	~4 €
Battery holder AA	~1 €
Neodymium magnets (Ø 8 mm x 3 mm)	~0.1 €
Miscellaneous (Wiring, printable polymer,…)	~1 €

The built-in Hall effect sensor from the ESP32 chip produces significant noise in its readings when the sensor is tested only under the presence of earth’s magnetic field. This can be seen as a trade-off due to the low price of the chip given its manifold capabilities. Since the Hall sensor can be scanned quickly, an averaging of the sensor readings was implemented over a defined number of readings (averaging window) in the supervised student thesis [93] in order to reduce this noise. However, it was observed that the more scans of the sensor that are taken into account for averaging (the larger the window), the less averaged values can be sent to an external receiving device over the BLE connection. Figure 4-2 shows the standard deviation of the built-in Hall sensor from an ESP32 development board when it is not exposed to any dedicated but only earth’s magnetic field against the window length used for averaging the sensor readings. Additionally, the number of transmittable, averaged values to an external computing device are shown. It can be observed that the standard deviation, which is taken as a measure for the noise, is approximately 2.5 mT when an averaging of sensor readings is not applied (x-axis value of 1). The deviation in the signal is drastically reduced when a measurement value is defined as the average over 50 scans of the sensor. At the same time, the number of received measurements from the chip is not significantly affected. Beyond 50 averaged scans per measurement value up to 2000, the standard deviation appears to show a slight linearly decreasing trend. However, beyond 100 scans per measurement value, the number of measurements that can be sent over the BLE connection reduces in an inversely proportional manner. Hence, an averaging over 100 scans of the Hall sensor was taken as a configuration for the measurements in the following subsections. The standard deviation is reduced to approximately 0.5 mT while the number of transmittable measurements per second remains well above 100 in this case. This means that the internal Hall sensor is scanned about 10,000 times a second. Every 100 scans, the average over these 100 scans is calculated and sent over the BLE connection. Due to the effectively received 100 averaged measurements per second, a good resolution of the movement of the tension lever of the bobbin carrier during the braiding process is ensured.

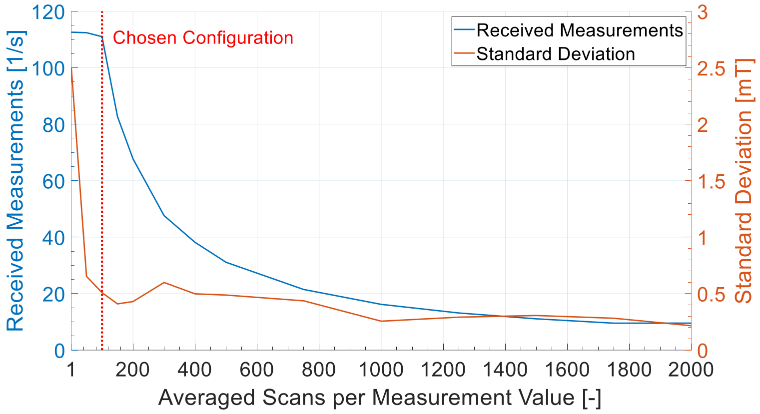

Figure 4-2: Number of measurements received over BLE and standard deviation of the measurements against the length of the averaging window; programmed configuration indicated by a red-dotted line; diagram taken from supervised student thesis [93] and adapted

4.1.1 Demonstration of the Continuous Detectability of Unwinding Irregularities in an Operating Braiding Machine

According to the standard braiding scenario described in the introductory section 1.2, the configuration as shown in Figure 4-1, right was tested during overbraiding of a cylindrical mandrel with a diameter of $d = 65\,mm$ under a braiding angle of $\varphi = 45°$ with carbon fibers of the type Tenax®-E HTS40 F13 12k from Teijin Carbon Europe GmbH. The speed of horn gear rotation of the RF 1/128-100 braiding machine was set to $r = 130\,rpm$. A defect-free reference measurement and a measurement with a simulated defect was conducted. The defect was simulated by a rubber band that was applied onto the winding of the yarn material on the bobbin. By placing the band near the edge of the bobbin, the band only temporarily hampered the unwinding process. This way, an exemplary case of a self-untying fibrous ring was replicated.

The measurement shown in Figure 4-3 was jointly conducted by the author of the dissertation at hand and the student [93]. It is observable that during unobstructed unwinding of the yarn from the bobbin, there is a first distinct periodic fluctuation in the sensor signals with a period duration of approximately seven seconds. On a finer level, there is a second oscillation with a period duration of approximately 0.5 s that is superimposed on the fluctuation with the longer period duration. During braiding with the simulated defect, a temporary, sharp increase in the measurements from the sensor chip is noticeable. These increased measurement values partly show a superimposed oscillation and partly a saturation of the sensor signal.

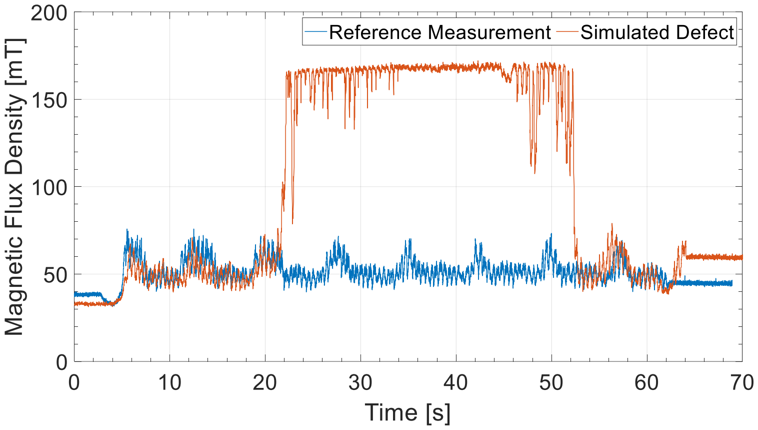

Figure 4-3: Comparison of signals from the sensor integrated carrier during defect-free braiding (blue) and braiding with a simulated unwinding irregularity (red); similar diagram in supervised student thesis [93] because student and author conducted the experiment together

The periodic fluctuation in the sensor signals is explainable by the fact that the measurement was acquired on a vertically oriented radial braiding machine. Since the speed of horn gear rotation of the machine was set to $r = 130\,rpm$ and since there are 32 horn gears in the machine, the time for a bobbin carrier to complete a full 360°-revolution through the machine, according to equation (2-5), calculates to

$$t_{360°} = \frac{32}{2 \cdot \frac{130\,\frac{1}{min}}{60\,\frac{s}{min}}} \approx 7.38\,s \tag{4-1}$$

This corresponds to the observed period duration of the first distinct periodic fluctuation. Since the braiding experiments were started when the sensor integrated carrier was located at the bottom of the braiding machine, it can be said that the periodic increase always occurs when the sensor integrated carrier is oriented upright. When it is oriented horizontally or upside down, the measurements of the sensor chip, which reflect the deflection of the tension lever of the compensation device on the carrier, are significantly lower. This observation is in line with the explanation to Figure 3-14, right, in which it is described that a play of the bobbin along the central axis of a carrier (cf. Figure 3-15) can cause fluctuations both in yarn tension and in the deflection of the tension lever of a carrier. In Figure 3-14, right, the displacement of the bobbin along the axis of the carrier was induced by a high yarn tension that was able to lift the bobbin against its own weight depending on the unwinding angle (angle of force application). In the data presented in the above Figure 4-3, the bobbin is displaced by the different directions of gravity that act onto the bobbin. When the carrier is oriented upright, the weight force of the bobbin moves the bobbin towards the foot of the carrier. Thereby, the gap between the foot of the carrier and the lateral notches of the bobbin, which the locking pin has to bridge in order to brake the bobbin, is minimized. Hence, the locking pin needs to be retracted further, which corresponds to higher yarn tensions and larger deflections of the tension lever. When the bobbin is at its top position in the vertically set up radial braiding machine, it is moved towards the quick lock of the carrier. The gap between the foot of the carrier and the lateral notches of the bobbin is in turn maximized. This corresponds to lower yarn tensions, lower deflections of the tension lever and thus lower measurement values of the sensor chip. When the carrier is oriented horizontally, there is no dedicated force pushing the bobbin towards the foot of the carrier. It appears plausible that the bobbin is moved away from the foot of the carrier towards the quick lock by the pawl spring (cf. Figure 3-3) that pushes the locking pin laterally against the bobbin. This way, decreased sensor signals are measured for this configuration as it is the case for a carrier that is oriented upside down. The total number of seven completed oscillations with a period duration of 7.38 s over the experiment also underpins the given explanation by orientations of the bobbin carrier. The braided length $l_{360°}$ along the longitudinal axis of the mandrel during a full 360°-revolution of a carrier can be obtained by multiplying formula (2-4) with the time it takes a carrier to complete such a full revolution $t_{360°}$.

$$l_{360°} = \frac{\pi \cdot d}{tan(45°)} = \frac{\pi \cdot 65\,mm}{tan(45°)} \approx 204\,mm \qquad (4\text{-}2)$$

Since the mandrel that was used is $l_{mandrel} = 1.5\ m$ long, the number of full revolutions of the carriers through the machine must be

$$n_{360°} = \frac{l_{mandrel}}{l_{360°}} \approx \frac{1.5\,m}{0.204\,m} \approx 7.35 \approx 7 \qquad (4\text{-}3).$$

The second oscillation in the sensor signals is not due to noise from the sensor. Instead, it can be attributed to the working principle of the compensation device to even out differences in yarn length due to the meandering courses of the carriers. Since there are 32 horn gears in the braiding machine but there are only 16 oscillations every 7.38 s, this indicates that the braiding ring is mounted to the machine with a displacement in axial direction. The clear indication of the impediment of the unwinding process by a rubber band shows that the detection of a defect such as a fibrous ring by the sensor mounted to the carrier is not impeded by vibrations of the carrier when it travels at almost full speed through the braiding machine. Thereby, the detection concept of unwinding related irregularities and the assembly of the sensor integrated carrier have shown to be operational under near-production conditions.

4.1.2 Investigations on the Possibility of Indicating the Remaining Filling Degree of a Bobbin

In further characterization experiments of the sensor integrated carrier in the RF 1/128-100 braiding machine, it was observed that there is a drift in measurement values as the bobbin that is mounted to the sensor integrated carrier empties. This behavior was systematically investigated by means of the test setup shown in Figure 4-4, left. 250 m of Tenax®-E HTS40 F13 12k fibers from Teijin Carbon Europe GmbH were wound onto a single bobbin. The bobbin was mounted to the sensor integrated carrier. A rotating drum with a diameter of $d = 200\,mm$ pulled the yarn at a speed of approximately $40\ \frac{mm}{s}$ as the braiding machine was operating at a speed of horn gear rotation of $r = 130\ rpm$. A spring with a rating of 350 g was used for yarn tension creation inside the tube of the sensor integrated carrier. Five repetitions of the described experiment were conducted. Since no continuous lateral movement of the drum was programmed, the winding of the fibers thickened by about 1 cm during the experiment. Due to the constant rotational speed of the drum, this caused the haul-off speed of the yarn to increase by, according to relation (4-4), about 10 % from start to end of the measurement.

$$\frac{\pi \cdot (200\,mm + 2 \cdot 10\,mm)}{\pi \cdot 200\,mm} = 1.1 \tag{4-4}$$

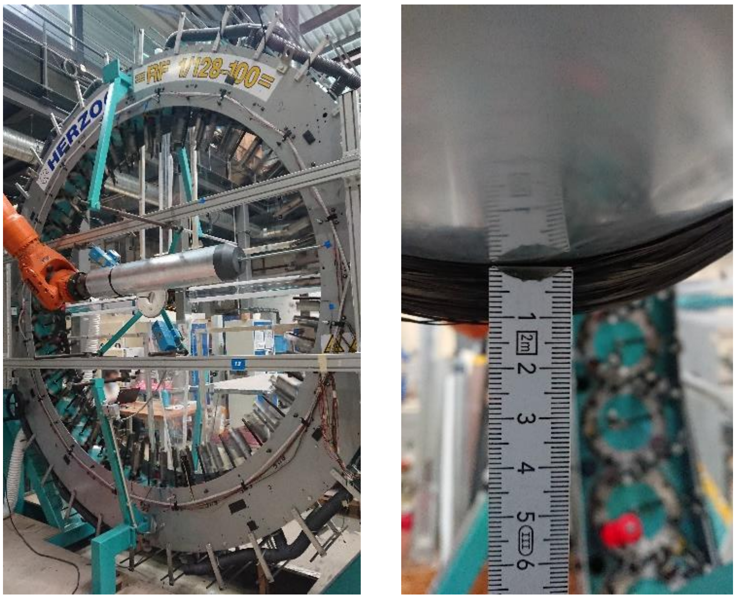

Figure 4-4: Unwinding of a single bobbin that is mounted to the sensor integrated carrier by means of a rotating drum (left); thickening of the winding on the drum (right)

The above-mentioned drift in measurement values from the internal Hall sensor of the ESP32 is exemplarily illustrated in Figure 4-5, left. Due to the long duration of the experiment, the ratcheting mechanism of the tension lever is visible as a broad measurement band. Whereas a defined trend of the local maxima of the band cannot be identified over the course of the measurement, there is a clear upward trend of the local minima of the measurement band. On close observation, such an upward trend of the local minima is also observable in the signal from the

Hall sensor in Figure 3-14, right. This diagram also shows the response of a Hall sensor that indirectly measures the position of the tension lever of a carrier during full unwinding of a bobbin. However, only 50 m of yarn were unwound in Figure 3-14 in contrast to 250 m in Figure 4-5. The periodic superimposed fluctuation in Hall voltage and yarn tension in Figure 3-14 was shown to be due to the fact that the acting yarn tension is able to lift the bobbin on the carrier depending on the direction of force application. Note that the different measurement units Voltage and Millitesla in Figure 3-14 and Figure 4-5 are due to the different types of sensors but essentially express the same physical relation (distance of the magnet to the Hall probe). The measurements in Figure 3-14 were acquired by an analog Hall sensor. The measurement unit is therefore voltage. The ESP32 used in Figure 4-5 converts the measurements from its internal Hall sensor first to a digital signal and then to Millitesla. Figure 4-5, right, shows the moving mean of the magnetic flux density measured by the ESP32 over an averaging window of ten 360°-revolutions of the sensor integrated carrier in the RF 1/128-100 braiding machine. The moving average smoothes out the oscillating movement of the tension lever so that the increasing trend in magnetic flux density can be better quantified. The blue line marked as “Bobbin 1” corresponds to the measurement shown in Figure 4-5, left. The other four curves demonstrate the good repeatability of the observed upward drift. It appears plausible that by defining a threshold in the moving mean of the magnetic flux density of, in this case, 50 mT, the final 10 % of filling degree of a bobbin can be identified. Moreover, it is conceivable that a tracking of filling degree on the bobbins by the moving mean of the magnetic flux density can be used as an input for intra-company logistics to trigger the rewinding of new bobbins and their delivery to a braiding machine whose bobbins are about to run empty.

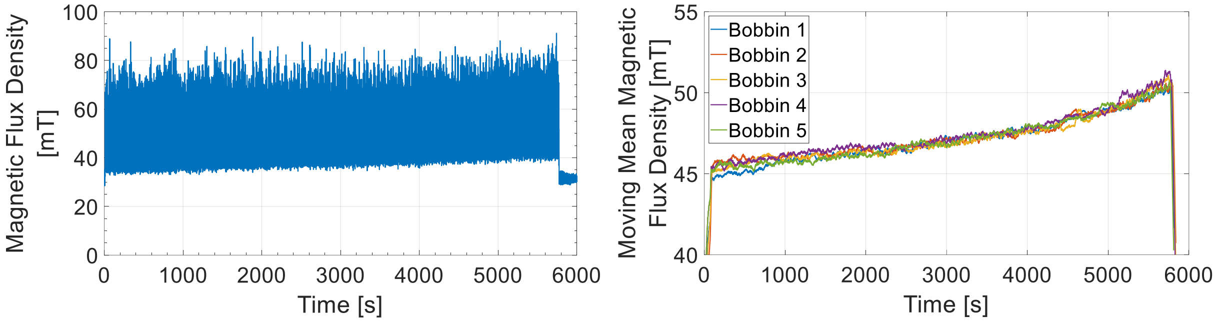

Figure 4-5: Magnetic flux density measured by the ESP32 on the sensor integrated carrier during full unwinding of a single bobbin in the RF 1/128-100 braiding machine at a rate of approximately 40 $\frac{mm}{s}$ (left); moving mean of the magnetic flux density over ten 360°-revolutions of the sensor integrated carrier in the braiding machine from five independent repetitions (right)

In subsection 3.1.1, it was already explained that the values of the local maxima in Hall voltage are determined by the width of the gap between foot of the carrier and lateral notches in the bobbin. This is due to the fact that these maxima represent the point at which the locking pin, which is part of the foot of the carrier, disengages with the lateral notches in the bobbin. Since fundamental changes in the geometry of the interaction between locking pin and bobbin do not occur in the measurement in Figure 4-5, left, the local maxima remain in a similar range over the course of the experiment. Subordinate effects such as a play of the bobbin along the central axis of the carrier are present but not distinguishable in the diagram due to the long duration of the measurement. Also in subsection 3.1.1 and particularly in the description to Figure 3-9, it is mentioned that frictional effects on the carrier can have an effect on the lower envelope of the measurements from the Hall sensor. Thus, friction-related causes of the observed upward trend of the local minima in magnetic flux density were further investigated.

Firstly, a possible change in frictional forces at the bobbin carrier due to the increasing haul-off speed of the yarn over the course of the experiment was examined. For this, a cylindrical mandrel with a diameter of $d = 65\ mm$ was overbraided with Tenax®-E HTS40 F13 12k fibers under a braiding angle of $\varphi = 45°$ on the RF 1/128-100 braiding machine. The speed of horn gear rotation was again set to $r = 130\ rpm$. Thereby, the haul-off speed of the yarn was kept constant at

$$v_{yarn} = \frac{\pi \cdot d}{t_{360°} \cdot \cos\varphi} \approx 39.1\ \frac{mm}{s} \tag{4-5}$$

The above relation is a variation of formula (2-4), which describes the haul-off speed of an overbraidable mandrel. The experiment was conducted with all available carrier springs for yarn tension creation (ratings of 130 g, 350 g, 600 g, 700 g, 800 g and 950 g) at three different filling degrees of the bobbin (“full”, “half full”, “almost empty”). The filling degree “full” corresponded to a remaining yarn mass on the bobbin of about 200 g, “half full” to a yarn mass of about 100 g and “almost empty” to a yarn mass of about 20 g. Figure 4-6 shows the mean values of the magnetic flux density measured by the sensor integrated carrier for each braiding test. Due to the broad band of measurement values (cf. Figure 4-5, left), the standard deviations are not drawn-in. It can be observed that the curves almost unanimously increase from a full bobbin to an almost empty one. Only the measurement for the 600 g-spring and a half full bobbin must be seen as an outlier of this trend. Furthermore, a shift of the curves towards lower magnetic flux densities is recognizable with higher ratings of the carrier spring (higher yarn tension).

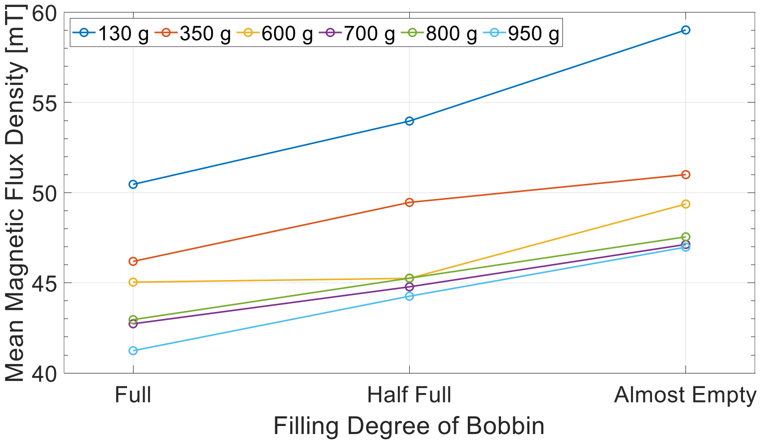

Figure 4-6: Mean magnetic flux densities obtained from the sensor integrated carrier during braiding at six different yarn tensions and three different filling degrees of the bobbin

The results from this test series confirm the finding from the unwinding experiments with the rotating drum from above. For instance, the results of approximately 46 mT for a full bobbin and of approximately 51 mT in case of the 350 g-spring almost match the values plotted in

Figure 4-5, right. This shows that the moderately increasing haul-off speed of the yarn as the winding on the rotating drum thickened can be ruled out as a reason for the observed trend towards higher magnetic flux densities and therefore also higher yarn tensions. Thus, there must be a systematic effect that accounts for the reproducible observation of increasing yarn tension on bobbin carriers with guide plate. Carriers with guide plate were specifically developed in order to minimize yarn damage during processing of brittle reinforcement fibers. Due to the fact that the dissertation at hand focuses on the use case of braiding of reinforcement fibers for the production of composite parts, the observed effect is investigated and explained in more detail in the following subsection.

Extension of a formula for prediction of minimum braiding yarn tension to carriers with guide plate

The second friction-related approach to explain the observed increasing trend was inspired by theoretical considerations made by Kyosev in his book “Braiding Technology for Textiles” [19]. He set up analytical relations in order to calculate the force of the yarn when it leaves the bobbin carrier under neglect of the ratcheting mechanism of the compensation device. He argues that as the bobbin empties, the unwinding radius of the yarn from the bobbin decreases. Assuming constant frictional forces between the rotating bobbin and the carrier, this would cause an increase in yarn tension because the lever arm of force application decreases. However, the frictional interaction between the rotating bobbin and the carrier is not constant. As the bobbin empties, the yarn mass on the bobbin decreases, which also causes the friction between bobbin and carrier to decrease. Hence, the yarn tension must also decrease due to this effect. In order to find out which effect is more dominant, Kyosev [19] set up the following equations.

The frictional moment M_{fr} at the bobbin is calculated by the weight of the bobbin, the coefficient of friction μ and the frictional radius ra_{fr}. The weight of the bobbin is given by the mass of the bobbin m_{bobbin} and earth’s gravitational constant g.

$$M_{fr} = m_{bobbin}\left(ra_{unwinding}\right) \cdot g \cdot \mu \cdot ra_{fr} \tag{4-6}$$

Note that Kyosev [19] includes the mass of the bobbin m_{bobbin}, earth’s gravitational constant g and the coefficient of friction μ in one variable. For reasons of clarity, the author preferred to name them separately in the above equation (4-6). Kyosev [19] then expresses the mass of the bobbin as a function of the unwinding radius $ra_{unwinding}$

$$\begin{gathered} m_{bobbin}\left(ra_{unwinding}\right) = \\ = \left(ra_{unwinding}^2 - ra_{bobbin,shaft}{}^2\right) \cdot \pi \cdot h \cdot \rho + m_{bobbin,empty} \end{gathered} \qquad \text{(4-7),}$$

whereby $ra_{bobbin,shaft}$ is the radius of the shaft of the bobbin, h is the height of that part of the bobbin that is actually used for storing the yarn, ρ stands for the packing density of the yarn on the bobbin and $m_{bobbin,empty}$ equals the mass of the bobbin itself without any yarn material. Kyosev [19] writes the equation of motion as

$$J \cdot \ddot{\omega} = F_{Yarn,Bobbin} \cdot ra_{unwinding} - m_{bobbin}\left(ra_{unwinding}\right) \cdot g \cdot \mu \cdot ra_{fr} \qquad \text{(4-8)},$$

whereby J corresponds to the rotational moment of inertia of the bobbin around its longitudinal axis, $\ddot{\omega}$ is the angular acceleration of the bobbin and $F_{Yarn,Bobbin}$ is the resulting yarn force when the yarn leaves the bobbin. Kyosev [19] then assumes that

$$\ddot{\omega} \overset{!}{=} 0 \qquad \text{(4-9)},$$

which leads to the expression of the yarn force at the point when the yarn leaves the bobbin

$$F_{Yarn,Bobbin} = \\ = \begin{bmatrix} ra_{unwinding} \cdot \pi \cdot h \cdot \rho + \\ + \dfrac{1}{ra_{unwinding}} \cdot \left(m_{bobbin,empty} - \pi \cdot h \cdot \rho \cdot {ra_{bobbin,shaft}}^{2}\right) \end{bmatrix} \cdot \\ \cdot g \cdot \mu \cdot ra_{fr} \qquad \text{(4-10)}.$$

Applying the geometric parameters of the bobbins used in the thesis at hand, a measured frictional radius of $ra_{fr} = 0.9\ cm$, an estimated coefficient of friction $\mu = 0.3$ and a measured packing density of the 12k carbon yarns on the bobbin of $\rho = 0.75\ \frac{g}{cm^3}$ leads to the course of the yarn force $F_{Yarn,Bobbin}$ shown in Figure 4-7.

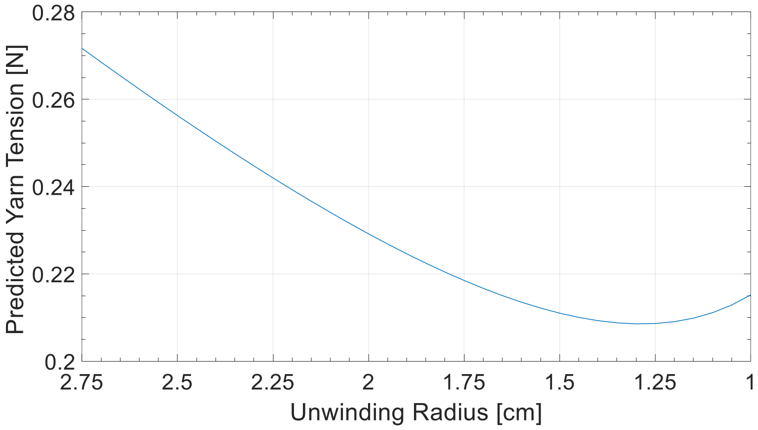

Figure 4-7: Yarn tension at the point where the yarn leaves the bobbin (not the carrier!) depending on unwinding radius according to the model by Kyosev [19] applied to the bobbins of the RF 1/128-100 braiding machine

Kyosev [19] notes that the portion of the yarn tension that turns the bobbin also depends on the unwinding angle of the yarn from the bobbin γ. The reader is referred to Figure 1-3, right for an illustration of the unwinding angle γ. Only when $\gamma = 90°$, the full yarn tension turns the bobbin. When γ deviates from 90°, a higher yarn tension must act in order to turn the bobbin. In order to reflect this issue, Kyosev [19] extends equation (4-10) by a time dependent unwinding angle $\gamma(t)$ to

$$\begin{gathered} F_{Yarn,Bobbin} = \frac{1}{sin\gamma(t)} \cdot \\ \cdot \left[\begin{gathered} ra_{unwinding} \cdot \pi \cdot h \cdot \rho + \\ + \frac{1}{ra_{unwinding}} \cdot \left(m_{bobbin,empty} - \pi \cdot h \cdot \rho \cdot {ra_{bobbin,shaft}}^2 \right) \end{gathered} \right] \cdot \\ \cdot g \cdot \mu \cdot ra_{fr} \end{gathered} \tag{4-11}$$

Finally, he notes that equation (4-11) only applies when the bobbin brake is released because otherwise the compensation mechanism defines the yarn tension. This is why Kyosev [19] actually writes equations (4-10) and (4-11) with a “>”-sign instead of a “=”-sign. For the considerations herein, which do not include any compensation action, the “=”-sign shall be sufficient.

The course of the yarn tension illustrated in Figure 4-7 constitutes a discrepancy to the measured tendency in magnetic flux density from the sensor integrated bobbin carrier (cf. Figure 4-5 and Figure 4-6). The yarn tension in Figure 4-7 decreases at first because the frictional forces decrease due to a reducing yarn mass on the bobbin. Eventually, at an unwinding radius of approximately 1.25 cm, the yarn tension is predicted to increase because the reduction in unwinding radius becomes more dominant. The measured magnetic flux density, which indirectly represents the acting yarn tension when the yarn exits the carrier, however increases throughout the course of the measurement. Hence, also this second friction-related approach cannot explain the observed behavior. The author then investigated why the above relations (4-6) to (4-11) do not reflect the indirectly observed tendency of increasing yarn forces with emptying bobbin.

To the author, the assumption of $\ddot{\omega} \overset{!}{=} 0$ in the equation of motion (4-8) was not intuitive. Kyosev [19] argues that the assumption is fulfilled at the moment the bobbin is released by the brake. The author is of the opinion that the angular velocity $\dot{\omega}$ of the bobbin must be

$$\dot{\omega} \overset{!}{=} 0 \tag{4-12}$$

at the moment the brake is released. The angular acceleration $\ddot{\omega}$ must be greater than zero because the bobbin apparently starts to turn when the brake is released. It could however be the case that the moment just before the brake begins to engage with the bobbin again, $\ddot{\omega}$ is small enough to justify the assumption $\ddot{\omega} \overset{!}{=} 0$.

To validate equations (4-10) and (4-11), the author set up a first variant of an experiment in which $\ddot{\omega} \overset{!}{=} 0$ was fulfilled at any time (variant 1). For this, the pawl spring inside the foot of the carrier was removed (cf. Figure 3-3, top right for pawl spring). This way, the compensation device of the carrier was disabled. When yarn was unwound from this manipulated carrier on the stationary unwinding test stand as described in subsection 3.1.1, the bobbin turned continuously. This fulfilled the assumption of zero angular acceleration. The bobbin was not actively braked in this unwinding setup. Thus, all yarn tension was created only by frictional effects. The response in yarn tension of 250 m of Tenax®-E HTS40 F13 12k carbon fibers from Teijin

Carbon Europe GmbH during the unwinding experiment was measured by an M1391 yarn tension measurement unit from Tensometric Messtechnik GmbH after the yarn had exited the carrier. The yarn was unwound at a rate of 40 $\frac{mm}{s}$ and the experiment was repeated five times.

The course of the measured yarn tension can be read from Figure 4-8, left. The same moving average filter as in Figure 4-5 was applied to the sensor signal. It can be observed that the measured yarn tension remains in a constant range of approximately 2-2.5 N. At first glance, this is not in agreement with the model shown in Figure 4-7. However, the decrease in predicted yarn tension in Figure 4-7 is only 0.06 N. Given the scaling of the y-axis in Figure 4-8, left, such an effect would hardly be visible. Also, frictional effects at the guide plate and the yarn deflection elements on the carrier are not included in the model (4-10) from above. These effects can explain the higher measured forces than the predicted ones. Hence, the result shown in Figure 4-8, left can be stated to at least not disagree with the model (4-10) from above. It is however notable that an increase with emptying bobbin as observed in Figure 4-5 and Figure 4-6 cannot be identified in the measurements either.

The author suspected that an increase in yarn tension as the bobbin empties was not observable due to the fact that there is no yarn brake in place that creates a relevant yarn tension when the yarn leaves the bobbin. Therefore, the unwinding experiment was further modified in a second variant in a way that the bobbin was braked but the condition $\ddot{\omega} \overset{!}{=} 0$ was still met (variant 2). This was achieved by replacing the standard spacer disc (cf. Figure 3-15 and Figure 4-9, right), which allows a bit of play between the bobbin and the quick lock of the carrier, by a rubber ring and an adjusting washer (cf. Figure 4-9, left). The thickness of the adjusting washer was chosen so that the bobbin was slightly clamped and thus braked when the quick lock of the carrier was closed. This created a yarn tension similar to the compensation device when the yarn left the bobbin but without an interruption of the rotation of the bobbin due to the ratcheting mechanism. The results from this experiment can be seen in Figure 4-8, right. A strong increase in yarn tension is observable as the bobbin empties. This confirms the tendency measured by the sensor integrated bobbin carrier in Figure 4-5 and Figure 4-6, which were obtained with an enabled compensation device of the carrier. Also, superimposed fluctuations in yarn tension with an amplitude of approximately 1 N and a period duration in the order of 10 m (in the beginning of the experiments) to 5 m (towards the end of the experiments) are present.

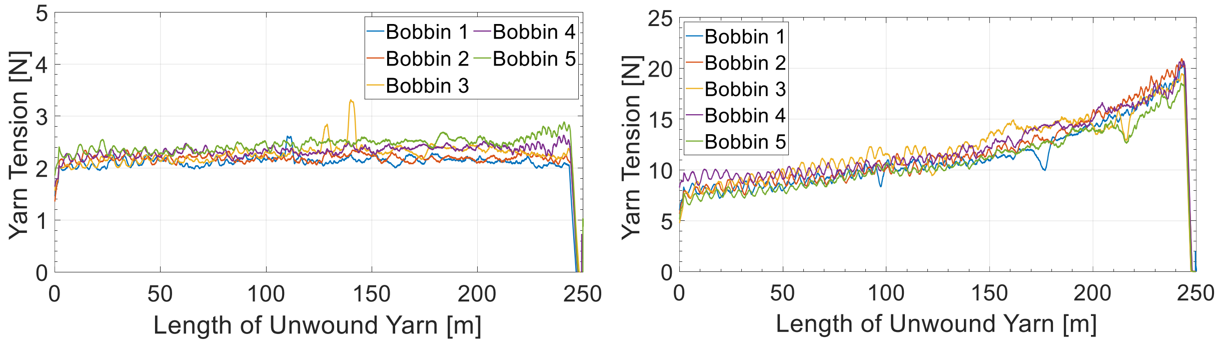

Figure 4-8: Yarn tension during unwinding with disabled compensation mechanism: no bobbin brake (variant 1, left), bobbin brake by rubber ring and adjusting washer (variant 2, right)

The author attributes the superimposed fluctuations in yarn tension to the periodic change in unwinding angle of the yarn from the bobbin that is explained by relation (4-11). A plausible reason for the different behavior with and without braking of the bobbin can be found in the changing deflection angle at the guide plate of the carrier. The change in deflection angle depicted in Figure 4-9, middle and right occurs in both variants of the experiment (with and without braking of the bobbin). However, when the bobbin is not braked, the yarn only lies loosely around the edge of the guide plate. Thereby, almost no friction is induced at this edge. This is why an increase of the warp angle of the yarn around the edge of the plate does not cause an increase in yarn tension. When the bobbin is braked, the yarn is guided tightly around the edge of the guide plate. As the bobbin empties, the warp angle around the edge of the plate increases. This time, the yarn tension increases with increasing warp angle according to the Euler-Eytelwein (frictional rope) relation.

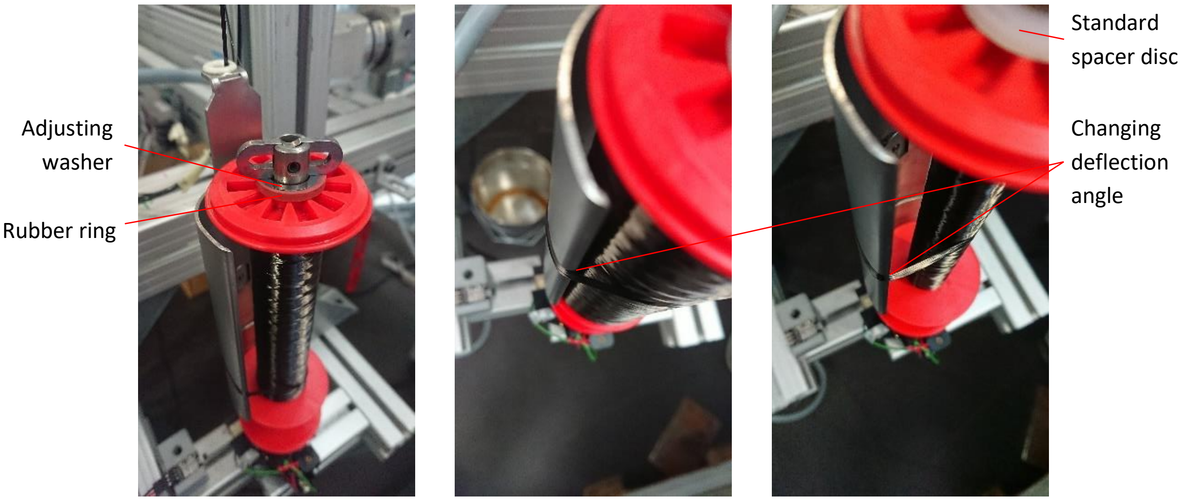

Figure 4-9: Braking of bobbin with adjusting washer and rubber ring according to experiment variant 2 in order to maintain $\ddot{\omega} = 0$ (left); changing deflection angle at the guide plate of the carrier: obtuse angle when the bobbin is full (middle), right angle when the bobbin is almost empty (right)

The explanation from above is underpinned by an extension of the above formula (4-10) by frictional effects according to the Euler-Eytelwein relation. When the bobbin is not braked but free to rotate (variant 1), the tension of the yarn when it exits the carrier $F_{Yarn,exit}$ can be expressed as

$$\begin{aligned} F_{Yarn,exit} &= F_{Yarn,Bobbin} \cdot e^{\mu \cdot \delta_1} \cdot e^{\mu \cdot \delta_2} \cdot e^{\mu \cdot \delta_3} = F_{Yarn,Bobbin} \cdot e^{\mu \cdot (\delta_1 + \delta_2 + \delta_3)} = \\ &= F_{Yarn,Bobbin} \cdot e^{\mu \cdot \left(\pi + \frac{\pi}{2} + \frac{\pi}{2}\right)} = F_{Yarn,Bobbin} \cdot e^{\mu \cdot 2\pi} \end{aligned} \quad (4\text{-}13).$$

μ is the coefficient of friction between the carbon yarn and the metal yarn guides of the carrier. As in the relations (4-6) to (4-11), it is again estimated to $\mu = 0.3$. δ_1 is the deflection angle of the yarn at the 180°-deflecting element of the compensation device. δ_2 is the deflection angle at the stationary 90°-deflecting element that is attached to the guide plate and δ_3 is the deflection angle around the guide plate. For reasons of clarity, the locations of the assumed deflection angles δ of the yarn on the carrier are indicated in Figure 4-10.

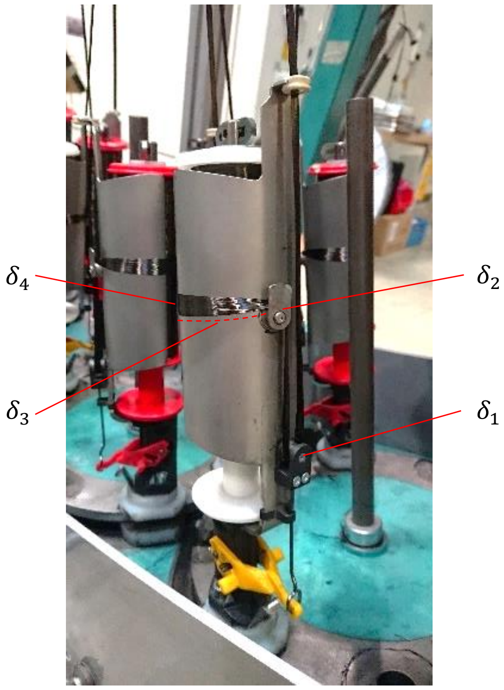

Figure 4-10: Deflection angles $\delta_1 - \delta_4$ of the yarn on the IFDA-100 carrier with guide plate from HERZOG GmbH

According to the measurements from Figure 4-8, left, a value of 2.25 N can be assumed for $F_{Yarn,exit}$. Hence $F_{Yarn,Bobbin}$, which describes the yarn tension at the point where the yarn leaves the bobbin, calculates to

$$F_{Yarn,Bobbin} = \frac{F_{Yarn,exit}}{e^{\mu \cdot 2\pi}} \approx \frac{2.25\ N}{e^{0.3 \cdot 2\pi}} \approx 0.34\ N \tag{4-14}$$

This value for $F_{Yarn,Bobbin}$ is in a similar order and, given the fact that the coefficient of friction μ was only estimated and that no bending stiffness of the yarn was accounted for in formula (4-10), in reasonable agreement to the predicted yarn tension from formula (4-10), particularly when the bobbin is full (cf. Figure 4-7). Relation (4-13) can be amended by a further yarn deflection δ_4. This represents the deflection at the edge of the guide plate, which only takes effect when the yarn is guided tightly around the edge of the plate. This is only the case when the yarn is pretensioned by a braked bobbin, either by an enabled compensation device of the carrier or by the arrangement with the rubber ring and the adjusting washer in variant 2 of the unwinding experiment.

$$\begin{aligned} F_{Yarn,exit}(\delta_4) &= F_{Yarn,Bobbin,braked} \cdot e^{\mu \cdot (\delta_1 + \delta_2 + \delta_3 + \delta_4)} = \\ &= F_{Yarn,Bobbin,braked} \cdot e^{\mu \cdot (2\pi + \delta_4)} \end{aligned} \tag{4-15}$$

Based on Figure 4-9, middle and right, δ_4 is assumed to vary between 20° and 90° as the bobbin empties. This way, $F_{Yarn,Bobbin,braked}(\delta_4)$ can be calculated. $F_{Yarn,Bobbin,braked}(\delta_4)$ represents the yarn tension at the point the yarn leaves the bobbin, which is braked according to variant 2 of the experiment, as a function of the deflection angle δ_4 at the guide plate. From Figure 4-8, right, $F_{Yarn,exit}(\delta_4 = 20°)$, which describes the yarn tension after the yarn has exited the carrier at the beginning of the experiment (bobbin still full), can be read to approximately 7 N. This leads to a value for $F_{Yarn,Bobbin,braked}(\delta_4 = 20°)$ of

$$F_{Yarn,Bobbin,braked}(20°) = \frac{F_{Yarn,exit}(20°)}{e^{\mu\cdot(2\pi+\delta_4)}} \approx \frac{7\,N}{e^{0.3\cdot\left(2\pi+\frac{20°}{180°}\cdot\pi\right)}} \approx 0.96\,N \tag{4-16}$$

From this value, a new value for $m_{bobbin,empty}$ can be calculated according to relation (4-10). The recalculation of this value is necessary in order to account for the lateral clamping of the bobbin due to the rubber ring and the adjusting washer.

$$\begin{gathered} m_{bobbin,empty,new} = \\ = \left(\frac{F_{Yarn,Bobbin,braked}}{g\cdot\mu\cdot ra_{fr}} - ra_{unwinding}\cdot\pi\cdot h\cdot\rho\right)\cdot ra_{unwinding} + \\ +\pi\cdot h\cdot\rho\cdot {ra_{bobbin,shaft}}^2 \approx \\ \approx 793.60\,g \end{gathered} \tag{4-17}$$

The clamping of the bobbin is accounted for in the variable of the mass of the empty bobbin itself because the lateral clamping force remains constant as the bobbin empties. This modified “mass” of the empty bobbin can then be used in equation (4-10) in order to calculate the yarn tension $F_{Yarn,Bobbin,braked}(\delta_4 = 90°)$ at the point the yarn leaves the bobbin when the bobbin is almost empty. The argument $(\delta_4 = 90°)$ practically means that $ra_{bobbin,shaft}$ needs to be used for the unwinding radius $ra_{unwinding}$ in equation (4-10).

$$\begin{gathered} F_{Yarn,Bobbin,braked}(90°) = \\ = \left[\begin{gathered} ra_{bobbin,shaft}\cdot\pi\cdot h\cdot\rho + \\ +\frac{1}{ra_{bobbin,shaft}}\cdot\left(m_{bobbin,empty,new} - \pi\cdot h\cdot\rho\cdot {ra_{bobbin,shaft}}^2\right) \end{gathered}\right]\cdot \\ \cdot g\cdot\mu\cdot ra_{fr} \approx 2.10\,N \end{gathered} \tag{4-18}$$

This is the yarn tension at the point when the yarn leaves the bobbin in case of the braked bobbin (second experiment variant) and when the bobbin is almost empty. The frictional interaction between carbon yarn and carrier can now be accounted for by applying the result from (4-18) in relation (4-15).

$$F_{Yarn,exit}(90°) = F_{Yarn,Bobbin,braked}(90°)\cdot e^{0.3\cdot\left(2\pi+\frac{\pi}{2}\right)} \approx 22.16\,N \tag{4-19}$$

Again, this value is in good agreement to the measured yarn tension towards the end of the experiments of variant 2 (cf. Figure 4-8, right). This finding in combination with the reasonable agreement between the back calculation (4-14) and the modelling result from Figure 4-7 shows that the consideration of changing frictional angle at the edge of the guide plate can explain the indirectly observed increase in yarn tension by the sensor integrated bobbin carrier. Due to this, the author proposes to extend the model from Kyosev [19] in relation (4-10) by the above terms for frictional interaction between yarn and carrier for the case of a carrier with guide plate, which is often used in braiding of reinforcement fibers. In case of a braked bobbin, the equation for the yarn tension at the point the yarn exits the bobbin carrier can be written as

$$
\begin{aligned}
&F_{Yarn,exit} = \\
&= \left[\begin{array}{c} ra_{unwinding} \cdot \pi \cdot h \cdot \rho + \\ + \dfrac{1}{ra_{unwinding}} \cdot \left(m_{bobbin,empty} - \pi \cdot h \cdot \rho \cdot {ra_{bobbin,shaft}}^{2} \right) \end{array} \right] \cdot \\
&\cdot g \cdot \mu \cdot ra_{fr} \cdot e^{\mu \cdot (\delta_1 + \delta_2 + \delta_3 + \delta_4)}
\end{aligned}
\qquad (4\text{-}20).
$$

In order to account for a change in unwinding angle of the yarn from the bobbin, the inverse of the sinus of the unwinding angle γ, as in relation (4-11), needs to be multiplied to the extended formula (4-20).

In conclusion of the above section 4.1 on the concept and the sensitivity assessment of the sensor integrated bobbin carrier, the following points can be made:

- An ESP32 sensor chip from Espressif Systems Co., Ltd. with internal Hall sensor can, in conjunction with a magnet attached to the tension lever of a bobbin carrier, serve as monitoring device for braiding that is retrofittable to existing carriers.
- Due to the fact that the sensor chip unites functions such as sensory device, programmable processing unit as well as transmission unit in one part, the installation effort to the carrier is minimized.
- A battery powered variant (without energy harvesting) of the sensor integrated carrier comes with material costs of approximately 13 € (<10% the costs of a carrier with guide plate).
- The magnetic flux density measured by the sensor chip on the carrier shows an increasing trend as the bobbin empties.
- This trend is in contrast to a model for yarn tension prediction on a standard bobbin carrier for textile production from Kyosev [19].
- An extension of this model by the Euler-Eytelwein (frictional rope) formula in order to cover frictional effects at the guide plate of a carrier, which are not present in standard bobbin carriers for textile production, was proposed.
- Applying the extended model to emptying bobbins on a stationary unwinding test stand shows good agreement to the measurement values in unwinding yarn tension.

4.2 Explorations on Different Variants for Self-Sufficient Powering by Energy Harvesting

As explained in the introductory remarks to chapter 4, not only low costs and installation effort are desirable development criteria for a sensor integrated bobbin carrier but also the elimination of the need for changing empty batteries as power supply units. This is due to the fact that the periodic replacement and recharging of empty batteries creates significant additional make-ready times, especially for braiding machines with a large number of carriers. In the following subsections, concepts for self-sufficient energy harvesting on sensor integrated carriers are proposed and discussed. The first concept features a shaker generator that harnesses the meandering movement of the carriers in horn gear-based braiding machines (cf. subsection 4.2.1). It was inspired by flashlights that need to be shaked in order to make them glow. The concept was prototypically implemented in a sensor integrated bobbin carrier for the RF 1/128-100 braiding machine at the Chair of Carbon Composites. The second concept that is introduced is based on the patent application by Reinisch et al [76]. It is made up of magnets that are attached to the stationary body of the braiding machine and an induction coil that is attached to the foot of the moving bobbin carrier. This concept was investigated because it appears to be easier to implement and more suitable to braiding machines with smaller horn gear diameters than the shaker generator. However, as will be shown in subsection 4.2.2, the generated electric power of this concept is about one order of magnitude smaller than the power obtained from the chosen shaker generator. The discussion of this concept of generator therefore serves as a justification for the choice of the shaker generator for the proposed prototype of the sensor integrated carrier. The third concept that is presented herein is made up of a generator whose rotor is comprised of a circular arrangement of permanent neodymium magnets on the rotor shaft in alternating magnetic polarity. The stator is comprised of the coil windings of the generator. When this type of generator is moved over a non-magnetic metal plate, the magnets on the rotor induce eddy currents in the plate that create local magnetic fields. These local magnetic fields in turn cause the rotor of the generator to spin. This concept was inspired by newly emerged bicycle dynamos that operate without touching contact to the tire or rim [95]. The concept was not practically implemented in the RF 1/128-100 braiding machine because it would have required extensive modifications to the machine. Nevertheless, for the case of a manufacturer of braiding machines developing a new machine, this theoretical concept shall nevertheless be presented within this thesis. Particularly in future braiding machines with fast moving carriers ($> 3\,\frac{m}{s}$) for extremely high material throughput and limited space around the feet of the carriers that do not allow the installation of the shaker generator, the concept of an eddy current generator may be worthwhile to consider.

4.2.1 Development and Analysis of the Practically Implemented Shaker Generator

In horn gear-based braiding machines, the carriers follow meandering tracks in order to form the interlacement structure of the braid. Thereby, a carrier in such a machine is subject to a centripetal acceleration that, with respect to a frame of reference that is fixed to the carrier, periodically reverses its direction. According to general physics, the centripetal acceleration $acc_{centripetal}$ of a single carrier that moves at the speed $v_{carrier}$ around a horn gear of diameter $d_{horn\ gear}$ can be written as

$$acc_{centripetal} = \frac{{v_{carrier}}^{2}}{\frac{d_{horn\ gear}}{2}} = \dot{\omega}^{2} \cdot \frac{d_{horn\ gear}}{2} \qquad (4\text{-}21).$$

In accordance with the considerations on the rotation of a bobbin in subsection 4.1.2, $\dot{\omega}$ is herein defined as the angular speed of rotation of the horn gear. The pseudo-acceleration that is experienced by the components of the carrier due to their moment of inertia is called centrifugal acceleration $acc_{centrifugal}$. This pseudo-acceleration $acc_{centrifugal}$ is of identical value as the centripetal acceleration $acc_{centripetal}$. However, the occurring centripetal acceleration $a_{centripetal}$ is directed towards the center of the horn gear and actually causes the bobbin to turn. The experienced centrifugal acceleration $acc_{centrifugal}$ is directed away from the center of the horn gear (cf. Figure 4-11).

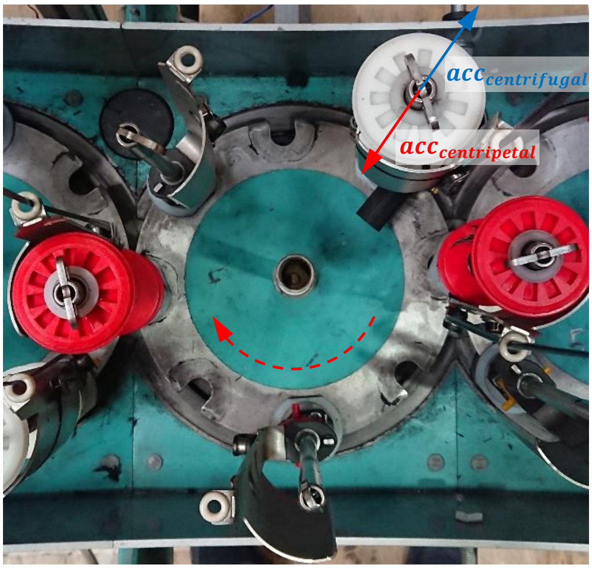

Figure 4-11: Rotating horn gear with acting centripetal acceleration $acc_{centripetal}$ and experienced centrifugal acceleration $acc_{centrifugal}$ of a bobbin carrier

The experienced centrifugal acceleration $acc_{centrifugal}$ of the components on the carrier due to their moment of inertia was harnessed for energy generation purposes by means of a 3D printed intermediate piece that can be placed between the foot the carrier and its sliding shoe (cf. Figure 4-12). The intermediate piece comprised a tube with an inner diameter of $d_{tube} = 21\ mm$ and a length of $l_{tube} = 95\ mm$. This length is close to the maximum length possible to avoid collisions with the other carriers and the body of the RF 1/128-100 braiding machine. The diameter of the tube was chosen so that it could house a cylindrical neodymium magnet of quality class N42 with a diameter and height of 20 mm. In the realized prototype, the tube was closed by means of adhesive tape after the magnet was inserted. In an industrial application, the use of a screw cap is also conceivable. A coil from enameled copper wire was wound around the center of the tube. This was possible because the spacer elements between foot of the carrier and sliding shoe were subdivided into two separate parts with a gap for the coil in between them. The spacer elements each featured a hole to insert threaded rods from non-magnetic A4 stainless steel. The threaded rods were screwed into the already existing threads in the sliding shoe, the bobbin carrier was added on top of the spacer elements and fixed by nuts from non-magnetic A4 stainless steel. The reason for using non-magnetic screw material was to not interfere with the motion of the cylindrical magnet inside the tube. When the braiding machine is running, the magnet inside the tube is pushed from one side to the other and vice versa due to the periodically changing centrifugal acceleration $a_{centrifugal}$, which the magnet experiences. An alternating electric current is generated when the field of the magnet enters and when it leaves the coil.

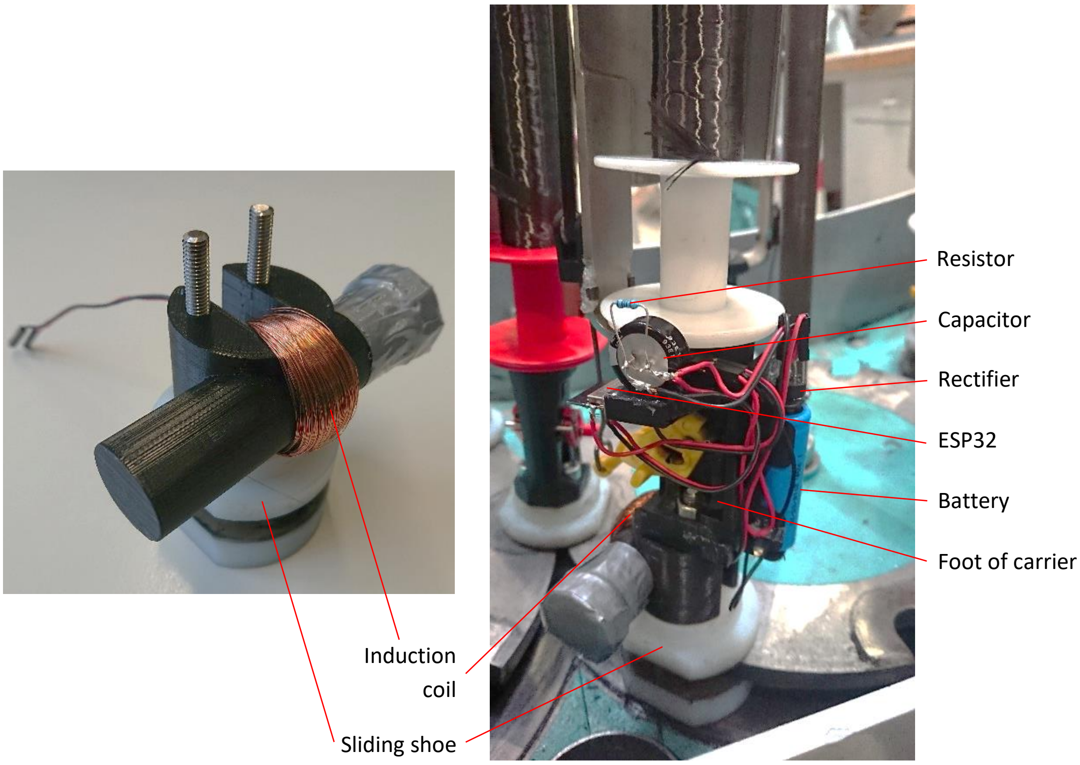

Figure 4-12: 3D printed intermediate piece with an induction coil wound around its tube that houses a cylindrical magnet (left); intermediate piece fitted between the sliding shoe and the foot of a carrier as well as an electric circuit for measuring the generated electric power during braiding (right)

The reader may wonder if the movement of such a big magnet interferes with measurements from the internal Hall sensor of the ESP32 sensor chip installed on the carrier. Such an undesirable behavior that would have required a magnetic shielding was not observed. This is attributed to the considerable distance between sensor chip and tube for the magnet (~6 cm) and to the fact that the integrated Hall sensor only detects a magnetic field when its field lines run perpendicularly through the main plane (26 mm x 18 mm) of the chip. In the picture in Figure 4-12, right, the direction perpendicular to the main plane of the chip would be oriented vertically (parallel to the central axis of the carrier). Since the central axis of the cylindrical magnet is aligned with the central axis of the tube of the intermediate piece, the magnetic field lines of the magnet are predominantly oriented in parallel to the main plane of the sensor chip. Therefore, they do not significantly affect the measurement results from the internal Hall sensor.

In order to measure the electric power generated by this kind of generator, a W005G-E4/51 rectifier from Vishay Intertechnology, Inc., a capacitor with an initial capacity of $C = 1000\ \mu F$ and a resistor with a resistance of $R = 100\ \Omega$ were connected in an electric circuit. The voltage U_R over the resistor was measured directly on the carrier via the voltage difference of two analog inputs of the ESP32 chip. For this purpose, the analog inputs of the chip were calibrated by means of a known reference voltage from an adjustable voltage source. As in section 4.1, the ESP32 chip, which now acted as voltmeter, was powered by an IFR14500 LiFePo4 battery and a step-up converter of the type U1V11F3 from Pololu Corporation for delivering a constant operating voltage of 3.3 V. The measurement data from the ESP32 was sent to an office laptop over BLE. A script written in MATLAB R2021a enabled the data acquisition by the nearby laptop. The circuit retrofitted to the bobbin carrier can be seen in Figure 4-12, right. Since the exact wiring is difficult to oversee, the wiring diagram for measuring the delivered power by the shaker generator is given in Figure 4-13.

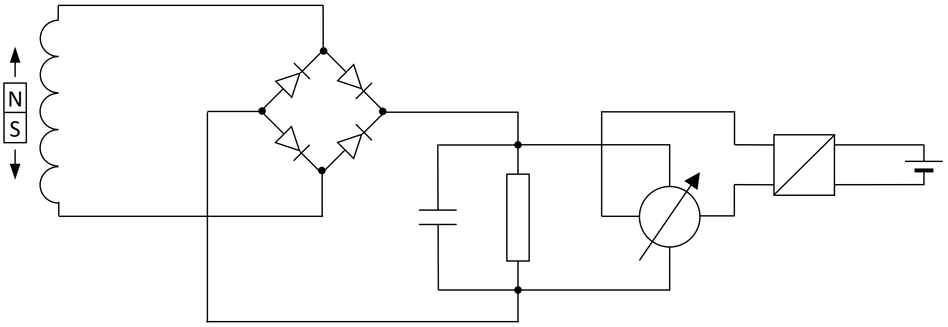

Figure 4-13: Wiring diagram for measuring the power generated by the shaker generator with functional elements from left to right: coil around the tube of the 3D printed intermediate piece, rectifier, capacitor, resistor, ESP32 chip as voltmeter powered via a voltage regulator by a battery

This measurement circuit was used to determine the electric power generated by five different windings of the coil around the tube of the intermediate piece. For the different variants, the diameter of the copper wire in the coil was varied between $d_{wire} = \{0.05\ mm; 0.1\ mm; 0.2\ mm; 0.3\ mm; 0.4\ mm\}$. Since there was a given amount of space for the coil on the intermediate piece, the different diameters of the copper wire resulted in different wire lengths that could be wound around the tube $l_{wire} =$

$\{1500\ m; 450\ m; 110\ m; 50\ m; 35\ m\}$. The reason for testing these different variants was that the number of windings in the coil is higher for thinner diameters d_{wire}. Thus, the generated voltage and power is potentially higher. However, the internal resistance of the coils drastically increase with reduced wire diameter d_{wire} and greater length of the wire l_{wire}. The test series was therefore intended to find a near-optimum configuration for the winding of the coil around the tube.

Each variant was retrofitted to the carrier with the integrated measurement circuit (cf. Figure 4-12) and tested in the operating RF 1/128-100 braiding machine. The speed of horn gear rotation of the machine r was varied between multiples of 16.25 rpm up to 130 rpm. Finally, the maximum speed of the machine of $r = 139\ rpm$ was tested. The generated power $P_{average}$ was determined by

$$P_{average} = \frac{1}{R \cdot n} \cdot \sum_{i=1}^{n} U_{R,equillibrium}{}^{2} \tag{4-22}$$

when the capacitor was charged and the voltage over the resistor had reached its equilibrium state $U_{R,equillibrium}$. i thereby corresponds to the enumeration of the data points, which were acquired by the ESP32 at an approximate rate of 100 scans/s. The averaging term was necessary because although a capacitor was integrated into the electric circuit, significant fluctuations in the measured voltage were still observable due to the movement of the large magnet through the coil. The results on generated electric power for the five different variants under the different speeds of horn gear rotation are plotted in Figure 4-14. For all variants, it is observable that the generated power increases with higher machine speeds. The variant with a diameter of the copper wire of $d_{wire} = 0.2\ mm$ represents an optimum regarding power output compared to the other variants. For this reason, the wire diameter of $d_{wire} = 0.2\ mm$ was chosen for further analyses.

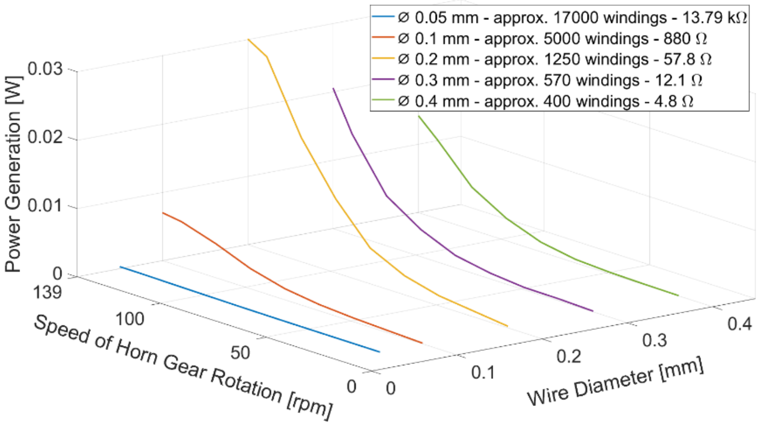

Figure 4-14: Generated power of the shaker generator depending on wire diameter of the coil winding and machine speed; capacitor in the electric circuit with $C = 1000\ \mu F$

When powered by an IFR14500 LiFePo4 battery, the power consumption of the ESP32 chip in BLE active mode (sending 100 scans/s) including losses originating from the step-up converter could be determined by its current draw measured by a multimeter to 0.166 W. From the data shown above, it becomes apparent that the proposed generator cannot continuously power the chip in this mode of operation. It however needs to be noted that it provides limited benefit when all carriers of a braiding machine constantly send data. It is of nearly identical value when the sensor integrated carriers only send data upon occurrence of an unwinding-related process irregularity. For such cases, the ESP32 can be operated in the so-called light sleep mode. In this mode of operation, the radio connection is shut down and the chip rests in a standby mode. In this mode of operation and still including losses originating from the step-up converter, the power consumption was measured to be reduced to 0.009 W, which is significantly less than the maximum generated power by the shaker generator in Figure 4-14. The chip can periodically be woken up by a timer, for instance in order to check the remaining yarn mass on the bobbin according to the relations explained in subsection 4.1.2. Moreover, peripherals such as digital inputs can still be used to wake up the chip. The latter possibility is particularly useful when the chip shall send an alarm upon detection of an unwinding-related irregularity.

In either case, the electric circuit in which the chip is integrated needs to be able to store electric energy as long as the chip is in light sleep mode and release the stored energy when the chip switches into active mode. It was found that a capacitor of the initial capacity of $C = 1000\ \mu F$ was not able to continuously power the sensor chip. A capacitor of the type 473120 from Thomsen-Elektronik GmbH with a significantly higher capacity of $C = 1\ F$ was found to be able to power the sensor chip in light sleep mode. This is why this type of capacitor was applied in the further analyses. Note that this type of capacitor is already shown in Figure 4-12, right.

The RF 1/128-100 braiding machine features horn gears with a comparably large diameter. This is due to the fact that the horn gears show eight notches in order for the machine to be able to produce a 4x4 braid interlacement structure. In general braiding however, the 2x2 interlacement structure and thus smaller horn gears are more common. Since there may not be enough space for the long tube of the shaker generator with $l_{tube} = 95\ mm$ shown in Figure 4-12 in these machines, the power generation of shorter tube lengths of $l_{tube} = \{85\ mm; 75\ mm; 65\ mm; 55\ mm; 45\ mm\}$ were also investigated. The results on the generated power of these modified generator setups for the optimum wire diameter of $d_{wire} = 0.2\ mm$, a speed of horn gear rotation of $r = 139\ rpm$ and the newly introduced capacitor with $C = 1\ F$ are illustrated in the diagram in Figure 4-15. It can be observed that the generated power decreases approximately linearly from a tube length of $l_{tube} = 95\ mm$ down to a tube length of $l_{tube} = 65\ mm$. Below $l_{tube} = 65\ mm$, the linear downward trend is even more pronounced. Except for the case of $l_{tube} = 45\ mm$, the generated power of the shorter tube lengths is still more than the required 0.009 W for enabling a light sleep mode of the ESP32 chip.

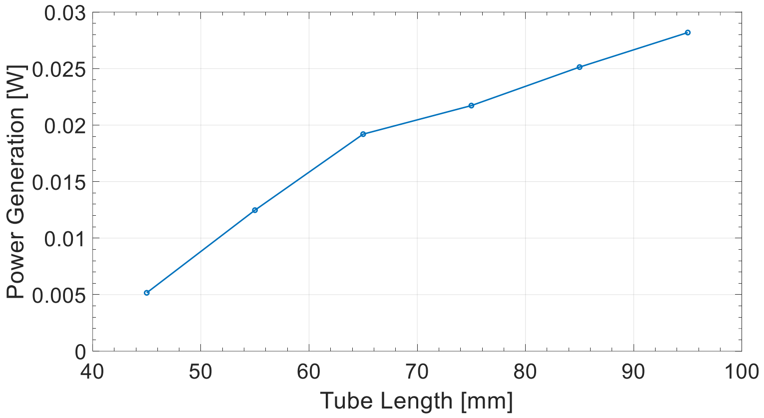

Figure 4-15: Generated power of the shaker generator depending on length of the tube that houses the magnet; wire diameter of coil winding $d_{wire} = 0.2\ mm$, speed of horn gear rotation $r = 139\ rpm$, capacitor in the electric circuit with $C = 1\ F$

The data point on a tube length of $l_{tube} = 95\ mm$ (0.028 W) in Figure 4-15 shows a small difference to the data point in Figure 4-14 on the maximum machine speed and a wire diameter of $d_{wire} = 0.2\ mm$ (0.030 W). Since the same tube length of $l_{tube} = 95\ mm$ was investigated in both cases, this discrepancy can be attributed to the use of the capacitor with the higher capacity of $C = 1\ F$ in Figure 4-15. Although the larger capacitor was charged for five minutes in the running braiding machine (until its voltage did, at least on inspection of the data by eye, not increase any more) and the measurement on the generated power was carried out over the course of the sixth minute of the experiment, it may take the larger capacitor even longer to reach a full equilibrium state of charge. This may explain the slight difference in measurement results between the two types of capacitors. Nevertheless, this can be regarded as a minor difference and rather as a confirmation that the measured power output from the generator does not significantly differ depending on which type of capacitor is used.

The fact that only the tube length of $l_{tube} = 45\ mm$ fails to meet the power requirement of the light sleep mode can however still not be taken as a guarantee that the other tube lengths are sufficient for fully powering the sensor chip. The problem that was observed is that the sensor chip shows a peak in current draw the moment it switches from light sleep mode to normal operating mode. This peak in current draw was measured to approximately 150 mA by means of a multimeter. The actual current peak may even be higher when an oscilloscope of high temporal resolution is used for the measurement. Such a high current peak could not even be maintained by the larger capacitor. This is why it is proposed to still integrate a LiFePo4 battery of the type IFR14500 into the circuit of the final version of the prototype of the sensor integrated bobbin carrier. The schematic wiring diagram of the proposed prototype is given in Figure 4-16. The alternating current generated by the coil around the tube that houses the magnet is converted into direct current by a rectifier. The direct current is used to charge the capacitor with a capacity of $C = 1\ F$. Although the capacitor itself can, due to its design, not be overcharged, the maximum operating voltage of the U1V11F3 voltage regulator is 5.5 V. To protect the voltage regulator from overvoltage, a Zener diode of the type BZX85C5V1-TR from Vishay Intertechnology, Inc. was added to the electronic circuit. Due to the Zener voltage of 5.1 V, the capacitor is discharged before the voltage reaches values that could break the voltage regulator. In order to protect the Zener diode from excessive discharging current, a resistor with a resistance of $R = 100\ \Omega$ was added. The value of this protective resistor was selected based on the Zener voltage of 5.1 V and the admissible Zener current of this particular type of diode of 200 mA, thereby leaving enough margin for a voltage peak from the generator at the moment the diode is about to turn conductive. The 3.3 V generated by the voltage regulator is intended to power the ESP32 chip in light sleep mode and also as a charging voltage to the battery. The leakage current from the battery through the voltage regulator in case of an uncharged capacitor was measured to 2µA and can therefore be regarded as negligible. The chip is programmed in a way that its default mode of operation is light sleep. As long as the switch at the very right of Figure 4-16 connects the ground level to a digital input of the chip, the chip remains in light sleep mode. The value of the pull-down resistor was chosen to $R = 100\ k\Omega$ in order to minimize any leakage current. As soon as the switch gets pushed, the chip changes to active mode and sends data from its internal Hall sensor over BLE. The operation of the sensor chip is then maintained by the battery since the capacitor cannot deliver enough current to cover the high current draw by the chip. The BLE data stream can be detected and analyzed by a machine control unit in order to stop the braiding machine.

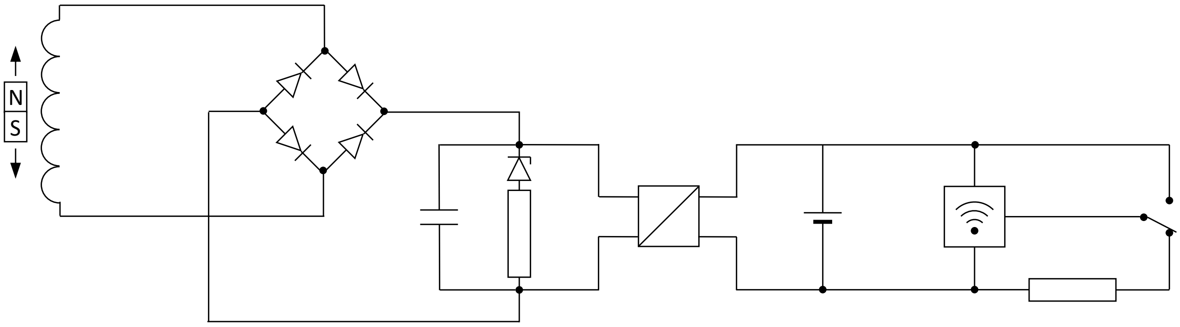

Figure 4-16: Wiring diagram for the prototype of the sensor integrated bobbin carrier with functional elements from left to right: coil around the tube of the 3D printed intermediate piece, rectifier, capacitor, Zener diode with protective resistor, voltage regulator, battery, ESP32 chip as transmitting unit, pull-down resistor and switch

Photographs of the proposed prototype of the sensor integrated bobbin carrier are shown in Figure 4-17. It is observable that both a capacitor and a battery are used to power the sensor chip. The battery is intended to power the sensor chip when the capacitor is not charged yet from the machine movement (e.g. due to a recent startup of the braiding machine) and when the sensor chip switches from light sleep mode to active mode. The switch from light sleep to active mode is triggered by a button that is pushed by the tension lever of the yarn tensioning unit. As explained in section 3.1, the tension lever is pulled to its uppermost position (when it can push the switch) only when an unwinding related irregularity occurs. The sensor chip needs to be reset in order to get it back into light sleep mode after the resolve of an irregularity. In the prototype, this is achieved by removing the battery from one contact in the battery holder for a few seconds. It is also conceivable to integrate another pushbutton as a reset button or to implement in the code of the chip that it returns into light sleep mode after a certain period of time (e.g. 30 s) or upon receival of a BLE signal from an external machine control unit. The return to light sleep mode after the resolve of the error cause is vital because the active mode would otherwise empty the battery over time, which would eventually force its replacement and recharge.

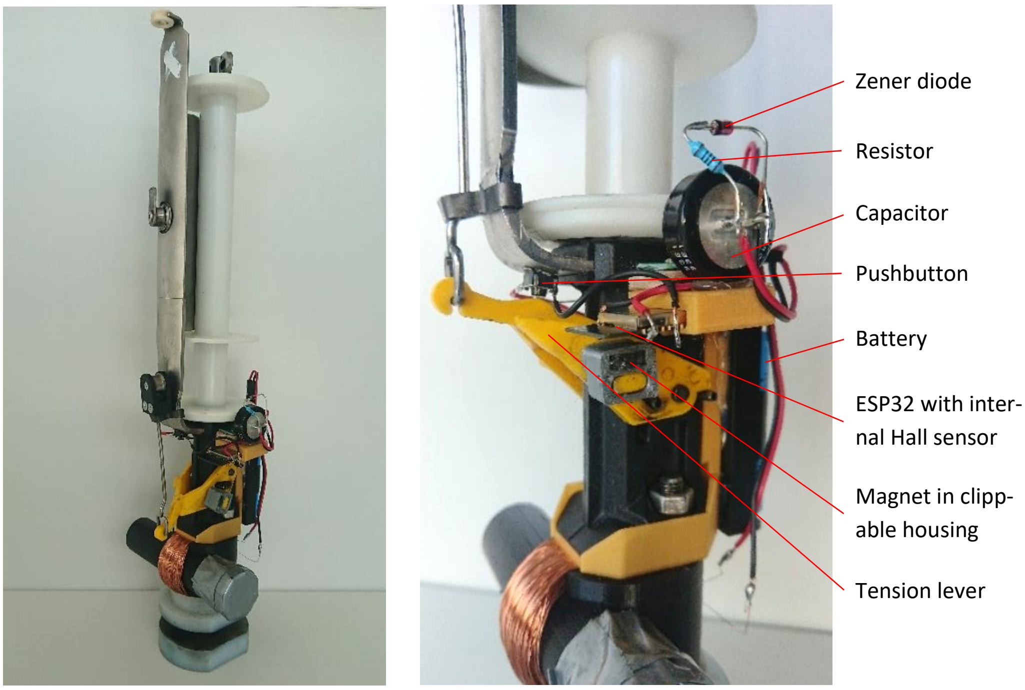

Figure 4-17: Overview (left) and detailed view (right) of the proposed prototype of the sensor integrated carrier; note the button that is pushed by the tension lever of the carrier in order to trigger a wakeup of the sensor chip

The additional material costs of the above sensor integrated carrier can roughly be summed up to 30 € (years of bid solicitation for taking inflation into account: 2020-2022, cf. Table 4-2). This falls within the initially defined range of target material costs of 10-15 % of a mechanical carrier with guide plate ($\approx 250\,€ \cdot 0.1 \approx 25\,€$, $\approx 250\,€ \cdot 0.15 \approx 37.5\,€$). Of course, these costs do not include any assembly effort or a profit margin. It must however also be noted that the approximate prices are single piece prices and do not include any economies of scale as a manufacturer of braiding machines would be able to harness when equipping one or more machines with the sensor circuit. All in all, this consideration of costs is not meant to constitute a thorough economic assessment. It shall only demonstrate that it is possible to upgrade an existing bobbin carrier with sensing devices and an energy harvesting unit at a level of costs that is in a reasonable relation to the costs of a carrier with guide plate. It may also be the case that there will be future models of a sensor chip that succeed the chosen ESP32 and that are even more power-saving. Particularly when the peak in current draw when switching from light sleep mode to active mode can be reduced, the possibility of eradicating the need for a battery would be opened. Finally, it needs to be noted that there may be more efficient ways to realize such a prototype even today. For instance, the number of coil windings was only selected by making efficient use of the available installation space in the considerations above. The voltage induced by the generator could be measured in a short circuit and the number of coil windings could consequently be optimized in order to achieve a peak generator voltage that matches the requirements of the particular components of the electric circuit best (e.g. the throttle consisting of Zener diode and resistor). Also, the generatable electric power could be further increased by higher numbers of coil windings of the same wire diameter d_{wire}. Moreover, the protective elements Zener diode and resistor could be replaced by a DC/DC converter with a wide input voltage range (that matches the peak voltage of the generator) to ensure a limitation of the voltage for the sensor chip and the battery. This could be more efficient than a voltage limitation by means of a Zener diode and a resistor. Furthermore, the voltage for the sensor chip could be decoupled from the battery voltage by means of a charging controller. This way, the charging process of the battery could be tailored to the requirements of a specific type of battery. It was however not front and center of this dissertation at hand to optimize electric circuits as an electrical engineer would do. The above investigations on the operating principles are meant for technology demonstration purposes and can serve manufacturers and operators of braiding machines as a starting point for improved and industrialized versions of cost-efficient sensor integrated bobbin carriers.

Table 4-2: List of main components for the proposed prototype of the sensor integrated carrier and approximate net prices from the years 2020-2022

Component	Approximate net price
Enameled copper wire	~5 €
Rectifier W005G-E4/51	~0.5 €
Capacitor 473120	~6 €
Zener diode BZX85C5V1-TR	~0.2 €
Voltage regulator U1V11F3	~4 €
Battery IFR14500 600 mAh	~4 €
Battery holder AA	~1 €
ESP32-SOLO-1	~3 €
Neodymium magnet (Ø 20 mm x 20 mm)	~4 €
Neodymium magnets (Ø 8 mm x 3 mm)	~0.1 €
Miscellaneous (Wiring, printable polymer, resistors, switch, threaded bolts and nuts…)	~2 €

In conclusion of this subsection on the implemented shaker generator for an energy harvesting from machine movement, the following statements can be made:

- The shaker generator can be fitted between the foot of an existing IFDA-100 carrier with guide plate and its sliding shoe. In the available RF 1/128-100 braiding machine from HERZOG GmbH, this did not lead to any collisions of the carriers with the retrofitted devices.
- An influence of the application of the shaker generator on the measurement values from the internal Hall sensor of the ESP32 sensor chip could not be observed. Hence, a magnetic shielding of the magnet in the generator does not appear necessary.
- A near-optimum winding of the coil for the generator was found to be a wire diameter of $d_{wire} = 0.2\,mm$ at a wire length of $l_{wire} = 110\,m$. The maximum generatable power by the shaker generator implemented in the RF 1/128-100 braiding machine was measured to be approximately 0.03 W.

- The less space there is around the foot of the carrier, the shorter the tube length l_{tube} may be in order to avoid collisions. Shorter tube lengths l_{tube} result in less power generation.
- The RF 1/128-100 braiding machine features horn gears with a comparatively large diameter (much space for large tube lengths l_{tube}) but its maximum speed of horn gear rotation is low compared to other braiding machines ($r_{max} = 139\ rpm$, limit for power output). The performance of the generator in machines with smaller horn gears that turn faster remains to be evaluated in future research.
- In the above-described configuration, the default mode of operation for the sensor chip needs to be the light sleep due to constraints regarding power consumption (measured consumption in light sleep: ~0.009 W). The chip can be woken up and send data from its internal Hall sensor via BLE by means of a periodic timer or upon occurrence of an external impulse such as the push of a button (measured consumption in active mode: ~0.166 W). Thereby, the sensor chip can be used to regularly check the filling degree of the bobbin or to notify the machine control of a process defect.
- In the proposed prototype of the sensor integrated bobbin carrier, a battery is still required to cover the high current draw when the sensor chip switches from light sleep to active mode. Future developments in energy-saving sensing technology may eradicate the need for a battery.

4.2.2 Analyses on Further Concepts for Supplying Electric Energy to Moving Bobbin Carriers

The above-described shaker generator was retrofitted to an IFDA-100 carrier with guide plate and tested in the RF 1/128-100 braiding machine at the Chair of Carbon Composites. For reasons of available space around the feet of the carriers, the above generator concept may however not be suitable for all use cases and types of braiding machines. Since other types of machines were not available to the author during preparation of the dissertation at hand, the author could not develop and test numerous other variants that may be better suitable for other types of braiding machines. Nevertheless, the author would in this subsection like to briefly document findings that he made on other types of generators during the development process towards the realized shaker generator as a starting point for any possible future research on this issue.

Apart from the bobbin carrier built by von Reden [45] and von Reden et al. [77] (cf. Figure 2-14), particularly the patent application by Reinisch et al. [76] lists several other concepts for supplying electric power to moving carriers, including…

- a power supply by conductive braiding yarns,
- a dynamo on the carrier driven by a friction wheel,
- an electric generator on the carrier that brakes the bobbin,
- stationary magnets in combination with induction coils on the moving carriers and
- sliding contacts of which one pair of contacts is attached to the moving carrier and another pair of contacts is attached stationarily to the body of the braiding machine.

As mentioned in the introductory section to chapter 4, the concept by von Reden [45] and von Reden et al. [77] may come with high costs compared to the carrier itself. A power supply by conductive braiding yarns can be a viable option when metal wires are braided. In braiding of reinforcement yarns, the concept appears problematic because fraying fibers may cause short circuits. Whereas carbon still exhibits some degree of electrical conductance, glass fibers completely lack this capability, for instance. Sliding contacts between carriers and stationary parts of the braiding machine may be an easily implementable option but also appear problematic against the background of the given industrial use case of braiding of carbon fibers due to short circuits from frayed fibers and conductive fiber dust. Generating significant amount of electric power from braking the rotating bobbin in the carrier does not appear plausible to the author due to the low rotational speed of the bobbin. The remaining two options for powering devices on the carrier namely stationary magnets in combination with induction coils on the carrier as well as a dynamo driven by the relative motion between carrier and braiding machine do appear realizable to the author in the context of composites braiding. This is why these concepts are briefly investigated and discussed within the scope of the following subsections.

Stationary Magnets in Combination with an Induction Coil on the Carrier

Attaching induction coils to the feet of the moving carriers would require significantly less space than the developed intermediate piece with the tube that houses an accelerated cylindrical magnet. Hence, such a solution would particularly be suitable for an application in braiding machines with comparatively small horn gear diameters. Since the electric circuit for the measurement of the generated electric power was already installed on one sensor integrated carrier (cf. Figure 4-12 and Figure 4-13), the power output from such a generator type was measured and compared to the chosen shaker generator. For this, a modified intermediate piece to be inserted between the sliding shoe and the foot of the carrier was 3D printed and an induction coil from enameled copper wire was wound around it. The coil was only wound on one side of the foot of the carrier for reasons of simplicity. If the approach had proven to be a viable option, a second coil could have been added to the other side of the foot of the carrier to double the generated electric power. Moreover, the coils could have been directly attached to the foot of the carrier without a 3D printed intermediary piece. The same copper wire ($d_{wire} = 0.2\,mm$, $l_{wire} = 110\,m$) that was found to be optimal for the shaker generator was used for the induction coil. Also, the same neodymium magnets of 20 mm in diameter and height that were used in the shaker generator were stationarily attached to the body of the RF 1/128-100 braiding machine. Since an induction coil was only attached to one side of the foot of the carrier, the magnets were placed adjacent to every second horn gear. The dimensions of the modified intermediary piece were selected so that the gap between the stationary magnets and the induction coil was minimized. As can be seen in Figure 4-18, the remaining gap was about 3 mm in size. Such a gap size was necessary due to the curved path of the carrier, which caused the intermediary piece to almost touch the magnet upon approach to and departure from the magnet.

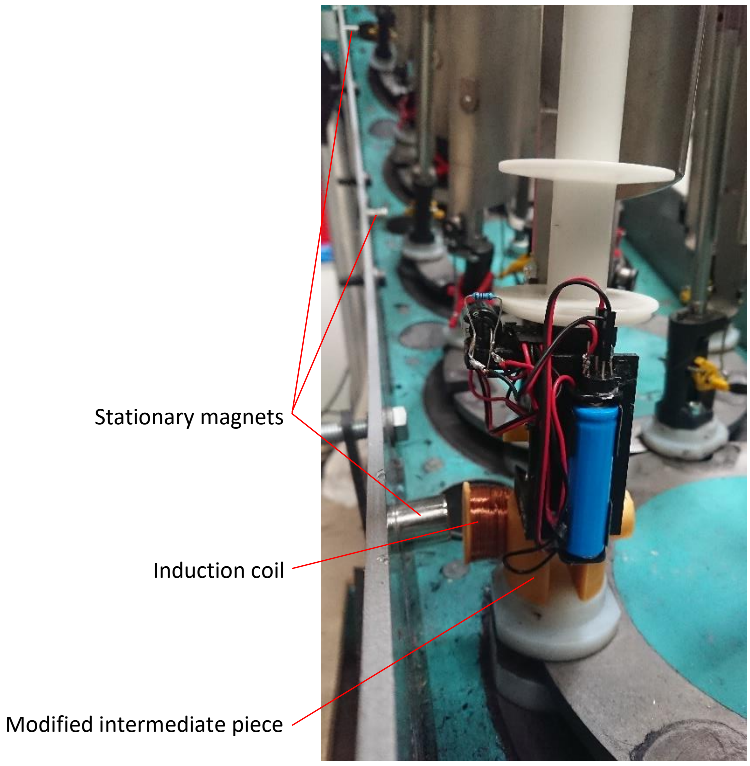

Figure 4-18: Induction coil on one side of the foot of the carrier and stationary magnets attached to the body of the braiding machine

The electric power that was generated by the setup shown above during braiding at a speed of horn gear rotation of $r = 139\,rpm$ could be measured to approximately $5.85 \cdot 10^{-4}\,W$. Accounting for the fact that an induction coil was only mounted to one side of the foot of the carrier leads to a theoretical potential of power generation for the given setup of $2 \cdot 5.85 \cdot 10^{-4}\,W = 1.17 \cdot 10^{-3}\,W$. This is only 4 % of the measured electric power of the shaker generator with otherwise comparable setup (maximum: $3 \cdot 10^{-2}\,W$, cf. Figure 4-14). One could argue that there is still ample space around the horn gears in Figure 4-18 for more stationary magnets to be placed there in order to achieve a higher power generation. This is certainly the case for the investigated RF 1/128-100 braiding machine, but since such an approach is anticipated to be particularly suitable for machines with smaller horn gear diameters, such an argument is considerably weakened.

The author attributes this discrepancy in generated power to the fact that the field of the magnet is in much more intense interaction with the coil in case of the shaker generator than in case of the separate induction coil. Firstly, there is barely a gap between magnet and coil in case of the shaker generator because the wall thickness of the tube is only 1 mm. Secondly, the entirety of the magnetic field actually “dives” through the coil in case of the shaker generator instead of relying on its spacial extent along the central axis of the cylindrical magnet. Thirdly, only in a fraction of the wound wire length of the separate induction coil in Figure 4-18 an actual generation of power can take place. This is due to the fact that maximum power generation takes place when the orientation of the wire is perpendicular to the relative motion between wire and magnetic field. In the top and bottom area of the coil shown in Figure 4-18, the wire orientation is identical to the motion vector of the carrier. Hence, no power can actually be generated in these areas. In case of the shaker generator, every infinitesimal length of the wound wire can fully contribute to the power generation because the entirety of the wire length is oriented perpendicularly to the motion of the magnetic field. Summing up the findings on the induction coil in combination with stationary magnets attached to the body of the machine, it can be said that there can certainly be made improvements to the setup illustrated in Figure 4-18 (e.g. a flatter coil in order to reduce the effective distance between coil and magnet). However, if a tube with an accelerated magnet can be installed at the foot of a carrier, such an approach can conceptually be regarded as more promising in terms of expectable energy output compared to stationary magnets. This is why the shaker generator was chosen as the type of generator in the proposed prototype of a sensor integrated bobbin carrier (cf. subsection 4.2.1).

Eddy Current Generator as Contactless Dynamo

The idea of generating significant electric power from the relative motion between moving carrier and stationary body of the machine by means of a friction wheel and a dynamo as proposed by Reinisch et al. [76] appeared as a partly viable option to the author. On the one hand, the speed of the carrier with respect to the body of the machine is typically in the order of $1 - 2\,\frac{m}{s}$ (cf. formula (3-16) in subsection 3.3.2), which is, in contrast to the rotational speed of a bobbin on the carrier, conceivable to generate a significant amount of power. On the other hand, the contact area between sliding shoe of a carrier and the stationary body of the machine is often heavily oiled. This poses a potential problem when a friction wheel seeks to find traction. Moreover, the oil is mixed with fiber dust that was grinded down from reinforcement filaments. In case of processing conductive carbon fiber, this may damage a dynamo when it is not properly sealed against environmental media.

For these reasons, the author came up with a concept of an eddy current generator that can conceptually be housed completely inside the sliding shoe of a carrier because it does not require physical (touching) contact to a surface moving relative to the generator. The eddy current generator proposed herein only requires a movement of the carrier relative to a non-magnetic but electrically conductive material. The concept was inspired by an invention by Strothmann [95]. The patent specification describes the invention as a contactless dynamo for bicycles (cf. Figure 4-19, left). The main feature of the generator is the rotor (2) that consists of a shaft on which magnets are arranged in alternating polarity (2b, 2c). As the aluminum bicycle rim (1) turns, the shaft with the attached magnets starts to rotate. This in turn creates an alternating current in the coil (7) wound around the rotor. The detailed working principle is illustrated in Figure 4-19, right. When for instance a magnetic north pole from the rotor is closest to the turning bicycle rim (1), a magnetic south pole (5a, eddy current in counterclockwise direction) is induced on the surface of the rim slightly ahead of the north pole on the rotor. Moreover, a magnetic north pole (5b, eddy current in clockwise direction) is induced on the surface of the rim slightly behind the north pole on the rotor. The north pole on the rotor is attracted to the south pole on the surface of the rim and repelled by the north pole on the surface of the rim. This makes the rotor turn in clockwise direction. When the succeeding south pole on the rotor gets closest to the rim, it maintains the previously established north pole on the surface of the rim (5b). However, this pole is now slightly ahead of the south pole on the rotor. Additionally, a new south pole on the surface of the rim is created that is slightly behind the south pole on the rotor. The maintained north pole on the surface of the rim attracts the south pole on the rotor. Likewise, the newly created south pole on the surface of the rim repels the south pole on the rotor. Thereby, the rotation of the rotor is maintained as long as the rim turns.

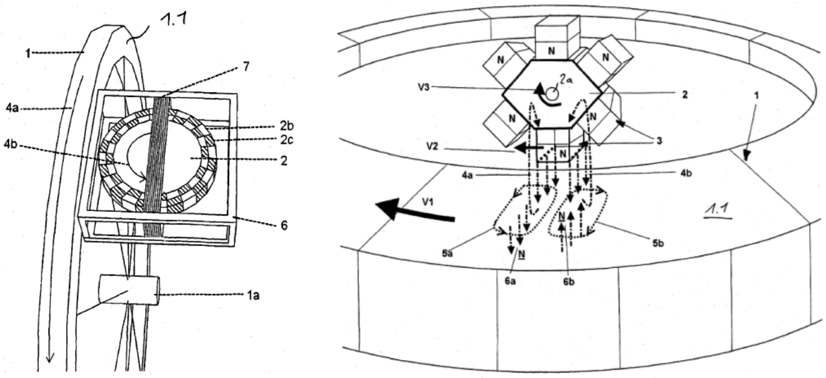

Figure 4-19: Eddy current generator as contactless bicycle dynamo (left), working principle of the generator by eddy currents (right); both drawings taken from [95]

The concept from above can in principle not only be used for contactless bicycle dynamos but potentially also for electric generators on sensor integrated bobbin carriers. In this case, the generator would be housed in the foot of the carrier. The base plate of the braiding machine, against which the carrier moves as it travels along its track, would take the place of the bicycle rim as counterpart to the generator.

An important prerequisite is however that the base plate of the braiding machine must be made from non-magnetic metal such as aluminum or austenitic steel (e.g. stainless steel). Conventional machinery steel usually contains portions of ferritic or martensitic structure, which are both magnetic. In case of a magnetic counterpart, the rotor of the generator cannot turn. This is because the magnetic attraction between base plate and the magnetic pole on the rotor that is closest to the base plate is far greater than the magnetic interaction due to the induced eddy currents. Moreover, the sliding shoe of the carriers and the part of the horn gear that is in contact with the sliding shoe need to be made from non-magnetic and electrically isolating material (e.g. plastic). Otherwise, the rotational motion of the rotor would be slowed down due to eddy currents induced either in the sliding shoe or the horn gear. If it is not possible for a manufacturer of braiding machines to make the machine bed from non-magnetic metal, e.g. for reasons of durability or costs, there is the option of introducing notches into the machine bed that are perpendicular to the direction of movement of the carriers. As can be seen in Figure 2-14 and Figure 4-11 there is a groove that is milled into the machine bed directly below the horn gears along which the carriers travel. In the same process of milling this groove, notches perpendicular to this groove could be milled into the machine bed at a spacing that corresponds to the spacing of the magnets on the rotor of the generator. This way, the rotor of the generator would not be turned by induced eddy currents but by a kind of “magnetic gears”.

Even though none of the options described in the above paragraph was possible for the author to implement in the RF 1/128-100 braiding machine, a cavity was exemplarily milled into the sliding shoe of a carrier and a small eddy current generator jointly manufactured by the student [93] and the author was inserted. Figure 4-20 shows the generator, which was made up of a custom made steel shaft on which cuboid neodymium magnets of quality class N52 and of dimensions 35 mm x 4 mm x 2 mm were attached. The coil winding was made from enameled copper wire of $d_{wire} = 0.2\ mm$ and applied to a 3D printed cage.

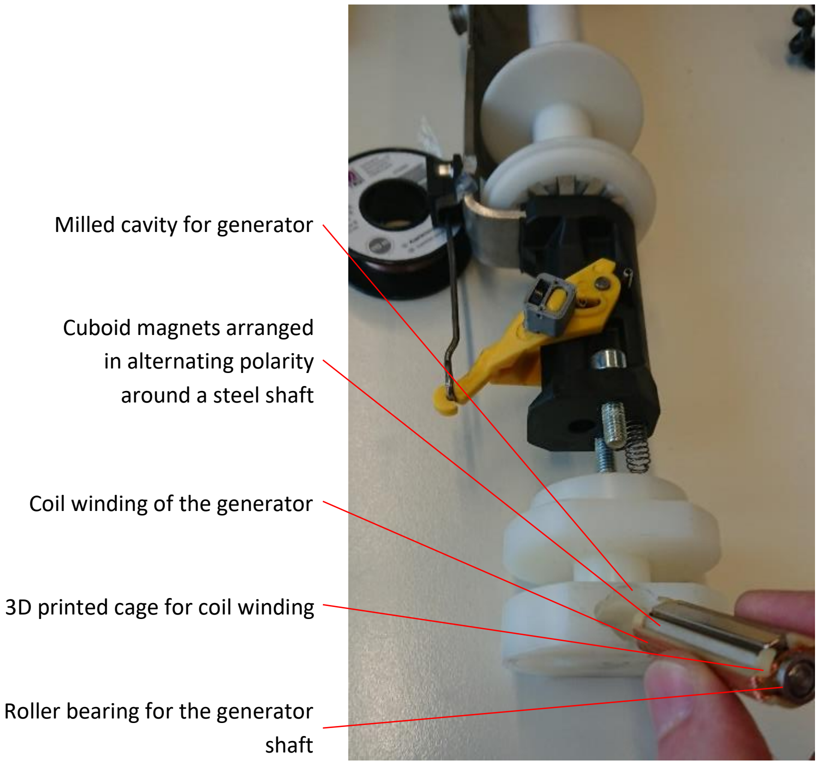

Figure 4-20: Fitting of an eddy current generator into a milled cavity in a plastic sliding shoe of an IFDA-100 carrier

The theoretically obtainable electric power from this eddy current generator was measured by placing it closely above an aluminum disc (electrically conductive but non-magnetic) that was turning at a rotational speed of $r = 130\ rpm$. The radial distance between the eddy current generator and the center of the disc was set to 22.5 cm, which is similar to the effective radius of the horn gears in the RF 1/128-100 braiding machine. As measurement circuit, in principle the same circuit as shown in Figure 4-13 was used expect for the fact that a standard voltmeter could be applied to measure the voltage over the resistor instead of the ESP32 sensor chip. Although the rotational speed of the rotor of the generator reached values in the order of 1500 rpm, the generated power could only be measured to $9 \cdot 10^{-5}\ W$.

The author attributes the low power output to the small size of the applied magnets and the limited number of coil windings. Both are due to the limited height that the lower plate of the sliding shoe offers for integration of electric devices (thickness of plate: ~13 mm). If a manufacturer of braiding machines develops a new machine and makes changes to the base plate of the machine as described above, the thickness of the lower plate of the sliding shoes can also be adapted. This is why a significantly larger eddy current bicycle dynamo of the type NOVA was purchased from the Danish company Reelight ApS (height of generator: ~20 mm, cf. Figure 4-21) for research purposes.

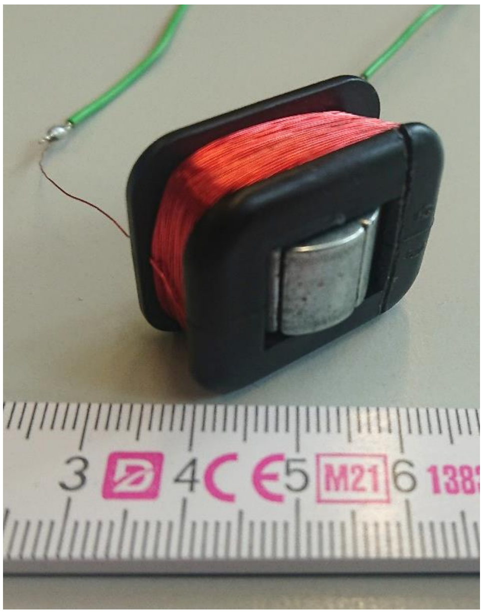

Figure 4-21: Eddy current generator inside the contactless dynamo of the type NOVA from Reelight ApS

Like the small self-manufactured eddy current generator, the power output of this larger generator was measured by means of placing it closely above a rotating aluminum disc. The measurement series under variation of the rotational speed of the disc was intended to provide an orientation for future developments of braiding machines how much energy can be harvested from the movement of bobbin carriers by this type of generator. As can be seen in Figure 4-22, the generated electric power increases exponentially up to approximately 0.4 W at a rotational speed of the disc of $r = 406.25\ rpm$. Accounting for the effective radius of the disc of 22.5 cm, this results in a relative speed between generator and disc of $4.79\frac{m}{s}$. At a rotational speed of $r = 139\ rpm$, which is the maximum speed of the RF 1/128-100 braiding machine, the generated power was measured to 0.017 W, which is less than the 0.03 W obtained from the shaker generator at the same speed of horn gear rotation.

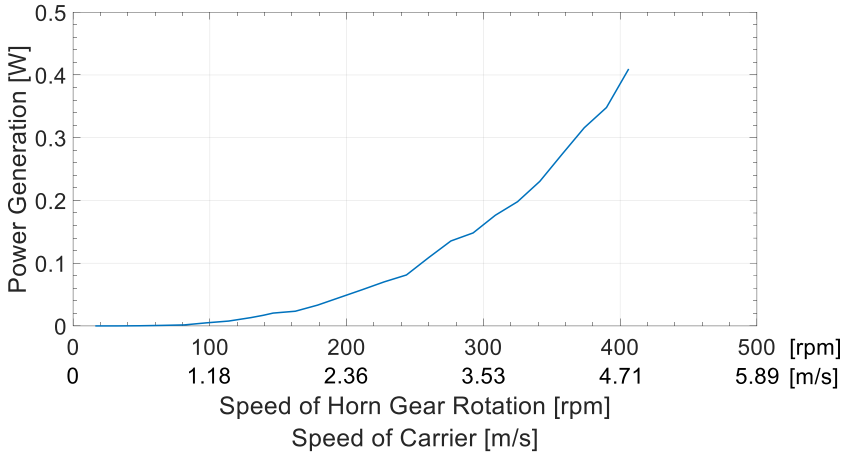

Figure 4-22: Electric power generated by the eddy current generator inside the contactless dynamo of the type NOVA from Reelight ApS under variation of the relative speed between aluminum plate and generator

Due to the exponential nature of the measurement curve, an eddy current generator of the investigated or similar type in the foot of the sliding shoe of a carrier appears particularly interesting when the carriers reach speeds of more than $3\,\frac{m}{s}$ relative to the machine bed. This is about twice as fast as the carriers move in the RF 1/128-100 braiding machine (cf. formula (3-16)). Beyond $3.5\,\frac{m}{s}$ carrier speed, this type of generator may even be able to continuously power the ESP32 sensor chip in full active mode with constant data stream over a BLE connection. The behavior of the shaker generator could not be tested at the corresponding speeds of horn gear rotation of $r > 300\ rpm$ because such a machine was not available to the author during preparation of the thesis at hand. The facts that the measurement curves obtained from the shaker generator also show an exponential behavior (cf. Figure 4-14) and that this generator outputs more electric power up to the investigated level of horn gear rotation of $r = 139\ rpm$ than the investigated contactless dynamo suggest that the shaker generator may also generate more power at higher speeds of horn gear rotation. An argument in favor of the eddy current generator is its smooth run due to purely rotational movement. Particularly at high speeds of horn gear rotation, the shaker generator may behave increasingly “violently” due to the constant back and forth movement of the large magnet.

As a summary on this subsection on further concepts for the generation of electric energy on moving bobbin carriers, the following statements can be made:

- Stationary magnets attached to the body of a braiding machine in conjunction with induction coils on the moving carriers appear as easier to implement than the shaker generator particularly when the space around the feet of the bobbin carriers is limited. Under usage of identical components (magnets, enameled copper wire) such an approach was however observed to generate an electric power that is approximately one order of magnitude smaller than the power generated from the shaker generator. This finding serves as a justification for the implementation of a shaker generator in the proposed prototype of a sensor integrated bobbin carrier with energy harvesting capabilities.

- An eddy current generator requires extensive modifications to the current design of braiding machines (e.g. choice of materials, dimensions of sliding shoes of carriers). Particularly at high relative speeds between the carriers and the bed of the braiding machine ($> 3\,\frac{m}{s}$), such generators may be of interest due to their smooth run and high expectable power output.
- An investigation of the behavior of the shaker generator and therefore a comparison to the eddy current generator at such high machine speeds remains open for future research.

5 Comparison of the Developed Approaches and Their Relation to the Literature

The commercially available switches that jut into the tracks of the bobbin carriers can be seen as a baseline technique for braiding process monitoring. Upon occurrence of a yarn breakage or an empty bobbin, they deliver a control signal that can be used to stop the machine in order not to produce large lengths of unusable braid. By means of a consideration of the stopping distance of the machine or, even more exact, by means of rotary position transducers attached to the horn gears, the defective carrier can precisely be identified. Problematic about this approach is the fact that it only detects a defect when major effort to restart the braiding process is inevitable. Such effort may include rethreading broken yarns, cutting off unusable braids and forming a new braid interlacement structure after a braided strand had to be cut off, for instance. The invention by Lenkeit [66] is capable of detecting yarns of deviating yarn tension by means of a skid that is attached to a force sensor and that touches the braiding yarns. Hence, a defective yarn can exactly be identified before it breaks. This way, effort to resolve the error is potentially minimized since an error cause, such as a fibrous ring, can often be removed by hand with scissors. No rethreading of the yarn or cutting off a whole defective braided strand is required in this case. The downside of this approach that brittle reinforcement yarns, such as carbon yarns, often react with additional yarn damage when they are subject to normal forces or bending in their dry state. As Ebel et al. already describe it, the goal should be to “interfere as little as possible with the yarn” [46]. The newly invented **stationary Hall sensors** by Maidl et al. [64,65,81], which measure the position of the levers or sliders of the bobbin carriers as they pass by, manage to check the tension of each braiding yarn without any additional yarn contact because the already existing compensation device on each carrier is used as a kind of spring balance and no new yarn deflecting elements are required. The high sensitivity of the measurement approach was proven by correlating clearly distinguishable anomalies in the measurement results with geometrical imperfections of the bobbins, which were measured by 3D scanning to be in the order of 0.01-0.1 mm (cf. Figure 3-9, left, Figure 3-12 and Figure 3-13). The dead time that is equally involved in both the invention by Lenkeit [66] and the invention by Maidl et al. [64,65,81] was put into perspective by analyzing the statistical distribution of lever deflections before a yarn actually breaks. On the basis of an allowed false negative rate of 3.4 defects per million opportunities (six sigma), it was found that for the investigated Tenax®-E HTS40 F13 12k carbon yarn material and a typical use case of braiding of these reinforcement fibers (part diameter $d = 65\,mm$, braiding angle $\varphi = 45°$) the installation of one stationary Hall sensor per track of carriers is sufficient in order to detect a yarn tension anomaly before the yarn actually breaks. By calculating the used yarn length per 360°-revolution of a carrier through the braiding machine, the required number of stationary sensors per track can be scaled up when parts of larger circumference or smaller braiding angle φ shall be braided. Moreover, due to the fact that the yarn tensioning unit is used secondarily as a spring balance, it was found that the required number of stationary sensors increases the higher the spring rating and therefore the higher the set braiding yarn tension is. In case of a 700 g-spring, a component with a diameter of $d = 130\ mm$ and a braiding angle of $\varphi = 45°$, the required number of stationary sensors is increased to four per track of carriers, for instance (cf. Table 3-2). In any case, it can be said that the required number of these low-cost Hall sensors is limited and therefore incurs, even when all necessary magnets for all carriers are taken into account, extremely little investment costs. The installation effort for the invention by Maidl et al. [64,65,81] could be characterized as moderately increased compared to the invention by Lenkeit [66] since the tension lever of each carrier needs to be equipped with a magnet that can be detected by the stationary sensors. However, the installation effort can be minimized to a few seconds per carrier when housings for the magnets are designed that are clippable to the extensions of the tension levers. A difference to the invention by Lenkeit [66] is that this invention conceptually appears to be capable of detecting entanglements of frayed yarns in the braid formation zone. The stationary Hall sensors are not able to do this because they can only measure irregularities that originate from the bobbin or the carrier. Moreover, the stationary hall sensors depend on carriers that use a bobbin independent yarn length compensation device (cf. Figure 3-2). In the vast majority of cases, this prerequisite is however fulfilled [19].

A possible way of deriving how many stationary Hall sensors are necessary was only proposed for the case that a yarn breakage may not be overlooked. Gaps in the braided preform, which occur prior to a yarn breakage, were not further investigated as defects to be avoided. For such cases of defects that result from finer errors during the braiding process, a continuous process monitoring by **sensor integrated braiding rings** [88] was developed. As an extension to the concept of integrating force sensors into a braiding ring in order to detect anomalously tensed 0°-filler yarns mentioned in the patent application by Brockmanns et al. [67], it was demonstrated that by applying a trainable algorithm of neural networks, also the moving braiding yarns can be monitored by sensor integrated braiding rings. Due to the fact that the algorithm is trainable, the sensor elements do not need to show high levels of accuracy in their measurements (inexpensive force sensing resistors) as long as their behavior is repeatable (precise measurement). Monitoring all braiding yarns is otherwise known from spring mounted braid condensing devices that feature switches for delivering a control signal to stop the braiding machine [71,73]. The switch is pushed when a knot in a braiding yarn does not fit through the braid condensing device or when an eccentric load, e.g. due to an unwinding related irregularity at a carrier, is applied. Such sensory braid condensing devices are usually used in braiding of rope-like products (e.g. laces or cords). In braiding of tubular preforms from reinforcement fibers, such devices are not applied. Firstly, braided preforms from reinforcement fibers do in most cases not show a circular cross section but often even a changing cross section. Hence, a knot detection by a tightly fitting ring shaped element would not be possible to implement. Secondly, the tubular preforms are often bent which would constantly cause eccentric loads that would trigger the switch on the braid condensing device. As successfully demonstrated by an S-shaped mandrel with trapezoidal cross section, the developed sensor integrated braiding rings in combination with the trainable algorithm have shown to be applicable to a near-production scenario of overbraiding complexly shaped mandrels even when shaker motors for an actuation of the braiding rings heavily disturb the data acquisition. The accuracy in predicting the correct defect location on the basis of eighth braiding machine segments was experimentally determined to 92.2 % in case of a simulated defect and to 77.3 % in case a real fibrous ring had to be located in the machine. False negative and, even more important, false positive defect detections of the algorithm could in either case not be observed (cf. Table 3-4). These figures could even be improved (cf. appendix A, Additional data to subsection 3.2.2) by more elaborate neural networks. The chosen architecture of the neural networks is however particularly lean so that they can be expected to be executable on standard microcontrollers. An advantage compared to the stationary Hall sensors is that the developed sensor integrated braiding rings may also be able to detect yarn entanglements in the braid formation zone due to frayed fibers. A disadvantage is however that only a group of carriers can be identified by the trained algorithm. The stationary Hall sensors, the invention by Lenkeit [66] and the commercially available switches that jut into the tracks of the bobbin carriers are able to precisely identify which yarn is the defective one. A further difficulty in applying the sensor integrated braiding rings is that the algorithm needs to be referenced for each geometry and possibly even after each variation in production parameters (e.g. reteaching of the path of the robot, change in production speed) because this may influence the distribution of reaction forces at the braiding ring. Although the neural networks do not necessarily have to be retrained, the referencing step requires skilled production personnel. Particularly due to the need for skilled personnel for newly referencing the measurement data to defect-free braiding after process modifications, the potential effort and costs of applying the developed sensor integrated braiding rings is to be estimated higher than for the stationary Hall sensors.

An **optical inspection of the braid formation zone** was developed and analyzed because it conceptually opened the possibility to precisely determine which yarn was defective without any significant dead time. Hence, it would have constituted a conceptual synthesis of the approaches from the above two paragraphs. The concept of measuring deviating yarn distances by a stationary sensor as mentioned by Brockmanns et al. in their patent application [67] was put into practice by means of a light barrier in the braid formation zone. At least under the given near-production scenario of reinforcement fibers, this concept was found to not be a suitable method for a reliable defect detection during braiding. The reasons for this were mainly natural process fluctuations that led to anomalously tensed yarns being overlooked or the assignment of clockwise and counterclockwise yarns being disrupted. A camera-based inspection of the braid formation zone solved these problems. So far, only the optical tracking of the braid formation point during braiding of rope-like braids as developed by Branscomb [69] and Branscomb et al. [70] was known from the literature. Since their approach relies on the braid formation point being pulled towards the direction of a yarn with increased tension (no braid condensing device was used), this development is not applicable to composites braiding. This is because a mandrel is usually rigidly guided by one or even two robots through the braid formation zone. Firstly, a distinct braid formation point does not exist in this case. Secondly, the guided mandrel is – if it is not made from flexible material – usually confined from any radial movement due a pull from a defective yarn. With the newly developed camera-based approach presented in the dissertation at hand, it is possible to optically monitor all braiding yarns at once also during braiding of reinforcement fibers. It was also shown that the algorithm can be modified in a way that it can cope with the view to parts of the braid formation zone being obstructed (e.g. due to bent mandrels or a second robot for guiding the mandrel, cf. appendix A). However, in the analysis of the data, it became apparent that a reliable defect detection without any false positive or false negative detections is only possible when the image analysis algorithm has the opportunity to average over several video frames. Although a defect often clearly shows itself in the data after a low two digit number of frames, frame numbers in the order of 200 were required to achieve a completely reliable defect detection in the conducted experiments on $n_{yarn} = 64$ braiding yarns. In case of $n_{yarn} = 32$, where the yarns show less curvature and therefore a tension increase causes less deviation in yarn distances from the defect-free mode of operation, the algorithm had to average over approximately 1000 video frames for a correct defect detection without any false positive or false negative detections. These figures show that a defect detection by optical inspection of the whole braid formation zone without any conceptual dead times is only theoretically possible. Taking natural process fluctuations into account, it still requires a certain amount of time until the defect is detected. Finally, it needs to be considered that this approach requires the most computational power among the presented approaches due to the necessity to analyze frames of the braid formation zone in real time. Such computer hardware, e.g. microcontrollers with dedicated graphics cards, may be costly. Moreover, highly skilled personnel is needed for the programming of such devices and also for the curation of the image analysis algorithm. This makes the optical inspection of the braid formation zone appear to involve most effort and costs compared to the previously mentioned approaches. In contrast to the neural networks that were applied to analyze the data from the sensor integrated braiding rings, the behavior of the image analysis algorithm is however visually well explainable. This may be of advantage when convincing regulatory authorities that a company can rely on the monitoring results from the optical inspection of the braid formation zone.

The above approaches can be categorized as bobbin carrier independent systems. As a carrier dependent system, a **sensor integrated carrier with energy harvesting unit** was developed. Different levels of complexity of sensor integrated carriers are known from the literature. The carrier made by Reuter et al. [74] is able to exactly measure the acting yarn tension by a load cell and to send the acquired data wirelessly to an external analysis unit. The sensing and data transmission module is powered by a battery that needs to be changed when it is empty. An electronic bobbin carrier of otherwise similar capabilities but with the addition of an electric motor to actively drive or brake the bobbin was invented by Braeuner [75]. The energy supply still relies on a battery in his concept. Reinisch et al. [76] mention several ways of delivering electric energy to the moving bobbin carrier in order to avoid the need for changing batteries. Their proposal of stationary magnets attached to the body of the braiding machine in conjunction with a coil attached to the carrier was found to generate about one order of magnitude less electric power than the shaker generator developed within the dissertation at hand under otherwise identical parameters. However, especially in case of limited space around the carriers, this approach may, provided further developments in power-saving sensing and telemetry devices, still be worthwhile to consider. Their suggestion of a dynamo on the carrier that is driven by a friction wheel was at least theoretically further advanced by applying the concept of an eddy current generator for bicycles by Strothmann [95] to carriers of a braiding machine. The measurement results showed that harnessing the relative speed between moving carrier and stationary bed of the machine delivers approximately 45 % less electric power than the developed shaker generator when both concepts are applied in a scenario of the RF 1/128-100 braiding machine operating at its full speed of $r = 139\ rpm$ (~$1.5\frac{m}{s}$ relative speed between carrier and bed of machine). Although a dynamo, especially when driven by eddy currents, requires significant modifications to existing designs of braiding machines, the concept may be of interest when braiding machines with particularly fast moving carriers for high material throughput are designed. The electronic carrier built by von Reden [45] and von Reden et al. [77] relies on an inductive transmitter that is mounted to the center of the horn gears and a receiver at the foot of the carrier. With an averaged power transfer to the carrier in the order of 1 W, this approach currently appears as the concept that can wirelessly deliver the most energy to a moving carrier. With such a high transmitted electric power, this concept can be regarded as the most promising when features like an actively driven or braked bobbin, potentially even with a close-loop yarn tension control, shall be implemented. Such a development is however expected to be extremely costly and it may be doubted if it actually finds its way into actual application, particularly given the fact that in composites braiding, usually ≥64 carriers are applied. For this reason, the development of a sensor integrated carrier within the scope of the thesis at hand does not include features such as an actively driven bobbin. To keep costs in a reasonable ratio to the costs of a carrier with guide plate that is usually used in braiding of reinforcement yarns, the concept focused on sensing and defect detection capabilities instead. A shaker generator was developed and measured to produce up to 0.03 W of electric power to maintain the operation of a sensor chip at the foot of the carrier in light sleep mode (power consumption: 0.009 W). Only upon occurrence of a yarn tension increase, the chip on the sensor integrated carrier switches into active mode and sends data over a BLE connection to an external analysis unit. Due to the increased power consumption of 0.166 W and particularly due to the peak in current draw the moment the mode of operation is changed, a battery is used to supply the sensor chip with enough power in case an alarm signal shall be sent. As a byproduct, it was found to be possible to estimate the remaining filling degree of the bobbin from the measurements of the sensor chip. This is because a change in frictional interaction at the edge of the guide plate affects the deflection of the tension lever of the carrier, which the sensor chip on the carrier is able to measure. In case these latter capabilities are of interest for future developments, e.g. for purposes of intra-company logistics including the rewinding of new bobbins and their delivery to a braiding machine whose bobbins are about to run empty, the sensor chip can also be programmed to periodically wake up from is light sleep mode and send measurement data on the estimated filling degree of the bobbin.

All in all, the author can particularly recommend the application of the newly invented stationary Hall sensors. The approach is simple to implement and incurs extremely limited installation costs. Also, based on personal experience of the author, a broad majority of time-consuming braiding defects can be detected at an early stage of formation (Pareto principle). The functionality is easily understandable and potential malfunctions are expected to be quickly solvable by production personnel. This makes the approach a viable option for both the installation in new machines and for a retrofitting to existing production lines. If it is in a particular use case of interest what defects may occur in the braid formation zone, the stationary Hall sensors should be complemented either by a sensor integrated braiding ring that measures axial reaction forces or by an optical inspection of the braid formation zone by camera. This is because the stationary Hall sensors cannot detect any anomalies that do not originate from the bobbin, e.g. an entanglement of frayed fibers in the braid formation zone. A sensor integrated braiding ring appears to be easier to implement than the camera-based approach because it requires less powerful computing hardware and less programming effort. However, the behavior of neural networks may upon malfunctions appear as a black box and the certification of such a monitoring approach in critical applications may therefore be difficult. The choice between sensor integrated braiding ring and camera may in the end depend on the availability of skilled programming personnel or if a company chooses to further develop the camera-based monitoring approach into a market-ready product. The potential to gather programming personnel within a company that is possibly specialized in automation technology (not a typical braiding firm) and the visually well-explainable behavior of the algorithm to potential customers appears to make the approach of optical inspection by camera particularly suitable to turn into a product. The sensor integrated bobbin carrier as proposed in this dissertation was purposefully designed as a minimal system that focuses on sensing capabilities. The first reason for this was that the development is ensured to fit into the academically defined research gap between rudimentary, cost-efficient bobbin carrier independent systems and sophisticated but extremely cost-intensive bobbin carrier dependent approaches. The second reason was to maintain a viable economic perspective of transferring the developed sensor integrated carrier into a production environment. When considering the implementation of sensor integrated carriers, it should be taken into account that even though the approach requires great installation effort (replacing or retrofitting each carrier) it still cannot detect any defects that originate from the braid formation zone (e.g. entanglements of frayed braiding yarns). The possibility to estimate the remaining filling degree on the bobbin is however unique. If this monitoring capability was desired, the installation of, for instance, one sensor integrated carrier per track of carriers would be sufficient. This would even put the application of sensor integrated carriers, which are otherwise often seen as too expensive, into an economically competitive position against the other approaches presented.

6 Summary and Outlook

In the thesis at hand, it was initially outlined that different kinds of defects may occur during braiding of reinforcement fibers. Whereas defects caused by operating errors (cf. subsection 2.1.1) can be avoided by careful engineering planning and attentive production personnel, defects caused by yarn damage (cf. subsection 2.1.2) may occur suddenly and can only partly be avoided by trained personnel. It was described that particularly the formation of fibrous rings during braiding of reinforcement fibers can both lead to a significant deterioration in mechanical properties of a finished part [54,55] as well as to major machine downtimes due to the time it takes to locate and resolve the error cause [46,52].

Subsequently, the state of the art regarding monitoring systems for the braiding process was researched. It was found that current bobbin carrier independent systems come with drawbacks such as late response times (commercially available switches that jut into the tracks of the bobbin carriers, cf. Figure 2-8), potential damages to brittle reinforcement yarns (force sensor with skid that is touched by the braiding yarns [66], cf. Figure 2-9) or a lack of applicability to an industrial use case of braiding preforms for composite parts (optical tracking of the braid formation point [69,70], cf. Figure 2-11, or sensory braid condensing devices [71,73], cf. Figure 2-12). Bobbin carrier dependent concepts generally allow a finer surveillance of the process and partly offer additional functions such as an active yarn tension control [45,75–77]. However, these concepts involve disadvantages such as high installation effort and costs (due to the large numbers of carriers to be equipped with sensory devices) or the need to replace empty batteries (carrier by Reuter et al. [74], cf. Figure 2-13, or by Braeuner [75]).

The research objective that was derived from this research gap was to develop new types of sensor systems for the composite braiding industry that are, on the one hand, cost-efficient and, on the other hand, able to detect defects early during their formation for both reduced error correction effort and minimized mechanical effects of defects. The developed sensor systems should be characterized in order to compare them in terms of application range, sensitivity and approximate installation effort amongst each other and in relation to the concepts from the literature.

Four major developments within the scope of this dissertation were made to close the outlined research gap. Firstly, an invention of stationary Hall sensors that are able to indirectly measure the acting yarn tension when the respective carrier passes by was made. In initial characterization experiments of the new concept on a stationary test stand, the sensitivity of the measurement principle was demonstrated (cf. subsection 3.1.1). Moreover, a statistical method to determine the required number of stationary sensors in order not to miss the breakage of a yarn was proposed. The sensors were then successfully tested in the operating RF 1/128-100 radial braiding machine from HERZOG GmbH at the Chair of Carbon Composites as well as in an axial machine from a project partner to replicate near-industrial use cases (cf. subsection 3.1.2). Secondly, sensor integrated braiding rings to monitor the tension of the moving braiding yarns were developed. In initial braiding experiments with a simplified geometry of a cylindrical mandrel, the characteristic differences between measuring radial and axial reaction forces at the braiding ring were shown and analyzed (cf. subsection 3.2.1). At the example of a near-industrial use case of overbraiding a generic complexly shaped mandrel, the development of a new, trainable algorithm that is able to detect and localize a defective yarn on the level of eighth segments of a braiding machine was shown (cf. subsection 3.2.2). In an academic test of the algorithm, it did not produce any false positive or false negative detections. Although the algorithm was trained on data that was acquired by means of braiding with a yarn brake attached to a carrier (simulated defect), the algorithm demonstrated that it was also capable of correctly detecting a natural defect during a near-industrial braiding process. As a third contribution to the research objective, an optical inspection of the braid formation zone was investigated. In early experiments, it could be shown that, at least under the given braiding scenario, an approach from patent literature [67] of measuring yarn transit intervals by a stationary laser in the braid formation zone was subject to severe disruptions due to naturally occurring process fluctuations (cf. subsection 3.3.1). As became apparent in the successive development of a novel approach of a camera-based monitoring of the whole braid formation zone including a dedicated image analysis algorithm, the measurement principle is still capable of reliably detecting anomalously tensed yarns during braiding (cf. subsection 3.3.2). It was also described that the image analysis algorithm can be modified in case the view on parts of the braid formation zone is obstructed, e.g. by bent mandrels or by a second handling robot. Thereby, the usability of the new development in the main application area of braiding (complex profiles) is ensured. As fourth and final result of the conducted research, a sensor integrated bobbin carrier with energy harvesting unit was developed. The sensitivity of the measurement approach was demonstrated in introductory experiments on the concept (cf. subsection 4.1.1). Moreover, an analytical model was set up and verified that allows an inference on the remaining filling degree of a bobbin based on the (indirectly) measured yarn tension (cf. subsection 4.1.2). The model practically represents an extension of a formula by Kyosev [19], which was intended for ordinary carriers without guide plate, to the case of carriers with guide plate, which are usually used in braiding of brittle reinforcement fibers. Furthermore, concepts for self-sufficient powering of the sensor integrated carrier were investigated (cf. section 4.2). A practically implemented shaker generator was measured to produce approximately 0.03 W of electric power while the RF 1/128-100 braiding machine operated at its full speed of $r = 139\ rpm$. This is more than the selected sensor chip required in its light sleep mode (approximately 0.009 W). Only in case the chip detects a defect and switches into active mode, it needs to rely on a battery that can cover the occurring peak in current draw. Eventually, the new developments made in the dissertation at hand were compared amongst each other, it was described how they extend the current state of the art and what combinations of the developed sensor modules in an integrated sensor system appear most promising (cf. chapter 5).

Further development steps can, on the one hand, be conducted on an incremental basis to the above-described research. For example, the localization of a defect in an eighth segment of a braiding machine can be further narrowed down by the application of a higher number of sensors incorporated into the braiding ring or by improvements to the localization algorithm itself. Also the application of piezo-resistive load cells, which may allow a more accurate force measurement, may lead to improved localization results. It however needs to be ensured that potentially more accurate measurement equipment is as durable in withstanding vibrations of an actuated braiding ring as the selected force sensing resistors. Another point that can be improved is the optical inspection of a braid formation zone that is made up of $n_{yarn} = 128$ braiding yarns. Whereas an improvement of the image analysis algorithm may be an option, the author recommends applying a backlight illumination with a larger diameter than the investigated one. This is because an algorithm of enhanced capabilities may require even more powerful computing hardware. The good detectability of anomalously tensed yarns in case of $n_{yarn} = 64$ suggests that it is still possible to detect an anomalously tensed yarn among $n_{yarn} = 128$ yarns even though the yarn distance measurement is conducted further outwards and therefore the yarn distances are increasingly determined by the spacing of the carriers themselves. Finally, the developed energy harvesting unit can be further analyzed and improved. Particularly the behavior of the shaker generator in machines with smaller horn gear diameters can be further investigated. Braiding machines with smaller horn gear diameters are usually operated at speeds of horn gear rotation that are way higher (up to $r = 400\ rpm$) than in the tested RF1/128-100 machine. A potentially even exponential power output with increasing speed of horn gear rotation r may allow a much higher power generation. However, in machines with smaller horn gears, there is less space around the feet of the carriers which only allows shorter tube lengths for the accelerated magnet. This was shown to reduce the generatable electric power. Hence, it would be interesting to see which effect is more pronounced. As already mentioned in subsection 4.2.1, also the efficiency of the electric circuit for the sensor integrated carrier can be improved. This could be achieved by incorporating a DC/DC converter with a wide input voltage instead of the overvoltage protection by a Zener diode and a resistor. The coil windings and therefore the maximum voltage of the generator under a given machine speed can be optimized to meet the specifications of the DC/DC converter and a charge regulator can be used to charge the battery with a defined profile. Of course, also more energy-saving sensor chips than the applied ESP32 may be available in the future that may allow smaller and even more cost-efficient energy harvesting units on the carriers. For instance, if the capabilities regarding the estimation of the remaining filling degree of the bobbin are not needed, it is conceivable to only integrate an active RFID circuit on the carrier that is solely triggered upon the push of the button in Figure 4-17, right by the tension lever due to an unwinding-related irregularity (e.g. a fibrous ring). This way, any power consumption of the carrier during regular braiding could be eliminated because no computational processes need to be maintained. This would however deprive the approach of a localization of the defective carrier or at least significantly complicate it. If a dedicated sensor chip continues to be used, 3D acceleration sensors attached to each carrier could at least in a vertically set up braiding machine (radial or axial type) indicate the position of the carrier that raised an alarm to an external machine control unit and consequently to operating personnel by determining the direction of gravitational acceleration.

On the other hand, there are several ways the whole concept of braiding process monitoring can be further advanced or even transferred to other manufacturing techniques in composite production. Recapitulating the introductory remarks on the monitoring system in the light of digitalization, particularly the aspects of Industry 4.0 of "interconnection", "technical assistance" and "autonomous systems" as listed by Hopmann and Schmitz [6] (cf. Figure 1-1) appear as sensible development steps. As for the aspect of "interconnection", the set-up relation between measured yarn tension by a sensor integrated carrier and the remaining filling degree of its bobbin could be used as an input for intra-company logistics to deliver freshly rewound bobbins on time to a braiding machine whose bobbins are about to run empty. In this case, the sensor integrated carriers would act as a kind of IoT sensors, only that IoT would stand for "Intranet of Things" instead of "Internet of Things", thereby reflecting the fact that the acquired data remains within a given production site of a company. Regarding the aspect of "technical assistance", the position of the error cause detected by the stationary Hall sensors in the RF 1/128-100 braiding machine was already displayed to operating personnel by an LED strip. It is however conceivable to display results from any of the newly developed sensor modules, e.g. the position of the error cause along with further data on the expected type of defect and suggested countermeasures, to operating personnel by means of augmented reality glasses. This way, the teaching of new personnel or personnel from other professional backgrounds could be accelerated and operating errors could be minimized. Regarding the aspect of "automonous systems", it is conceivable to not only train a defect detection algorithm for the sensor integrated braiding rings once for a given mandrel geometry, but to allow a continuous improvement process for the detection algorithm. Especially when large quantities of preforms are braided, quality data from a subsequent optical inspection, be it by eye or by image analysis, could be used to be fed into a control loop that readjusts the trained detection algorithm. Previously undetectable defects (because they were initially not trained) could become detectable over time as they occur more frequently and more process data becomes available on them. Of course, this requires a seamless traceability of a manufactured semi-finished product through a production facility for an exact match of production data from the process monitoring system to quality data from a quality inspection further downstream. Furthermore, especially when products of high quality requirements are braided, the predictability of such an evolution of a detection algorithm in production may pose a particular challenge to prove to regulatory authorities and still involves major research effort. Finally, aspects and methods of the newly developed monitoring approaches may also be of interest for further digitalizing other manufacturing techniques in composites production. For instance, in the emerging production of hydrogen pressure vessels from towpreg material by filament winding, the width of the towpreg material is expected to vary. An optical yarn detection and measurement of its width during winding could be used for a quality control of the incoming material and may even allow an adaption of the movement of the yarn guiding eyelet in real time. This way, a more even deposition of yarn material of varying width without gaps or overlaps could be achieved. Neural networks and particularly convolutional neural networks for pattern recognition in images could be applied in Automated Fiber Placement when the freshly deposited tapes need to be scanned for gaps, overlaps, twists or wrinkles. Thereby, quality inspection could become more objective compared to an inspection by eye. When a broad range of process parameters influences part quality, for instance when long process chains including sequential preforming with binder activation, joining of sub-preforms and a subsequent resin injection in an RTM process are necessary, the training of neural networks with process and quality data may be an option to find interdependencies between quality defining parameters (so-called Bayesian networks). Often, process parameters are gathered anyway by production machinery and quality data is available from part inspection to meet regulatory requirements. A synthesis of these already available types of data by trainable algorithms could support manufacturing engineers and enable a quicker troubleshooting in production, particularly when interdependencies are conditional and time-dependent.

References

[1] Landes DS. The unbound Prometheus: technological change and industrial development in Western Europe from 1750 to the present: Cambridge University Press; 2003.

[2] Horn J, Rosenband LN, Smith MR. Reconceptualizing the industrial revolution: MIT press; 2010.

[3] Wrigley EA. Reconsidering the industrial revolution: England and Wales. Journal of Interdisciplinary History 2018;49(01):9–42.

[4] Voigtländer N, Voth H-J. Why England? Demographic factors, structural change and physical capital accumulation during the Industrial Revolution. Journal of economic growth 2006;11(4):319–61.

[5] Spear B. Textile patents and the GB Industrial Revolution. World Patent Information 2016;44:53–6.

[6] Hopmann C, Schmitz M. Plastics Industry 4.0: Potentials and Applications in Plastics Technology. Munich: Carl Hanser Verlag; 2020.

[7] Bauer K, Diegner B, Diemer Jea. Umsetzungsempfehlungen für das Zukunftsprojekt Industrie 4.0: Abschlussbericht des Arbeitskreises Industrie 4.0. [June 07, 2021]; Available from: https://www.bmbf.de/files/Umsetzungsempfehlungen_Industrie4_0.pdf.

[8] Schwab K. The Fourth Industrial Revolution: What It Means and How to Respond. [June 07, 2021]; Available from: https://www.foreignaffairs.com/articles/2015-12-12/fourth-industrial-revolution.

[9] Townsley JR. BP: Time for a Change. Radiocarbon 2017;59(1):177–8.

[10] Kohen M. The Venus of Willendorf. American Imago 1946;3(4):49–60.

[11] White R. The Women of Brassempouy: A Century of Research and Interpretation. J Archaeol Method Theory 2006;13(4):250–303.

[12] Gries T, Reimer V, Kuckhoff B, Lengersdorf M, Schäfer J. Self-optimization of the Radial Braiding Process. [June 08, 2021]; Available from: https://www.iop.rwth-aachen.de/cms/Produktionstechnik/Forschung/Demonstratoren/~hpfz/Selbstoptimierung-des-Radialflechtprozes/?lidx=1.

[13] Gries T, Veit D, Wulfhorst B. Textile Fertigungsverfahren: Eine Einführung. 2nd ed. Munich: Carl Hanser Verlag; 2014.

[14] Relligmann H. Unterrichtshilfen Textiltechnik: Maschinengeflechte. Frankfurt/Main; 1981.

[15] Rosenbaum JU. Flechten: Rationelle Fertigung faserverstärkter Kunststoffbauteile. In: Michaeli W, editor. Ingenieurwissenschaften Kunststoffverarbeitung. Cologne: Verlag TÜV Rheinland; 1991.

[16] Laourine E. Geflochtene Halbzeuge und Flechttechniken. In: Cherif C, editor. Textile Werkstoffe für den Leichtbau: Techniken - Verfahren - Materialien - Eigenschaften. Berlin: Springer; 2011, p. 307–25.

[17] Deutsches Institut für Normung. Textilien; Grundbegriffe(German Industrial Standard DIN 60000); 1969.

[18] Branscomb D, Beale D, Broughton R. New directions in braiding. Journal of Engineered Fibers and Fabrics 2013;8(2):155892501300800202.

[19] Kyosev Y. Braiding Technology for Textiles. Cambridge: Woodhead Publishing; 2015.

[20] Lengersdorf M, Gries T. Three-dimensional (3D)-maypole braiding. In: Kyosev Y, editor. Advances in Braiding Technology: Specialized Techniques and Applications. Duxford: Woodhead Publishing; 2016, p. 89–105.

[21] Muller JA. Braiding machine(United States Patent Specification US2197111A); 1940.

[22] Culp CH, Hastings SM, Brown RT. Braiding apparatus(United States Patent Specifiaction US4753150A); 1988.

[23] Kyosev Y, Müller B. Lever arm braiding. In: Kyosev Y, editor. Advances in Braiding Technology: Specialized Techniques and Applications. Duxford: Woodhead Publishing; 2016, p. 209–22.

[24] HERZOG GmbH. Highest performance for Fishing and Seafaring. [June 08, 2021]; Available from: https://herzog-online.com/fishing-and-seafaring/.

[25] Michael M, Kern C, Heinze T. Braiding process for braided ropes. In: Kyosev Y, editor. Advances in Braiding Technology: Specialized Techniques and Applications. Duxford: Woodhead Publishing; 2016, p. 225–43.

[26] HERZOG GmbH. Highest performance for Sports and Leisure. [June 08, 2021]; Available from: https://herzog-online.com/sports-and-leisure/.

[27] HERZOG GmbH. The right technique for the future. [June 08, 2021]; Available from: https://herzog-online.com/technical-braids/.

[28] HERZOG GmbH. The latest state-of-the-art for the medical industry. [June 08, 2021]; Available from: https://herzog-online.com/medical-industry/.

[29] Aibibu D, Hild M, Cherif C. An overview of braiding structure in medical textile: fiber-based implants and tissue engineering. In: Kyosev Y, editor. Advances in Braiding Technology: Specialized Techniques and Applications. Duxford: Woodhead Publishing; 2016, p. 171–90.

[30] Bulat M, Ahlborn H, Gnädinger F, Michaelis D. Braided carbon fiber composites. In: Kyosev Y, editor. Advances in Braiding Technology: Specialized Techniques and Applications. Duxford: Woodhead Publishing; 2016, p. 383–94.

[31] Hill J. Adhesively bonded structural composites for Aston Martin vehicles. [October 31, 2021]; Available from: https://www.audiclubsouthafrica.co.za/yabbfiles/Attachments/b01.pdf.

[32] Thuis H. The development of composite landing gear components for aerospace applications. [October 31, 2021]; Available from: https://citeseerx.ist.psu.edu/viewdoc/download?doi=10.1.1.157.3791&rep=rep1&type=pdf.

[33] Thuis H. Composite landing gear components for aerospace applications. ICAS 2004 - 24th International Congress of the Aeronautical Sciences. Yokohama, Japan; 2004.

[34] van Ravenhorst JH, Akkerman R. Overbraiding simulation. In: Kyosev Y, editor. Advances in Braiding Technology: Specialized Techniques and Applications. Duxford: Woodhead Publishing; 2016, p. 431–55.

[35] van Ravenhorst JH. Design tools for circular overbraiding of complex mandrels. Dissertation. University of Twente, Twente, the Netherlands; 2018.

[36] Zuurendonk B. Carbon Fibre Composite Rim: An automation feasibility study. Master Thesis. Delft University of Technology, Delft, the Netherlands; 2018.

[37] Kind K, Drechsler K. Method for the production of braided CFRP bicycle rims. SAMPE Europe Conference 15, Amiens, France 2015.

[38] Weimer C, Mitschang P. Preformverfahren. In: Neitzel M, Mitschang P, editors. Handbuch Verbundwerkstoffe: Werkstoffe, Verarbeitung, Anwendung. Munich: Carl Hanser Verlag; 2004, p. 73–104.

[39] Braley M, Dingeldein M. Advancements in braided materials technology. International SAMPE Symposium and Exhibition 2001:2445–54.

[40] Ebel CS. Hochgeschwindigkeitsumflechten für die Fertigung von Faserverbundbauteilen. Dissertation. Technical University of Munich, Munich, Germany; 2017.

[41] Mitwalsky M. Strategien zur Steigerung der Variabilität bei der Herstellung von geflochtenen Hohlbauteilen. Dissertation. Technical University of Munich, Munich, Germany; 2015.

[42] Heß C. Beitrag zur Qualitätssicherung für die serientaugliche Herstellung von textilen Preformen. Dissertation. Technical University of Munich, Munich, Germany; 2016.

[43] Eschler E, Hüls J, Zaremba S, Drechsler K. Analysis of a Process Approach for Production of Triaxial Braids with Locally Customized Filler Yarn Count. Key Engineering Materials 2019;809:360–6.

[44] Eschler E, Miadowitz T, Zaremba S, Drechsler K. Design Optimization of a Braided Roof Frame Reinforcement by Process-Integrated Local Customization of Component Properties. Appl Compos Mater 2020;27(1):75–91.

[45] von Reden T. Erweiterung der Systemgrenzen der Flechttechnik durch elektronisch gesteuerte Klöppel. Dissertation. Technical University of Munich, Munich, Germany; 2015.

[46] Ebel C, Mierzwa A, Kind K. Yarn damage during braiding of reinforcement fibers for composites. In: Kyosev Y, editor. Advances in Braiding Technology: Specialized Techniques and Applications. Duxford: Woodhead Publishing; 2016, p. 319–54.

[47] Risicato J-V, Kelly F, Soulat D, Legrand X, Trümper W, Cochrane C et al. A complex shaped reinforced thermoplastic composite part made of commingled yarns with integrated sensor. Appl Compos Mater 2015;22(1):81–98.

[48] Barfuss D, Garthaus C, Gude M. Advanced Waviness modelling of thermoplastic tape braids. ICCM20 - 20th International Conference on Composite Materials, Copenhagen, Denmark; 2015.

[49] Ramasamy A, Wang Y, Muzzy J. Braided thermoplastic composites from powder-coated towpregs. Part I: Towpreg characterization. Polymer composites 1996;17(3):497–504.

[50] Ramasamy A, Wang Y, Muzzy J. Braided thermoplastic composites from powder-coated towpregs. Part II: Braiding characteristics of towpregs. Polymer composites 1996;17(3):505–14.

[51] Ramasamy A, Wang Y, Muzzy J. Braided thermoplastic composites from powder-coated towpregs. Part III: Consolidation and mechanical properties. Polymer composites 1996;17(3):515–22.

[52] Ebel C, Brand M, Drechsler K. Effect of Fiber Damage on the Efficiency of the Braiding Process. 11th Composites Week @ Leuven and TexComp-11 Conference. Leuven, Belgium; 2013.

[53] Mierzwa A, Ebel C, Harbers T, Drechsler K. Investigation on Creation of Fibrous Rings and Their Influence on the Braided Preform Quality. ECCM17 - 17th European Conference on Composite Materials. Munich, Germany; 2016.

[54] Mierzwa A, Ebel C, Drechsler K. Influence of yarn gaps on the mechanical performance of braided carbon fiber reinforced plastics. Zeitschrift Kunststofftechnik / Journal of Plastics Technology 2018;14(2):146–73.

[55] Mierzwa A. Zur Entstehung und Auswirkung von Garnlücken in Carbonbiaxialgeflechten. Dissertation. Technical University of Munich, Munich, Germany; 2019.

[56] Hering E, Triemel J, Blank H-P. Qualitätsmanagement für Ingenieure: Ein praxisnahes Lehrbuch für die Planung und Steuerung von Qualitätsprozessen. Wiesbaden: Springer Vieweg; 2013.

[57] Heieck F, Hermann F, Middendorf P, Schladitz K. Influence of the cover factor of 2D biaxial and triaxial braided carbon composites on their in-plane mechanical properties. Composite Structures 2017;163:114–22.

[58] Heieck F, Middendorf P. Effect of the Cover Factor of 2D Biaxial and Triaxial Braided Carbon Composites on their In-Plane Mechanical Properties. ECCM17 - 17th European Conference on Composite Materials. Munich, Germany; 2016.

[59] Putze L. Lichtschranken als Detektionsmöglichkeit von Garnlücken beim Flechten von Carbonfasern. Bachelor Thesis. Technical University of Munich, Garching, Germany; 2019.

[60] Birkefeld K. Virtuelle Optimierung von Geflecht-Preforms unter Berücksichtigung von Fertigungsaspekten. Dissertation. University of Stuttgart, Stuttgart, Germany; 2013.

[61] Bulat M. Untersuchung des Einflusses der Fadenspannungen beim Flechten auf Faserschädigung und Bauteilkennwerte. Diplomarbeit. Reutlingen University, Reutlingen, Germany; 2007.

[62] Erber A, Weng A, Drechsler K. Effect of Designed Yarn Damages on the Out-of-Plane Properties of Braided Composite Parts. Recent Advances in Textile Composites-TEXCOMP 10 2010:490–7.

[63] Kowtsch C, Hoffmann G, Kleicke R. Gewebte Halbzeuge und Webtechniken. In: Cherif C, editor. Textile Werkstoffe für den Leichtbau: Techniken - Verfahren - Materialien - Eigenschaften. Berlin: Springer; 2011, p. 171–224.

[64] Maidl S, Sabieraj M, Mierzwa A, Ebel C, Drechsler K. Investigating the unwinding behavior of technical yarns and development of a new sensor system for the braiding process. IOP Conf. Ser.: Mater. Sci. Eng. 2018;406:12065.

[65] Maidl S, Mierzwa A, Ebel C, Drechsler K. Development of a Novel Type of Online Monitoring System for the Braiding Process. ECCM18 - 18th European Conference on Composite Materials. Athens, Greece; 2018.

[66] Lenkeit J. Verfahren zur Zugkraftmessung an laufenden Fäden einer Fadengruppe sowie Vorrichtung zur Ausübung des Verfahrens(German Patent Specification DE19730965C1); 1997.

[67] Brockmanns K-J, Kümpers F-J, Baumgart G, Leifeld M. Radialflechtmaschine(German Patent Application DE102012223127A1); 2014.

[68] van Ravenhorst JH, Akkerman R. A yarn interaction model for circular braiding. Composites Part A: Applied Science and Manufacturing 2016;81:254–63.

[69] Branscomb DJ. A machine vision and sensing system for braid defect detection, diagnosis and prevention during manufacture. Master Thesis. Auburn University, Auburn, United States of America; 2007.

[70] Branscomb DJ, Beale DG. Fault detection in braiding utilizing low-cost USB machine vision. The Journal of The Textile Institute 2011;102(7):568–81.

[71] Schneider H. Flechtscholle(European Patent Specification EP0498944B1); 1992.

[72] AUGUST HERZOG MASCHINENFABRIK GmbH & Co. Kommanditgesellschaft. Jahresabschluss zum Geschäftsjahr vom 01.01.2017 bis zum 31.12.2017. Bundesanzeiger Verlag 2019.

[73] Schneider H. Flechtscholle für eine Flechtmaschine(European Patent Specification EP2003234B1); 2008.

[74] Reuter S, Printz S, Schaub M, Fürtjes T, Wagner R, Lengersdorf M et al. Schlussbericht zu dem IGF-Vorhaben: Wirtschaftliche Serienfertigung textiler Preforms mittels Umflechtverfahren durch Integration automatisierter Handlingsmethoden und online Qualitätssicherung. [December 23, 2021]; Available from: https://www.tib.eu/de/suchen/id/TIBKAT%3A789081776.

[75] Braeuner MO. Klöppel für eine Flechtmaschine, Flechtmaschine sowie Verfahren zum Steuern und Regeln einer auf ein Flechtmaterial aufgebrachten Spannung(German Patent Specification DE102014016381B4); 2014.

[76] Reinisch H, Müller B, Nägele B. Spulenträger für eine Flecht-, Wickel- oder Spiralisiermaschine(German Patent Application DE102014014149A1); 2014.

[77] von Reden T, Becker S, Drechsler K. Design and Energy Transmission for an Electronic Controlled Lace Bobbin. Proceedings of the Technical Conference and “Table Top” Exhibition of the Society for the Advancement of Materials & Process Engineering 2010.

[78] Hunt AJ. A Machine Vision System for the Real-Time Fiber Orientation Measurement of Tubular Braided Preforms. Master Thesis. University of Alberta, Edmonton, Canada; 2017.

[79] PROFACTOR GmbH. Faserverbungwerkstoffe. [June 30, 2021]; Available from: https://www.profactor.at/loesungen/bildverarbeitung-machine-vision/faserverbundwerkstoffe/.

[80] Heieck F. Qualitätsbewertung von Faser-Kunststoff-Verbunden mittels optischer Texturanalyse auf 3D-Preformoberflächen. Dissertation. University of Stuttgart, Stuttgart, Germany; 2019.

[81] Maidl S, Mierzwa A, Matschinski A. Thread Tension Anomalies Detection(European Patent Specification EP3784826B1); 2021.

[82] Sabieraj M. Charakterisierung des Abspulverhaltens von technischen Garnen im Flechtprozess. Bachelor Thesis. Technical University of Munich, Garching, Germany; 2018.

[83] Fella B. Untersuchung von Carbonfasern in einem Faserreibungsprüfstand. Bachelor Thesis. Technical University of Munich, Garching, Germany; 2015.

[84] Helling GmbH. Sicherheitsdatenblatt: Standard-Chek Medium Nr. 3 Entwickler. [October 19, 2021]; Available from: https://www.helling.de/wp-content/uploads/Standard-Chek-Medium-Nr.-3-Entwickler-11-D-de-121.200.502503504.pdf.

[85] Wolf T. Ursachen von Ablagelücken und deren Auswirkungen auf den Flechtprozess und die Geflechtsqualität. Term Project. Technical University of Munich, Garching, Germany; 2016.

[86] Rauch J. Auswirkung von Faserringen auf die Stabilität des Flechtprozesses. Term Project. Technical University of Munich, Garching, Germany; 2016.

[87] Fernández Villalba Á. Advancement of a Floating Supported Braiding Ring for the Sensory Detection of Braiding Defects. Master Thesis. Technical University of Munich, Garching, Germany; 2018.

[88] Maidl S, Fernández Villalba Á, Kind K, Drechsler K. Development of sensor integrated braiding rings for the automated detection of braiding defects. Materials Today: Proceedings 2020.

[89] Maidl S, Hilbck M, Kind K, Drechsler K. Optical inspection of the braid formation zone during manufacturing of preforms from reinforcement fibers for defect detection purposes. Front. Mater. 2023;10.

[90] Maidl S, Putze L, Kind K, Drechsler K. Automated Detection of Yarn Gaps during Radial Braiding of Carbon Fiber by Means of Light Barriers. ECCM20 - 20th European Conference on Composite Materials. Lausanne, Switzerland; 2022.

[91] Hilbck M. Optische Vermessung und Analyse der Fadenkrümmungen beim Radialflechtprozess zur frühzeitigen Erkennung von Prozessfehlern. Term Project. Technical University of Munich, Garching, Germany; 2022.

[92] Eckardt B. Optimierung einer Additive Manufacturing Anlage zur Herstellung eines Inline Monitoring Systems für den Flechtprozess. TUMKolleg Project. Technical University of Munich, Garching, Germany; 2018.

[93] Mondelli FG. Weiterentwicklung eines sensorintegrierten Klöppels zur Überwachung des Flechtprozesses. Bachelor Thesis. Technical University of Munich, Garching, Germany; 2021.

[94] Gessler R, Krause T. Wireless-Netzwerke für den Nahbereich: Eingebettete Funksysteme: Vergleich von standardisierten und proprietären Verfahren. 2nd ed. Wiesbaden: Springer Vieweg; 2015.

[95] Strothmann D. Contactless Current Generator, Especially Dynamo, for Bicycle and for Lighting Systems of Vehicle(European Patent Specification EP2593351B1); 2015.

Appendix A: Additional Data

Additional data to subsection 3.1.1

In subsection 3.1.1, flawless reference measurements on a stationary test stand are discussed as an initial sensitivity assessment of the Hall sensor module. Although the sensor module is capable of resolving fine anomalies in the motion of the tension lever, it is mentioned that it is not possible to calculate an accurate yarn tension from the measured position of the lever. A more detailed explanation to this is provided in Figure A-1. Here, the acting yarn tension from the experimental sequence shown in Figure 3-9, right is referred to the measured Hall voltage. A hysteresis characterizes the relation between the two measurands. When the bobbin is prohibited from rotating, the measured Hall voltage is lagging behind in the reflection of the resulting increase in yarn tension. Similarly, when the bobbin is free to rotate and the yarn tension decreases again, the measured Hall voltage is again lagging behind in the reflection of the resulting decrease in yarn tension. This can be explained by the frictional interaction between the moving components of the yarn tensioning unit (e.g. lever joint, locking pin). When the yarn tension passes through a local minimum and starts increasing again, a considerable frictional force has to be overcome until the tension lever of the bobbin carrier starts moving upwards. Likewise, when the yarn tension passes over a local maximum and begins to decrease again, the tension lever of the bobbin carrier tends to remain in its elevated position until the frictional force in the tensioning mechanism is overcome by the difference between actual yarn tension and restoring force of the spring mechanism. Another effect that can be seen in the diagram in Figure A-1 is that the individual hystereses representing an oscillation cycle each are scattered along the y-axis by approximately 0.1 V. This behavior can be explained by the geometrical imperfection of the notched area of the bobbin illustrated in Figure 3-12 and Figure 3-13. When the gap that the locking pin has to bridge to engage with the lateral notches is small/large, then the point of engagement and disengagement with the notches is reached at larger/smaller lever deflections resulting in higher/lower Hall voltages. Consequently, the corresponding hysteresis is shifted to a higher/lower level along the y-axis. Due to the explained hysteretic relation between Hall voltage and yarn tension as well as the observed scatter, an exact calculation of yarn tension from Hall voltage is not possible.

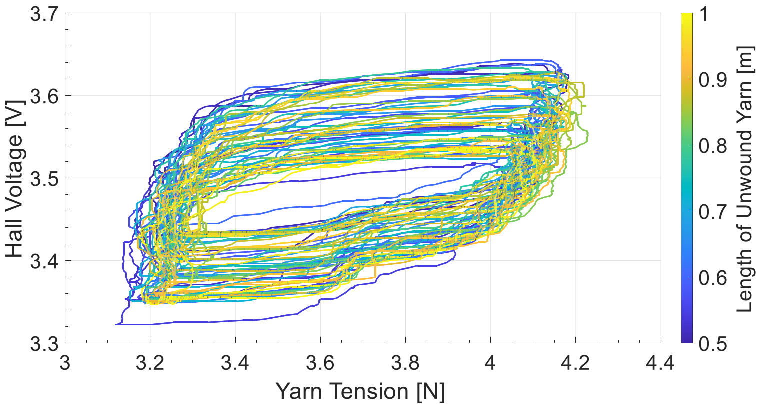

Figure A-1: Measured Hall voltage referred to acting yarn tension from the experimental sequence shown in Figure 3-9, right

Additional data to subsection 3.2.2

In Figure 3-39, only the confusion matrices of the neural networks that process data from the axial ring under controlled simulation of a defect are given. For the sake of completeness, the test confusion matrices for the defect free test are given in Figure A-2 below. As already stated in section 3.2.2, they are mainly made up of zero entries, which is why they are not shown in the main part of this thesis. The matrices show that when there is no defect present, the networks do not make any false positive predictions. This is of particular importance for an interruption-free braiding when the monitoring system is used during regular braiding without any defect present.

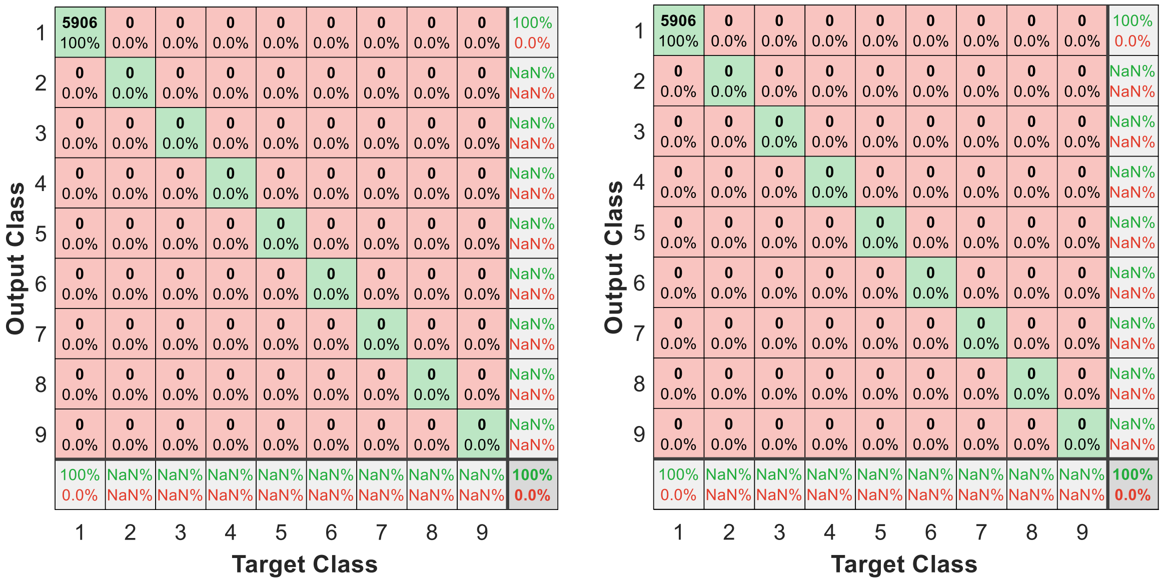

	1	2	3	4	5	6	7	8	9	
1	5906 100%	0 0.0%	0 0.0%	0 0.0%	0 0.0%	0 0.0%	0 0.0%	0 0.0%	0 0.0%	100% 0.0%
2	0 0.0%	0 0.0%	0 0.0%	0 0.0%	0 0.0%	0 0.0%	0 0.0%	0 0.0%	0 0.0%	NaN% NaN%
3	0 0.0%	0 0.0%	0 0.0%	0 0.0%	0 0.0%	0 0.0%	0 0.0%	0 0.0%	0 0.0%	NaN% NaN%
4	0 0.0%	0 0.0%	0 0.0%	0 0.0%	0 0.0%	0 0.0%	0 0.0%	0 0.0%	0 0.0%	NaN% NaN%
5	0 0.0%	0 0.0%	0 0.0%	0 0.0%	0 0.0%	0 0.0%	0 0.0%	0 0.0%	0 0.0%	NaN% NaN%
6	0 0.0%	0 0.0%	0 0.0%	0 0.0%	0 0.0%	0 0.0%	0 0.0%	0 0.0%	0 0.0%	NaN% NaN%
7	0 0.0%	0 0.0%	0 0.0%	0 0.0%	0 0.0%	0 0.0%	0 0.0%	0 0.0%	0 0.0%	NaN% NaN%
8	0 0.0%	0 0.0%	0 0.0%	0 0.0%	0 0.0%	0 0.0%	0 0.0%	0 0.0%	0 0.0%	NaN% NaN%
9	0 0.0%	0 0.0%	0 0.0%	0 0.0%	0 0.0%	0 0.0%	0 0.0%	0 0.0%	0 0.0%	NaN% NaN%
	100% 0.0%	NaN% NaN%	NaN% NaN%	NaN% NaN%	NaN% NaN%	NaN% NaN%	NaN% NaN%	NaN% NaN%	NaN% NaN%	**100%** **0.0%**

	1	2	3	4	5	6	7	8	9	
1	5906 100%	0 0.0%	0 0.0%	0 0.0%	0 0.0%	0 0.0%	0 0.0%	0 0.0%	0 0.0%	100% 0.0%
2	0 0.0%	0 0.0%	0 0.0%	0 0.0%	0 0.0%	0 0.0%	0 0.0%	0 0.0%	0 0.0%	NaN% NaN%
3	0 0.0%	0 0.0%	0 0.0%	0 0.0%	0 0.0%	0 0.0%	0 0.0%	0 0.0%	0 0.0%	NaN% NaN%
4	0 0.0%	0 0.0%	0 0.0%	0 0.0%	0 0.0%	0 0.0%	0 0.0%	0 0.0%	0 0.0%	NaN% NaN%
5	0 0.0%	0 0.0%	0 0.0%	0 0.0%	0 0.0%	0 0.0%	0 0.0%	0 0.0%	0 0.0%	NaN% NaN%
6	0 0.0%	0 0.0%	0 0.0%	0 0.0%	0 0.0%	0 0.0%	0 0.0%	0 0.0%	0 0.0%	NaN% NaN%
7	0 0.0%	0 0.0%	0 0.0%	0 0.0%	0 0.0%	0 0.0%	0 0.0%	0 0.0%	0 0.0%	NaN% NaN%
8	0 0.0%	0 0.0%	0 0.0%	0 0.0%	0 0.0%	0 0.0%	0 0.0%	0 0.0%	0 0.0%	NaN% NaN%
9	0 0.0%	0 0.0%	0 0.0%	0 0.0%	0 0.0%	0 0.0%	0 0.0%	0 0.0%	0 0.0%	NaN% NaN%
	100% 0.0%	NaN% NaN%	NaN% NaN%	NaN% NaN%	NaN% NaN%	NaN% NaN%	NaN% NaN%	NaN% NaN%	NaN% NaN%	**100%** **0.0%**

Figure A-2: Test confusion matrices of the neural network trained to distinguish between "no defect" (class "0") and a defect location in the segments 1-8 (left) as well as confusion matrix of the network trained to distinguish between "no defect" and a defect location in the segments 9-16 (right) by means of sensor data obtained from the axial braiding ring during defect-free braiding

The confusion matrices for the networks trained on data from the radial braiding ring are on a qualitative basis similar to the networks trained on data from the axial ring. This is why they are not explicitly given in the main part of the thesis but in this appendix. The matrices for the tests of the networks on the fifth measurement with a simulated defect are shown in Figure A-3.

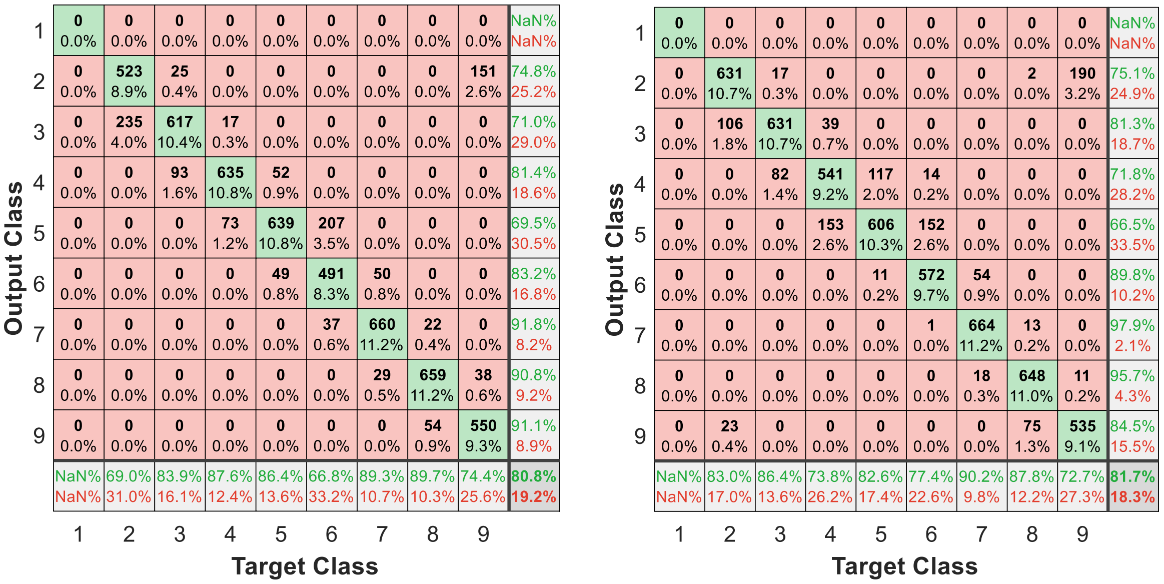

	1	2	3	4	5	6	7	8	9	
1	0 0.0%	0 0.0%	0 0.0%	0 0.0%	0 0.0%	0 0.0%	0 0.0%	0 0.0%	0 0.0%	NaN% NaN%
2	0 0.0%	523 8.9%	25 0.4%	0 0.0%	0 0.0%	0 0.0%	0 0.0%	0 0.0%	151 2.6%	74.8% 25.2%
3	0 0.0%	235 4.0%	617 10.4%	17 0.3%	0 0.0%	0 0.0%	0 0.0%	0 0.0%	0 0.0%	71.0% 29.0%
4	0 0.0%	0 0.0%	93 1.6%	635 10.8%	52 0.9%	0 0.0%	0 0.0%	0 0.0%	0 0.0%	81.4% 18.6%
5	0 0.0%	0 0.0%	0 0.0%	73 1.2%	639 10.8%	207 3.5%	0 0.0%	0 0.0%	0 0.0%	69.5% 30.5%
6	0 0.0%	0 0.0%	0 0.0%	0 0.0%	49 0.8%	491 8.3%	50 0.8%	0 0.0%	0 0.0%	83.2% 16.8%
7	0 0.0%	0 0.0%	0 0.0%	0 0.0%	0 0.0%	37 0.6%	660 11.2%	22 0.4%	0 0.0%	91.8% 8.2%
8	0 0.0%	0 0.0%	0 0.0%	0 0.0%	0 0.0%	0 0.0%	29 0.5%	659 11.2%	38 0.6%	90.8% 9.2%
9	0 0.0%	0 0.0%	0 0.0%	0 0.0%	0 0.0%	0 0.0%	0 0.0%	54 0.9%	550 9.3%	91.1% 8.9%
	NaN% NaN%	69.0% 31.0%	83.9% 16.1%	87.6% 12.4%	86.4% 13.6%	66.8% 33.2%	89.3% 10.7%	89.7% 10.3%	74.4% 25.6%	**80.8%** **19.2%**

	1	2	3	4	5	6	7	8	9	
1	0 0.0%	0 0.0%	0 0.0%	0 0.0%	0 0.0%	0 0.0%	0 0.0%	0 0.0%	0 0.0%	NaN% NaN%
2	0 0.0%	631 10.7%	17 0.3%	0 0.0%	0 0.0%	0 0.0%	0 0.0%	2 0.0%	190 3.2%	75.1% 24.9%
3	0 0.0%	106 1.8%	631 10.7%	39 0.7%	0 0.0%	0 0.0%	0 0.0%	0 0.0%	0 0.0%	81.3% 18.7%
4	0 0.0%	0 0.0%	82 1.4%	541 9.2%	117 2.0%	14 0.2%	0 0.0%	0 0.0%	0 0.0%	71.8% 28.2%
5	0 0.0%	0 0.0%	0 0.0%	153 2.6%	606 10.3%	152 2.6%	0 0.0%	0 0.0%	0 0.0%	66.5% 33.5%
6	0 0.0%	0 0.0%	0 0.0%	0 0.0%	11 0.2%	572 9.7%	54 0.9%	0 0.0%	0 0.0%	89.8% 10.2%
7	0 0.0%	0 0.0%	0 0.0%	0 0.0%	0 0.0%	1 0.0%	664 11.2%	13 0.2%	0 0.0%	97.9% 2.1%
8	0 0.0%	0 0.0%	0 0.0%	0 0.0%	0 0.0%	0 0.0%	18 0.3%	648 11.0%	11 0.2%	95.7% 4.3%
9	0 0.0%	23 0.4%	0 0.0%	0 0.0%	0 0.0%	0 0.0%	0 0.0%	75 1.3%	535 9.1%	84.5% 15.5%
	NaN% NaN%	83.0% 17.0%	86.4% 13.6%	73.8% 26.2%	82.6% 17.4%	77.4% 22.6%	90.2% 9.8%	87.8% 12.2%	72.7% 27.3%	**81.7%** **18.3%**

Figure A-3: Test confusion matrices of the neural network trained to distinguish between "no defect" (class "0") and a defect location in the segments 1-8 (left) as well as confusion matrix of the network trained to distinguish between "no defect" and a defect location in the segments 9-16 (right) by means of sensor data obtained from the radial braiding ring during braiding with a simulated defect

The matrices for the tests of the networks on the fifth defect-free reference measurement with the radial braiding ring are shown in Figure A-4. Again, the absence of any false positive defect detections is of vital importance for an interruption-free braiding when the monitoring system is used during regular braiding without any defect present.

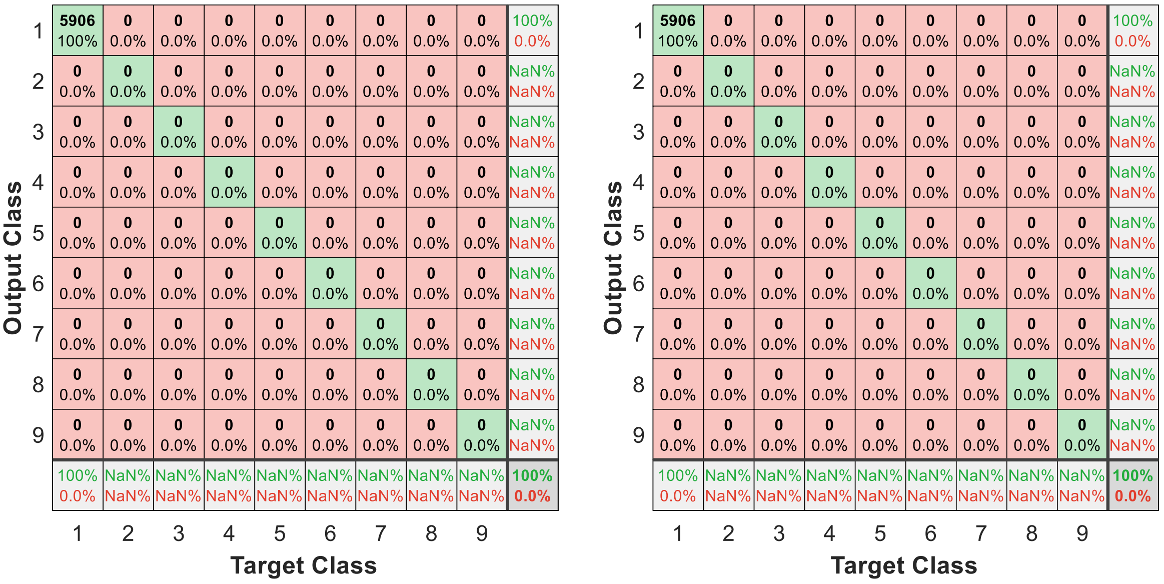

	1	2	3	4	5	6	7	8	9	
1	5906 100%	0 0.0%	0 0.0%	0 0.0%	0 0.0%	0 0.0%	0 0.0%	0 0.0%	0 0.0%	100% 0.0%
2	0 0.0%	0 0.0%	0 0.0%	0 0.0%	0 0.0%	0 0.0%	0 0.0%	0 0.0%	0 0.0%	NaN% NaN%
3	0 0.0%	0 0.0%	0 0.0%	0 0.0%	0 0.0%	0 0.0%	0 0.0%	0 0.0%	0 0.0%	NaN% NaN%
4	0 0.0%	0 0.0%	0 0.0%	0 0.0%	0 0.0%	0 0.0%	0 0.0%	0 0.0%	0 0.0%	NaN% NaN%
5	0 0.0%	0 0.0%	0 0.0%	0 0.0%	0 0.0%	0 0.0%	0 0.0%	0 0.0%	0 0.0%	NaN% NaN%
6	0 0.0%	0 0.0%	0 0.0%	0 0.0%	0 0.0%	0 0.0%	0 0.0%	0 0.0%	0 0.0%	NaN% NaN%
7	0 0.0%	0 0.0%	0 0.0%	0 0.0%	0 0.0%	0 0.0%	0 0.0%	0 0.0%	0 0.0%	NaN% NaN%
8	0 0.0%	0 0.0%	0 0.0%	0 0.0%	0 0.0%	0 0.0%	0 0.0%	0 0.0%	0 0.0%	NaN% NaN%
9	0 0.0%	0 0.0%	0 0.0%	0 0.0%	0 0.0%	0 0.0%	0 0.0%	0 0.0%	0 0.0%	NaN% NaN%
	100% 0.0%	NaN% NaN%	NaN% NaN%	NaN% NaN%	NaN% NaN%	NaN% NaN%	NaN% NaN%	NaN% NaN%	NaN% NaN%	**100%** **0.0%**

	1	2	3	4	5	6	7	8	9	
1	5906 100%	0 0.0%	0 0.0%	0 0.0%	0 0.0%	0 0.0%	0 0.0%	0 0.0%	0 0.0%	100% 0.0%
2	0 0.0%	0 0.0%	0 0.0%	0 0.0%	0 0.0%	0 0.0%	0 0.0%	0 0.0%	0 0.0%	NaN% NaN%
3	0 0.0%	0 0.0%	0 0.0%	0 0.0%	0 0.0%	0 0.0%	0 0.0%	0 0.0%	0 0.0%	NaN% NaN%
4	0 0.0%	0 0.0%	0 0.0%	0 0.0%	0 0.0%	0 0.0%	0 0.0%	0 0.0%	0 0.0%	NaN% NaN%
5	0 0.0%	0 0.0%	0 0.0%	0 0.0%	0 0.0%	0 0.0%	0 0.0%	0 0.0%	0 0.0%	NaN% NaN%
6	0 0.0%	0 0.0%	0 0.0%	0 0.0%	0 0.0%	0 0.0%	0 0.0%	0 0.0%	0 0.0%	NaN% NaN%
7	0 0.0%	0 0.0%	0 0.0%	0 0.0%	0 0.0%	0 0.0%	0 0.0%	0 0.0%	0 0.0%	NaN% NaN%
8	0 0.0%	0 0.0%	0 0.0%	0 0.0%	0 0.0%	0 0.0%	0 0.0%	0 0.0%	0 0.0%	NaN% NaN%
9	0 0.0%	0 0.0%	0 0.0%	0 0.0%	0 0.0%	0 0.0%	0 0.0%	0 0.0%	0 0.0%	NaN% NaN%
	100% 0.0%	NaN% NaN%	NaN% NaN%	NaN% NaN%	NaN% NaN%	NaN% NaN%	NaN% NaN%	NaN% NaN%	NaN% NaN%	**100%** **0.0%**

Figure A-4: Test confusion matrices of the neural network trained to distinguish between "no defect" (class "0") and a defect location in the segments 1-8 (left) as well as confusion matrix of the network trained to distinguish between "no defect" and a defect location in the segments 9-16 (right) by means of sensor data obtained from the radial braiding ring during defect-free braiding

In Table 3-4, the accuracies of the detection algorithms regarding segment prediction as well as the false positive and false negative detections on the independent test data set 1 are shown. In the introductory explanations on the derivation of the defect detection algorithms, it is mentioned that the author used an interleaved method for subdividing data from the first four reference and defective measurements to obtain training and validation data sets. Given natural process fluctuations, it is argued that the interleaved data subdivision method is expected to create trained networks that can better generalize on unknown data. A comparison of the performance of the algorithms trained on data sets obtained by interleaved (data without brackets) and random data subdivision (data in brackets) is given in Table A-1. The figures in the table were obtained when testing the algorithms on independent data from test data set 1 (fifth defect-free measurement and fifth measurement with a simulated defect). Note that the results on the random data subdivision were solely generated for the reader's better understanding after the development of the detection algorithms. They were not taken into account during the development of the algorithms. Except for the accuracy in segment prediction of network 1 for data from the radial braiding ring, the accuracy values can generally be observed to be slightly lower for the random data subdivision compared to the interleaved data subdivision. However, these differences, especially the 0.2 percentage points in case of the combined approach, can be regarded as minor. The difference between the two methods of data subdivision becomes more pronounced when the combined network approach is tested on data with a real fibrous ring. As detailed in the explanation to Figure 3-41, the interleaved data subdivision method achieved an accuracy in segment prediction of 77.3 % in case of the axial braiding ring and 53.7 % in case of the radial braiding ring. A random data subdivision yielded 76.2 % for the axial and 52.6 % for the radial ring, respectively. Although the difference is still not substantial, this increased difference of 1.1 percentage points in case the algorithms are tested on data with a real braiding defect suggests that an interleaved data subdivision for the training phase actually leads to a higher ability of the trained networks to generalize on unknown data.

Table A-1: Accuracies of segment prediction, false negative and false positive rates for the neural networks processing data from the axial as well as from the radial braiding ring; data obtained by applying the networks to independent test data set 1 (defect-free and simulated defect) that was not used for training; data without brackets from neural networks trained on data sets obtained from subdivision by the interleaved method; data in brackets from networks trained on data sets obtained from random subdivision

	Axial Braiding Ring			**Radial Braiding Ring**		
	Accuracy Segment Prediction	False Negative Rate	False Positive Rate	Accuracy Segment Prediction	False Negative Rate	False Positive Rate
Network 1 Seg. 1-8	85.8 % (85.5 %)	0 % (0 %)	0 % (0 %)	80.2 % (81.3 %)	0 % (0 %)	0 % (0 %)
Network 2 Seg. 9-16	83.0 % (82.9 %)	0 % (0 %)	0 % (0 %)	81.7 % (81.0 %)	0 % (0 %)	0 % (0 %)
Combined Approach	92.2 % (92.0 %)	0 % (0 %)	0 % (0 %)	90.7 % (90.5 %)	0 % (0 %)	0 % (0 %)

In the explanation to Figure 3-36, it is mentioned that the minimal architecture of the neural networks of the detection algorithms with only one hidden layer of four neurons was chosen for reasons of limited training effort and the opportunity to implement the algorithms on microcontrollers while still allowing a real-time capable process monitoring. Nevertheless, the author would like to show what impact more elaborate networks may have on the quality of the defect detection. As with the above additional data on subdivision methods, note that the results on the more elaborate networks were generated after the development of the detection algorithms and solely in order to provide the reader with a broader picture on the matter. This additional data was not taken into account during the development of the detection algorithms. In Table A-2, the detection parameters are shown for neural networks of two hidden layers of four neurons each (data without brackets) and neural networks of one hidden layer consisting of eight neurons (data in brackets). It can be observed that the combined networks with two hidden layers of four neurons do not result in any significant improvement in correct segment prediction compared to the networks with one hidden layer of four neurons (cf. Table 3-4 or data without brackets in Table A-1). The combined networks that feature only one larger hidden layer of eight neurons achieve higher detection accuracies of 2.1 and 1.7 percentage points, respectively. As mentioned in the outlook in chapter 6, this shows that there is room for improvement of the trainable detection algorithms for the sensor integrated braiding rings. However, major improvements cannot be expected without significantly increasing the sizes of the networks, which may counteract the benefits of minimal network architectures of limited training effort and executability on systems with limited computational power.

Table A-2: Accuracies of segment prediction, false negative and false positive rates for the neural networks processing data from the axial as well as from the radial braiding ring; data obtained by applying the networks to independent test data set 1 (defect-free and simulated defect) that was not used for training; data without brackets from neural networks comprised of two hidden layers of four neurons each, data in brackets from neural networks comprised of one hidden layer with eight neurons

	Axial Braiding Ring			**Radial Braiding Ring**		
	Accuracy Segment Prediction	False Negative Rate	False Positive Rate	Accuracy Segment Prediction	False Negative Rate	False Positive Rate
Network 1 Seg. 1-8	84.4 % (85.5 %)	0 % (0 %)	0 % (0 %)	81.7 % (82.2 %)	0 % (0 %)	0 % (0 %)
Network 2 Seg. 9-16	83.1 % (86.3 %)	0 % (0 %)	0 % (0 %)	81.2 % (83.4 %)	0 % (0 %)	0 % (0 %)
Combined Approach	92.5 % (94.3 %)	0 % (0 %)	0 % (0 %)	89.2 % (92.4 %)	0 % (0 %)	0 % (0 %)

Additional data to subsection 3.3.1

In subsection 3.3.1, only exemplary measurement results from the photodiode are given because they already show the limitations of the approach of discretely monitoring the braid formation zone by a single sensor and therefore justify the need for a camera-based inspection of the whole braid formation zone. Nevertheless, the diagram in Figure A-5 shall reassure the reader that the characteristic differences in yarn transit intervals in conjunction with a defective yarn are also observable at different braiding angles. The transit interval between the yarn preceding the defective yarn and the defective yarn itself is labeled I1 (cf. orange color in Figure 3-42). The interval between the defective yarn and its succeeding yarn is labeled as I2 (cf. blue color in Figure 3-42). It can be observed that the mean values of I1 are significantly smaller than the mean values of I2 in all experiment variants. Furthermore, the values both for I1 and I2 differ significantly from the expected interval length if no defect would be present. This can be seen from the horizontal dotted line, which is drawn-in at 0.4615 s. As explained in the own publication [90], this value is defined by the number of horn gears $n_{horn\ gears} = 32$ in the RF 1/128-100 braiding machine, which was used for the experiments, the speed of horn gear rotation $r = 65\ rpm$ and the number of braiding yarns $n_{yarn} = 64$. The time it takes a carrier to complete a full 360°-circulation through the machine can be calculated to

$$t_{360°} = \frac{n_{horn\ gears}}{2 \cdot \frac{r}{60\ \frac{s}{min}}} = \frac{32}{2 \cdot \frac{65\ rpm}{60\ \frac{s}{min}}} \approx 14.77\ s \qquad \text{(A-1).}$$

The factor 2 in the denominator is due to the fact that a carrier covers two horn gears as the horn gears fulfill one complete revolution. The interval length $t_{transit\ interval}$ between yarn transits of the same direction of circulation through the light barrier then calculates to

$$t_{transit\ interval} = \frac{t_{360°}}{\frac{n_{yarn}}{2}} \approx \frac{14.77\ s}{\frac{64}{2}} \approx 0.4615\ s \qquad \text{(A-2).}$$

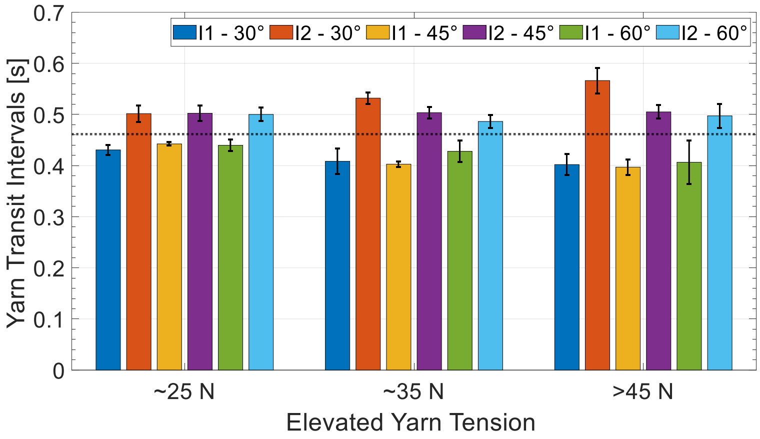

Figure A-5: Mean yarn transit intervals and their standard deviation in conjunction with the defective yarn depending on level of elevated yarn tension and braiding angle φ; the drawn-in horizontal line indicates the expected interval length if no defect would be present

The fact that I1 and I2 are distinct from this expected value in all configurations shows that the different yarn curvatures and thus yarn distances due to anomalous yarns tensions are equally observable at different braiding angles φ. This means that the detection principle is not expected to be negatively influenced by a particular change in braiding angle φ. From the illustrated data, a slight trend towards a larger difference between I1 and I2 is observable with the two higher levels of increased yarn tension of ~35 N and >45 N compared to the lower level of yarn tension of ~25 N. This suggests that higher levels of anomalous yarn tension are easier to detect than moderate yarn tension increases. The fact that I2 appears to decrease with higher braiding angles φ at yarn tensions of ~35 N and >45 N may hint at different frictional interaction between the yarns and the braiding ring due to different cone angles β and reaction forces. However, it is to be noted that, due to the limited length of the cylindrical mandrel and the cutting-off of settling effects at the beginning of braiding, the bars for a braiding angle of $\varphi = 30°$ are only calculated from three data points each. This makes an interpretation of this particular data and the derivation of a trend difficult. As stated in subsection 3.3.1, the bars for $\varphi = 45°$ and $\varphi = 60°$ are calculated from five and nine data points, respectively, and are therefore more reliable.

Additional data to subsection 3.3.2

In the final paragraph on the development of the optical defect detection algorithm, it is explained that the measurement of yarn distances does not have to be operated on the whole braid formation zone. It can instead be modified in a way that it operates separately on distinct segments, e.g. quarters, of the braid formation zone. Thereby, a monitoring of the braiding process and a measurement of yarn distances by camera is ensured even when the view on certain areas of the braid formation zone is obstructed. This may be the case when mandrels that are bent need to be overbraided or when robots on either side of a braiding machine guide a fragile mandrel through the braiding machine. Figure A-6 shows the graphical result of the optical yarn distance measurements obtained from the modified version of the algorithm during braiding of $n_{yarn} = 64$ 12k yarns and an elevated tension of a single yarn of ~35 N. This is exactly the same experiment that is illustrated in the compilation of diagrams in Figure 3-53. The only difference is that in Figure 3-53, the image processing algorithm was set to operate on the whole braid formation zone. This means that the imaginary circles as shown in Figure 3-51, right are sought to intersect with the yarns $n_{yarn} = 64$ times. In Figure A-6, the algorithm was modified in a way that it operates independently on the four quarters of the braid formation zone. This means that the imaginary circles are sought to intersect with yarns $\frac{n_{yarn}}{4} = 16$ times on each quarter segment. If this condition is not met in a specific quarter, only this specific quarter is not taken into account for the measurement of yarn distances. The other quarters can still be evaluated. This is in contrast to the unmodified version of the image processing algorithm as presented in subsection 3.3.2. As shown in Figure 3-53, only the frame numbers 1, 2, 4, 5, 7, 10, 11, 13 and 15 meet all implemented plausibility checks including $n_{yarn} = 64$ yarn intersections of the imaginary circles. In Figure A-6, it is observable that exactly these frames produce measurable data on all four quarters of the braid formation zone. In the other frames, at least one quarter is not evaluable by the algorithm. This is why these frames are dropped in the unmodified version of the algorithm and do not appear in Figure 3-53. An exception to this is frame number 8. This frame produces data on all four segments of the braid formation zone in Figure A-6 but does not appear in Figure 3-53. A reason for this can be the failure to meet one of the other implemented plausibility checks, e.g. an even number of yarns in both directions of circulation, in the unmodified version of the algorithm. As can be seen in the diagrams in Figure A-6 below, the modified algorithm cannot calculate distances to yarns that are adjacent to the segment edges. It may therefore also be the case that in frame number 8 a yarn that is adjacent to the edge of a quarter segment fails to meet a plausibility check in the unmodified version of the algorithm, which does not carry any weight in the modified version of the algorithm.

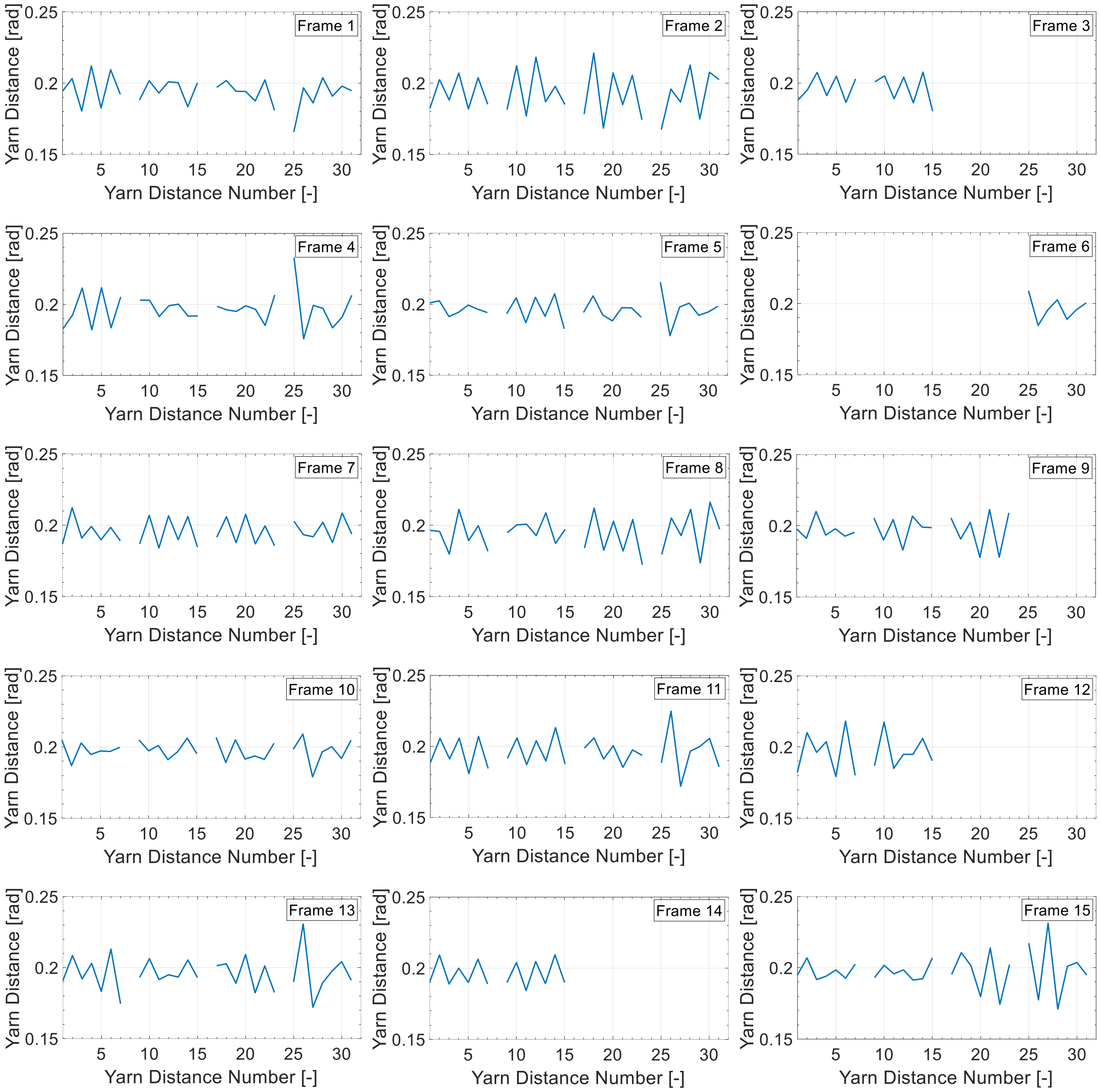

Figure A-6: Angular yarn distances of the counterclockwise yarns for the first 15 video frames from the experiment with the 12k yarns and an increased tension of a single yarn of ~35 N evaluated separately on the four quarters of the braid formation zone

Figure A-7 shows the yarn distance diagram that is obtained when averaging all distance measurements per yarn over the first 15 frames as shown in Figure A-6. In principle, this diagram is comparable to the diagram shown in Figure 3-54. The only difference is that the diagram in Figure A-7 is calculated from the measurement results of the modified algorithm that operates on the quarter segments of the braid formation zone separately and Figure 3-54 is calculated from the unmodified version of the algorithm that operates on the whole braid formation zone. In Figure A-7, it can be observed that even though the modified algorithm cannot take the yarns into account that are adjacent to the edges of the quarter segments, it is still able to gather data on each yarn. This is because the yarns circularly move through the braiding machine over the course of the first 15 video frames and therefore the particular yarn that cannot be taken into account constantly changes. When further interpreting the output of the averaging step in Figure A-7, it can be said that there appears to be a yarn of higher tension that contributes to the yarn distance measurements 24 and 25. This interpretation result from the first 15 video frames processed by the modified algorithm is the same as can be obtained from the unmodified algorithm as shown in Figure 3-54. The fact that the defect-characteristic anomaly in the averaged data between distance measurement number 24 and 25 is less pronounced in Figure A-7 than in Figure 3-54 is due to the unfortunate coincidence that the defective yarn is adjacent to an edge of a quarter segment in at least the first three of the 15 frames (cf. Figure A-6) and therefore cannot properly be evaluated by the modified algorithm in these frames.

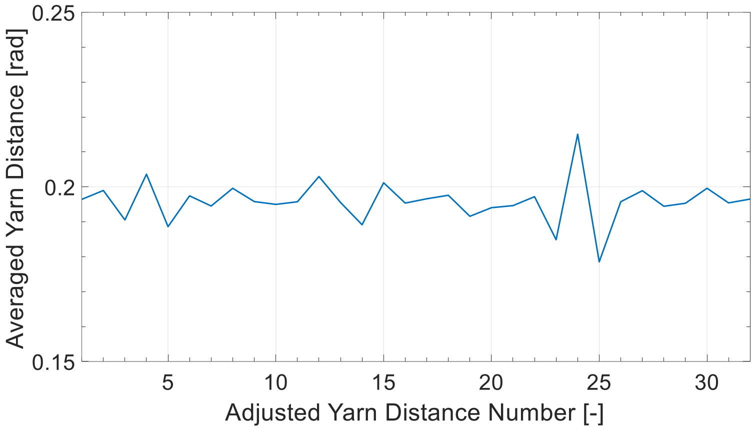

Figure A-7: Averaged yarn distances over the 15 video frames shown in Figure A-6; yarn distance numbers referenced to frame number 1 in Figure A-6

Appendix B: Publications

Granted Patent

[81] Maidl S, Mierzwa A, Matschinski A. Thread Tension Anomalies Detection (European Patent Specification EP3784826B1); 2021.

Within the scope of the application process, the above patent was also published with identical content under the numbers EP3561165A1, WO2019206648A1 and EP3784826A1.

Reviewed Papers

[64] Maidl S, Sabieraj M, Mierzwa A, Ebel C, Drechsler K. Investigating the unwinding behavior of technical yarns and development of a new sensor system for the braiding process. IOP Conf. Ser.: Mater. Sci. Eng. 2018;406:12065.

[88] Maidl S, Fernández Villalba Á, Kind K, Drechsler K. Development of sensor integrated braiding rings for the automated detection of braiding defects. Materials Today: Proceedings 2020.

[89] Maidl S, Hilbck M, Kind K, Drechsler K. Optical inspection of the braid formation zone during manufacturing of preforms from reinforcement fibers for defect detection purposes. Front. Mater. 2023;10.

The above paper [89] was written during examination of the thesis at hand and is listed here for the sake of completeness of the academic work conducted.

Non-Reviewed Conference Papers

[65] Maidl S, Mierzwa A, Ebel C, Drechsler K. Development of a Novel Type of Online Monitoring System for the Braiding Process. ECCM18 - 18th European Conference on Composite Materials. Athens, Greece; 2018.

[90] Maidl S, Putze L, Kind K, Drechsler K. Automated Detection of Yarn Gaps during Radial Braiding of Carbon Fiber by Means of Light Barriers. ECCM20 - 20th European Conference on Composite Materials. Lausanne, Switzerland; 2022.

Appendix C: Supervised Student Theses

Within the framework of the dissertation at hand, the following student theses at the Chair of Carbon Composites of Technical University of Munich were co-supervised by the author of the dissertation at hand and contributed in part to the present dissertation. The theses were conducted under substantial scientific, technical and contentual guidance from the author of the dissertation at hand. The author would like to thank all students for their dedication to the conducted work and wishes them all the best for their future.

[59] Putze L. Lichtschranken als Detektionsmöglichkeit von Garnlücken beim Flechten von Carbonfasern. Bachelor Thesis. Technical University of Munich, Garching, Germany; 2019.

[82] Sabieraj M. Charakterisierung des Abspulverhaltens von technischen Garnen im Flechtprozess. Bachelor Thesis. Technical University of Munich, Garching, Germany; 2018.

[87] Fernández Villalba Á. Advancement of a Floating Supported Braiding Ring for the Sensory Detection of Braiding Defects. Master Thesis. Technical University of Munich, Garching, Germany; 2018.

[91] Hilbck M. Optische Vermessung und Analyse der Fadenkrümmungen beim Radialflechtprozess zur frühzeitigen Erkennung von Prozessfehlern. Term Project. Technical University of Munich, Garching, Germany; 2022.

[92] Eckardt B. Optimierung einer Additive Manufacturing Anlage zur Herstellung eines Inline Monitoring Systems für den Flechtprozess. TUMKolleg Project. Technical University of Munich, Garching, Germany; 2018.

[93] Mondelli FG. Weiterentwicklung eines sensorintegrierten Klöppels zur Überwachung des Flechtprozesses. Bachelor Thesis. Technical University of Munich, Garching, Germany; 2021.

The following student thesis were also co-supervised within the framework of the employment of the author of the dissertation at hand at the Chair of Carbon Composites during the preparation of the present dissertation. These theses were also conducted under substantial scientific, technical and contentual guidance from the author of the dissertation at hand but did not contribute to the present dissertation and are therefore not explicitly cited in this dissertation. Nevertheless, the author still learned from co-supervising these theses. The author also wishes these students all the best for their future.

[96] Wanninger M. Entwicklung eines Auslegers für landwirtschaftliche Feldspritzen aus faserverstärktem Kunststoff, Term project, Garching, Germany, 2018.

[97] Rickert TC. Klassifizierung verschiedener Textilien auf Basis von 2D-Bilddaten mit Hilfe künstlicher Intelligenz, Master Thesis, Garching, Germany, 2019.

[98] Dickes D. Evaluation of tungsten fiber reinforced plastics concerning manufacturability, mechanical properties, and potential applications, Master Thesis, Technical University of Munich, Garching, Germany, 2019.

[99] van Linn H. Lokalisierung von greifbaren Textilsäumen in 2D Bildern mittels einer auf synthetischen Daten trainierten künstlichen Intelligenz, Master Thesis, Technical University of Munich, Garching, Germany, 2019.

[100] Glas JK. Weiterentwicklung zweier selbst regelnder Fadenbremsen für den Umspulprozess beim Flechten von technischen Textilien. Bachelor Thesis, Technical University of Munich, Garching, Germany, 2019.

[101] Nitzl R. Online Prozessmonitoring beim Wickeln von kohlenstofffaserverstärkten Kunststoffen, Bachelor Thesis, Technical University of Munich, Garching, Germany, 2020.